Title

Aerosol Deposition in Healthy and Emphysematous Rat Lungs : : Insights From MRI Measurements and Computational Simulations

Permalink

Author

Oakes, Jessica M.

Publication Date

2013

Peer reviewed|Thesis/dissertation

UNIVERSITY OF CALIFORNIA, SAN DIEGO

Aerosol Deposition in Healthy and Emphysematous Rat Lungs: Insights From MRI Measurements and Computational Simulations

A dissertation submitted in partial satisfaction of the
requirements for the degree
Doctor of Philosophy

in

Engineering Sciences (Mechanical Engineering)

by

Jessica M. Oakes

Committee in charge:

Alison L. Marsden, Co-Chair
Chantal Darquenne, Co-Chair
Richard Buxton
Juan C. del Alamo
Sutanu Sarkar
Irene Vignon-Clementel

2013

The dissertation of Jessica M. Oakes is approved, and it is acceptable in quality and form for publication on microfilm and electronically:

Co-Chair

Co-Chair

University of California, San Diego

2013

DEDICATION

To Tom:

Whose love and support
has made this possible

EPIGRAPH

A dream doesn't become reality
through magic; it takes sweat,
determination and hard work.
—Colin Powell

Learn from yesterday, live for today,
hope for tomorrow.
The important thing is not to stop questioning.
–Albert Einstein

In order to succeed, your desire
for success should be greater
than your fear of failure.
–Bill Cosby

TABLE OF CONTENTS

LIST OF FIGURES

LIST OF TABLES

ACKNOWLEDGEMENTS

This PhD work would not have been possible without my advisers, Chantal Darquenne and Alison Marsden. Both advisers were instrumental in my success, supporting me both professionally and personally. Chantal taught me how to perform careful and mindful exposure experiments. She was always willing to share her admirable expertise in pulmonary physiology and teach me about aerosol transport in the lung. Many times I became tired or frustrated with how things were progressing and Chantal would remind me to relax and she would give me another way to look at the problem. One of the most important things I learned from Chantal was how to write. Chantal helped me to put together papers that were scientifically important, but easy to understand. I will always be grateful of the time and energy that Chantal used to help me and this work.

Alison welcomed me into her research group about half way through my first year of studies which helped me to become more integrated with other engineering students and faculty as well as learn about sophisticated numerical methods. Alison's vast knowledge in computational physics was extremely helpful in helping me to perform my simulations. Even though I will always be thankful that Alison taught me how to perform numerical experiments, I think I will be most thankful for the mentor-ship and support Alison gave to me. Alison was always interested in helping me make my work better as well as helping me with my personal growth. She guided me in making difficult decisions, both professionally and personally. Alison was always patient, reminding me often of the importance and bigger picture of this work.

In July of 2011 I was given the opportunity to go to INRIA Paris Rocquencourt in France to study with Irene Vignon-Clementel and Celine Grandmont for three months. Before this trip, I was starting to lose interest in my project. However, working with Irene and Celine helped me to become excited about research again and I further learned how my experimental work could be useful in performing numerical experiments. Irene was especially helpful, dedicating much of her time to me while I was visiting INRIA. She continued to meet with me on a weekly basis for the following two years, sharing her knowledge in CFD simulations

and boundary conditions. Irene helped me to build confidence in both myself and my work. She pushed me to do careful simulations, while challenging me to think about the problem with the point of view of a mathematician. I am very thankful that I was given the opportunity to work with Irene and am very excited to go to INRIA to perform a post doctoral-ship with Irene and Celine.

Much of this work would not be possible without the help form Shawn Shadden, Miriam Scadeng and Ellen Breen. Shawn gracefully shared his particle tracking code with me that I used in Chapters 6 and 7. Miriam spent many nights with me the fMRI center at UCSD. Without her time and willingness to meet with me, I would never have been able to collect so much imaging data. Ellen showed Chantal and I how to perform the animal exposure experiments, how to induce emphysema and how to slice and image the lungs to determine the linear mean intercepts. I am very thankful for the time Ellen spent with me and her patience with sharing physiology laboratory space with a mechanical engineer.

I am very lucky to have friends that have supported me through this PhD. First, I would like to thank Rui Carlos Sá. Rui encouraged me daily to continue with my PhD and advised me on how to move forward. He was always willing to set aside his important work to help me figure out a problem that I was stuck on. I am also thankful that Rui took the time to read and edit many of the chapters of this dissertation. Next, I would like to thank Mahdi Esmaily-Moghadam. The work in this dissertation would not have been possible without Mahdi's numerical expertise and implementation. Mahdi was always willing to take the time to explain things to me and to help me to use his software. Additionally, Mahdi also took the time to read and edit one of the chapters of this dissertation. I would also like to acknowledge the other members of our lab group: Abhay Ramachandra, Weiguang Yang, Ethan Kung, Sethu Sankaran, Chris Long and Sharouz Alimohammidi. Each of these students or postdocs helped me selflessly and happily. I would also like to acknowledge my friends Eric Arobone, Patrick Folz, Matt Lave and Michael Gollner. This five of us started our graduate studies at UCSD together and were fortunate enough to continue to be friends throughout the past 5 years. I was also lucky to become good friends will Silvana Sartori. After Silvana graduated, we continued to talk almost daily, giving me much needed support and advice. There will always be a place in my heart for Katie Osterday. Katie was the kindest most energetic person I have ever had the privilege to know. Everyday I try to embody Katie and to ”Live Life like Katie did”. Thank you Katie for teaching me these valuable lessons.

I have been fortunate enough to work with some great undergraduates. Ghislain Tchantchou, Maria Borja, Kevin Tang and Miho Yoshida all helped me with data analysis. Without their dedication, much of the work presented in this dissertation would not be possible. I would also like to acknowledge the other members of the NASA group; Kim Prisk, Cortney Henderson, Trevor Cooper and Janelle Fine. Kim helped me with my MRI experiments (chapter 4), giving me honest and helpful advice. Cortney encouraged me and my work and always spent a few minutes of her time to listen to me. Both Janelle and Trevor were helpful in computer, software and experiment problems. I would also like to thank Sue Henderson with helping me with implementing and understanding the statistics used in chapter 5. I would also like to thank Jeff Struthers and Harrieth Wagner. Both Jeff and Harrieth helped me with equipment at the MTF as well as with ordering supplies.

My family, Marie Walters, David Oakes, Chris Oakes Ruth Oakes and Betty and Dominick Farina always gave me love and support through this dissertation. The fact that they are proud of me has helped me to push through some of the most difficult times of this dissertation. I would like to give the deepest thanks to my husband, Thomas Diewald. Tom is my number 1 supporter, encouraging me to continue to work hard and to never give up. It might seem weird, but I would also like to thank my dog, Zoey. Zoey brings the utmost joy to my life, bringing a smile to my face no matter how my day went.

I would like to thank the financial institutions that supported myself and this work. This work was supported by a graduate fellowship from the National Science Foundation, a travel grant from the Burroughs Wellcome Fund, a Burroughs Fund Career Award (Alison Marsden), associated INRIA team grant (Irene Vignon-Clementel and Celine Grandmont), and 1R21HL087805-02 from the

NHLBI. This dissertation has resulted in the following papers that have been published or submitted for publication. The dissertation author was the primary investigator and author of these publications

Chapter 3

Jessica M. Oakes, Miriam Scadeng, Ellen C. Breen, Alison L. Marsden, Chantal Darquenne. "Rat Airway Morphometry Measured from In Situ MRI-Based Geometric Models", *Journal of Applied Physiology.* 112: 1921-1931. 2012.

Chapter 4

Jessica M. Oakes, Miriam Scadeng, Ellen C. Breen, G. Kim Prisk, Chantal Darquenne. "Regional Distribution of Aerosol Deposition in Rat Lungs Using Magnetic Resonance Imaging", *Annals of Biomedical Engineering.* 41(5): 967-978. 2013

Chapter 6

Jessica M. Oakes, Alison Marsden, Celine Grandmont, Shawn Shadden, Chantal Darquenne, Irene Vignon-Clementel "Towards Animal Specific Airflow Simulation and Particle Deposition in Health and Emphysema: From In-Vivo to In-Silco Experiments", *Submitted.*

VITA and PUBLICATIONS

2008	B. S. in Mechanical Engineering, Rochester Institute of Technology
2008	M. S. in Mechanical Engineering, Rochester Institute of Technology
2013	Ph. D. in Engineering Sciences (Mechanical Engineering), University of California, San Diego

PUBLICATIONS

Jessica M. Oakes, Steven Day, Steven J. Weinstein, Risa J. Robinson ”Flow Field Analysis in Expanding Healthy and Emphysematous Alveolar Models Using Particle Image Velocimetry”, *Journal of Biomechanical Engineering*, 132(2): 021008-1 - 021008-9. 2010.

Jessica M. Oakes, Miriam Scadeng, Ellen C. Breen, Alison L. Marsden, Chantal Darquenne. ”Rat Airway Morphometry Measured from In Situ MRI-Based Geometric Models”, *Journal of Applied Physiology*. 112: 1921-1931. 2012.

Jessica M. Oakes, Miriam Scadeng, Ellen C. Breen, G. Kim Prisk, Chantal Darquenne. ”Regional Distribution of Aerosol Deposition in Rat Lungs Using Magnetic Resonance Imaging”, *Annals of Biomedical Engineering*. 41(5): 967-978. 2013

Jessica M. Oakes, Alison Marsden, Celine Grandmont, Shawn Shadden, Chantal Darquenne, Irene Vignon-Clementel ”Towards Animal Specific Airflow Simulation and Particle Deposition in Health and Emphysema: From In-Vivo to In-Silco Experiments”, *Submitted*.

AWARDS

National Science Foundation Fellowship
Burroughs Wellcome Fund Travel Grant
Whitacker Scholarship

DISSERTATION ABSTRACT

Aerosol Deposition in Healthy and Emphysematous Rat Lungs: Insights From MRI Measurements and Computational Simulations

by

Jessica M. Oakes

Doctor of Philosophy in Engineering Sciences (Mechanical Engineering)

University of California, San Diego, 2013

Alison L. Marsden, Co-Chair
Chantal Darquenne, Co-Chair

Understanding the fate of inhaled aerosol particles in healthy and diseased lungs may help in assessing the toxic health effects of airborne particulate matter or the efficiency of therapeutic drugs delivered through the lung. This dissertation focused on determining aerosol particle deposition patterns in healthy and emphysematous rats lungs by utilizing experimental and numerical methods. In the experimental part of the study, both airway morphometry and deposition patterns were determined by MRI. In the morphometry study, healthy rat lungs were imaged in vivo. Airway geometries were extracted from the MR images and the morphometric dimensions were validated against previous studies. In the aerosol deposition study, healthy and emphysematous rats were exposed by mechanical ventilation to iron-oxide particles with $1.22\mu m$ mass mean aerodynamic diameter (MMAD). The lungs were imaged with a MR gradient echo sequence and the signal decay rate, R_2^*, was calculated from the signal intensity images. Data showed a significantly higher R_2^* in the rats exposed to particles than in the control rats (no aerosol exposure) both for the healthy and emphysematous groups. A calibration experiment showed that concentration of deposited particles in tissue samples was linearly related to R_2^*. Particle concentration and relative dispersion of particle deposition sites in all lung lobes tended to be higher in the emphysematous rats compared to the healthy rats.

To further study particle deposition sites in the rat lungs, multi-scale computational fluid dynamics (CFD) simulations were performed. The global resistance and compliance of the rat lungs were determined by solving a global resistance/compliance (RC) model. This same RC model was then employed as Neumann boundary conditions in the 0D-3D simulations. Deposition and distribution of particles to the rat lobes was determined for particles with the same diameter as those used in the experiments. Simulations were performed representing healthy, homogeneous and localized emphysema. Emphysema location was determined by utilizing findings from the experimental data. Deposition in the 3D model was higher in the emphysematous cases compared to the healthy cases. Additionally, there was an increase in delivery of particle-laden air to the diseased regions of the lung, compared to the healthy regions. Good agreement was found when comparing the simulated normalized delivery of particles to each lobe to the normalized experimental deposition data. This work is the first to compare deposition sites found numerically and experimentally in both healthy and emphysematous lungs. In future studies, the multi-scale CFD models developed here may be advanced to include particle tracking downstream of the 3D model.

Chapter 1

Introduction

1.1 Lung Physiology

The respiratory system's main function is to perform gas exchange. In respiration, venous blood is pumped into the pulmonary capillaries by the right ventricle where oxygen is absorbed by the blood and carbon dioxide is exchanged with the inhaled air, the oxygenated blood is then delivered to the rest of the body. The carbon dioxide rich air is exhaled out of the body. Besides gas exchange, the lung metabolizes compounds, acts as the first line of defense against inhaled pathogens, and produces airflow for speech. The pulmonary airways may be characterized into three sections: (1) the upper respiratory airways, (2) the conducting zone and the (3) acinus, or respiratory zone (see Figure 1.1). The upper airways include the mouth/nose, as well as the throat and larynx. The airflow in the upper airways is turbulent or transitional, which is mainly caused by the decreased cross sectional area of the larynx, and is often described as the laryngeal jet. This turbulence continues in the conducting airways and then dissipates after a few airway generations. Once the airflow reaches the respiratory zone, the flow is moving very slowly with Reynolds numbers approximately equal to one.

Respiration is driven by a pressure gradient between the respiratory zone and the mouth, caused by the downward movement of the diaphragm. During inspiration, the negative pressure, relative to atmosphere, draws oxygen-rich air into the lungs until the pressure within the alveolar region is equal to the atmospheric pressure. During quiet normal breathing, expiration is caused by a passive relaxation of the diaphragm. The pressure versus volume relationship during inflation and deflation is not equal (i.e. the volume for a given pressure is greater during exhalation).

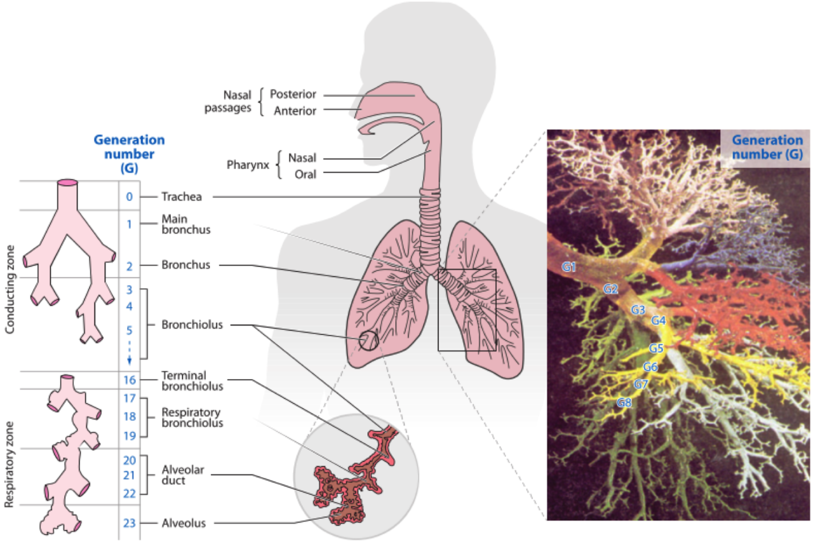

Figure 1.1: Schematic of the human respiratory system and cast of human airways. Figure from Kleinstreuer et al. 2010 [36]

1.2 Particle Deposition in the Lung

Inhaled small particles have the potential to systematically enter the body after they deposit on the lung surface. Once deposited, these particles may either be cleared from the lungs by mucociliary clearance or by macrophage uptake. Particles that are not cleared from the lung may enter the blood stream through the capillaries in the lung septa. While only a small percentage of inhaled particles enters the body, there has been a significant amount of research dedicated to understanding the mechanisms of deposition. These studies are motivated by the potential to reduce exposure to toxic ariborne particulates or to develop efficient and cost effective inhalable aerosol medications.

The region of the lung where deposition occurs is influenced by the deposition mechanism as well as influenced by the geometry of the airways, the breathing pattern, disease presence and the particle's properties. Particles are typically classified based on their mass median aerodynamics diameter (MMAD). The MMAD is defined as:

$$d_{ae} = d_g \sqrt{\frac{\rho_p}{\rho_0 \chi}} \tag{1.1}$$

where d_g is the geometric diameter of the particle, ρ_p is the density of the particle, ρ_0 is the density of water, and χ is the shape parameter. In humans, particles with a MMAD less than 5 μm have the potential to deposition on the lung wall [11], while particles with MMAD greater than $5 \mu m$ are more likely to deposit in the upper respiratory tract. Figure 1.2 shows the size and terminology classification of several airborne particulates.

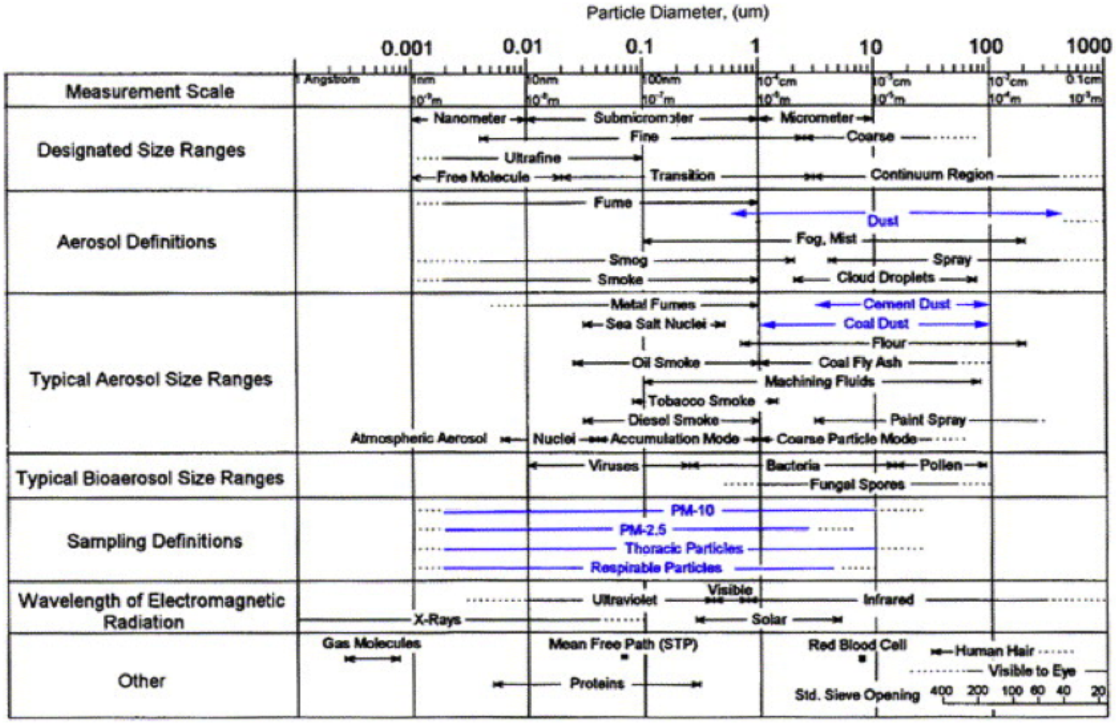

Figure 1.2: Size classification of common airborne particles. Figure from Hinds 1999 [32]

The main mechanisms of particle deposition in the lung, for spherical particles that are not in the presence of magnetic or electrostatic forces, are: inertial impaction, gravitational sedimentation, and brownian diffusion. Figure 1.3 shows a cartoon of the three deposition mechanisms. While the transport of particles in a flow field can be modeled by summation of forces (see Section 2.3.1), the probability of a particle to deposit based on the three above deposition mechanisms may be determined from non-dimensional parameters.

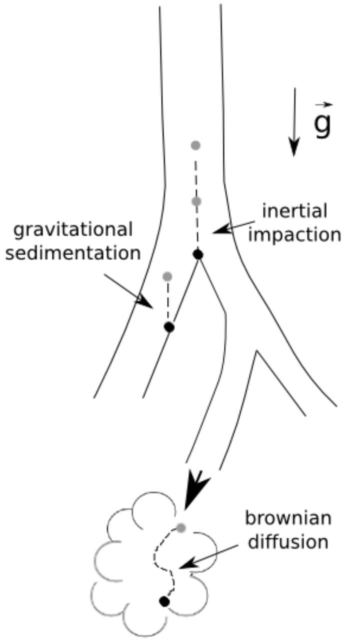

Figure 1.3: Schematic of the deposition mechanisms (inertial impaction, gravitational sedimentation, and diffusion) in the respiratory tract.

The impaction of particles due to inertial forces occurs when a particle momentum causes the particle not to follow the flow field when the flow changes direction. Inertial impaction mainly occurs at bifurcation areas, where a particle may continue in its original direction and impact on the surface of the bifurcation, while the carrier gas moves along the bifurcation. The likelihood of a particle to deposit due to inertial impaction is dependent on the particle's Stokes number.

$$Stk = \frac{\rho_p d_p^2 U}{18\mu d} \tag{1.2}$$

where ρ_p is the particle density, d_p is the particle diameter, μ is the carrier gas viscosity, d is the diameter of the airway, and U is the carrier gas speed. Recently, it has been shown that particles with a Stoke's number < 0.01 are likely to follow the flow field and not deposit due to inertial impaction [18]. The chance of a particle to deposit due to gravitational sedimentation is given by

$$\epsilon = \frac{3V_sL}{8aU} \tag{1.3}$$

where U is the mean speed of the carrier gas, L is the length of the airway, a is the particle radius and V_s is defined as

$$V_s = \frac{mg}{6\pi\mu r} \tag{1.4}$$

where g is gravity, m is the mass of the particle and r is the radius of the airway. The larger ϵ is, the greater the probability for a particle to deposit due to gravitational sedimentation. Sedimentation of particles in the lung mainly occurs in the small airways, as the flow decreases the further in the lung it goes, therefore giving a particle the chance to sediment. Small particles that reach the acinus region of the lung are likely to deposit due to Brownian Diffusion. The rate of diffusion of particles is proportional to the particle's Brownian diffusion coefficient:

$$D = \frac{ckT}{3\pi\mu d_p} \tag{1.5}$$

where c is the Cunningham correction factor for small particles, T is the carrier gas temperature, k is Boltzmann's constant.

While the above non-dimensional relationships include other parameters besides particle diameter, the main determinant of deposition is the particle size. In humans it is well known that particles with diameters greater than 5 μm are most likely to deposit due to inertial impaction, particles with diameters between 0.5 and 5 μm will probably deposit due to gravitational sedimentation and particles with diameters less than 0.5 μm are apt to deposit due to diffusion [17].

1.3 Emphysema

Emphysema, a chronic obstructive pulmonary disease, is characterized by alveolar wall destruction, air space enlargement, loss of alveolar surface area [67], and a decrease in small airway diameter. In the United States 3.7 million people [1] have been diagnosed with this irreversible disease. Emphysema can either be caused by inhalation of toxic particles over a long period of time, or can be caused by an α_1-deficiency in elderly patients. The study of particulate behavior in this susceptible population is important because over time emphysema is worsened or aggravated by continued inhalation of toxic particles. Deposition in emphysematous lungs has been previously studied in human patients [9], animal models [64], in vitro models [54], empirical models [63] and numerical models [30], however several questions are still left unanswered. For example, Sweeney et al. [64] found a decrease in particle deposition in the periphery and an increase in deposition in the central airways for a hamster model exposed to 0.46 μm diameter particles, while Brand et al. [9] found increased deposition in human patients for particles with a diameter of 4 μm. Empirical [59, 63] and experimental replica models [54] have supported the findings of decreased deposition in emphysema. In a separate human study, it was found deposition was 50 percent higher in COPD patients compared to healthy subjects [8], however the authors hypothesized that this increase was due to the increase in airway resistance in bronchitis, rather than the changes that occur in emphysema. Consequently, deposition in emphysema is not fully understood and and therefore is a current important area of research.

1.4 Imaging the Lung: State of the Art

1.4.1 Ventilation

Even though the ventilation distribution in the lung has been studied for many years [34], there are still many challenges that need to be addressed. Unlike blood flow, unaltered inhaled air cannot be directly measured with ultrasound, CT or MRI. Instead, carrier particles or gases must be used. Carrier particles are typically radioactive particles [34] and therefore may pose significant healthy risks. Gases that have "free" protons, and therefore can be imaged with MR, are expensive [12, 22, 40, 52] or requires special equipment. Figure 1.4B shows a ventilation MR image of an asthmatic human lung, where areas of ventilation deficiency may be clearly seen. Recently, a new method that uses O_2 has been employed to study ventilation distribution in the human lung [56] (see Figure 1.4A), which has the benefit of not being a rare gas and not requiring additional MR equipment. The healthy ventilation image (see Figure 1.4A) clearly shows that the dependent lung (the bottom half of the lung) has higher specific ventilation than the top part of the image. This is because the gravity dependent region of the lung expands more during inspiration than the non-gravity dependent regions. However, this oxygen enhanced MRI method [56] has yet to be applied to study ventilation in 3D or the influence of disease on ventilation distribution.

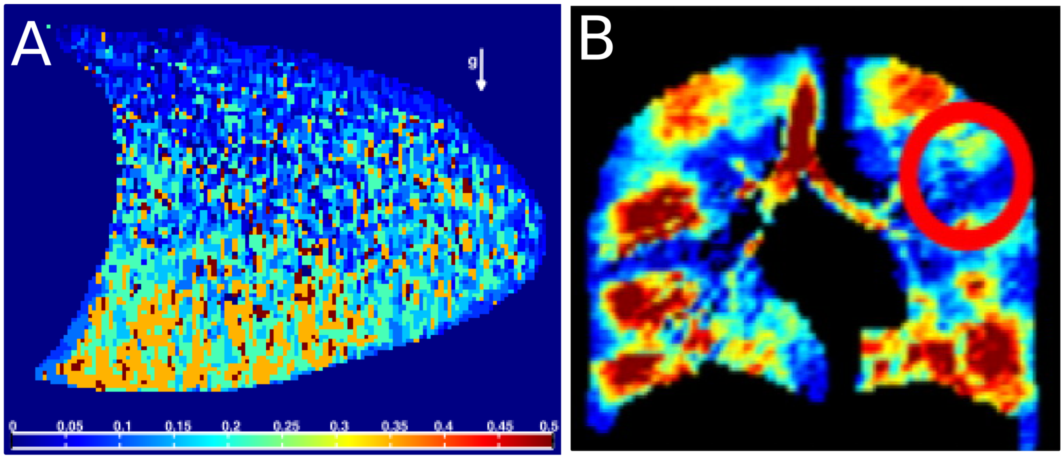

Figure 1.4: Ventilation images derived from MR for healthy (panel A) and asthmatic patients. Red values indicate areas of high ventilation and blue areas of low ventilation. Panel A: from Sa et al. [56] and Panel B from Campana et al. [12].

Emphysema

Ventilation and the apparent diffusion coefficient (ADC) has been measured with MRI in both healthy and emphysematous human patients [35, 74] (see Figure 1.5) and in rodents [23, 40, 66] . These maps show areas of the lung where the disease has caused dead spaces and destructed tissues, or areas that are not being well ventilated with new air. They also show that the ADC is greater in emphysematous lungs, compared to healthy lungs. Even though these types of maps provide spatial information on the disease, the sensitivity of such measurements and their potential for clinical application is still unknown.

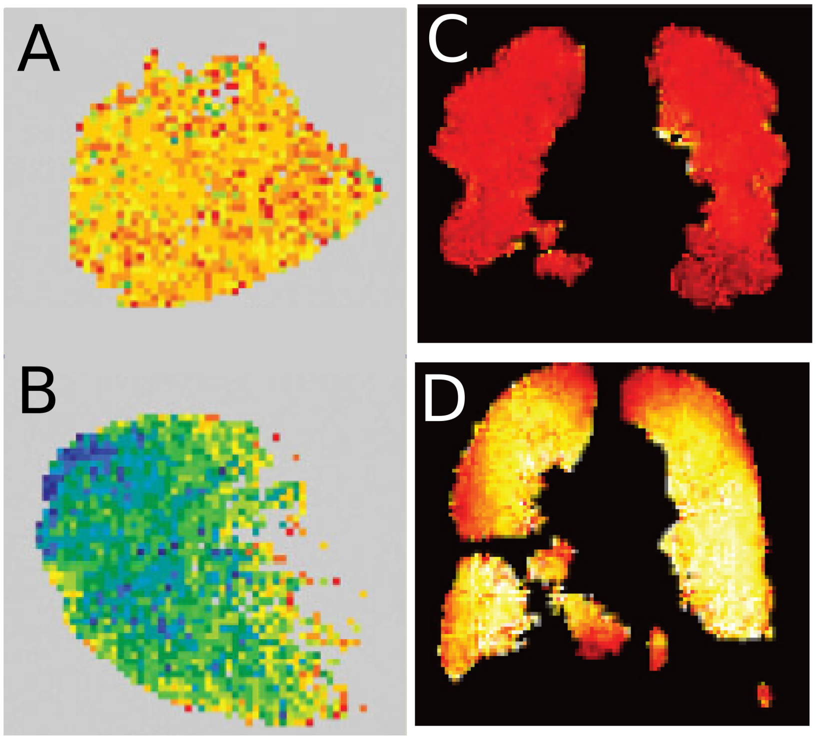

Figure 1.5: Diffusion maps for stage 2 (panel C), and stage 4 (panel D) chronic obstructive pulmonary disease (COPD) [35] and for control (panel A) and emphysema lung (panel B) [74]. Panels A and B, red values indicate low diffusion and blue values represent high diffusion and figures are from Kirby et al [35] and panels C and D, red values are low diffusion and yellow values are high diffusion, figures are from Woods et al. [74].

1.4.2 Particle Deposition

Radionuclide Imaging Techniques

Imaging methods, such as gamma scintigraphy [7, 10, 69, 80], PET [24] and SPECT [25, 37], are often employed to study aerosol deposition and clearance. Gamma scintigraphy and SPECT both image radiolabeled particles (typically ^{99m}Tc), whereas PET uses positron-emitting radionuclides that may be attached directly to the drug molecule. While gamma scintigraphy is the most widely used technique, it is limited as data can only be viewed in two dimensions. Also, the 2D nature of the images complicates the analysis of the left lung because of overlapping activity from the stomach. These limitations disappear with SPECT, as it provides 3D images of aerosol deposition, however the analysis of deposition data is more complex than that for data obtained by gamma scintigraphy. PET provides greater image resolution than gamma scintigraphy or SPECT, however PET scanners are currently not widely available. Furthermore, attaching the radionuclides to the drug molecule is expensive and half-lives of the radiotracers are rather short. In order to relate the deposition maps to anatomy, all three imaging modalities require additional CT imaging.

Several studies have used radionuclide imaging to study aerosol deposition in healthy [4, 37] and diseased rodents [64, 75]. Using scintillation counting on small lung sections, Asgharian et al. [4] measured total deposition in rats following nose-only exposure to $^{56}FeCl_3$ particles with aerodynamic diameters ranging from 0.9 to 4.2 μm. They found that total lung deposition was less than 10 % for most particles sizes except for the 3.5 μm diameter particles, where deposition was about 15 %. Wu et al. [75] used SPECT/CT imaging to determine clearance rates in a guinea pig model of COPD. They exposed [^{99m}Tc]DTPA particles (particle size not given) to control and cigarette-exposed guinea pigs and found that the clearance rate was higher in cigarette-exposed animals than in controls. Also using SPECT/CT imaging, Kuehl et al. [37] determined regional deposition in healthy rats and mice exposed to four sets of polydispersed particles with MMAD of 0.5, 1.0, 3.0 and 5.0 μm. Particle deposition in the lung increased with decreasing particle sizes, whereas the deposition in the oral/nasal area increased with increasing particle sizes. Using an in-house onion model, Kuehl et al. [37] also showed that deposition increased as the distance from the center of mass of the lung increased.

MRI Techniques: Advantages and Limitations

While there have been several MRI particle deposition studies in rodents [50, 61, 62], there has only been one study in human subjects [29]. This is mainly because of the high amounts of contrast agent needed, i.e. ~ 0.5 mg of Gd-DTPA per voxel, in order to detect the presence of the particles. While smaller amounts of iron oxide may be used, as the MR is more sensitive to these particles compared to Gd-DTPA, these particles have potential negative health consequences.

Most of these MR studies of aerosol inhalation in small animals were based on the longitudinal relaxation time T1 [50, 61, 62]. Using ventilated newborn pigs, Sood et al. [61] imaged the lungs, kidneys, liver, skeletal muscle and heart to determine the uptake and distribution of particles once they enter the body. In a follow-up study, the same group [62] acquired 3D images of piglets ventilated with aerosolized Gd-DPTA, however aerosol delivery to the lungs was indirectly measured through increase in signal intensity in the kidneys and again no quantification of aerosol deposition was reported. In a different study, Martin et al. [50] determined the concentration of deposited particles delivered to mice in nose-only inhalation chambers. Imaging was performed post-mortem. The group calibrated the concentration of particles based on phantom experiments. While performed in-situ, the lung vasculature had a large effect on the signal rate and caused artifacts in the images. In post-processing, a significant amount of the voxels were removed from the images, therefore limiting the amount of the images that could be used for particle concentration measurements. Even though it had some limitations, this study was the first attempt at quantifying the number of deposited particles in lung tissues using MRI.

1.5 Computational Modeling of the Lung: State of the Art

1.5.1 Airflow

Computational respiratory airflow models must be designed to mimic realistic pulmonary physiology. Therefore, ideally, respiratory computational models must include realistic airway geometry, breathing patterns and tissue mechanics. The airflow in the pulmonary airways is highly dynamic and changes depending on its location in the lung. The airflow is considered to be transitional or turbulent in the upper respiratory zone, the turbulent eddies dissipate within a few airway generations and the flow continues to be non-linear with Reynolds number on the order of 100 in the conducting airways, and then the flow becomes creeping (i.e. Stokes flow) as it reaches the acinus of the lung. These varying flow characteristics are one of the many reasons that modeling the lung is challenging.

Only recently, CFD airway models have included animal or patient specific geometry. Advances in medical imaging have made it possible to create 3D airway geometries of the upper airways [19] and tracheobronchial regions of the lung [21, 55]. Incorporating realistic geometry is important, as the airflow pattern and structures is highly dependent on the airway geometry [20, 51, 72, 77]. For example, symmetric airway bifurcation and curvature may cause dean-like flow structures, while realistic bifurcations result in more complex structures (see Figure 1.6) [36]. Figure 1.7 shows two examples of flow patterns in patient-specific airway geometry.

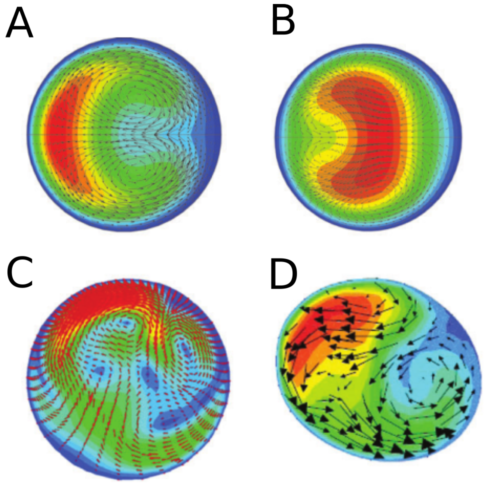

Figure 1.6: Flow patterns in a symmetric airflow model (panels A and B), flow in assymetric airflow model and CT airway model. From Kleinstreuer et al. [36]

All CFD models must include a description of the airflow or pressure on all boundaries in the model, i.e. boundary conditions. These boundary conditions must be as realistic as possible, as the resulting flow field in the 3D domain is highly dependent on these boundary conditions. Traditionally, in respiratory CFD simulations, a constant pressure [20] or flow rate [13, 26] boundary condition is

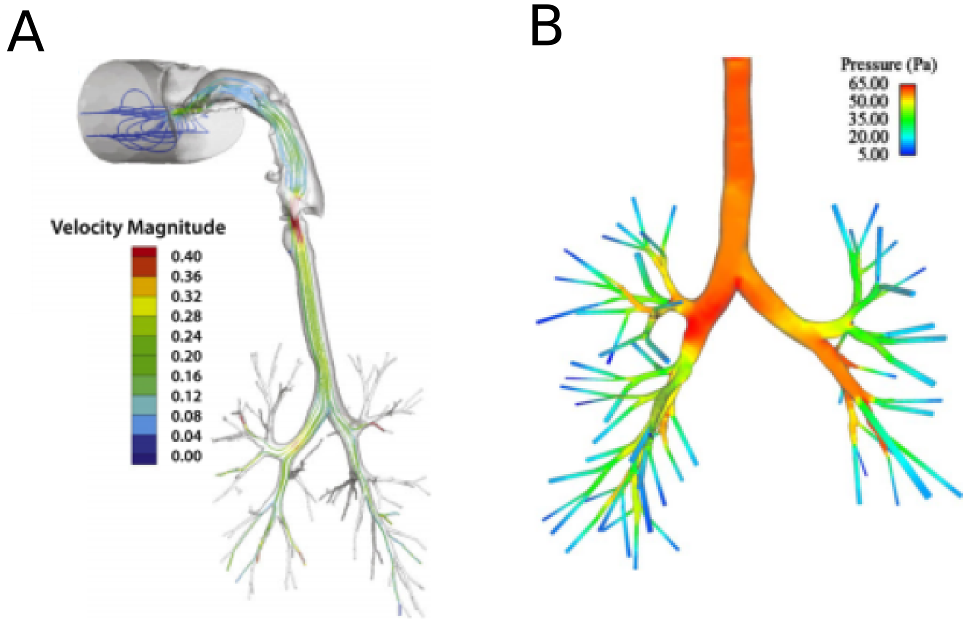

Figure 1.7: State of the art of CFD models. Panel A shows streamlines in upper respiratory and trachea-bronchial region model and panel B shows pressure fields in a tracheal-bronchial model. Panel A: From Kuprat et al. [39], Panel B: From Comerford et al. [15].

applied at the mouth or trachea. Additionally, constant pressure [16, 20, 26, 60] or flow rate [13, 51] are typically implemented at the distal downstream airway faces. A constant pressure is highly unrealistic, as the pressure in the airways is constantly changing, as the act of breathing is pressure driven. Additionally, assuming constant pressure at an outlet unrealistically prescribes that the pressure drop from the mouth or trachea to the distal airways is the same between all airways. It is currently impossible to take in-vivo measurements of pressure in the airways downstream from the trachea. Recent work has applied CT [13] or MRI [51] measured flow as a boundary condition to the distal faces, however these measurements were taken at one or two instances in time and therefore do not include the unsteady nature of breathing.

Due to the vast computational costs and complexity of the lung, there are currently no computational models that are able to simulate airflow in the entire lung. Therefore, to simulate the unsteady dynamics of breathing, multi-scale methods must be used. Such multi-scale modeling techniques have been implemented to study the cardiovascular system for several years [38, 53, 70]. However, only recently, have these multi-scale methods been applied to the respiratory system [6, 27, 39, 49]. Typically, a multi-scale numerical model includes a 3D CFD description of the large airways and a 1D [49] or 0D [6, 39] lower-dimensional model that represents the smaller airways and peripheral tissue (see Figure 1.8). Figure 1.8 shows a 3D model connected to 0D lower-dimensional models (panel A) and a 3D model that was connected to a patient-specific 1D model (panel B). With such multi-scale models, it is possible to perform unsteady simulations, where both the flow and pressure may accurately be solved for [27]. However, if neither a full deformable lung or multi-scale model is simulated, the flow and pressure will be in phase and therefore resulting in unrealistically low pressure fields [14].

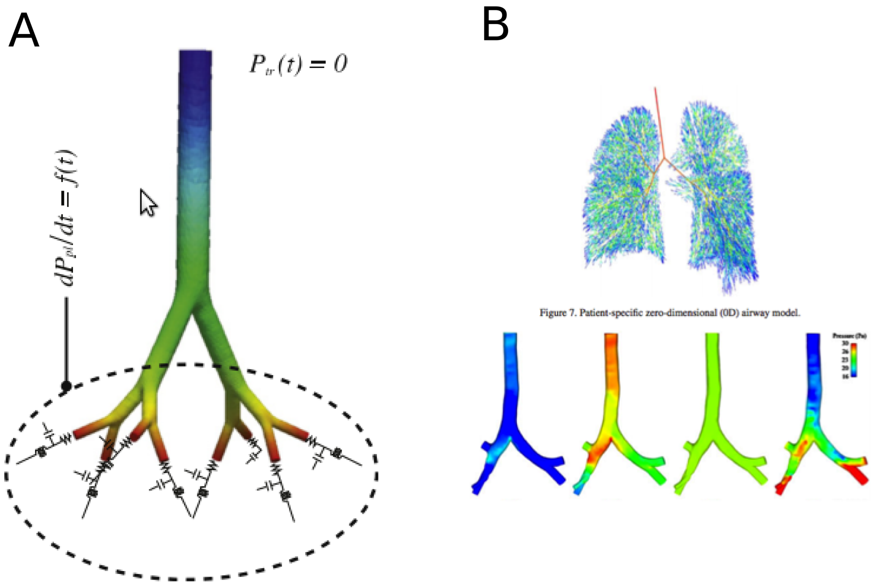

Figure 1.8: Multiscale respiratory CFD models. Panel A: 3D model connected to lower dimensional 0D model (from Kuprat et al. [39]. Panel B: 3D model connected to patient-specific 1D model (from Gravemeier et al. [27].

There have only been a few studies that have solved both the structure movement and fluid flow in the conducting airways. These fluid-structure interaction (FSI) simulations in the upper airways and tracheal-bronchial regions are typically applicable to studying forced breathing or ventilated induced injury [48, 71], as the pressure fields are most important in these applications. As in traditional CFD simulations, it is assumed that the main bronchi do not move much during breathing. However, recently it has been shown that there is significant movement in these upper airways and perhaps it is important to include this movement, especially if accurate pressure fields or shear stress in these regions are needed. Figure 1.9 shows two recent FSI examples of the movement of the tracheal-bronchial region during simulated breathing.

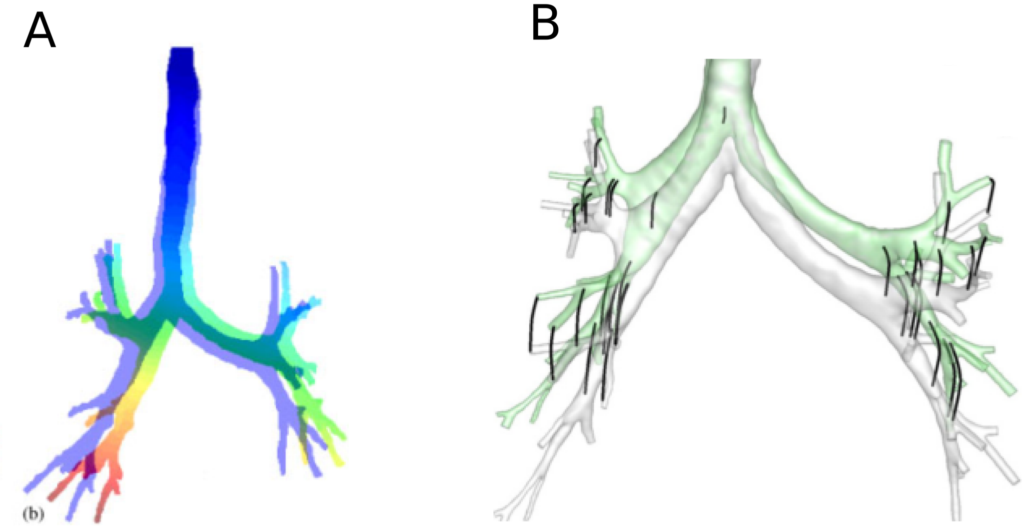

Figure 1.9: Movement of the tracheal-bronchial region of the lung during FSI simulations during breathing. Panel A is from Wall et al. [71] and Panel B is from Yin et al [76].

The acinus region of the lung expands and contracts to inhale and exhale air. Therefore, CFD simulations of these regions of the lung must include moving boundaries, as this movement drives the creeping flow. In many cases the displacement of the alveolar wall is ideally prescribed [30, 45, 65], as the lung tissue properties are complex and is still an area of current research. Figure 1.10 shows two examples of alveolar region CFD simulations.

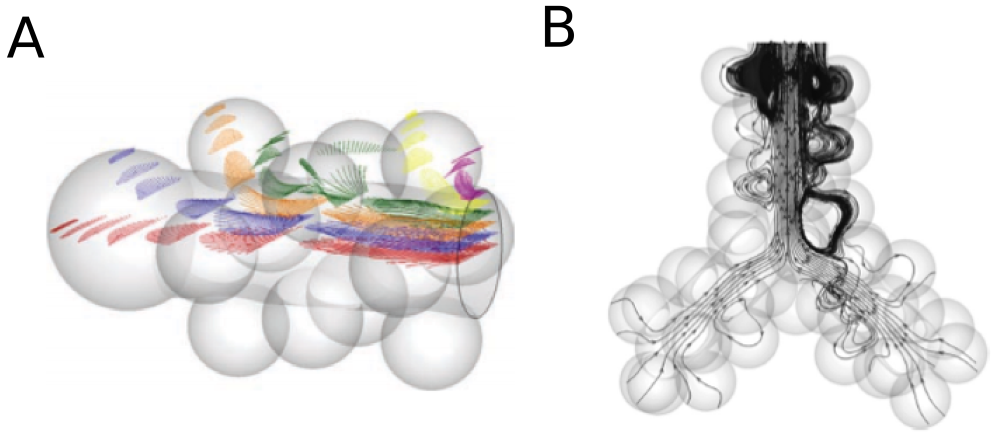

Figure 1.10: Velocity profiles (panel A) and streamlines (panel B) from CFD simulations of the alveolar region of the lung. Panel A: From Harding and Robinson 2010 [31] and Panel B: Ma and Darquenne (2011) [44].

1.5.2 Particle Deposition and Distribution

Once the CFD simulations are performed, particles may be tracked in the flow field by solving the particle transport equations. Depending on the size and concentration of particles in the carrier gas, an Eulerian or a Lagrangian particle tracking scheme may be used. An Eulerian, or particle concentration, description is most applicable for small particles that are likely to diffuse or for high particle concentrations. In contrast, a Lagrangian particle tracking scheme, where each individual particle's motion and position is solved over time, is applicable to larger particles that are mainly influenced by inertia and gravitational sedimentation or for dilute concentrations. Eulerian methods are less computationally expensive than Lagrangian methods. However, with Eulerian methods, an individual particle is not tracked, only the concentration of particles.

Numerical models of particle transport in the lung supply information about local deposition sites, total particle deposition, and distribution of particles in the lung. Unlike in experiments, it is relatively simple to test the influence of particle MMAD, orientation of the airway model and breathing patterns on particle deposition. Figure 1.11A shows deposition locations of particles with diameter of 1, 10 and 30 μm in a anatomically accurate human CFD model and Figure 1.11B shows deposition of 1 μm diameter particles in idealized alveolar sacs for two different orientations with respect to gravity. As Figure 1.11 shows, there is significant deposition in the upper airways for all particle sizes and no deposition in the conducting airways for particles with diameters of 30 μm. In an alveolar model, Figure 1.11 shows that the orientation of the alveolar sacs greatly influences the deposition locations for 1 μm diameter particles.

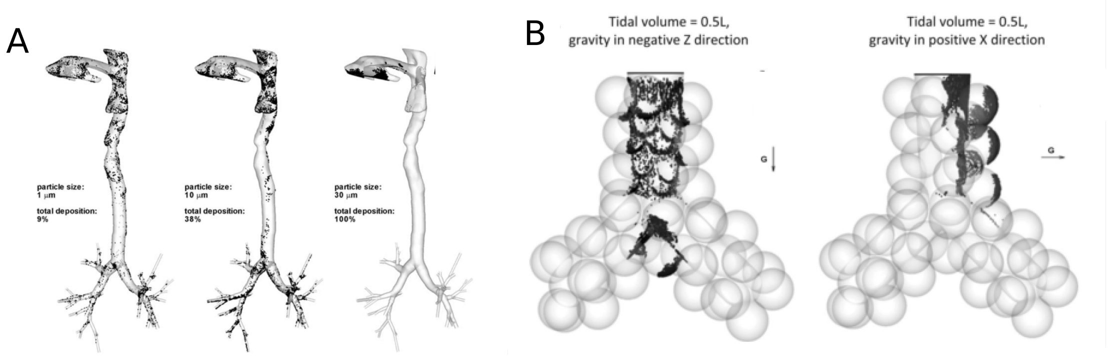

Figure 1.11: Particle deposition in a realistic human upper and conducting airway model (from Ma et al. [46]) and particle deposition in alveolar model with gravity in two different orientations (from Ma and Darquenne [44])

Despite being used extensively for toxicology [28, 73] and therapeutic studies [2] there have been relatively few airflow [16, 51, 58] and particle deposition [33] numerical simulations in the rat. Minard et al. [51] showed good agreement between the airflow measured using CFD and MRI, their simulations were performed under steady state conditions. Unsteady CFD simulations were performed by Schroeter et al. [58] and Jiang et al. [33], however these simulations only included the rat's nose. Some groups have developed empirical models to predict particle deposition in the rat [3, 57], however, as far as the author is aware, there has not been any 3D simulations of particle transport and deposition in rat airways.

Several groups have started to move towards modeling the interaction of the carrier gas with the aerosol particles. In these situations the particle may evaporate, condensate or grow hygroscopicly. Recently, Longest et al. developed an enhanced condensation growth model [42] that has the ability to model particle growth as it moves down the respiratory tract. This model [42] may be applied to the development of inhalable aerosol medication therapy. Other groups [16, 82] have started to model volatile and non-volatile gases in the lung. These models may be applied to study toxic gases and particles, (e.g. such as cigarette smoke [82] or diesel exhaust).

Currently, there are no models that have the ability to track and predict deposition during both inspiration and expiration. However, Tian et al. [68] has developed a single path model that is able to track particles downstream of the 3D airway model. This individual path model does not model the acinus region and it does not model lung heterogeneity. To predict global deposition, Angivel et al. [3] developed a multiple path particle deposition (MPPD) model that essentially models the deposition efficiency in the airways. The deposition efficiency is predicted based on empirical solutions to the particle equations or relationships developed from deposition experiments. With the MPPD model, the breathing parameters and airway geometry may be altered to predict deposition in, for example, rats [3] or in humans [5]. Applying the MPPD model, Ashgharian et al. [5] showed that there was little difference between uniform and non-uniform lung expansion on the total deposition fraction (see Figure 1.12). This MPPD model may potentially be connected to a 3D airway model to predict deposition throughout both inspiration and expiration.

1.5.3 Diseased Computational Models

Relatively few CFD simulations have been performed to study the influence of disease on airflow and particle deposition. Mainly this is because it is a complex problem and there is incomplete knowledge of disease physiology and medical images. However, Zhang and Papadakis [81] studied airflow and particle deposition in an idealized asthma model and Malve et al [49] researched airflow in a stented

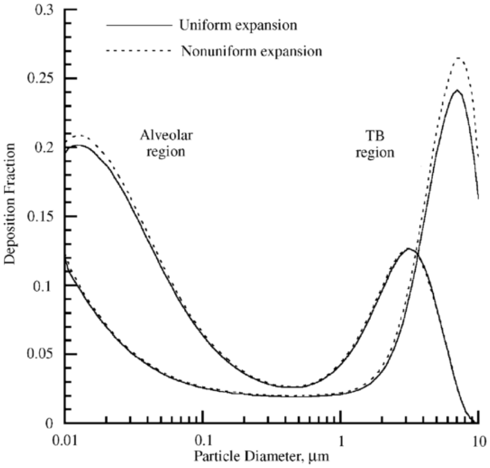

Figure 1.12: Prediction of particle deposition with MPPD model [3, 5] for uniform and non-uniform lung expansion. Figure from Asgharian et al. [5]

trachea with impedance boundary conditions. There have been no CFD models of emphysema. The only emphysema model that has been developed was a stochastic model based on idealized healthy and emphysematous alveolar geometry [63].

1.5.4 Validation of CFD Models

Over the years there has been an extensive number of respiratory CFD models developed. However, very few of these models have been validated with experimental data. These models are typically validated with replica in-vitro experimental models [41, 43, 47] (see Figure 1.13A) or in-vivo total deposition measured with bolus tests [46]. Recently, Minard et al. [51] compared airflow measured with MRI and predicted with CFD for steady conditions in the rat lung (see Figure 1.13). However, there has been no work that has directly validated deposition sites in vivo with computational predictions.

1.6 Outline of the Dissertation

Chapter 2 provides the theory and governing principles behind the work of this dissertation. This includes MRI theory as well as the specific MR methods

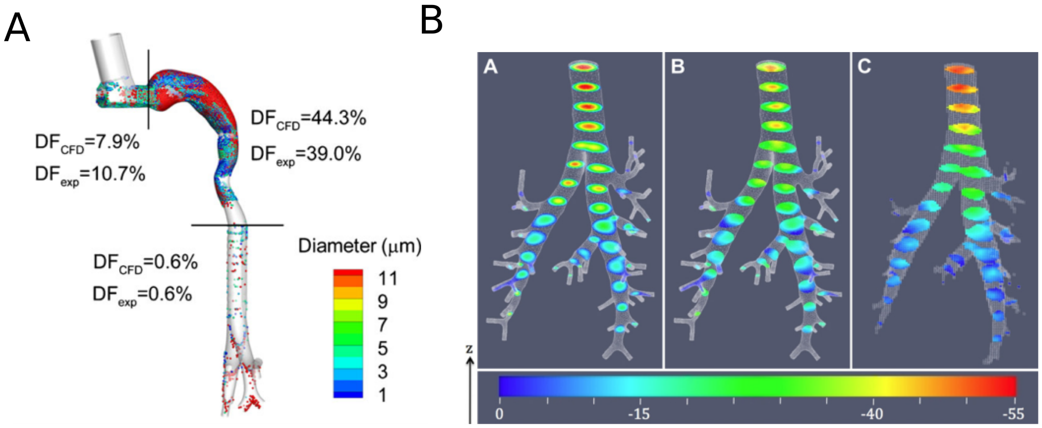

Figure 1.13: Examples of validation of particle deposition in upper respiratory tract of idealized human model (panel A) and of steady airflow in rat airways validated with MRI.

that were employed in this dissertation (section 2.1). The Finite Element methods used in Chapters 5 and 7 are discussed in section 2.2, including the theory behind the implementation of monolithic and iterative boundary conditions. Section 2.3 discusses the particle transport equations and a validation of the code used within this dissertation. Chapter 3 presents the rat airway geometry that was created from MR images as well as the validation of the geometric measurements taken from these geometries. The MR methods developed to quantify particle deposition in rat lungs is discussed in Chapter 4. This chapter also quantifies deposition of various regions of the left lung in healthy rats. The methods developed in Chapter 4 are expanded to study the deposition in the five rat lobes in healthy and emphysematous rats in Chapter 5. This chapter discusses the findings that both particle deposition and the dispersion of particles within the lung is higher in emphysematous rats compared to healthy rats. Chapter 6 employs the flow measurements taken in Chapter 5 to determine the global respiratory resistance and compliance of the healthy and emphysematous rats lungs. Additionally, the 0D-3D multi-scale CFD framework and simulations employed to study airflow and particle deposition are discussed in Chapter 6. Chapter 7 expands on this framework to simulate airflow and particle deposition in an extended airway model. Additionally, Chapter

7 compares deposition data found numerically and experimentally in both healthy and emphysematous rat lungs. The conclusion, and broader impact, of this dissertation are given in Chapter 8, as well a discussion of potential future work.

1.7 Accomplishments

The major contributions of the work presented in this dissertation are summarized below.

- In-situ airway morphometric measurements were collected from four healthy rats and the inter-animal variability was assessed. Additional measurements were taken on an extended model for one rat and organized in such a fashion to achieve low intra-animal variability. See Chapter 3.

- An MRI method to image, analyze and quantify particle deposition in rat lungs was developed and the spatial distribution of particles in the left lung of healthy rats was determined. See Chapter 4.

- Examined particle deposition in the five rat lobes in healthy rats. Determined differences in deposition based on of the apex to base location in the lung, and the central versus peripheral region of the lung. See Chapter 4 and 5.

- Successfully induced emphysema in rats and quantified the location of emphysema by measuring the alveolar space dimension and the signal decay rate quantified from MR images. See Chapter 5.

- Showed that the deposition is higher and more heterogeneously distributed in emphysema rats compared to healthy rats that were mechanically ventilated to iron oxide particles with MMAD of 1.22 μm. See Chapter 5.

- Determined the global resistance and compliance of healthy and emphysematous rats by solving a 0D lumped parameter model using flow data collected experimentally. See Chapter 6.

- Developed a 0D-3D multi-scale respiratory CFD framework for both healthy and emphysematous rats. Determined the influence of disease location on particle distribution in the lung. See Chapter 6.

- Simulated airflow and particle transport and deposition in an extended airway model for both healthy, homogeneous and localized emphysema. See Chapter 7.

- Showed good agreement between simulated delivery of particles and particle deposition measurements determined experimentally to the five rat lung lobes. See Chapter 7.

1.8 Bibliography

[1] American Lung Association, 2009.

[2] Agu, R. U., and Ugwoke, M. I. In vitro and in vivo testing methods for respiratory drug delivery. *Expert Opinion Drug Delivery2 1* (2011), 57–69.

[3] Angivel, S., and Asgharian, B. A Multiple-Path Model of Particle Deposition in the Rat Lung. *Toxicological Sciences 28*, 1 (Nov. 1995), 41–50.

[4] Asgharian, B., Kelly, J. T., and Tewksbury, E. W. Respiratory deposition and inhalability of monodisperse aerosols in Long-Evans rats. *Toxicological sciences : an official journal of the Society of Toxicology 71*, 1 (Jan. 2003), 104–11.

[5] Asgharian, B., Price, O., and Hofmann, W. Prediction of particle deposition in the human lung using realistic models of lung ventilation. *Journal of Aerosol Science 37*, 10 (Oct. 2006), 1209–1221.

[6] Baffico, L., Grandmont, C., and Maury, B. Multiscale Modeling of the Respiratory Tract. *Mathematical Models and Methods in Applied Sciences 20*, 01 (2010), 59.

[7] Bennett, W. D., Herbst, M., Alexis, N. E., Zeman, K. L., Wu, J., Hernandez, M. L., and Peden, D. B. Effect of inhaled dust mite allergen on regional particle deposition and mucociliary clearance in allergic asthmatics. *Clinical and Experimental Allergy 41*, 12 (Dec. 2011), 1719–1728.

[8] Bennett, W. D., Zeman, K. L., Kim, C., Mascarella, J., William, D., Kirby, L., and Enhanced, J. Enhanced Deposition of Fine Particles in Copd Patients Spontaneously Breathing At Rest. *Inhalation Toxicology 9*, 1 (Jan. 1997), 1–14.

[9] Brand, P., Schulte, M., Wencker, M., Herpich, C. H., Klein, G., Hanna, K., and Meyer, T. Lung deposition of inhaled alpha1-proteinase inhibitor in cystic fibrosis and alpha1-antitrypsin deficiency. *The European Respiratory Journal 34*, 2 (Aug. 2009), 354–60.

[10] Brown, J. S., K. L. Zeman, W. D. B. Ultrafine particle deposition and clearance in the healthy and obstructed lung. *American Journal of Respiratory and Critical Care Medicine 166*, 9 (Aug. 2002), 1240–1247.

[11] Byron, P. R., and Patton, J. S. Drug Delivery Respiratory. *Journal of Aerosol Medicine 7*, 1 (1994), 49–75.

[12] Campana, L., Kenyon, J., Zhalehdoust-Sani, S., Tzeng, Y.-S., Sun, Y., Albert, M., and Lutchen, K. R. Probing airway conditions governing ventilation defects in asthma via hyperpolarized MRI image functional modeling. *Journal of applied physiology 106*, 4 (Apr. 2009), 1293–300.

[13] Choi, J., Tawhai, M. H., Hoffman, E. a., and Lin, C.-L. On intra- and intersubject variabilities of airflow in the human lungs. *Physics of fluids 21*, 10 (Oct. 2009), 101901.

[14] Comerford, A., Förster, C., and Wall, W. a. Structured tree impedance outflow boundary conditions for 3D lung simulation. *Journal of Biomechanical Engineering 132*, 8 (Aug. 2010), 081002:1–10.

[15] Comerford, A., Förster, C., and Wall, W. a. Structured tree impedance outflow boundary conditions for 3D lung simulations. *Journal of Biomechanical Engineering 132*, 8 (Aug. 2010), 081002.

[16] Corley, R. A., Kabilan, S., Kuprat, A. P., Carson, J. P., Minard, K. R., Jacob, R. E., Timchalk, C., Glenny, R., Pipavath, S., Cox, T., Wallis, C. D., Larson, R. F., Fanucchi, M. V., Postlethwait, E. M., and Einstein, D. R. Comparative Computational Modeling of Airflows and Vapor Dosimetry in the Respiratory Tracts of Rat , Monkey , and Human. *Toxicological Sciences 128*, 2 (2012), 500–516.

[17] Darquenne, C. Particle Deposition in the Lung. *Respiratory Medicine* (2006), 300–304.

[18] Darquenne, C., Van Ertbruggen, C., and Prisk, G. K. Convective flow dominates aerosol delivery to the lung segments. *Journal of Applied Physiology 111*, 1 (July 2011), 48–54.

[19] De Backer, J. W., Vos, W. G., Burnell, P., Verhulst, S. L., Salmon, P., De Clerck, N., and De Backer, W. Study of the variability in upper and lower airway morphology in Sprague-Dawley rats using modern micro-CT scan-based segmentation techniques. *The Anatomical Record 292*, 5 (May 2009), 720–7.

[20] De Backer, J. W., Vos, W. G., Gorl, C. D., Germonpre, P., Partoens, B., Wuyts, F. L., Parizel, P. M., and De Backer, W. Flow analyses in the lower airways : Patient-specific model and boundary conditions. *Medical Engineering & Physics 30* (2008), 872–879.

[21] Einstein, D. R., Neradilak, B., Pollisar, N., Minard, K. R., Wallis, C., Fanucchi, M., Carson, J. P., Kuprat, A. P., Kabilan, S., Jacob, R. E., and Corley, R. a. An automated self-similarity analysis of the pulmonary tree of the Sprague-Dawley rat. *Anatomical Record 291*, 12 (Dec. 2008), 1628–48.

[22] Emami, K., Cadman, R. V., Woodburn, J. M., Fischer, M. C., Kadlecek, S. J., Zhu, J., Pickup, S., Guyer, R. a., Law, M., Vahdat, V., Friscia, M. E., Ishii, M., Yu, J., Gefter, W. B., Shrager, J. B., and Rizi, R. R. Early changes of lung function and structure in an elastase model of emphysema–a hyperpolarized 3He MRI study. *Journal of applied physiology 104*, 3 (Mar. 2008), 773–786.

[23] Emami, K., Chia, E., Kadlecek, S., Macduffie-Woodburn, J. P., Zhu, J., Pickup, S., Blum, A., Ishii, M., and Rizi, R. R. Regional correlation of emphysematous changes in lung function and structure: a comparison between pulmonary function testing and hyperpolarized MRI metrics. *Journal of Applied Physiology 110*, 1 (Jan. 2011), 225–35.

[24] Fleming, J. S., and Conway, J. H. Three dimensional imaging of aerosol deposition. *Journal of Aerosol Medicine 14*, 2 (2001), 147–153.

[25] Fleming, J. S., Quint, M., Bolt, L., Martonen, T. B., and Conway, J. H. Comparison of SPECT aerosol deposition data with twenty-four-hour clearance measurements. *Journal of Aerosol Medicine 19*, 3 (Jan. 2006), 261–267.

[26] Gemci, T., Ponyavin, V., Chen, Y., Chen, H., and Collins, R. Computational model of airflow in upper 17 generations of human respiratory tract. *Journal of Biomechanics 41*, 9 (Jan. 2008), 2047–54.

[27] Gravemeier, V., Comerford, A., Yoshihara, L., and Ismail, M. A novel formulation for Neumann inflow boundary conditions in biomechanics. *International Journal for Numerical Methods in Biomedical Engineering 28* (2012), 560–573.

[28] Griffiths, N. M., Van der Meeren, A., Fritsch, P., Abram, M.-C., Bernaudin, J.-F., and Poncy, J. L. Late-occurring pulmonary pathologies following inhalation of mixed oxide (uranium + plutonium oxide) aerosol in the rat. *Health Physics 99*, 3 (Sept. 2010), 347–56.

[29] Haage, P., Karaagac, S., Spüntrup, E., Truong, H. T., Schmidt, T., and Günther, R. W. Feasibility of pulmonary ventilation visualization with aerosolized magnetic resonance contrast media. *Investigative radiology 40*, 2 (Feb. 2005), 85–8.

[30] Harding, E. M. *Particle Deposition in Replica Healthy and Emphysematous Using Computational Fluid Dynamics.* PhD thesis, 2010.

[31] Harding, E. M., and Robinson, R. J. Flow in a terminal alveolar sac model with expanding walls using computational fluid dynamics. *Inhalation toxicology 22*, 8 (July 2010), 669–78.

[32] Hinds, W. C. *Aerosol Technology Properties, Behavior, and Measurement of Airborne Particles*, 2nd ed. John Wiley & Sons, Inc., 1999.

[33] Jiang, J., and Zhao, K. Airflow and nanoparticle deposition in rat nose under various breathing and sniffing conditions. *Journal of Aerosol Science 41*, 11 (2011), 1030–1043.

[34] Kaneko, K., Dolovich, M. B., Dawson, A., and Bates, D. V. Regional distribution of ventilation and perfusion as a function of body position . Regional perfusion distribution of ventilation and as a function of body position . *Journal of Applied Physiology 21* (1966), 767–777.

[35] Kirby, M., Svenningsen, S., Kanhere, N., Owrangi, A., Wheatley, A., Coxson, H. O., Santyr, G. E., Paterson, N. A., McCormack, D. G., and Parraga, G. Pulmonary Ventilation Visualized using Hyperpolarized Helium-3 and Xenon-129 Magnetic Resonance Imaging: Differences in COPD and Relationship to Emphysema. *Journal of applied physiology*, December 2012 (Dec. 2012), 707–715.

[36] Kleinstreuer, C., and Zhang, Z. Airflow and Particle Transport in the Human Respiratory System. *Annual Review of Fluid Mechanics 42*, 1 (Jan. 2010), 301–334.

[37] Kuehl, P. J., Anderson, T. L., Candelaria, G., Gershman, B., Harlin, K., Hesterman, J. Y., Holmes, T., Hoppin, J., Lackas, C., Norenberg, J. P., Yu, H., and McDonald, J. D. Regional particle size dependent deposition of inhaled aerosols in rats and mice. *Inhalation Toxicology 24*, 1 (Dec. 2012), 27–35.

[38] Kung, E., Baretta, A., Baker, C., Arbia, G., Biglino, G., Corsini, C., Schievano, S., Vignon-Clementel, I. E., Dubini, G., Pennati, G., Taylor, A., Dorfman, A., Hlavacek, A. M., Marsden, A. L., Hsia, T.-Y., and Migliavacca, F. Predictive modeling of the virtual Hemi-Fontan operation for second stage single ventricle palliation: two patient-specific cases. *Journal of Biomechanics 46*, 2 (Jan. 2013), 423–9.

[39] Kuprat, A., Kabilan, S., Carson, J., Corley, R., and Einstein, D. A bidirectional coupling procedure applied to multiscale respiratory modeling. *Journal of Computational Physics In-Press*.

[40] Kyriazis, A., Rodriguez, I., Nin, N., Izquierdo-Garcia, J. L., Lorente, J. a., Perez-Sanchez, J. M., Pesic, J., Olsson, L. E., and Ruiz-Cabello, J. Dynamic ventilation 3He MRI for the quantification of disease in the rat lung. *IEEE Transactions on Bio-Medical engineering 59*, 3 (Mar. 2012), 777–86.

[41] Longest, P. W., and Oldham, M. J. Mutual enhancements of CFD modeling and experimental data: a case study of 1-mum particle deposition in a branching airway model. *Inhalation toxicology 18*, 10 (Sept. 2006), 761–71.

[42] Longest, P. W., Tian, G., and Hindle, M. Improving the lung delivery of nasally administered aerosols during noninvasive ventilation-an application of enhanced condensational growth (ECG). *Journal of aerosol medicine and pulmonary drug delivery 24*, 2 (Apr. 2011), 103–18.

[43] Longest, P. W., Tian, G., Walenga, R. L., and Hindle, M. Comparing MDI and DPI aerosol deposition using in vitro experiments and a new stochastic individual path (SIP) model of the conducting airways. *Pharmaceutical Research 29*, 6 (June 2012), 1670–88.

[44] Ma, B., and Darquenne, C. Aerosol deposition characteristics in distal acinar airways under cyclic breathing conditions. *Journal of Applied Physiology 110*, 5 (May 2011), 1271–1282.

[45] Ma, B., and Darquenne, C. Aerosol bolus dispersion in acinar airways–influence of gravity and airway asymmetry. *Journal of applied physiology 113*, 3 (Aug. 2012), 442–50.

[46] Ma, B., and Lutchen, K. R. CFD simulation of aerosol deposition in an anatomically based human large-medium airway model. *Annals of Biomedical Engineering 37*, 2 (Feb. 2009), 271–85.

[47] Ma, B., Ruwet, V., Corieri, P., Theunissen, R., Riethmuller, M., and Darquenne, C. CFD Simulation and Experimental Validation of Fluid Flow and Particle Transport in a Model of Alveolated Airways. *Journal of aerosol science 40*, 5 (May 2009), 403–141.

[48] Malvè, M., Pérez del Palomar, a., Trabelsi, O., López-Villalobos, J., Ginel, a., and Doblaré, M. Modeling of the fluid structure interaction of a human trachea under different ventilation conditions. *International Communications in Heat and Mass Transfer 38*, 1 (Jan. 2011), 10–15.

[49] Malve, M., Chandra, S., Lopez-Villalobos, J.L., Finol, E.A., Ginel, A., Doblare, M. CFD analysis of the human airways under impedance- based boundary conditions: application to healthy, diseased and stented trachea. *Computer Methods in Biomechanics and Biomedical Engineering*, March (2013), 37–41.

[50] Martin, A. R., Thompson, R. B., and Finlay, W. H. MRI measurement of regional lung deposition in mice exposed nose-only to nebulized superparamagnetic iron oxide nanoparticles. *Journal of Aerosol Medicine and Pulmonary Drug Delivery 21*, 4 (Dec. 2008), 335–342.

[51] Minard, K. R., Kuprat, A. P., Kabilan, S., Jacob, R. E., Einstein, D. R., Carson, J. P., and Corley, R. a. Phase-contrast MRI and CFD modeling of apparent (3)He gas flow in rat pulmonary airways. *Journal of magnetic resonance 221* (May 2012), 129–138.

[52] Mistry, N. N., Qi, Y., Hedlund, L. W., and Johnson, G. A. Ventilation/perfusion imaging in a rat model of airway obstruction. *Magnetic resonance in medicine 63*, 3 (Mar. 2010), 728–35.

[53] Moghadam, M. E., Vignon-Clementel, I. E., Figliola, R., and Marsden, A. L. A modular numerical method for implicit 0D/3D coupling in cardiovascular finite element simulations. *Journal of Computational Physics*.

[54] Oakes, J. M., Day, S., Weinstein, S. J., and Robinson, R. J. Flow field analysis in expanding healthy and emphysematous alveolar models using particle image velocimetry. *Journal of Biomechanical Engineering 132*, 2 (Feb. 2010), 021008.

[55] Oakes, J. M., Scadeng, M., Breen, E. C., Marsden, A. L., and Darquenne, C. Rat airway morhometry measured from in-situ mri-based geometric models. *Journal of Applied Physiology 112*, 12 (Mar. 2012), 1921–1931.

[56] Sá, R. C., Cronin, M. V., Henderson, a. C., Holverda, S., Theilmann, R. J., Arai, T. J., Dubowitz, D. J., Hopkins, S. R., Buxton, R. B., and Prisk, G. K. Vertical distribution of specific ventilation in normal supine humans measured by oxygen-enhanced proton MRI. *Journal of Applied Physiology 109*, 6 (Dec. 2010), 1950–1959.

[57] Schmid, O., Bolle, I., Harder, V., Karg, E., Takenaka, S., Schulz, H., and Ferron, G. a. Model for the deposition of aerosol particles in the respiratory tract of the rat. I. Nonhygroscopic particle deposition. *Journal of Aerosol Medicine and Pulmonary Drug Delivery 21*, 3 (Sept. 2008), 291–307.

[58] Schroeter, J. D., Kimbell, J. S., Gross, E. a., Willson, G. a., Dorman, D. C., Tan, Y.-M., and Clewell, H. J. Application of physiological computational fluid dynamics models to predict interspecies nasal dosimetry of inhaled acrolein. *Inhalation Toxicology 20*, 3 (Feb. 2008), 227–43.

[59] Segal, R. A., Hill, C., Carolina, N., and Shearer, M. Computer simulations of particle deposition in the lungs of chronic obstructuve pulmonary disease patients. *Inhalation Toxicology 14* (2002), 705–720.

[60] Soni, B., and Thompson, D. Effects of temporally varying inlet conditions on flow and particle deposition in the small bronchial tubes. *International Journal for Numerical Methods in Biomedical Engineering 28* (2012), 915–936.

[61] Sood, B. G., Shen, Y., Latif, Z., Chen, X., Sharp, J., Neelavalli, J., Joshi, A., Slovis, T. L., and Haacke, E. M. Aerosol delivery in ventilated newborn pigs: an MRI evaluation. *Pediatric Research 64*, 2 (Aug. 2008), 159–164.

[62] Sood, B. G., Shen, Y., Latif, Z., Galli, B., Dawe, E. J., and Haacke, E. M. Effective aerosol delivery during high-frequency ventilation in neonatal pigs. *Respirology 15*, 3 (Apr. 2010), 551–5.

[63] Sturm, R., and Hofmann, W. Stochastic simulation of alveolar particle deposition in lungs affected by different types of emphysema. *Journal of Aerosol Medicine 17*, 4 (Jan. 2004), 357–72.

[64] Sweeney, T. D., Brain, J. D., Leavitt, S. a., and Godleski, J. J. Emphysema alters the deposition pattern of inhaled particles in hamsters. *The American journal of pathology 128*, 1 (July 1987), 19–28.

[65] Sznitman, J., Heimsch, T., Wildhaber, J. H., Tsuda, A., and Rösgen, T. Respiratory flow phenomena and gravitational deposition in a three-dimensional space-filling model of the pulmonary acinar tree. *Journal of biomechanical engineering 131*, 3 (Mar. 2009), 031010.

[66] Tanoli, T. S. K., Woods, J. C., Conradi, M. S., Bae, K. T., Gierada, D. S., Hogg, J. C., Cooper, J. D., and Yablonskiy, D. a. In vivo lung morphometry with hyperpolarized 3He diffusion MRI in canines with induced emphysema: disease progression and comparison with computed tomography. *Journal of Applied Physiology 102*, 1 (Jan. 2007), 477–84.

[67] Thurlbeck, W. M., and Muller, N. L. Emphysema: Definition, Imaging, and Quantification. *American Journal of Roentgenology 163* (1994), 1017–1025.

[68] Tian, G., Longest, P. W., Su, G., Walenga, R. L., and Hindle, M. Development of a stochastic individual path (SIP) model for predicting the tracheobronchial deposition of pharmaceutical aerosols: Effects of transient inhalation and sampling the airways. *Journal of Aerosol Science 42*, 11 (Nov. 2011), 781–799.

[69] Usmani, O. S., Biddiscombe, M. F., and Barnes, P. J. Regional lung deposition and bronchodilator response as a function of beta2-agonist particle size. *American Journal of Respiratory and Critical Care Medicine 172*, 12 (Dec. 2005), 1497–1504.

[70] Vignon-clementel, I., Albertofigueroa, C., Jansen, K., and Taylor, C. Outflow boundary conditions for three-dimensional finite element modeling of blood flow and pressure in arteries. *Computer Methods in Applied Mechanics and Engineering 195*, 29-32 (June 2006), 3776–3796.

[71] Wall, W. A., and Rabczuk, T. Fluid structure interaction in lower airways of CT-based lung geometries. *International Journal for Numerical Methods in Fluids 57* (2008), 653–675.

[72] Wall, W. A., Wiechert, L., Comerford, A., and Rausch, S. Towards a comprehensive computational model for the respiratory system. *International Journal for Numerical Methods in Biomedical Engineering 26* (2010), 807–827.

[73] Wichers, L. B., Rowan, W. H., Nolan, J. P., Ledbetter, A. D., McGee, J. K., Costa, D. L., and Watkinson, W. P. Particle deposition in spontaneously hypertensive rats exposed via whole-body inhalation: measured and estimated dose. *Toxicological Sciences 93*, 2 (Oct. 2006), 400–10.

[74] Woods, J. C., Choong, C. K., Yablonskiy, D. a., Bentley, J., Wong, J., Pierce, J. a., Cooper, J. D., Macklem, P. T., Conradi, M. S., and Hogg, J. C. Hyperpolarized 3He diffusion MRI and histology in pulmonary emphysema. *Magnetic resonance in medicine : official journal of the Society of Magnetic Resonance in Medicine / Society of Magnetic Resonance in Medicine 56*, 6 (Dec. 2006), 1293–300.

[75] Wu, Y., Kotzer, C. J., Makrogiannis, S., Logan, G. a., Haley, H., Barnette, M. S., and Sarkar, S. K. A noninvasive [99mTc]DTPA SPECT/CT imaging methodology as a measure of lung permeability in a

guinea pig model of COPD. *Molecular imaging and biology 13*, 5 (Oct. 2011), 923–9.

[76] Yin, Y., Choi, J., Hoffman, E. a., Tawhai, M. H., and Lin, C.-L. A multiscale MDCT image-based breathing lung model with time-varying regional ventilation. *Journal of Computational Physics*.

[77] Yin, Y., Choi, J., Hoffman, E. a., Tawhai, M. H., and Lin, C.-L. Simulation of pulmonary air flow with a subject-specific boundary condition. *Journal of Biomechanics 43*, 11 (Aug. 2010), 2159–63.

[78] Zarogoulidis, P., Chatzaki, E., Porpodis, K., Domvri, K., Hohenforst-Schmidt, W., Goldberg, E., Karamanos, N., and Zarogoulidis, K. Inhaled chemotherapy in lung cancer: future concept of nanomedicine. *International Journal of Nanomedicine 7* (2012), 1551–1572.

[79] Zarogoulidis, P., Papanas, N., Kouliatsis, G., Spyratos, D., Zarogoulidis, K., and Maltezos, E. Inhaled insulin too soon to be forgotten. *Journal of Aerosol Medicine and Pulmonary Drug Delivery 24*, 5 (2011), 213–223.

[80] Zeman, K. L., Wu, J., and Bennett, W. D. Targeting aerosolized drugs to the conducting airways using very large particles and extremely slow Inhalations. *Journal of Aerosol Medicine 23*, 6 (2010), 363–369.

[81] Zhang, H., and Papadakis, G. Computational analysis of flow structure and particle deposition in a single asthmatic human airway bifurcation. *Journal of Biomechanics 43*, 13 (Sept. 2010), 2453–9.

[82] Zhang, Z., Kleinstreuer, C., and Feng, Y. Vapor deposition during cigarette smoke inhalation in a subject-specific human airway model. *Journal of Aerosol Science 53* (Nov. 2012), 40–60.

Chapter 2

Theory and Governing Principles

2.1 Magnetic Resonance Imaging

Medical magnetic resonance imaging (MRI) takes advantage of protons, or ^1H nuclei, in the body. All protons and electrons have a spin, a constant angular momentum. In the case of nuclei with an even number of protons or neutrons, these spins cancel each other out. However, a magnetic dipole moment is created for nuclei with an odd number of protons or neutrons, as in the case with ^1H protons. When the ^1H nuclei is placed in a magnetic field, B_0, the nuclei tends to align with this magnetic field. Figure 2.1 shows a schematic of a proton spinning around the magnetic field, B_0. Protons spin at a precession frequency, which is defined as:

$$\nu_0 = \gamma B_0, \tag{2.1}$$

where γ is the gyro-magnetic ratio that remains constant and unique to each proton. For 1^H protons $\gamma = 42.58\frac{MHz}{T}$ [3]. The precession frequency, ν_0 is dependent on the magnetic field, B_0. Therefore protons will spin faster as the magnetic field becomes higher. Without the presence of a magnetic field, the protons are randomly orientated and therefore the net magnetization, M_0 is zero. However, once placed in an external magnetic field, the protons tend to align with the magnetic field and create a weak magnetic field (M_0) [3].

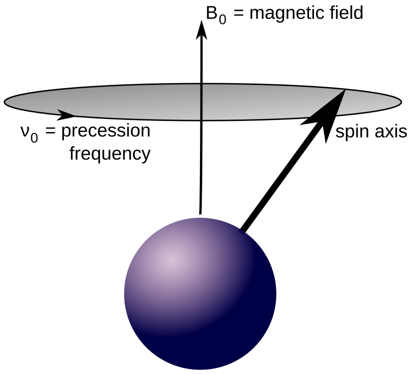

Figure 2.1: Schematic of magnetic dipole spinning due to the magnetic field, B_0. The dipole is spinning at the precession frequency, ν_0 (see Eq. 2.1). [3]

To produce a magnetization that is measurable, the ^1H nuclei are tipped away from B_0 with a radio frequency (RF) pulse applied at the exact ν_0 of the proton. This RF field is produced by a transmit and receive coil. Even though this pulse is much smaller than the magnetic field, it is able to flip the protons because the RF pulse is applied at the exact frequency of the spin. Figure 2.2 shows a schematic of a proton flipped with a flip angle of 90°. Just like a spinning top that is tipped off its axis, the proton will spin at a wider girth than its natural radius. This process creates a magnetization, M, that is measurable by the transmit and receive coil. [3] Once the RF pulse is stopped, the proton will start to decrease the diameter of its spin until it is back to its natural diameter and the proton begin to re-align with the magnetic field.

The time it takes for the protons to return to their natural precession is defined by the time constant T_2 (see Figure 2.3B) and the time for the protons to return their magnetic steady state is defined by the time constant T_1 (see Figure 2.3A). Both of these exponential time constants depend on the tissue being imaged and the magnetic field. Additionally, T_1 is typical longer than T_2.

The decay of a the MR signal is measured with an echo. The echo is created when a second RF pulse is applied. The MR signal intensity depends on the time at which this second RF pulse is applied, defined as the echo time (TE). For example, a short TE would result in a large (i.e. bright) signal intensity and a long TE would

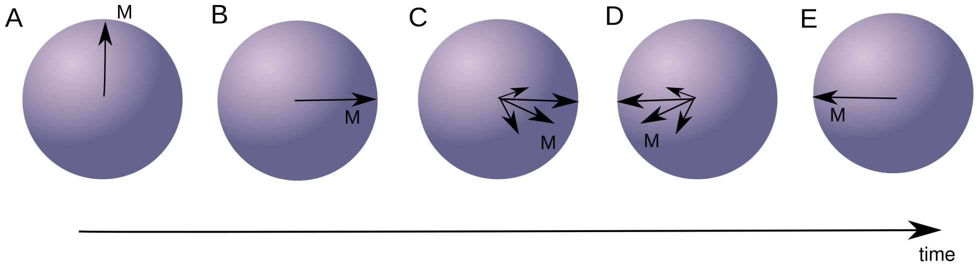

Figure 2.2: Schematic of the net average of the magnetic spins, M. First, the spins are aligned with the magnetic field, B_0 (panel A). Next a 90° pulse is applied at the resonant frequency of the proton (panel B). The spins begin to get out of phase with each other (panel C) because of the local inhomogeneities and the signal decays. Next, a 180° pulse is applied and the spins flip (panel D) and will become refocused (panel E). This is where the echo is created and the signal intensity measured at time TE (TE = echo time).

result is a low (i.e. dark) signal intensity (see Figure 2.3).

MRI experiments are typically described as T_1 weighted or T_2 weighted. This description mainly refers to what time constant is influencing the signal read-out. By controlling the imaging parameters, namely the repetition time (TR), it is possible to the remove the T1 dependence. For example, when the repetition time (TR) of the RF pulse is sufficiently long, the signal has increased and has little effect on the next RF pulse. Therefore, the image is T_2 weighted. However, when TR is short, the proton has not had sufficient time to return pointing towards B_0 and therefore the image is T_1 weighted.

The time constants, T_1 and T_2, depend on the tissue density. Therefore, differences in neighboring tissue densities may cause the spinning protons to become out of phase with each other (see Figure 2.2). As the spins become more and more out of phase the signal intensity decays at each greater rate. This decay time is characterized by T_2^* (see Figure 2.3B). Therefore, greater the inhomogeneities in the tissues, the shorter T_2^* will be and the faster the signal decay. This rapid decay maybe reversed by a process called a spin echo. In spin echo imaging a 180° RF pulse is applied after the spins have become out of phase (see Figure 2.2). This RF

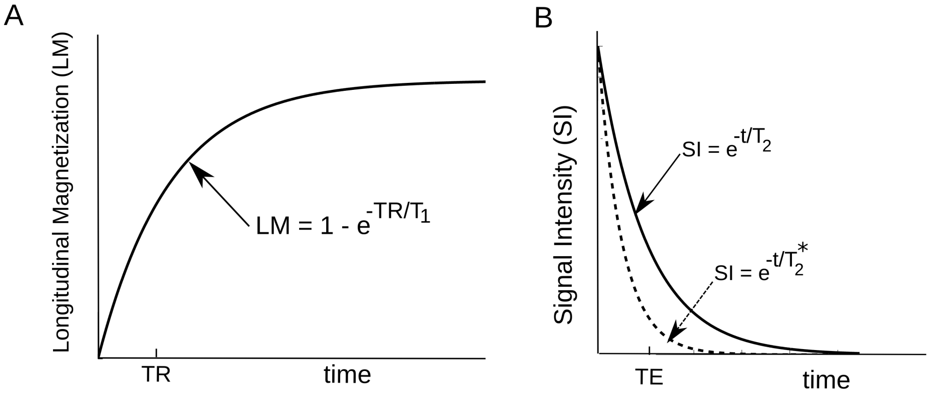

Figure 2.3: The time constant T_1 for the precession to align with the magnetic field (panel A) and free induction signal decay rate due to T_2 and T_2^* [3]

pulse flips the protons over and the protons go back into phase. Once the protons are back into phase the signal intensity is read at the time of the echo.

2.1.1 Gradient Echo Imaging

The work presented in this dissertation takes advantage of the rapid signal decay rate that occurs with local field inhomogeneities. In gradient echo imaging, the spinning protons are not subjected to the additional 180° pulse that is typically applied in spin-echo sequences that corrects for local field inhomogeneities (see Figure 2.2E). In gradient echo imaging the signal decay time constant (T_2^*) is defined as:

$$\frac{1}{T_2^*} = \frac{1}{T_2} + \frac{1}{T'} \tag{2.2}$$

where T' is the local magnetic field inhomogeneities. These inhomogeneities may be impacted by the RF coil, air/tissue interfaces and objects that induce magnetic susceptibility. In this dissertation, super-paramagnetic particles were employed to study particle deposition in rat lungs (see Chapter 4).

Super-paramagnetic particles (SPIO) have been used previously as contrasts agents for cell tracking [1, 5] and for detecting inflammatory tissues [9]. These particles cause signal de-phasing around labeled regions. This enhanced de-phasing causes a reduced T_2^* time constant compared to non-labeled regions. Therefore, as the signal intensity (SI) is related to T_2^* by

$$SI = A_0 e^{-\frac{-TE}{T_2^*}} \tag{2.3}$$

where A_0 is the initial signal intensity and TE is the echo time, the signal intensity in a given region is less where there are SPIO particles compared to a particle-free region. In chapter 4, the concentration of particles in the lung is related to the signal decay constant R_2^*, where $R_2^* = \frac{1}{T_2^*}$.

2.1.2 Image Analysis

In this dissertation, the signal decay rate, R_2^*, was calculated from MR signal intensity images acquired at four echo times (TE). To do this, R_2^* was calculated for each voxel and then average values of R_2^* was determined by drawing regions of interest (ROIs) around important areas on the image. The R_2^* was calculated by first taking the log of the signal intensity:

$$S = \log(SI_{i,j}^n) \tag{2.4}$$

where i denotes the echo time and i and j are the row and column, respectively, of the image map. Next, the slope of the linear signal intensity was calculated by employing a linear regression algorithm

$$m = \frac{[N_{TE}\sum_{n=1}^{N_{TE}} S_{i,j}^n TE^n - \sum_{n=1}^{N_{TE}} TE^n]\sum_{n=1}^{N_{TE}} S_{i,j}^n}{N_{TE}\sum_{n=1}^{N_{TE}} TE^{n2} - (\sum_{n=1}^{N_{TE}} TE^n)^2} \tag{2.5}$$

where N_{TE} is the number of echo times. Next,

$$R_2^* = m \tag{2.6}$$

The initial signal intensity then may be calculated as

$$A_0 = e^{\frac{\sum_{n=1}^{N_{TE}} S_{i,j}^n - m\sum_{n=1}^{N_{TE}} TE_i}{N_{TE}}}. \tag{2.7}$$

2.2 CFD Simulations

The 3D Navier-Stokes equations for an incompressible Newtonian fluid can be written as

$$\rho\frac{\partial\vec{v}}{\partial t}+\rho\vec{v}\cdot\nabla\vec{v}=-\nabla p+\mu\nabla^2\vec{v}+\vec{g} \tag{2.8}$$

for the momentum equation and

$$\nabla\cdot\vec{v}=0 \tag{2.9}$$

for the continuity equation, where $\vec{v}$ is the velocity vector in space and time, p is the pressure, $\nabla=\frac{\partial}{\partial x}+\frac{\partial}{\partial y}+\frac{\partial}{\partial z}$ and t is the time. Equations 2.8 and 2.9 may be solved on the domain, Ω, using appropriate boundary (Γ) and initial conditions. Boundary conditions can be either defined as Dirichlet (velocity prescribed), Γ_g or Neumann (pressure or mixed boundary condition), Γ_h.

Before being solved using Finite Element methods, the Navier-Stokes equations must be transformed from the strong form written in Eqs. 2.8 and 2.9 to the weak form. Once the weak from is obtained, the equations can be converted into a system of equations that may be solved numerically. The weak from is obtained by taking the inner product of Eqs. 2.8 and 2.9 with test functions. Following [18], the trial solution (S) and weighting functions (W,P) spaces are given as

$$\begin{aligned}
S &= [\vec{v}|\vec{v}(\vec{x},t)\in H^1(\Omega)^3, t\in[0,T], \vec{v}(\vec{x},t)\in P_h(\bar{\Gamma}_e), \vec{v}(\vec{x},t)=\vec{g}\,on\,\Gamma_g] && (2.10)\\
W &= [\vec{w}|\vec{w}(\vec{x},t)\in H^1(\Omega)^3, t\in[0,T], \vec{w}(\vec{x},t)=0\,on\,\Gamma_g] && (2.11)\\
P &= [p|p(\vec{x},t)\in H^1(\Omega), t\in[0,T]] && (2.12)
\end{aligned}$$

where $\vec{g}$ is the Dirichlet boundary condition, H^1 is the usual Sobolev (vector) space of functions with square-intergratable variables and $\vec{x}=x,y,z$. It must be noted that a stabilized formulation is employed which allows for equal-order velocity and pressure interpolation [7]. The stabilized methods employed here are shown in detail elsewhere [15, 19] The weak form, which resulted from the semi-discrete Galerkin finite element formulated results in:

Given:

$$\vec{f} : \Omega x(0,T) \rightarrow \Re^3 \tag{2.13}$$

$$\vec{g}\Gamma_g x(0,T) \rightarrow \Re^3 \tag{2.14}$$

Find $\vec{v} \in S$ and $p \in P$ such that every $\vec{w} \in W$ and $q \in P$.

$$\begin{aligned} B(\vec{w},q;\vec{v},p) &= 0 && (2.15) \\ B(\vec{w},q;\vec{v},p) &= \int_\Omega [\vec{w} \cdot [\frac{\partial \vec{v}}{\partial t} + \vec{v} \cdot \nabla \vec{v} - \vec{g}] + \nabla \vec{w} : && (2.16) \\ -\nabla p + \mu \nabla^2 \vec{v}]dx - \int_\Omega \nabla q \cdot \vec{v} dx & \\ - \int_{\Gamma_h} \vec{w} \cdot [-\nabla p + \mu \nabla^2 \vec{v}] \cdot \vec{n} ds & \\ + \int_\Gamma q\vec{v} \cdot \vec{n} ds & \end{aligned}$$

where $\vec{n}$ is the normal vector. The standard Galerkin method that was originally developed for solid finite elements is unstable for advection-dominated flows and in the diffusion dominated limit for equal-order interpolation of velocity and pressure. Therefore, a stabilized method was utilized to address these instabilities. Equation 2.17 may be written as a system of nonlinear ordinary differential equations. The residual vectors for the momentum equation, $\vec{R}_m^A$ and continuity R_c^A satisfies

$$\begin{bmatrix} R_m^A \\ R_c^A \end{bmatrix} = \begin{bmatrix} 0 \\ 0 \end{bmatrix}.$$

The residuals are computed for each element. The nonlinear equations that result from the Galerkin method are discretized and integrated in time using the Generalized α - Method developed for the Navier-Stokes equations [8].

2.2.1 Generalized Alpha Method

The generalized alpha method and the Newton Raphson method are employed to form the stiffness matrix. A schematic of the iteration loop used to solve the flow equations is showni n Figure 2.4.

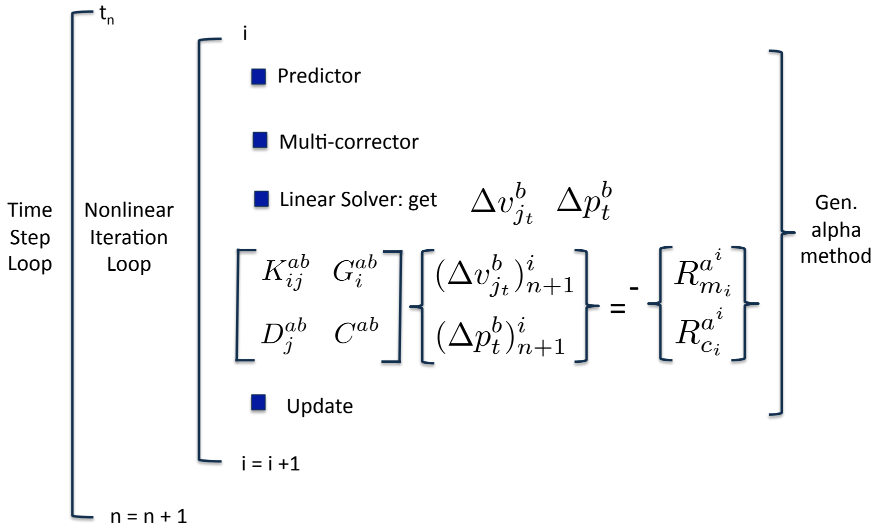

Figure 2.4: Schematic of the generalized alpha method and nonlinear and step iteration taken to solve the linearized flow equations [18]

where

$$K^{ab}_{ij} = \frac{\partial R^{a^i}_{m_i}}{\partial v^{b^{n+1}}_{j_t}} \tag{2.17}$$

$$G^{ab}_{i} = \frac{\partial R^{a^i}_{m_i}}{\partial p^{b^{n+1}}_{t}} \tag{2.18}$$

$$D^{ab}_{j} = \frac{\partial R^{a^i}_{c_i}}{\partial v^{b^{n+1}}_{j_t}} \tag{2.19}$$

$$C^{ab} = \frac{\partial R^{a^i}_{m_i}}{\partial p^{b^{n+1}}_{t}} \tag{2.20}$$

$$\tag{2.21}$$

where $v^b_{j,t}$ is the time derivative of velocity and p^b_t is the time derivative of pressure. The subscripts i and j indicate the spatial dimensions and the subscripts a and b represent the local nodal numbers [18]. The system is solved using a conjugate gradient method and a preconditioned Generalized Minimum Residual (GMRES) method [14].

2.2.2 Backflow Stabilization

Backflow divergence at an inlet/outlet of a computational model is a significant numerical problem that occurs in CFD simulations. This backflow numerical divergence may occur at inlets/outlets where a Neumann boundary condition is applied, at inlet/outlets where recirculating flow has developed or areas where there is bulk flow reversal. Figure 2.5 shows an example of backflow divergence that occurred with recirculated flow [6]. This type of divergence is common in respiratory simulations that model both inspiration and expiration. During expiration, the flow reverses and the small airways that were outlets during inspiration become inlets during expiration. Previous respiratory models have simply lengthened these airways, allowing for the flow to become fully developed. [16] However, these lengthened airways may change the flow field, airway resistance, and may not solve backflow divergence problems that occur when Neumann boundary conditions are prescribed. In this dissertation, Neumann boundary conditions were applied at all of the airway faces. With Neumann boundary conditions, the velocity profile is not prescribed and this therefore may lead to backflow divergence issues. Several solutions to backflow divergence are given and compared in Esmaily-Moghadam et al. [6].

The backflow divergence stability terms that were employed in this dissertation were developed and described in detail elsewhere [6]. Briefly, the solver employed in this dissertation applied Galerkin's method to the weak form of the Navier-Stokes equations 2.17. Equation 2.17 may be modified to include an additional term [2]

$$\tilde{B}(\vec{w}, q; \vec{v}, p) = B(\vec{w}, q; \vec{v}, p) - \beta(\vec{w}, \rho(\vec{v} \cdot \vec{n}) - \vec{v})_{\Gamma_h} \tag{2.22}$$

where β is a positive coefficient between 0 and 1 and the smaller the value of β is the less intrusive and more stable the system is. The $\vec{v} \cdot \vec{n}$ term is defined as

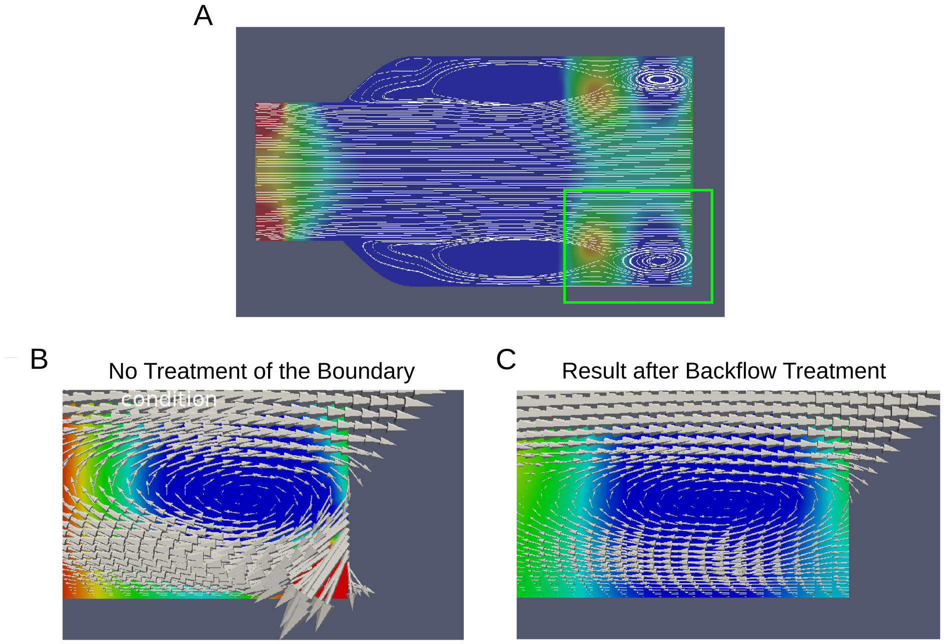

Figure 2.5: Example of backflow divergence that occurred in a re-circulating flow problem. Panel B shows resulting velocity vectors with no backflow treatment and Panel C shows flow vectors after backflow treatment [6]. Images were provided by Mahdi Esmaily Moghadam.

$$(\vec{v} \cdot \vec{n}) = \frac{\vec{v} \cdot \vec{n} - |\vec{v} \cdot \vec{n}|}{2} \tag{2.23}$$

which equals

$$\vec{v} \cdot \vec{n}, \quad \vec{v} \cdot \vec{n} < 0 \tag{2.24}$$

$$0, \quad \vec{v} \cdot \vec{n} \geq 0 \tag{2.25}$$

This essentially means that this term is opposite of the backflow and therefore is only turned on when backflow is occurring, otherwise it is 0. Figure 2.5C shows the result after the backflow stabilization term, β was implemented by [6].

2.2.3 Boundary Conditions

In this dissertation a resistance and capacitance circuit (RC) in series (see Figure 2.6 were employed as a boundary condition at the distal faces of all the airways. This RC boundary boundary condition may be implemented in solving the Navier-Stokes equations by a monolithic approach or an iterative approach. The theory behind both of these approaches and their implementation with this specific RC boundary condition are discussed in the next sections.

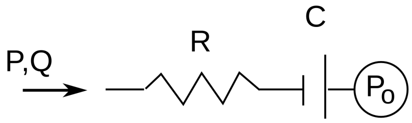

Figure 2.6: RC circuit implemented as a boundary condition in this dissertation

Monolithic BC Implementation

In the monolithic approach the 0D model is completely coupled to the flow solver equations (see Figure 2.4). Therefore this is a closed system of equations and the boundary conditions are solved simultaneously with the flow equations. Here, the analytical solution of the 0D model must be known as well as the relationship between pressure and flow. This monolithic implementation of boundary conditions was performed by and discussed in detail elsewhere [17, 18]. Briefly, the discretized boundary condition term can be written as

$$\begin{aligned} R^A_{m,M_i} = S^A_i * (R(1-\alpha_f)Q_n + R\alpha_f S^C_k v^C_{k,n+1} \\ + \sum_{l=0}^{n-1} \int_{t_l}^{t_{l+1}} \frac{1}{C}[Q_l \frac{t_{l+1}-t'}{t_{l+1}-t_l} + Q_{l+1}\frac{t'-t_l}{t_{l+1}-t_l}]dt' \\ + \int_{t_n}^{t_{n+\alpha_f}} \frac{1}{C}[Q_n \frac{t_{n+1}-t'}{t_{n+1}-t_n} + S^C_k v^c_{k,n+1}\frac{t'-t_n}{t_{n+1}-t_n}]dt') \end{aligned} \tag{2.26}$$

and the history term is

$$R^A_{m,Hi} = -S^A_i P_{peep} \tag{2.27}$$

and the total momentum residual is given as

$$R^A_{m_i} = R^A_{m,M_1} + R^A_{m,H_1} \tag{2.28}$$

where S are the shape functions, k is the direction, and c is the node number. The corresponding tangent matrix contribution is therefore

$$K^{AC}_{m_{jk}} = \Delta t \gamma S^A_i S^C_k \left[R\alpha_f + \int_{t_n}^{t_{n+\alpha_f}} \frac{1}{C} \frac{t' - t_n}{t_{n+1} - t_n} dt' \right] \tag{2.29}$$

It should be noted that R is the resistance or is defined as $\frac{dp}{dQ}$. Also, we can find velocity as

$$v^C_k(t') = v^C_{k,l} \left[\frac{t_{l+1} - t'}{t_{l+1} - t_l} \right] + v^C_{k,l+1} \left[\frac{t' - t_l}{t_{l+1} - t_l} \right] \tag{2.30}$$

and the flow rate is defined as

$$Q_l = \sum_c \sum_k \int_{\Gamma_B} N^C_k n_k d\Gamma * v^c_{k,l}. \tag{2.31}$$

In implementation of this RC boundary condition into the solver, the pressure is taken at each time step and is defined as

$$p_{old} = \sum_{l=0}^{n} \beta_l Q_l \tag{2.32}$$

and thus the residual becomes

$$\begin{aligned} R^{A,old}_{m,M_i} &= S^A_i * \sum_{l=0}^{n} \beta_l Q_l && (2.33) \\ &= S^A_i * R(1 - \alpha_f) Q_n && (2.34) \\ &+ \int_{t_n}^{t_{n+alpha_f}} \frac{1}{C} * Q_n \left[\frac{t_{n+1} - t'}{t_{n+1} - t_n} \right] \\ &+ \sum_{i=0}^{n-1} \int_{t_l}^{t_{l+1}} \frac{1}{C} * \left[Q_l \frac{t_{l+1} - t'}{t_{l+1} - t_l} \right] dt' \end{aligned}$$

with

$$R^{A,old}_{m,H_i} = 0 \tag{2.35}$$

$$R^{A,old}_{m_i} = R^{A,old}_{m,M_i} + R^{A,old}_{m,H_i} \tag{2.36}$$

where the β coefficients are:

$$\beta_0 = \int_0^{t_l} \frac{1}{C} \frac{t_1 - t'}{t_1} dt', n \geq 1 \tag{2.37}$$

$$\beta_l = \int_{t_l}^{t_{l+1}} \frac{1}{C} \frac{t_{l+1} - t'}{t_{l+1} - t_l} dt' + \int_{t_{l-1}}^{t_n} \frac{1}{C} \frac{t' - t_{l-1}}{t_l - t_{l-1}} dt', l = 1, n-1, n \geq 2 \tag{2.38}$$

$$\beta_n = R(1 - \alpha_f) + \int_{t_n}^{t_{n+\alpha_f}} \frac{1}{C} \frac{t_{n+1} - t'}{t_{n+1} - t_n} dt' + \int_{t_{n-1}}^{t_n} \frac{1}{C} \frac{t' - tn - 1}{t_n - t_{n-1}} dt', n \geq 1 \tag{2.39}$$

$$\beta_{n+1} = R\alpha_f + \int_{t_n}^{t_{n+\alpha_f}} \frac{1}{C} \frac{t' - t_n}{t_{n+1} - t_n} dt', n \geq 1 \tag{2.40}$$

where R and C are the resistance and compliance coefficients. The right hand formulation is the residuals and the left hand formulation is $K^{AC}_{m_{ik}}$.

Iterative BC Implementation

The iterative boundary conditions were implemented in the flow solver by Moghadam et al. [11] and therefore is discussed only briefly here. The iterative coupling scheme essentially solves a system of equations using the flow rate for the 3D solution to find pressure. Then the resistance, or $R = \frac{dP}{dQ}$, is put into the LHS formulation of the stiffness matrix (see Figure 2.4) to solve the system of equations. Due to the contribution of the lumped parameter network into the LHS, the overall scheme is implicit. Figure 2.7 shows a schematic of the passing of flow rate and pressure.

The following steps were employed to solve the couple system [11].

- The unknowns, $\vec{v}$ and p are predicted at the time step $n+1$ and at the kth iteration

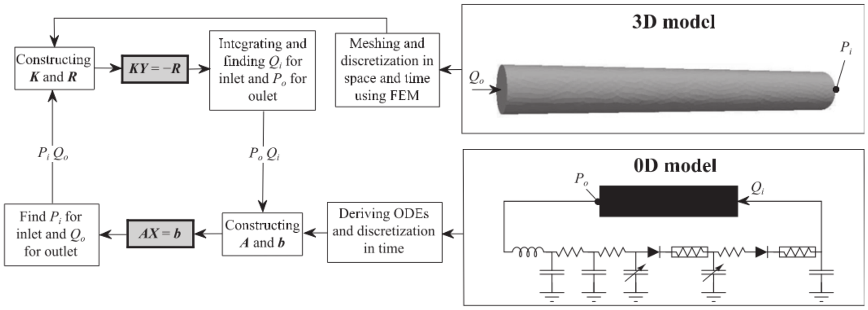

Figure 2.7: Schematic of the iterative scheme where flow rate is passed to the 0D model and pressure is based back to the 3D solver to construct the LHS matrix. Figure from [11].

$$\begin{aligned} k &= 0 && (2.41)\\ \vec{v}_k^{n+1} &= \vec{v} && (2.42)\\ p_k^{n+1} &= P^n && (2.43) \end{aligned}$$

- The flow rate and pressure is then computed at the boundaries with

  $$\begin{aligned} Q_i(t) &= \int_{\Gamma_i} \vec{v}\cdot\vec{n}d\Gamma && (2.44)\\ P_i(t) &= \frac{\int_{\Gamma_i} pd\Gamma}{\int_{\Gamma_i} d\Gamma} && (2.45) \end{aligned}$$

  and passed to the 0D domain.

- The flow and pressure are received at time steps n and $n+1$ and the ODEs are integrated using a 4th order Runge-Kutta scheme. Next, solve the linearized flow equations to find $\Delta v_{j,t}^b$ and Δp_t^b.

- The pressure and flow are passed back to the 3D scheme and the tractions are calculated

  $$\vec{h}(\vec{v}, p; \vec{x}, t) = -P_i\vec{n} \tag{2.46}$$

- The stiffness matrix (see Figure 2.4) were constructed for the residuals ($R^{a^i}_{m_i}$ and $R^{a^i}_{c_i}$) and K^{ab}_{ij}.
- The velocity and pressure terms are corrected

$$p^{n+1}_{k+1} = p^{n+1}_{k} + \alpha_f \gamma \Delta t \Delta p^b_t \tag{2.47}$$

$$\vec{v}^{n+1}_{k+1} = \vec{v}^{n+1}_{k} + \gamma \Delta t \Delta v^b_{j,t} \tag{2.48}$$

  where α_f and γ are from the generalized alpha formulation.

- k is then back stepped to $k+1$ to k if the residual is not small enough .

The resistance and compliance, for this dissertation, were broken into a system of ODEs, given as

$$\frac{dp}{dt}_i = \frac{Q_i}{C_i} \tag{2.49}$$

$$P_{\text{offset}} = R_i Q_i \tag{2.50}$$

2.2.4 Monolithic vs Iterative

The RC boundary condition was implemented using both the monolithic and iterative approach using the model and boundary conditions described in Chapter 6. Figure 2.8 show the flow rate at the trachea face for monolithic and iterative implementation. There was less than 1 % difference between the two implementations.

2.3 Particle Transport

For particle-laden respiratory airflows, it is typically assumed that particles are spherical, inert and do not influence the surrounding flow field. Therefore, for most cases, it is appropriate to to solve the particle transport equations de-coupled from

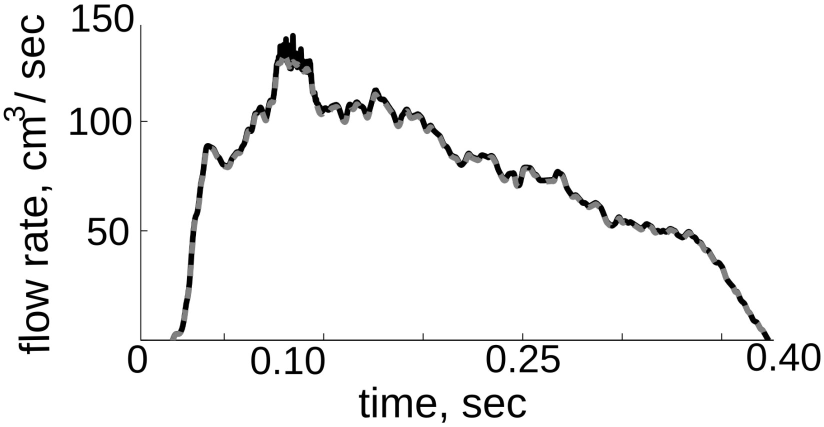

Figure 2.8: Flow rate during inspiration for monolithic (black line) and iterative (grey line) boundary conditions.

the flow equations. Whether an Eulerian coordinate or Lagrangian coordinate system is used depends mainly on how dilute the system is and the size of the particles being studied. For systems with high particle concentration or for small particles that are likely to diffuse an Eulerian coordinate system is typically used. In these cases the concentration of particles is solved over space and time. Otherwise, a Lagrangian coordinate system is employed, where each individual particle is tracked over space and time. Lagrangian tracking was used in this current work because the particles studied here had diameters greater than 1 μm and the system was dilute enough that the particles equations were able to be solved at a reasonable computational cost.

2.3.1 Particle Transport Equations

The motion of a particle for non-uniform, unsteady flow was defined by Maxey and Riley [10] as:

$$m_p \frac{d\mathbf{V}}{dt} = (m_p - m_F)\mathbf{g} + m_F \frac{D\mathbf{u}}{Dt} - \frac{1}{2} m_F \frac{d}{dt}\left[\mathbf{V} - \mathbf{u}(\mathbf{X}(t), t) - \frac{1}{10} a^2 \nabla^2 \mathbf{u}\right] \qquad (2.51)$$
$$-6\pi a \mu \mathbf{Q}(t) - 6\pi a^2 \mu \int_0^t d\tau \frac{dQ/d\tau}{(\pi(t-\tau))^{1/2}}$$

where $\mathbf{V}(t)$ is the particle velocity $\mathbf{u}(\mathbf{t}, \mathbf{X})$ is the fluid velocity, m_p is the particle mass, m_F is the mass of the fluid, a is the radius of the particle, and μ is the viscosity of the fluid. Starting from the right, the first term is the acceleration due to gravity, the second term is the fluid force on the particle, the third term is the added mass, the forth term is Stoke's drag and the last term is the Basset history term. For small particles, where the initial motion of the particle is not important, the Basset history term and Faxen correction may be neglected. With this, equation 6.5 becomes

$$\begin{aligned}(m_p + \frac{1}{2}m_F)\frac{d\mathbf{V}}{dt} = (m_p - m_F)\mathbf{g} + 6\pi a\mu(\mathbf{u}(\mathbf{X}(t)), t) - \mathbf{V}(t)) \\ + \frac{3}{2}m_F\frac{\partial u}{\partial t} + m_F(\mathbf{u} + \frac{1}{2}\mathbf{V}) \cdot \nabla\mathbf{u}.\end{aligned} \tag{2.52}$$

Additionally, if the Reynolds number of the particle, Re_p is < 1 ($Re_p = \frac{(u_p - u_f)d_p\rho_f}{\mu}$) and the density of the fluid is much less than the density of the particle, the particle transport equation reduces to

$$\frac{d\mathbf{v}}{dt} = \frac{6\pi a\mu}{m_p}[\mathbf{u} - \mathbf{v}] + \mathbf{g} \tag{2.53}$$

where $\mathbf{u}$ is the velocity of the fluid, $\mathbf{v}$ is the velocity of the particle, a is the radius of the particle and μ is the viscosity of the fluid. The particle mass is defined as $m_p = \rho_p V_p$, where ρ_p is the particle density and V_p is the volume of the particle.

Substituting in the mass of the particle gives

$$\frac{d\mathbf{v}}{dt} = \frac{18\mu}{\rho_p d_p^2}[\mathbf{u} - \mathbf{v}] + \mathbf{g}. \tag{2.54}$$

Non-dimensional variables may be defined as

$$\mathbf{u}* = \frac{\mathbf{u}}{U},\ \mathbf{v}* = \frac{\mathbf{v}}{U},\ t* = \frac{tU}{d},\ \mathbf{g}* = \frac{\mathbf{g}}{g} \tag{2.55}$$

where U is the mean velocity of the fluid and d is the diameter of the channel. Subbing and re-arranging results in:

$$\frac{\rho_p d_p^2 U}{18\mu d}\frac{d\mathbf{v}*}{dt*} = [\mathbf{u} * -\mathbf{v}*] + \frac{g\rho_p d_p^2}{18\mu U}\mathbf{g} * . \tag{2.56}$$

Defining

$$V_s = \frac{\rho_p g dp^2}{18\mu} \tag{2.57}$$

as the settling velocity and

$$Stk = \frac{\rho_p dp^2 U}{18\mu d} \tag{2.58}$$

as the Stokes number, the non-dimensional particle equation may be written as:

$$Stk\frac{d\mathbf{v}*}{dt*} = [\mathbf{u} * -\mathbf{v}*] + \frac{V_s}{U}\mathbf{g} * . \tag{2.59}$$

The relative importance of each term in equation 2.59 may be determined based on Stk number and $\frac{V_s}{U}$. The unsteady effects of the particle equation become relevant if the Stk's number is high and if the particle velocity is changing quickly with time. Even though we show that Stk's number is higher than the gravity term, we do not expect unsteady effects to be very influential in a horizontal cylinder. Unsteady effects do become important when the flow abruptly changes direction and consequently the particle velocity abruptly changes, as can be seen at airway bifurcations. However, particle velocity changes may become important if there is a high shear rate (ie: the velocity changes are high normal to the channel wall). Therefore, as the particle is falling it is experiencing velocity changes due to the parabolic profile.

2.3.2 Particle Validation

In this section two idealized cases were studied. Particle tracking was performed by using a Lagrangian code that solves equation 2.53 developed by Shawn Shadden (see Chapter 5). The first case that was studied was a horizontal cylindrical channel and the second case to be studied was a double bifurcation.

Horizontal Cylinder

A cylinder of length 40 mm and radius of 1 mm was created in in Simvascular and the flow was solved for using the flow solver discussed previously. The inlet boundary condition was a parabolic velocity profile based on a given flow rate and the outlet boundary condition was zero pressure. Three flow rates were tested, 5333, 2000 and 500 $\frac{mm^3}{sec}$. 5333 mm^3/sec is the flow rate at the inlet of the rat trachea and would be the maximum velocity in the airway model. The fluid density and viscosity were defined for air and the particle density defined as water. For each flow rate several different particle sizes were used. The flow was solved for using a delta time of 0.001 seconds for 40 time steps, with 5 integration steps for each time step. The particles used for all simulations were seeded based on a Cartesian mesh at the inlet, and resulted in 7639 particles. For each simulation the particles were only seeded once and the simulation was ran until all particles either deposited or exited the domain.

The particles were tagged in such a way that the starting position of each particle was known. The distribution of particles on the inlet face were then corrected based on this starting position using a parabolic mass density function. The efficiency, E, of deposition was compared to analytical solution given by Pich et al. [12]. The efficiency was given as

$$E = frac2\pi \left[2\epsilon\sqrt{1-\epsilon^{\frac{2}{3}}} - \epsilon^{\frac{1}{3}}\sqrt{1-\epsilon^{\frac{2}{3}}} + arcsin\epsilon^{\frac{1}{3}} \right] \tag{2.60}$$

where

$$\epsilon\frac{3V_sL}{8a\tilde{U}} \tag{2.61}$$

where V_s is the settling velocity of the particle (see Eq. 2.57), L is the length of the cylinder, a is radius of the cylinder and $\tilde{U}$ is the mean flow velocity in the cylinder. Figure 2.9 shows the particle deposition percentage versus the ϵ. Good agreement was found between the simulated deposition and the analytical deposition given by Pich et al [12].

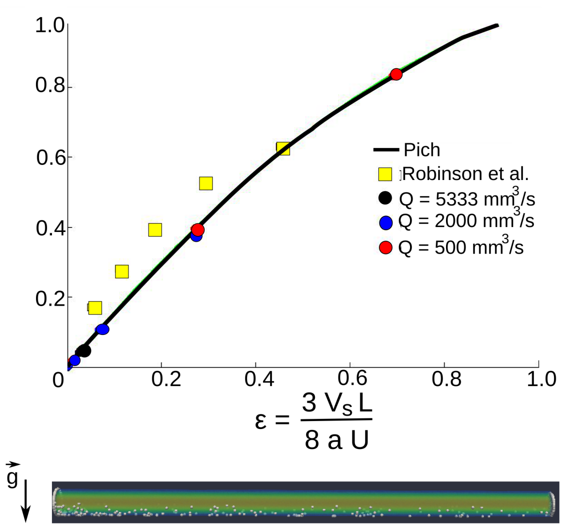

Figure 2.9: Horizontal cylinder used for particle validation study. Good agreement was shown between simulation and analytical solution given by Pich et al [13].

Simple Bifurcation

A simple bifurcation was created with inlet radius of 1 mm, daughter branch radius of 0.75 mm and bifurcation angle of 30 °. Airflow was solved in the bifurcation with mean flow rates of 5333, 2000 and 200 $\frac{mm^3}{sec}$. Particles were then tracked in the flow field with the same particle seeding employed for the horizontal cylinder. The percent of particles deposited were compared to analytical solution given by Cai et al [4]. The deposition efficiency was given as

$$\nu = G(\alpha, \frac{R}{R_0})Stk \tag{2.62}$$

where Stk is the Stokes number given in Eq. 2.58. The G function is given by:

$$G(\alpha, \frac{R}{R_0}) = \frac{8\text{sin}\alpha f_1(\alpha, \frac{R}{R_0})}{\frac{R}{R_0} f_0(\alpha, \frac{R}{R_0})} \tag{2.63}$$

where

$$f_0(\alpha, \frac{R}{R_0}) = \pi \left[1 - \frac{1}{4}\left(\frac{R}{R_0}\right)^2\right] - \frac{4}{3}\left[\frac{15}{16}\pi - 2\right]\left(\frac{R}{R_0}\right)^2 cos^2\alpha \tag{2.64}$$

and

$$f_1(\alpha, \frac{R}{R_0}) = 1 - \frac{1}{3}\left(\frac{R}{R_0}\right)^2 + (\pi - frac113)\left(\frac{R}{R_0}\right)^2 cos^2\alpha - \frac{1}{3}\left(\frac{R}{R_0}\right)^2 sin\alpha \quad (2.65)$$
$$+ \left(\frac{2}{3} - \frac{\pi}{8}\right)\left(\frac{R}{R_0}\right)^4 cos^2\alpha + \frac{1}{5}\left(\frac{R}{R_0}\right)^4 sin^2\alpha + \left(6 - \frac{15}{8}\pi\right)\left(\frac{R}{R_0}\right)^4 cos^4\alpha$$
$$+ \left(\frac{7}{15} - \frac{\pi}{8}\right)\left(\frac{R}{R_0}\right)^4 sin^2\alpha cos^2\alpha$$

where α is the bifurcation (30 ° in this case). The numerical solution compared to to the analytical solution is shown in Figure 2.10. Even though some of the particles in the numerical solution deposited on the artificial face of the bifurcation, there was good agreement between the numerical and analytical prediction of particle deposition.

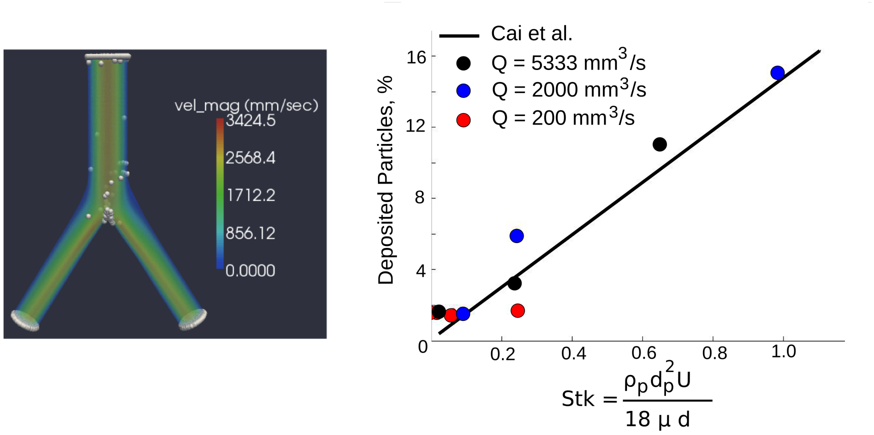

Figure 2.10: Idealized bifurcation and deposition of particles for steady flow at flow rates of 200, 2000 and 5000 $\frac{mm^3}{sec}$. Good agreement was shown when comparing deposition to analytical solution given by Cai et al. [4].

2.4 Bibliography

2.4.1 References

[1] Stasia a Anderson, John Glod, Ali S Arbab, Martha Noel, Parwana Ashari, Howard a Fine, and Joseph a Frank. Noninvasive MR imaging of magnetically

labeled stem cells to directly identify neovasculature in a glioma model. *Blood*, 105(1):420–5, January 2005.

[2] Y. Bazilevs, J.R. Gohean, T.J.R. Hughes, R.D. Moser, and Y. Zhang. Patient-specific isogeometric fluidstructure interaction analysis of thoracic aortic blood flow due to implantation of the Jarvik 2000 left ventricular assist device. *Computer Methods in Applied Mechanics and Engineering*, 198(45-46):3534–3550, September 2009.

[3] Richard B Buxton. *Introduction to Functional Magnetic Resonance Imaging. Principles and Techniques.* Cambridge University Press, New York, 2002.

[4] F.S. Cai and C.P. Yu. Inertial and interceptional deposition of spherical particles and fibers in a bifurcating airway. *Journal of Aerosol Science*, 19(6):679–688, December 1988.

[5] Hannes Dahnke, Wei Liu, Daniel Herzka, Joseph a Frank, and Tobias Schaeffter. Susceptibility gradient mapping (SGM): a new postprocessing method for positive contrast generation applied to superparamagnetic iron oxide particle (SPIO)-labeled cells. *Magnetic resonance in medicine*, 60(3):595–603, September 2008.

[6] Mahdi Esmaily Moghadam, Yuri Bazilevs, Tain-Yen Hsia, Irene E. Vignon-Clementel, and Alison L. Marsden. A comparison of outlet boundary treatments for prevention of backflow divergence with relevance to blood flow simulations. *Computational Mechanics*, 48(3):277–291, April 2011.

[7] Thomas J R Hughes. *The Finite Element Method.* General Publishing Company, Ltd, 2000.

[8] Kenneth E Jansen, Christian H Whiting, and Gregory M Hulbert. A generalized-α method for integrating the filtered Navier-Stokes equations with a stabilized finite element method. *Computer Methods in Applied Mechanics and Engineering*, 190:305–319, 2000.

[9] Taro Matsushita, Yoshinori Kusakabe, Hitomi Fujii, Katsutoshi Murase, Youichi Yamazaki, and Kenya Murase. Inflammatory imaging with ultrasmall superparamagnetic iron oxide. *Magnetic resonance imaging*, 29(2):173–8, February 2011.

[10] Martin R. Maxey and James J. Riley. Equation of motion for a small rigid sphere in nonuniform flow.pdf. *Physics of Fluids*, 26:883–889, 1983.

[11] Mahdi Esmaily Moghadam, Irene E. Vignon-Clementel, Richard Figliola, and Alison L. Marsden. A modular numerical method for implicit 0D/3D coupling in cardiovascular finite element simulations. *Journal of Computational Physics*.

[12] Josef Pich. Theory of gravitational deposition of particles from laminar flows in channels. *Journal of Aerosol Science*, 3(5):351–361, September 1972.

[13] Josef Pich. Theory of gravitational deposition of particles from laminar flows in channels. *Journal of Aerosol Science*, 3(5):351–361, September 1972.

[14] F Shakib, T Hughes, and Z Johan. A multi-element group preconditioned gmres algorithm for nonsymmetric systems arising in finite element analysis. *Computer Methods in Applied Mechanics and Engineering*, 75:415–456, 1989.

[15] C Taylor. Finite element modeling of blood flow in arteries. *Computer Methods in Applied Mechanics and Engineering*, 158(1-2):155–196, May 1998.

[16] Caroline van Ertbruggen, Charles Hirsch, and Manuel Paiva. Anatomically based three-dimensional model of airways to simulate flow and particle transport using computational fluid dynamics. *Journal of applied physiology (Bethesda, Md. : 1985)*, 98(3):970–80, March 2005.

[17] I Vignon-clementel, C Albertofigueroa, K Jansen, and C Taylor. Outflow boundary conditions for three-dimensional finite element modeling of blood flow and pressure in arteries. *Computer Methods in Applied Mechanics and Engineering*, 195(29-32):3776–3796, June 2006.

[18] Irene E. Vignon-Clementel. *A coupled Multidomain Method for Computational Modeling of Blood Flow.* PhD thesis, Stanford University, 2006.

[19] Christian H Whiting and Kenneth E Jansen. A stabilized finite element method for the incompressible Navier Stokes equations using a hierarchical basis. *International Journal for Numerical Methods in Fluids*, 35:93–116, 2001.

Chapter 3

Rat Airway Morphometry

3.1 Introduction

A comprehensive description of lung geometry is often required to accurately model pulmonary airflow and aerosol particle deposition. Both flow and particle transport are influenced by airway length, diameter, as well as bifurcation, gravitational and rotational angles [2, 21]. Such geometric descriptions are not only useful for studies of airflow and/or particle deposition in three-dimensional (3D) numerical models, but are also applicable in multi-scale approaches. Recently, Comerford et al. predicted airflow in a subject-specific model of the human large airways by coupling a 3D airway model to a 1D model of small airways using an impedance boundary condition [3]. Impedance was calculated based on airway morphometric measurements [15]. In blood flow simulations, both simple 0D resistance and Windkessel (resistance and capacitance) models as well as more sophisticated closed loop lumped parameter networks [16] have been used in multiscale models of the cardiovascular system [32]. Similar approaches could potentially be applied to model functional parameters in the pulmonary airways. Knowledge of airway resistance and impedance is essential in the study of lung mechanics in both health and disease [1, 8]. Furthermore, accurate morphometric measurements of the large and small airways can improve the precision of impedance and resistance calculations and therefore improve multi-scale coupling in numerical models and/or aid in characterization of disease states.

Rats have been widely used in experimental deposition studies [1, 34] and in studies aimed at understanding of the influence of particle composition on lung pathology [7, 25] as well as aiding in the development of drugs delivered as aerosols [14]. Therefore, an improved understanding of the rat three-dimensional airway morphometry may establish links between aerosol deposition and airway geometry. Previous studies of rat airway morphometry have used casting methods, or excised lungs, and leaving some doubt as to whether the geometric angles of the airways represented in these casting or ex vivo lungs represent a realistic in situ state. Raabe et al. [23] performed a complete morphometric analysis of the rat lung using silicone casts that were imaged by electron microscopy. Yeh et al. measured the morphometric parameters from a single silicone rat lung cast to develop a typical path lung model [35]. Rodriguez et al. [26] found that the number of generation of conducting airways varies in the different lobes of the rat lung with the lower lobes containing more airway generations than the upper lobes. For example, in the right upper (apical) lobe, conducting airways branch over a range of 8 to 25 generations, with an average of 15 generations while in the right lower (diaphragmatic) lobe, airways ranged from 13 to 32 generations.

The use of high-resolution three-dimensional imaging techniques, such as CT and MRI, has the advantage of obtaining three-dimensional data sets that may be analyzed more efficiently than the tedious reconstruction of data collected serially in two-dimensions. Using micro CT, de Backer et al. [4] imaged the upper respiratory tract and thoracic cavity of Sprague-Dawley rats, and Sera et al. [28] showed that for generations 8 - 16, airway diameter and length decrease exponentially with each generation. Einstein et al. [6] used magnetic resonance imaging and Lee et al. [12] used CT to obtain detailed images of rat lung silicone casts. With these data Einstein et al. [6] performed self-similarity analysis of the behavior of airway diameter and length as a function of path length, but did not extend this analysis to obtain bifurcation and gravitational angles. Lee et al. [12] performed a detailed analysis of morphometric data for six rats and argued that there was little inter-subject variability between the animals. However, a large variability was seen between airway generations in the intra-variability analysis.

This paper presents the first comprehensive set of in situ three-dimensional morphometric measurements of Wistar rat lungs obtained from MR images. The goals of this study were 1) to compare this in situ morphometry to previous measurements taken from excised airway casts, 2) determine the variability between animals of the same strain and weight, and 3) to provide all the morphometric measurements needed to fully describe the airways down to an image resolution and to spatial organization that is physiologically relevant.

3.2 Methods

3.2.1 Animal Preparation

.

This study protocol was approved by the University of California San Diego Institutional Animal Care and Use Committee (IACUC). Four healthy male Wistar rats (268 ± 14 g) were analyzed. The method for preparing and imaging of the lungs in situ has previously been described for mice [27]. Animals were deeply anesthetized with pentobarbital sodium (60 mg per kg of body weight, i.p.) and tracheostomized with a 15 G plastic cannula. Animals were injected (i.p.) with heparin (500 units) and 2 mL of gadolinium dimeglumine (Magnevist, Schering, Germany) to ensure a high level of contrast between the lung tissues and blood, and the airways during imaging. Animals were ventilated for 10 minutes with 100 % O_2 at an airway pressure of 10 cm H_2O and then euthanized with a second dose of pentobarbital sodium (60 mg per kg of body weight, i.p.) and instilled at a 45-degree angle. The lungs were first primed with a small amount of phosphate buffered saline (PBS), then filled with perfluorocarbon (PFC; Fomblin Solvay Solexis, Thorofare, New Jersey) to an airway pressure of 9 cm H2O, and finally filled with 0.05 % low-melt agarose in PBS (NuSieve Agarose, Cambrex, Rockland, ME) to a final airway pressure of 20 cm H_2O. This resulted in an approximate 70:30 ratio of PFC/PBS. The cannula was capped and the animals were immediately transferred to the MR scanner for imaging.

3.2.2 Magnetic Resonance (MR) Imaging

The lungs were imaged in situ in a 7T small animal MR scanner (Bruker Biospin Corporation WI) using a custom built Quadrature volume MR imaging coil. T_2-weighted coronal images were acquired using a Turbo-RARE 3D pulse sequence with TR/TE = 1500/43 msec and $FA = 180°$. The image matrix was 256 x 256 x 128, which generated a voxel dimension of 0.2 x 0.2 x 0.27 mm. Each MR scan took approximately 1 hour and 40 minutes. The resulting images had a high level of contrast between the airways (PFC filled: dark) and the surrounding tissue (gadolinium: bright) [27].

3.2.3 3D Airway Construction

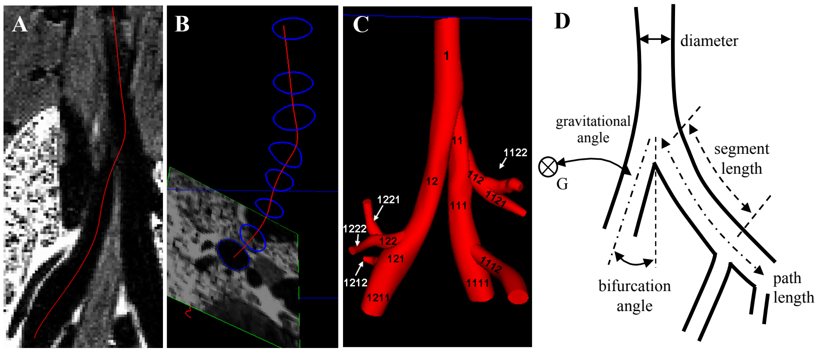

Figure 3.1: Airway models were constructed by (A) drawing lines through each airway, (B) outlining the airway perpendicular to the centerlines and (C) lofting the contours to create the 3D model. Panel D shows the measurements taken for each airway model.

Three-dimensional airway models were created from the MR images using a custom version of the open source software, SimVascular (simtk.org) [31], which has been used extensively for cardiovascular model construction in previous studies [10, 32]. The procedure involved drawing centerline paths interpolated with splines (Figure 1A), segmenting contours perpendicular to the path Figure 3.1B, and lofting segmentations to create a 3D geometric model (Figure 3.1C).

Each centerline began at its initial bifurcation point and followed the images through each major daughter bifurcation until the limits of image resolution were reached. Centerlines for each minor branch were created similarly until the entire 1D airway tree was defined. Segmentations spaced a few voxels apart were drawn perpendicular to the centerlines for all airways with a diameter greater than two pixels. Most airway segments contained at least three segmentations, except for airways with a length of less than 6 pixels. All segmentations were lofted together to create the final 3D geometry. Creating the geometry manually removed complications that arise in automated segmentation techniques, ie: extra faces, holes, and undesired merging of pulmonary vasculature and airways.

All airways were named with a unique numeric string following the binary numbering scheme rules given by Phalen et al. [20]. The string began at the trachea with the number 1. At each bifurcation a number was added to the end of the string; 1 for the major daughter and 2 for the minor daughter (Figure 3.1C). A few triple bifurcations were encountered and in this case a 3 was added to the airway with the smallest diameter.

3.2.4 Morphometry Measurements

Using custom software developed in Matlab, segment and path length, hydraulic diameter, minimum, mean and maximum radiuses, bifurcation, gravitational and rotational angles were measured for each segment independently from the centerlines and segmentations created in SimVascular (Figure 3.1C). Each segmentation was discretized into 50 points and each centerline was discretized into 50 to 100 points, depending on its length

Length Measurements

Each segment length was calculated by summing the distance between neighboring points on the centerline within the segment. Airway path length, defined by the distance between the main carina and the end of the airway segment, was then calculated by summing the lengths of all the segments included in the path. Consequently, the length measurements included the airway curvature.

Cross-section Analysis

The hydraulic diameter D was measured for each segmentation and was defined as

$$D = \frac{4A}{C} \tag{3.1}$$

where A and C are the area and circumference of the segmentation, respectively. The segmentation's area A, i.e. the cross section of the segment, was calculated by trapezoidal integration as follows

$$A = \sum_{i}^{i=1} (x_{i+1} - x_i) \left(\frac{y_i + y_{i+1}}{2} \right) \tag{3.2}$$

where x_i and y_i are the local 2D coordinates of each point on the segmentation. The circumference C was calculated by summing the distance between each point on the segmentation.

Minimum, mean and maximum radii were defined as the minimum, mean and maximum distance between the centroid of the contour and its perimeter. The deviation of the airway's cross-section from a perfect circle was then characterized by its eccentricity

$$e = \sqrt{1 - \frac{r_{min}^2}{r_{max}^2}} \tag{3.3}$$

where r_{min} is the minimum radius and r_{max} is the maximum radius. For a circular cross-section, $r_{min} = r_{max}$, and $e = 0$. The more the eccentricity increases the more the cross-section diverges from a perfect circle.

Angles

The bifurcation angle between a parent and daughter segments was calculated by

$$\theta_{bif} = cos^{-1} \left[\frac{\mathbf{p} \cdot \mathbf{d}}{L_p L_d} \right] \tag{3.4}$$

where **p** and **d** are the parent (**p**) and daughter (**d**) vectors and were defined by the beginning and ending points of the segments, L is the length of the vectors, and · denotes the dot product between the two vectors.

The gravitational angle was calculated for each segment by

$$\theta_{grav} = cos^{-1}\left[\frac{\mathbf{g}\cdot\mathbf{d}}{L_d}\right] \tag{3.5}$$

where **g** is the gravitational unit vector for a rat in the prone position and **d** is the daughter vector being analyzed.

Finally, the rotational angle was defined as the angle between two successive bifurcation planes. Using airway 11 as an example (Figure 3.1C), the rotational angle was calculated from the normal vectors of the planes defined from airways 1, 11, 12 and airways 11, 111, 112. The rotational angle was specified to be between 0 and 90 degrees.

Morphometric measurements were calculated for all four animals for the first four airway generations. The inter-animal variability was assessed by calculating the relative standard deviation (RSD) between the four animals, where RSD was defined as the standard deviation divided by the mean.

Because little inter-animal variability was found (see Results section), lung images from a single animal were used to create a more extended 3D model that included all airways identified in the images. Morphometric measurements from the extended model were organized based on airway generation. RSD was used to determine inter- and intra-generation variability.

3.2.5 Order Analysis

The morphometric data from the extended model were also organized using an ordering scheme [11]. Such organization facilitates the calculation of physiologically relevant parameters such as airway resistance and impedance [29]. The diameter-defined Strahler procedure outlined by Jiang et al. [11] was used because it is applicable to monopodial airways. In this procedure we first define the airway order using the Strahler ordering scheme and then correct each airway order based on its diameter. The Strahler scheme was applied by starting from the terminal airways and working backwards to the trachea [30]. Each terminal airway was assigned an order of 1. All other airways were assigned an order based on the order of their respective daughter branches. If both daughter branches were of the same order i, then the parent branch was assigned an order of $i + 1$; if the order of the two daughter branches differed, then the parent branch was assigned the same order as the highest ordered daughter.

An iterative process was then employed to adjust the Strahler order based on each airway's diameter following previous work [11]. First, the average and standard deviation of the diameter of all the segments within each order was calculated. Next, an upper and lower limit for the diameters in each order was determined by applying the following equations

$$D'_{1(n)} = [(D_{n-1} + SD_{n-1}) + (D_n - SD_n)]/2 \tag{3.6}$$

$$D'_{2(n)} = [(D_n + SD_n) + (D_{n+1} - SD_{n+1})]/2 \tag{3.7}$$

where n is the order number, D is the average diameter and SD is the standard deviation of the diameter within that order [11]. Each segment was assigned a new order based on these new limits. The correction procedure was performed iteratively until the values of $D'_{1(n)}$ and $D'_{2(n)}$ converged to within 1%.

Sequential airway segments of the same order were combined to create an element [11]. The diameter of an element was calculated as the average of the diameters of the segments making up the element, and the length was calculated as the sum of the segment lengths. In an electrical analogy, each element represents a single resistor. The combination of all the elements in the airway tree may be used to calculate the tree's total resistance and/or impedance. Following Jiang et al. [11], we defined a connectivity matrix describing the organization of the airway circuit. The columns and rows of the connectivity matrix contained the order of the daughter and parent elements, respectively. A component in the mth row and the nth column represents the average number of elements of order m that grow out of the elements of order n. For example, the value in row 2 and column 3 was calculated by summing the number of 2nd order branches that originated from 3rd order branches and dividing by the total number of 3rd order branches.

3.2.6 Lobar Volume

Finally, the image data set of each animal was analyzed with Amira software (Template Graphic Software, San Diego, CA) to determine lobar volumes. Volumes were calculated by multiplying the number of voxels within each lobe by the volume of a voxel.

3.3 Results

3.3.1 Inter-animal Variability

The morphometric measurements made on the four rats used in this study are displayed in Figure 3.2. Airway path length (Figure 3.2A), hydraulic diameter (Figure 3.2B), bifurcation (Figure 3.2C) and gravitational angles (Figure 3.2D) are shown for the first four generations of the respiratory tract and compared to measurements made on a lung cast of a female Long-Evans rat by Raabe et al. [23]. The cast was made of silicone rubber prepared by an in situ technique to replicate the normal lobar orientation and conducting airway sizes at a volume corresponding to end inspiration [23].

There was good agreement for both path lengths and gravitational angles between the two studies (Figs. 3.2A and 3.2D), while hydraulic diameters from this study were consistently smaller than Raabe's data (Figure 3.2B). Finally, there were large differences in bifurcation angles between the two studies (Figure 3.2C).

Figure 3 illustrates the inter-animal variability as characterized by RSD for path length (Fig. 3.3A), hydraulic diameter (Fig. 3.3B), bifurcation (Fig. 3.3C) and gravitational angles (Fig. 3.3D). There was little variability between animals for path length ($\text{RSD} = 0.18 \pm 0.07$, mean ± SD), hydraulic diameter (0.15 ± 0.15) and gravitational angle (0.12 ± 0.06). Measurements of bifurcation angles show higher variability (0.32 ± 0.22), most likely because the curvature of the airways makes angle measurements more challenging.

The minimum and maximum radius value for each contour was normalized by its mean value. The normalized minimum radius ranged from 0.9 to 0.93 and

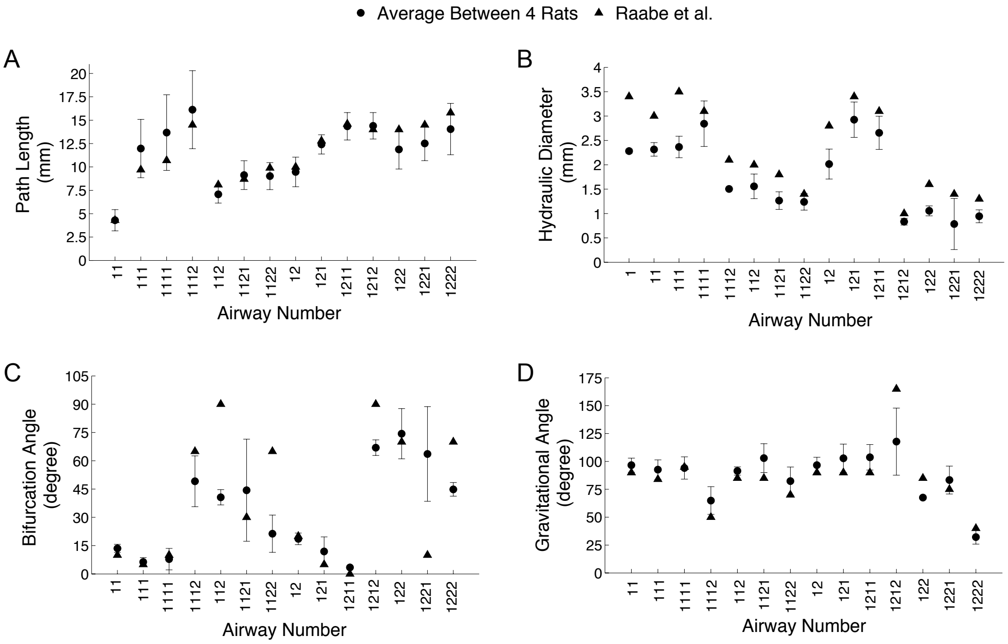

Figure 3.2: Path length (A), hydraulic diameter (B), bifurcation angle (C) and gravitational angle (D) averaged between the 4 airway models, with the error bars being the standard deviation.

the normalized maximum radius ranged from 1.06 to 1.12. Average eccentricity was calculated to be 0.54 ± 0.04, indicating that the airways have a consistent elliptical shape. Segments did become more elliptic as they reach a bifurcation, however the elliptical shape appeared far from the bifurcation and throughout the entire airway.

3.3.2 Lobar Volume

Lobar volumes are listed in Table 1 for the four rats. Data are shown in absolute values (mean ± SD, ml) and as a percentage of total lung volume to allow for comparison with previous studies of Raabe et al. [24] and Yeh et al. [35].

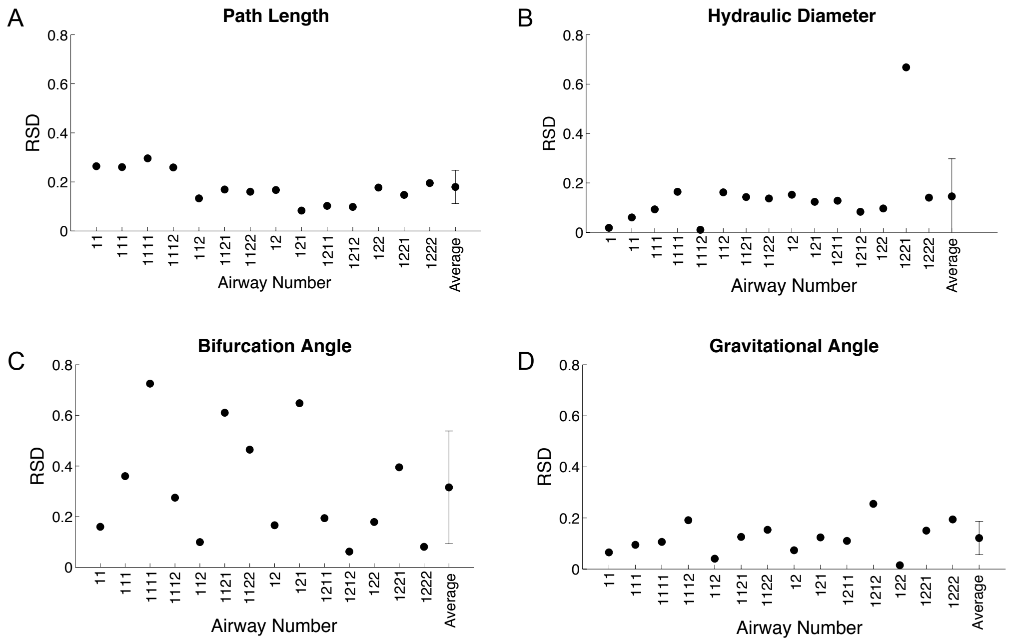

Figure 3.3: Inter-animal variability as characterized by RSD for path length (A), hydraulic diameter (B), bifurcation angle (C) and gravitational angle (D) for the four rats.

3.3.3 Extended Airway Model

The extended model built from MR images from a single animal is shown in Figure 4 and includes up to 16 airway generations and 81 terminal branches. The diameter of the minor daughter branches decreased below the limits of image resolution more proximally than that of the major daughter branches. Therefore, it was not possible to determine the airway diameter in the most distal generations for all airways. As a result, the first five generations accounts for all airways in the model.

Morphometric measurements (mean ± SD) from the extended model are shown in Figure 3.5 as a function of airway generation for hydraulic diameters (Fig. 3.5A), segment length (Fig. 3.5B), gravitational angles (Fig. 3.5C) and rotational angles (Fig. 5D). Bifurcation angles for both major and minor airways are shown in Figure 3.6. These measurements were compared to available data from previous studies [12, 23]. Raabe et al. [23] reported length, diameter, bifurcation

Table 3.1: Lobar volume distribution, average ± standard deviation for this study and compared to Raabe et al. and Yeh et al.

	Volume, ml	Fraction of total lung volume, %		
	Current Study	Current Study	Raabe et al [23]	Yeh et al. [35]
Right Apical	1.27 ± 0.14	11.0 ± 1.16	10.4	9.2
Right Diaphragmatic	3.25 ± 0.14	28.0 ± 1.02	28.8	9.2
Right Intermediate	1.56 ± 0.06	13.5 ± 0.36	13.9	13.3
Right Cardiac	1.35 ± 0.06	11.6 ± 0.51	12.1	12.5
Left Lung	4.15 ± 0.25	35.9 ± 1.3	34.8	33.3
Right Lung (all lobes)	7.42 ± 0.25	64.1 ± 1.3	65.2	66.8
Total Lung	11.57 ± 0.16			

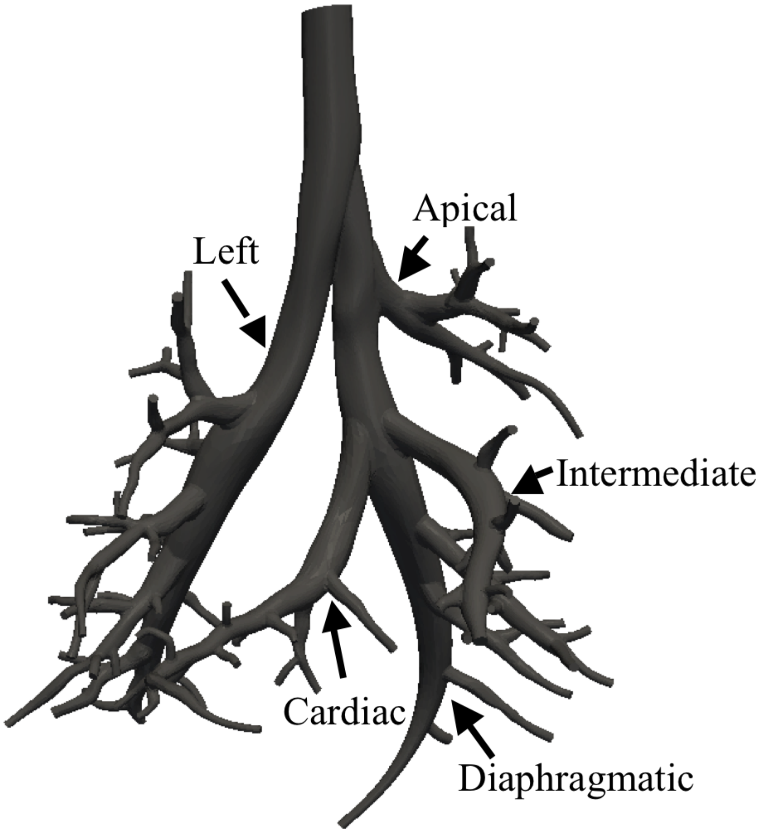

Figure 3.4: Extended airway model with the main lobar bronchi identified.

and gravitational angles for each airway individually and only data from the same airways as those identified in the present study are used in the comparison in

Figures 5 and 6. Lee et al. [12] reported airway length diameter and rotational angle averaged for each generation and mean values were used in the comparison. Hydraulic diameters were systematically smaller than Raabe's and Lee's data, while there was more variability between the datasets for segment length.

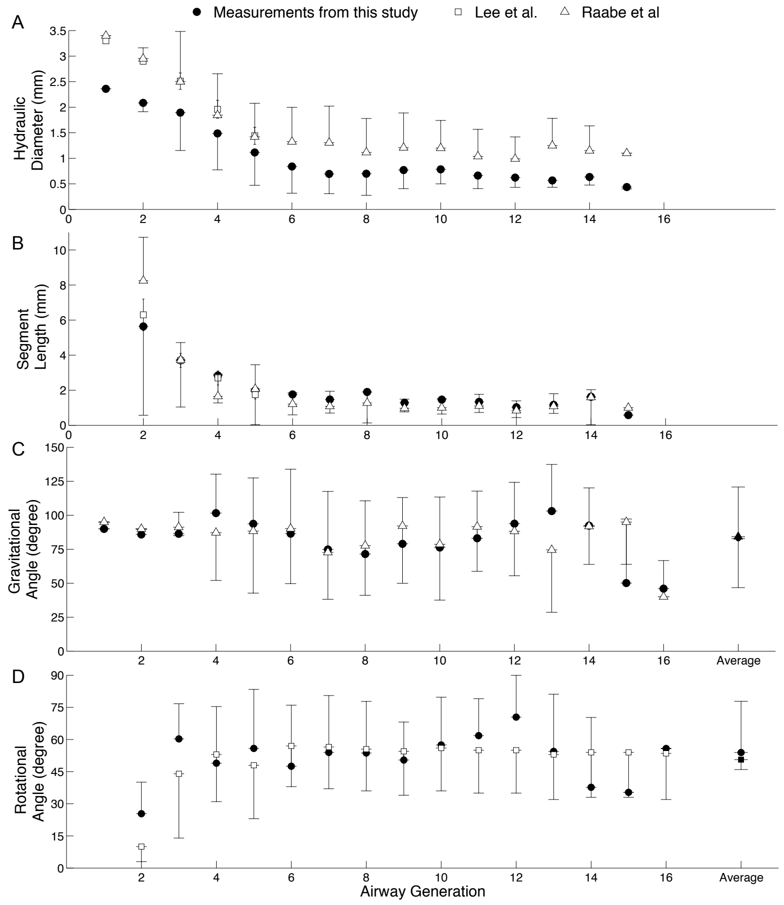

Figure 3.5: Average hydraulic diameter (panel A), segment length (panel B), gravitational angle (panel C) and rotational angle (panel D) for each generation of the single extended airway model. Each airways diameter, length and gravitational measurements were compared to data provided in Raabe et al. [23]. Only the first five generations for diameter and length were compared to the average values reported by Lee et al. [12]. Mean rotational angles for all generations were compared to Lee et al.

The RSD within each generation's diameter was on average 0.39; our measurements, 0.42; Raabe et al. [23] and the RSD for airway length was 0.67; our measurements, 0.5; Raabe et al. [23]. The high RSD indicated that there was a high variability in the diameter and length within each generation.

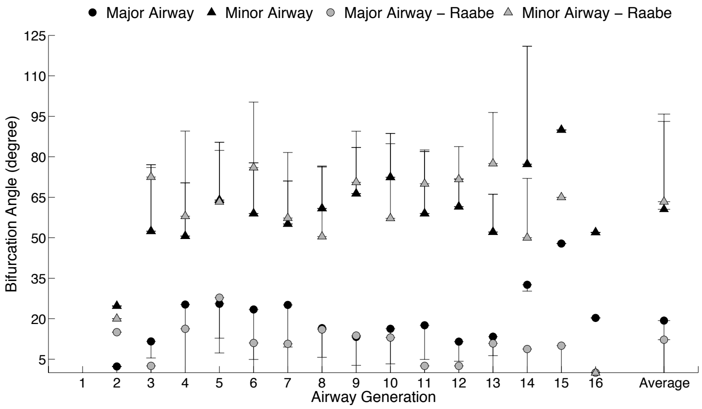

Figure 3.6: Bifurcation angles for major and minor airways of the single extended model compared to measurements by Raabe et al. [23]

Gravitational (Fig. 3.5C) and rotational angles (Fig. 3.5D) remained relatively constant across generations and agreed well with previous studies. Averaged over all airways, gravitational angle was 82.9 ± 37.9 degrees compared to 85.1 ± 35.6 degrees in Raabe et al.'s study [23], and rotational angle was 53.6 ± 24.1 degrees compared to 50.6 ± 20.4 degrees in Lee et al.'s study [12]. Figure 6 shows the bifurcation angles for each airway generation with the major daughter bifurcating at a smaller angle (19.3 ± 14.6 degrees) than the minor daughter branch (60.5 ± 19.4 degrees).

The diameter of the major and minor airways at each path length from the main carina is shown in Figure 3.7 for each lobe in the right lung (panels A and D) and for the left lung (panel E). Three diameter measurements at different locations within the segment were taken for each airway segment, except for short airways (less than a few pixels in length) for which only one or two measurements were made. Unlike the other lobes, the apical lobe branches dichotomously, as shown by similar major and minor branch diameters.

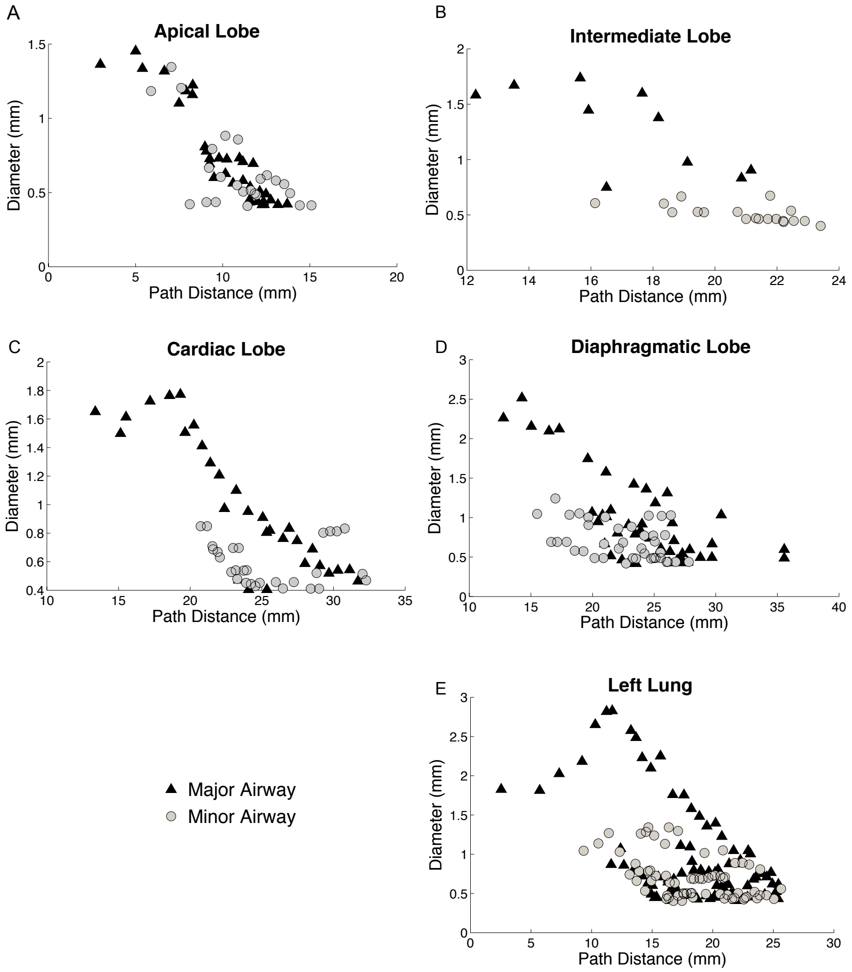

Figure 3.7: Airway diameter as a function of path length from the main carina for the four lobes in the right lung for the single expanded airway model. Major and minor airways are shown separately.

3.3.4 Order Analysis

The extended model contains five diameter-defined Strahler orders [11]. The resulting segment and element diameter determined by the iterative process is shown in Fig. 8A. Table 2 and Figure 3.2 give the average diameter and length for the major and minor branches in each order. The average segment and element diameter increases with order (Fig. 8A); a RSD of 0.12 ± 0.05 indicates low intra-order variability for segment diameter. The major and minor segment had similar

Table 3.2: Segment diameter and length for major and minor airways of each order. SD: standard deviation, N_{seg}: number of segments

	Major Airway					Minor Airway				
	Diameter (mm)		Length (mm)			Diameter (mm)		Length(mm)		
Order	Average	SD	Average	SD	N_{seg}	Average	SD	Average	SD	N_{seg}
1	0.45	0.06	0.24	0.54	44	0.44	0.06	0.25	0.55	34
2	0.72	0.10	1.22	1.08	39	0.75	0.12	1.32	1.11	24
3	1.29	0.20	2.68	1.87	17	1.23	0.25	1.77	1.09	9
4	2.22	0.07	1.44	1.31	5	2.08	0.15	5.36	3.68	4
5	2.50	0.16	1.08	1.02	5	2.70	0.00	2.01	0.00	1

lengths; except for order four segments (Fig. 3.8B). The RSD for length was 0.16 ± 0.16 and the order four segments have the highest intra-order variability. There are order five segments in-between order four segments because the rat airways increase in diameter in the first generations. The number of elements for each order and their average diameter and length are given in Table 3. Depending on their location in the airway tree, elements are either a series of multiple segments or just one segment.

The connectivity matrix is given in Table 4; the values are the number of daughter branches of each row order springing from parent elements of each column order, divided by the total number of branches in the column order. For example, the value 1.343 was calculated by dividing the total number or order one elements coming from order two elements, 47, by the total number of order two elements, 35. As shown by the values in the matrix diagonal, some elements of the same order may be connected in parallel if the minor and major branches have the same order. The value 0.4 in the lower triangle of the matrix shows that there are order five elements coming from order four elements.

3.4 Discussion

Despite numerous previous studies of conducting airway morphometry, none of these studies have included all measurements needed to describe the airways three-dimensionally. Most airway measurements were collected from excised sili-

Table 3.3: Element diameter and length for each order. SD: standard deviation, N_{elem}: number of segments

	Diameter (mm)		Length (mm)		
Order	Average	SD	Average	SD	N_{elem}
1	0.45	0.06	0.31	0.75	62
2	0.72	0.09	2.31	1.75	35
3	1.26	0.16	6.15	3.04	11
4	2.15	0.13	6.29	4.24	5
5	2.54	0.15	3.16	1.82	3

Table 3.4: Connectivity matrix of elements in airway tree. Values are number of elements in order m splitting from number of elements in order n, divided by the total number of elements in each order.

		Parent Element Order				
	1	2	3	4	5	
Daughter Element Order	1	0.016	1.343	1.273	0	0
	2	0	0.171	2	0.8	0.667
	3	0	0	0.091	1.4	0.667
	4	0	0	0	0	1.333
	5	0	0	0	0.4	0

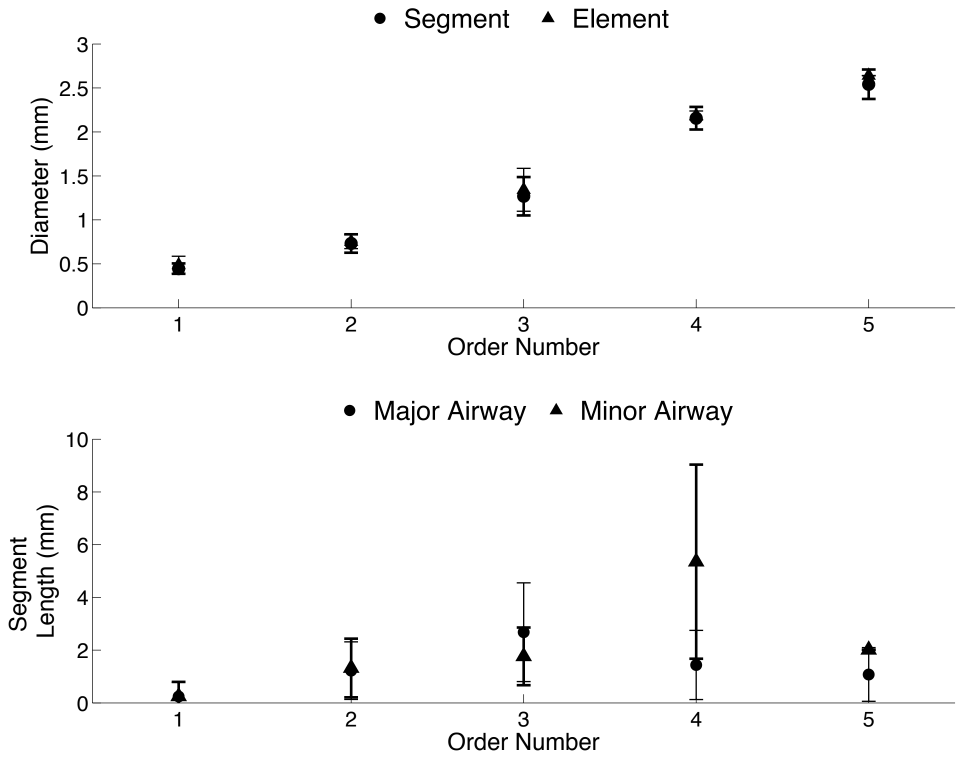

Figure 3.8: Order analysis. Panel A shows the diameter as a function of order number (diameter increases as order number increases) for both the segments and the elements. Panel B shows segment lengths for major and minor airways as a function of order.

cone lung casts imaged by electron microscopy [22] or from CT [12, 28, 35] MR [6]. Excellent contrast between the silicone airways and the background material resulted in a high image resolution [Lee et al. = 43 microns [12] and Einstein et al. = 125 microns [6]]. However, because imaging was performed ex vivo, there is a danger that the casts may have deformed from their original physiologic in situ shape. In-situ airway imaging in the Sprague-Dawley rat has been previously performed using micro-CT [4], however this study only captured the first few airway generations. Ideally, a 3D airway atlas should include airway diameter, length, gravitational, bifurcation and rotational angles taken from lungs in their most natural state at the highest resolution possible. The present study provides all relevant geometric measurements taken from in-situ lungs of Wistar rats at a greater resolution than previous in-situ studies. Airway variability between rats of similar weight was first analyzed for the first four generations of conducting airways. Next, measurements for up to 16 airway generations were compared to morphometric data from previous studies [12, 23]. Lastly, the highly monopodial airways were organized based on a diameter-defined Strahler ordering scheme [11].

Inter-animal Variability

Recently, patient or animal-specific 3D airway models have been used to study lung mechanics, airflow and particle deposition using computational methods [3, 13, 33, 36]. Because the accurate description of airway morphometry is laborious and time-intensive, subject-specific models need only be developed when inter-subject variability is high. Using solid casts of eight human lungs, Nikiforov and Schlesinger [18] previously measured the length, diameter and branching angle of the first nine generations of conducting airways by measuring directly from the cast, and showed high inter-subject variability in their measurements. The RSD of length, diameter and branching angle was 0.42 ± 0.11, 0.31 ± 0.8 and 0.76 ± 0.30, respectively. These results strongly advocate for the use of subject-specific models of the human lung. In contrast, the much lower inter-animal variability between the Wistar rat lung shown by our and previous results suggests that generic airway models may reliably be used in computational or lung mechanics studies of healthy rats of similar size. These findings agree with previous studies which also showed low inter-animal variability for same weight, strain and sex [15].

Sensitivity Analysis

An analysis was performed to assess user sensitivity of creating the morphometric models. An independent operator created and measured the airway path length and diameter of one of the rats used in the inter-animal variability study. All diameter and path length measurements were within one standard deviation measured between the four rats (see Fig. 3.2). Additionally, the average difference between the mean values of Fig. 3.2, were 8.1 % and 8.8 % for the diameter and path length, respectively. The operator sensitivity was small and therefore was assumed to be insignificant.

Extended Airway Model

Traditionally, airway tree dimensions have been organized based on generation number [15, 28]. Generation organization offers a straightforward technique with which the morphometric data from several different studies may be easily compared. Our results confirmed the expected finding that airway diameter and length decreased with increasing generation number (Figs. 3.5A and B). However, the variability of measurements within each generation was high and often larger than the intergeneration variability (Figs. 3.5C and D). The large intra-generation variability suggests that generation organization may not be the most appropriate method to describe rat airways.

The rat airway tree exhibits both monopodial and dichotomous branching characteristics depending on the branch location in the airway tree. The branches springing from the lobar bronchus have a smaller diameter than their major sibling (Fig. 3.4) for the left, diaphragmatic, cardiac and intermediate lobes. However, the differences between daughter branches are smaller towards the periphery of the lobe and as a consequence the branching pattern there becomes more dichotomous. In contrast, the apical lobe exhibits a dichotomous branching pattern from the lobar bronchus.

3.4.1 Comparison with Previous Studies

We observed relatively good agreement between our data and measurements from Raabe et al. and Lee et al. (Figs. 3.2 and 3.5). The generation average diameters for the extended model were 36.6 ± 11.4 % smaller than Raabe et al.'s measurements and 22.1 ± 6.7 % smaller than Lee et al. for the first seven generations (Fig. 3.5A). Raabe et al. [23] used a silicone cast of a 330 g female Long Evans rat at approximately TLC. This casting procedure caused the diameters of the major bronchi to increase by $\sim$15 % [23]. Lee et al.'s measurements were taken on 302 g Sprague - Dawley rats at an airway pressure of 30 cm H_2O.

Trachea diameter has been previously shown to increase with airway pressure [27]. The different techniques, different airway pressure and larger animal weight likely explain the higher values measured in these previous studies compared to data from the present study. Segment lengths matched well with the previous studies (Fig. 3.5B); however our measurements were slightly longer for most generations. Our length measurements included airway curvature, while previous studies only measured the linear length of the airway, and therefore this may have contributed to the longer lengths measured. Gravitational and rotational angle measurements agreed well with previous studies, while bifurcation angle did not. The average gravitational angle was 2.6 % smaller than Raabe et al. and the average rotational angle was 5.9 % larger than Lee et al. Since Lee et al. reported a possible error of 6 to 7 % in their angle measurements due to deformation of the cast while scanning, this provides a possible explanation for this difference. Our measured bifurcation angles (Fig. 3.6) were 36.7 % larger than those of Raabe et al. for the major airway and 4.6 % smaller than those of Raabe et al. for the minor airways. Raabe et al. reported a 0 bifurcation angle for many of the major bifurcations, however a bifurcation angle was found for all airways in this study and therefore explains the high difference between the numbers reported here and the number reported by Raabe et al.

Our results for percent lobe volume agreed well with data of Raabe et al [23] and Yeh et al. [35] (Table 1), with an average difference of 9.3 % compared to values reported by Yeh et al. and an average difference of 3.7 % compared to values reported by Raabe et al.

Order Organization

The diameter defined Strahler ordering scheme [11] was applied to the extended airway model to provide an alternate method for organizing the morphometric data that better allows for high intra-generation variability and missing airways due to the limitation in the image resolution. Incorporating both airway diameter and location in the airway tree ordering system allows us to obtain lower intra-order variability compared to ordering with diameter alone. Additionally, the increased variability found in the fourth-ordered segments (Fig. 3.8) is likely the result of the non-monotonic decrease of airway diameter from the trachea to the peripheral airways. Typically, in this type of order analysis, there would be only one segment of the highest order (order 5 in this case). However, because the diameter of the airways increases in the main bronchi before monotically decreasing with increasing generation number [6], six order 5 segments were measured.

A connectivity matrix describes the branching of the airway tree based on the number and order of the elements. The upper diagonal of Table 4 shows that most of the elements of order n branch from parent elements order $n + 1$. When daughter branches are of the same order as the parent branch, this appears as a diagonal entry in the connectivity matrix. Typically, daughter elements do not have a higher order than their parent element, however due to increasing diameter in the major right and left bronchi, there were order 5 elements springing from order 4 elements.

3.4.2 Physiological Relevance

An extended geometric description of the airways is highly desirable for accurate predictions of airflow and particle deposition. Airway dimensions and angle measurements are needed to solve equations that govern fluid dynamics or particle physics. The inclusive dataset provided here can be used to construct typical 3D rat airway trees for use in future computational studies.

Airway resistance, a physiological measure of pressure drop for a given flow rate, may be used to aid in airway disease diagnostics [1, 8]. Also, airway resistance may be used as a downstream boundary condition in numerical models [30]. Assuming Poiseuille flow, airway resistance may be calculated for each airway using

$$R = \frac{64\mu l}{\pi d^4} \tag{3.8}$$

where μ is the fluid viscosity, l is the length of the segment and d is the diameter of the segment. The resistance for airways in series is additive. The resistance for airways in parallel is the inverse of the sum of the inverse of the resistances. The total resistance in the rat airways for the bronchioles, that this model represents, was calculated by summing the resistance of each airway. The resistance calculated using the exact tree structure was compared to the an estimated resistance computed using the average lengths and diameters and the airway tree described by the connectivity matrix [29]. The total resistance was 0.0046 cm H2O-s/ml and the approximate resistance was 0.0039 cm $\frac{H_2O-s}{ml}$. The small difference (less than 15 %) demonstrates the usefulness of the connectivity matrix in estimating relevant physiological parameters.

Airway resistance in Wistar [17] and Fischer [5] rats has been previously measured using the alveolar capsule technique. Nagase et al. [17] found the airway resistance to be 0.066 ± 0.010 cm H2O-s/ml and Dolhnikoff et al. [5] found the airway resistance to be 0.051 ± 0.012 $\frac{cmH_2O-s}{ml}$. Both of these studies found the airway resistance to be larger than what was found using the morphometric data. However, the resistance calculated with the morphometric data only includes Poiseuille resistance, and not the additional resistance that occurs in the presence of bifurcating airways. Pedley et al. [19] described the resistance for a bifurcating system to be

$$R = \frac{R_p C}{4\sqrt{2}} \sqrt{Re \frac{d}{L}} \tag{3.9}$$

where R_p is the Poiseuille resistance, C is a constant, 1.85, Re is the Reynolds number, d is the diameter of the airway, and L is the length of the airway. Using the experimental breathing conditions given by Nagase et al. [17] (tidal volume of 9 $\frac{mL}{kg}$, breathing frequency of 60 $\frac{breaths}{min}$, the morphometric data of our extended rat model and applying Pedley's equation, the resistance was found to be 0.0489 $\frac{cmH_2O-s}{ml}$. Decreasing and increasing the airway diameter throughout the model by 5 % resulted in a calculated resistance of 0.060 $\frac{cmH_2O-s}{ml}$ and 0.0402 $\frac{cmH_2O-s}{ml}$, respectively. Assuming an isotropic expansion of the lung, a decrease in airway diameter of 5 % would result in a decrease in lung volume of ∼40 %. Our airway model is based on images of lungs inflated at an airway pressure of 20 cm H2O, which is close to total lung capacity. Reducing the lung volume by 40 % from total lung capacity would result in lung volumes similar to those occurring during tidal breathing, i.e to those encountered in Nagase et al. [17] and Dolhnikoff et al. [5] studies. The calculated resistance for the model with decreased airway diameter agrees well with those experimentally measured by the alveolar capsule technique.

3.4.3 Limitations

The rat airways were measured inside the thoracic cavity from in-situ MR images. While in-situ imaging offers the advantage of obtaining measurements from lungs in their most natural state, such approach resulted in images with a smaller resolution than previous studies have obtained with lung casts [6, 12]. The voxel size (0.2 x 0.2 x 0.27 mm) was chosen such that there was sufficient tissue to airway contrast. This resolution limited measurements to airways with a diameter larger than 0.4 mm, with a potential measurement error of 33 %. To obtain the in-situ images, the lungs were first filled with a contrasting fluid to avoid air / tissue artifacts and to be able to identify the airways in the images. In most cases the lung filled uniformly, except for the periphery of the diaphragmatic and intermediate lobes. The uneven filling resulted in a limited amount of contrast, which made it difficult to identify some of the peripheral airways in these lobes. The liquid-filled lungs may have expanded the lungs more than air-filled lungs, however this expansion is likely to be less than in silicone-filled lungs that are traditionally used in morphometric studies. Silicone has a larger viscosity than the PBS and agarose mixture used in this study and therefore requires a larger pressure force to fill the lungs [6]. Silicone-filled lungs may thus be artificially more over-expanded than liquid-filled lungs.

Errors in defining the bifurcation end point location may be present due to the difficulty in determining the exact bifurcation location of the airways from the MR images. In an attempt to decrease uncertainty, we also measured bifurcation angles using end points at mid-lengths of the daughter branches, however this did not reduce our variability as measured by RSD (Fig. 3.2). The 3D airway trees were manually segmented from the MR images, and additional uncertainties may arise from noise in image data. Despite these limitations, the airways were accurately described both geometrically and spatially, and findings agreed well with previously reported data.

It should be noted that airway disease may alter the morphometry of the lung and that these alterations are likely to be heterogeneously distributed among airways. A previous study by Lee et al. [12] demonstrated the importance of airway-to-airway comparison between animals in characterizing the influence of air pollutants on lung development. It is also known that bronchial airway diameter decreases with asthma and COPD [9], however the heterogeneous distribution has not been fully investigated.

3.4.4 Summary

This paper is the first to present in-situ morphometric measurements from MR for airway diameters greater than 0.4 mm in healthy Wistar rat lungs. The little inter-animal variability found in the first four airway generations strongly suggests that a generic model can adequately describe the airway morphometry of rats of similar size. Measurements from this study matched previous studies for airway length, gravitational, minor bifurcation and rotational angles. However the major bifurcation angles were larger than the previous studies and the airway diameters were smaller than in previous studies. The rat lungs proved to have both dichotomous and monopodial characteristics, depending on the lobe and location in the lung. Organizing the measurements using the diameter-defined Strahler ordering scheme resulted in low intra-order variability for airway lengths and diameters and proved to be a useful tool to calculate physiological parameters such as lung resistance.

3.5 Acknowledgements

Chapter 3, in full, is a reprint of the materials as it appears in Journal of Applied of Physiology as Jessica M. Oakes, Miriam Scadeng, Ellen C. Breen, Alison L. Marsden, Chantal Darquenne. "Rat Airway Morphometry Measured from In Situ MRI-Based Geometric Models", *Journal of Applied Physiology.* 112:

1921-1931. 2012. The dissertation author was the primary investigator and author of this paper.

3.6 Bibliography

[1] Jason H T Bates and Béla Suki. Assessment of peripheral lung mechanics. *Respiratory Physiology & Neurobiology*, 163(1-3):54–63, November 2008.

[2] F.S. Cai and C.P. Yu. Inertial and interceptional deposition of spherical particles and fibers in a bifurcating airway. *Journal of Aerosol Science*, 19(6):679–688, December 1988.

[3] Andrew Comerford, Christiane Förster, and Wolfgang a Wall. Structured tree impedance outflow boundary conditions for 3D lung simulations. *Journal of Biomechanical Engineering*, 132(8):081002, August 2010.

[4] Jan W De Backer, Wim G Vos, Patricia Burnell, Stijn L Verhulst, Phil Salmon, Nora De Clerck, and Wilfried De Backer. Study of the variability in upper and lower airway morphology in Sprague-Dawley rats using modern micro-CT scan-based segmentation techniques. *The Anatomical Record*, 292(5):720–7, May 2009.

[5] M Dolhnikoff, T Mauad, and M S Ludwig. Extracellular matrix and oscillatory mechanics of rat lung parenchyma in bleomycin-induced fibrosis. *American journal of respiratory and critical care medicine*, 160(5 Pt 1):1750–7, November 1999.

[6] Daniel R Einstein, Blazej Neradilak, Nayak Pollisar, Kevin R Minard, Chris Wallis, Michelle Fanucchi, James P Carson, Andrew P Kuprat, Senthil Kabilan, Richard E Jacob, and Richard a Corley. An automated self-similarity analysis of the pulmonary tree of the Sprague-Dawley rat. *The Anatomical Record*, 291(12):1628–48, December 2008.

[7] N M Griffiths, A Van der Meeren, P Fritsch, M-C Abram, J-F Bernaudin, and J L Poncy. Late-occurring pulmonary pathologies following inhalation of mixed oxide (uranium + plutonium oxide) aerosol in the rat. *Health Physics*, 99(3):347–56, September 2010.

[8] A. Cortney Henderson, Edward P Ingenito, Edgardo S Salcedo, Marilyn L Moy, John J Reilly, and Kenneth R Lutchen. Dynamic lung mechanics in late-stage emphysema before and after lung volume reduction surgery. *Respiratory Physiology & Neurobiology*, 155(3):234–42, March 2007.

[9] J C Hogg. Lung stucture and function in COPD. *Blood*, 12(5):467–479, 2008.

[10] K. Horsfield, G. Dart, D. E. Olson, G. F. Filley, and G. Cumming. Models of the human bronchial tree. *Journal Applied Physiology*, 31(2):207–217, 1971.

[11] Z L Jiang, G S Kassab, and Y C Fung. Diameter-defined Strahler system and connectivity matrix of the pulmonary arterial tree. *Journal Appl Physiology*, 76(2):882–92, February 1994.

[12] Dongyoub Lee, Michelle V Fanucchi, Charles G Plopper, Jennifer Fung, and Anthony S Wexler. Pulmonary architecture in the conducting regions of six rats. *Anatomical Record*, 291(8):916–26, August 2008.

[13] Baoshun Ma and Kenneth R Lutchen. CFD simulation of aerosol deposition in an anatomically based human large-medium airway model. *Annals of Biomedical Engineering*, 37(2):271–85, February 2009.

[14] Thomas H March, Patricia Y Cossey, Dolores C Esparza, Kelly J Dix, Jacob D McDonald, and Larry E Bowen. Inhalation administration of all-trans-retinoic acid for treatment of elastase-induced pulmonary emphysema in Fischer 344 rats. *Experimental Lung Research*, 30(5):383–404, 2004.

[15] M G Menache, A L Patra, and FJ Miller. Airway Structure Variability in the Long Evans Rat Lung. *Neuroscience and Biobehavioral Reviews*, (12):63–69, 1991.

[16] Francesco Migliavacca, Rossella Balossino, Giancarlo Pennati, Gabriele Dubini, Tain-Yen Hsia, Marc R de Leval, and Edward L Bove. Multiscale modelling in biofluidynamics: application to reconstructive paediatric cardiac surgery. *Journal of Biomechanics*, 39(6):1010–20, January 2006.

[17] T Nagase, T Aoki, H Matsui, E Ohga, H Katayama, S Teramoto, T Matsuse, Y Fukuchi, and Y Ouchi. Airway and lung tissue behaviour during endothelin-1 induced constriction in rats: effects of receptor antagonists. *Canadian journal of physiology and pharmacology*, 75(12):1369–74, December 1997.

[18] Andrey I. Nikiforov and Richard B. Schlesinger. Morphometric variability of the human upper bronchial tree. *Respiration Physiology*, 59(3):289–299, March 1985.

[19] T J Pedley, R C Schroter, and M F Sudlow. The prediction of pressure drop and variation of resistance within the human bronchial airways. *Respiration physiology*, 9(3):387–405, June 1970.

[20] R F Phalen, H C Yeh, G M Schum, and O G Raabe. Application of an idealized model to morphometry of the mammalian tracheobronchial tree. *The Anatomical Record*, 190(2):167–76, February 1978.

[21] Josef Pich. Theory of gravitational deposition of particles from laminar flows in channels. *Journal of Aerosol Science*, 3(5):351–361, September 1972.

[22] O. G. Raabe, H. C. Yeh, G. J. Newton, R. F. Phalen, and D. J. Velasquez. Deposition of inhaled monodisperse aerosols in small rodents. *Inhaled Particles*, 4(1):3 – 21, 1975.

[23] O G Raabe, H C Yeh, G M Schum, and R F Phalen. Tracheobronchial geometry; human, dog, rat, hamster. Technical report, Lovelace foundation for medical education and research, Alburquerque, New Mexico, 1976.

[24] Otto G. Raabe, Mohamed A. Al-Bayati, Stephen V. Teague, and Amiram Rasolt. Regional deposition of inhaled monodisperse Coarse and fine aerosol particles in small laboratory animals. *Annals Occupational Hygiene*, 32(6):53–63, 1988.

[25] Saravanan Rajendrasozhan, Jae-Woong Hwang, Hongwei Yao, Nandini Kishore, and Irfan Rahman. Anti-inflammatory effect of a selective IkappaB kinase-beta inhibitor in rat lung in response to LPS and cigarette smoke. *Pulmonary Pharmacology & Therapeutics*, 23(3):172–81, June 2010.

[26] M Rodriguez, S Bur, a Favre, and E R Weibel. Pulmonary acinus: geometry and morphometry of the peripheral airway system in rat and rabbit. *The American journal of anatomy*, 180(2):143–55, October 1987.

[27] Miriam Scadeng, Harry B Rossiter, David J Dubowitz, and Ellen C Breen. High-resolution three-dimensional magnetic resonance imaging of mouse lung in situ. *Investigative Radiology*, 42(1):50–7, January 2007.

[28] Toshihiro Sera, Hideki Fujioka, Hideo Yokota, and Akitake Makinouchi. Three-dimensional visualization and morphometry of small airways from microfocal X-ray computed tomography. *Journal of Biomechanics*, 36:1587–1594, 2003.

[29] Ryan L Spilker, Jeffrey a Feinstein, David W Parker, V Mohan Reddy, and Charles a Taylor. Morphometry-based impedance boundary conditions for patient-specific modeling of blood flow in pulmonary arteries. *Annals of Biomedical Engineering*, 35(4):546–59, April 2007.

[30] A N Strahler. Quantitative analysis of watershed geomorphomogy. *Trans. Am. Geophys. Union*, 38:913–920, 1957.

[31] C Taylor. Finite element modeling of blood flow in arteries. *Computer Methods in Applied Mechanics and Engineering*, 158(1-2):155–196, May 1998.

[32] I E Vignon-Clementel, C a Figueroa, K E Jansen, and C a Taylor. Outflow boundary conditions for 3D simulations of non-periodic blood flow and pressure fields in deformable arteries. *Computer Methods in Biomechanics and Biomedical Engineering*, 13(5):625–40, October 2010.

[33] Wolfgang A. Wall, Lena Wiechert, Andrew Comerford, and Sophie Rausch. Towards a comprehensive computational model for the respiratory system. *International Journal for Numerical Methods in Biomedical Engineering*, 26:807–827, 2010.

[34] Lindsay B Wichers, William H Rowan, Julianne P Nolan, Allen D Ledbetter, John K McGee, Daniel L Costa, and William P Watkinson. Particle deposition in spontaneously hypertensive rats exposed via whole-body inhalation: measured and estimated dose. *Toxicological Sciences*, 93(2):400–10, October 2006.

[35] H C Yeh, G M Schum, and M T Duggan. Anatomic models of the tracheobronchial and pulmonary regions of the rat. *The Anatomical Record*, 195(3):483–92, November 1979.

[36] Youbing Yin, Jiwoong Choi, Eric a Hoffman, Merryn H Tawhai, and Ching-Long Lin. Simulation of pulmonary air flow with a subject-specific boundary condition. *Journal of Biomechanics*, 43(11):2159–63, August 2010.

Chapter 4

Deposition of Aerosol Particles: Assessed with MRI

4.1 Introduction

Inhaled aerosolized particles are widely used for therapeutic drug delivery in patients with pulmonary diseases. Selective treatment of the lungs may be achieved by delivering high drug concentrations to the airways. For example, targeted deposition may improve the efficiency of therapeutics in asthmatic patients [24] or lead to the ability to deliver aerosolized chemotherapy to lung cancer patients [27]. Additionally, the lung is increasingly being used as a portal of entry for aerosolized drugs designed to act systemically [12, 18], e.g. insulin for diabetes patients [28]. The success of inhalation therapy does not only depend upon the pharmacological properties of the drugs being inhaled, but also upon the site, extent and distribution of deposition in the lung. As such, a better understanding of regional particle deposition could enhance both the safety and the efficiency of inhaled pharmaceuticals [30].

Several imaging methodologies have previously been developed to evaluate aerosol deposition in both human and animal subjects. These include gamma scintigraphy [3, 5, 24, 29], PET [7], SPECT, [8, 11] and more recently MRI [13, 19].

Gamma cameras capture either 2D (gamma scintigraphy) or 3D (SPECT) images of deposited particles labeled with a radionuclide (typically ^{99m}Tc) to measure peripheral and central distribution of deposition [5] as well as lung clearance [3]. The advantages of 3D PET lie in the ability to achieve a better image quality than SPECT [7], as well as the capability to attach the radionuclide label directly to the drug molecule. Thus far, deposition quantification using MRI has only been performed in animal studies, using either iron oxide particles [13] or gadolinium [4, 9, 9, 14, 19, 21].

Historically rodents have been utilized to study particle deposition mainly because they are inexpensive and commercially available, laboratory rodent strains are genetically identical, their anatomy is similar to humans, and highly invasive techniques may be used. Conventional slicing methods [16, 17, 22], MR imaging [13] and CT/SPECT imaging [11] have been used previously to study deposition in rodents. Raabe et al. [16] determined that there was an enhanced nasal-pharyngeal deposition for particles with diameter greater than 3 μm, compared to particles with diameters of 1 and 0.3 μm. In a different study, Raabe et al. [17] found that weight-normalized particle deposition was higher in the upper right lobe (apical) [1] compared to the other four lobes for 1 μm-diameter particles in rats. Sweeney et al. [22] found that particle deposition was lower in emphysematous hamsters, compared to healthy hamsters, for 0.45 μm-diameter particles. In mouse lungs, Martin et al. [13] found central deposition to be higher than peripheral deposition, for particle diameters of 5.6 μm. Recently, Kuehl et al. [11] characterized the deposition of several sizes of radioactive particles in both mice and rat lungs using 3D CT/SPECT imaging methods and found higher overall and peripheral deposition as the particle diameters were decreased from 5.0 to 0.5 μms. Each of these previous studies advanced the knowledge of particle behavior in the lung. However, these studies either exposed the rodent in an uncontrolled manner, used polydisperse particles [11, 13], required slicing of the lung [16, 22], or used imaging techniques that introduced large artifacts in the images which was caused by a large signal intensity in the vasculature [13].

The goal of the current study was to use MRI to characterize the 3D regional distribution of deposited particles in the lungs of healthy rats. To do so, super paramagnetic iron oxide (SPIO) particles were delivered to rat lungs in a controlled manner. The set of lungs were then excised, fixed at an airway pressure of 20 cm H_2O and then imaged in a MR scanner. The iron particles created local disturbances in the magnetic field, which resulted in an increased signal decay rate, R_2^*, compared to particle free lung tissue. Using data analysis methods similar to those used in gamma scintigraphy [5], regional deposition was characterized by the central to peripheral deposition ratio, $\frac{c}{p}$. This study is the first to quantify particle deposition in lungs using the MR signal decay rate, R_2^*. This work also improved on several previous MRI studies in animals that only reported global measures of ventilation [4, 9, 14] or whole lung deposition [19, 21].

4.2 Materials and Methods

4.2.1 Aerosol Delivery and Animal Preparation

The study protocol was approved by the University of California San Diego Institutional Animal Care and Use Committee (IACUC). Twelve adult male Wistar rats with mean body weight of 250 ± 14 grams were deeply anesthetized with an intraperitoneal injection of 60 mg of pentobarbital sodium per kg of body weight. Once the pain reflexes were abolished, a 15-gauge plastic catheter was inserted into the trachea.

Rats were connected to a rodent ventilator (Harvard, model # 683) and ventilated for 40 minutes at a tidal volume of 2 ml, a breathing frequency of 80 $\frac{breaths}{min}$, a positive expiratory pressure (Peep) of 1 cm H_2O, and a maximum pressure of 11.2 ± 0.8 cm H_2O, measured at the trachea. Twenty minutes into the delivery, and while the rats were still connected to the ventilator, 500 units of heparin were delivered intraperitonally to inhibit intravascular blood coagulation. Six control rats were ventilated with room air and six rats were ventilated with room air containing aerosolized SPIO particles. The particle delivery system is shown in Figure 4.1.

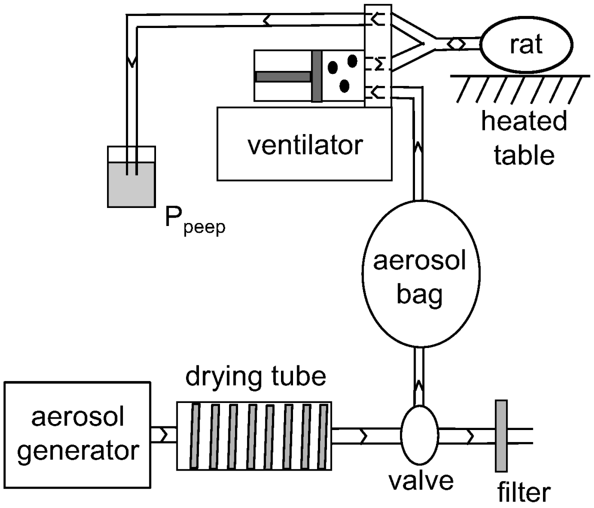

Figure 4.1: Rat aerosol delivery experiment configuration. Aerosol was generated with a nebulizer, dried by going through a heated diffusion dryer and then stored in a rubber aerosol bag. The mechanical ventilator pushed the aerosol into the rat lung during inhalation and then the rat passively exhaled into the P_{peep} jar during exhalation.

The aerosol was made of mono-disperse magnetic polystyrene particles with a geometric diameter of 0.95 μm and a coefficient of variation of $< 5\%$ (Kisher Biotechnologies). The particles were made by coating a layer of iron oxide and polystyrene on polystyrene core particles and they had a density of 1.35 $\frac{g}{cm^3}$, resulting in an aerodynamic diameter of 1.2 μm. The particles were supplied in suspension (25 $\frac{mg}{ml}$ water), and the concentrate was diluted in a 1:4 ratio with water and dispensed via an Acorn II nebulizer (Marquet Medical Products, Inc). Before being stored in a bag, the aerosol flowed through a heated tube and a diffusion dryer to remove water droplets. The aerosol concentration was ~ 5000 $\frac{particles}{ml}$ of air. The aerosol generated by the nebulizer was checked with a particle sizer (APS3321, TSI). The size analysis showed that the fraction of doublets and triplets in the aerosol was < 10 % with a mean geometric diameter of 1.04 μm. When doublets and triplets were excluded from the calculation, mean geometric diameter was 0.94 μm confirming the size provided by the manufacturer. MMAD of the samples was 1.218 μm.

After the aerosol exposure, rats were given a lethal dose of pentobarbital sodium intraperitonally. The blood was removed from the lungs by vascular perfusion with a mixture of heparin and saline (1mL heparin: 100 mL saline) through the pulmonary artery at a pressure of 15 cm H_2O for 10 minutes. The lungs were then perfusion fixed at an airway pressure of 20 cm H_2O with fixative (3 percent glutaraldehyde in 0.01 M phosphate buffer solution) for 20 minutes at a flow rate of 10 - 15 $\frac{ml}{min}$. The lungs were excised and stored in custom-made MR compatible containers. Each container held three sets of lungs immersed in fixative and held in place with gauze. Prior to imaging, each container was degassed under a light vacuum for approximately two weeks until all air bubbles were removed from the lungs. The container was then placed into the middle of a larger container of water (see Field Homogeneity section). This process minimized air/tissue/container interface artifacts during MR imaging.

4.2.2 Imaging

All MR imaging was performed on a 3T General Electric Signa HDX MR scanner. A gradient echo sequence was used with a repetition time (TR) of 2 sec, a flip angle of 20° and a field of view of 13 cm. The polyacrylate MR compatible container was placed in the center of the GE 18 cm diameter transmit and receive knee coil. Using the smallest diameter imaging coil that accommodated the sample container, maximized available signal to noise ratio. Approximately 32 transaxial images were obtained for four echo times (TE). The four TEs were chosen to fully describe the decay of the signal intensity. The shortest TE was 8.2 msec, the minimum prescribable by the scanner for the specified set of imaging parameters. The longest TE was chosen such that the resulting signal intensity was at least three times the standard deviation of the background noise. The resulting images had an in-plane resolution of 500 μm and a thickness of 1 mm. Three scan protocols were performed: field homogeneity validation, particle concentration calibration, and lung imaging. Each protocol required unique TEs and these are given in each respective section.

4.2.3 Calculation of R_2^*

The signal intensity decay for increasing echo time is characterized by the decay rate, R_2^*, where R_2^* is the reciprocal of the signal decay time constant, T_2^*. The rate of the signal decay can be approximated by

$$SI = A_0 e^{-R_2^* TE} \tag{4.1}$$

where SI is the signal intensity, A_0 is an unknown parameter that represents the signal intensity when TE is zero, and R_2^* is the rate of decay of the SI. An example of the decay curves are shown on Figure 4.2. For each transaxial slice, R_2^* was calculated for each voxel by linear regression of the log of equation 4.1. Only TEs for which the signal intensity was larger than three times the standard deviation of the background noise were used for the linear fits. Therefore, in some cases (less than 5 %), only three echo times were included in the linear regression. The coefficient of determination, R^2, was calculated for each fit and only voxels with $R^2 > 0.75$ were used for the statistical analysis.

4.2.4 Field Homogeneity

Prior to imaging the rat lungs, a field homogeneity analysis was performed. The container was filled with fixative and imaged with TEs of 8.2, 40, 100 and 300 msec. The measured signal decay rate, R_2^*, resulted from both the fluid being imaged (R_2) and the inhomogeneities in the magnetic field (R_2'), $R_2^* = R_2 + R_2'$. The inhomogeneities in the magnetic field, R_2', may be impacted by the RF coil, air/tissue interfaces and objects that induce magnetic susceptibility.

Large inhomogeneities were found when the polyacrylate container was filled with only fixative. Imaging was repeated with the container secured into the center of a cylinder of water with a diameter approximately 4 cm larger and 10 cm longer than the container. The signal decay rate, R_2^*, was calculated for each voxel and ROIs were drawn for each transaxial slice to calculate the mean and SD of R_2^*.

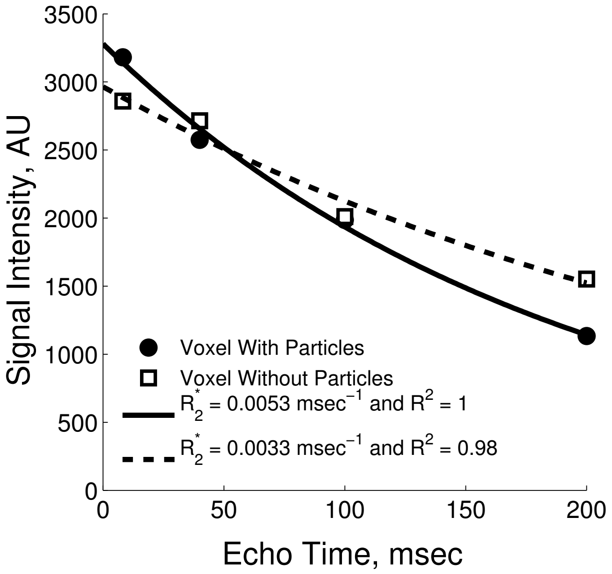

Figure 4.2: Example of the decay of the signal intensity for increasing TE for a voxel from a particle-free and exposed lung, respectively. In this example, signal intensity was the same for both voxels at the echo time of 100 msec. Exponential fits were found by linear regression of the log of the signal intensity. The R_2^* is higher (signal decay rate is more rapid) in the voxel containing the SPIO particles.

4.2.5 Particle Concentration Calibration

A calibration curve relating R_2^* and concentration of deposited particles was obtained by imaging known particle concentrations. Two containers were filled with a gel mixture (0.75 percent agarose with fixative) and punched with six evenly spaced cylindrical holes of 5 mm in diameter. The holes were filled with known particle concentrations of 0, 1.56, 3.13, 6.25, 12.5, 25.0 $\frac{\mu g}{mL}$ suspended in the agarose gel mixture (Figure 4.3, left panel). The containers were imaged with TEs of 8.2, 20, 40 and 80 msec. R_2^* was calculated for each voxel. ROIs were drawn around each particle concentration mixture for $\sim$ 12 transaxial slices. Linear regression with 95 % confidence intervals was performed to find the relationship between R_2^* and the known particle concentrations. An additional phantom experiment was performed where phosphate buffer solution (PBS) and agarose were used to create the phantom in order to test the sensitivity of the resulting slope on the medium in which the particles were embedded.

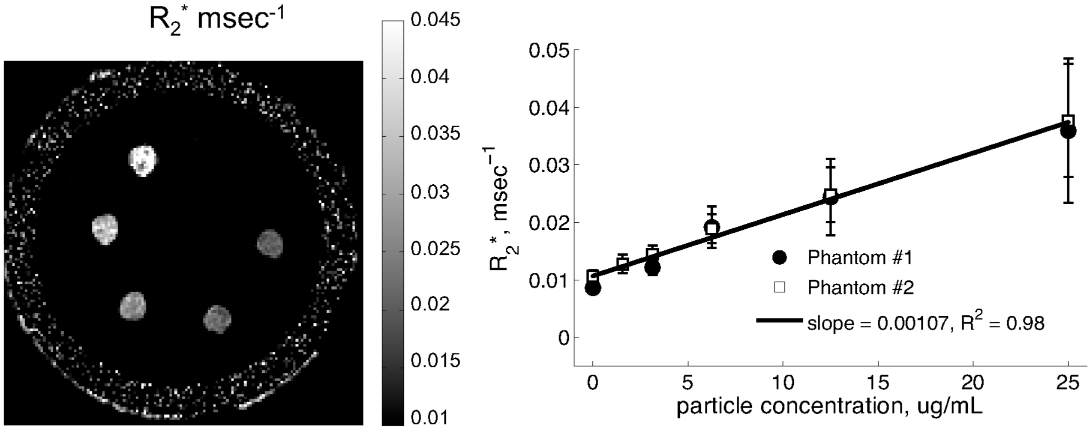

Figure 4.3: Left Panel: MR image of the particle concentration phantom with known particle concentrations. Brightest circle has the largest particle concentration and darkest circle (non detectable on this image) does not contain any particles. Right Panel: The linear relationship between R_2^* and the particle concentration. Data are shown as mean with error bars corresponding to the inter-voxel variability (SD) of particle concentration.

4.2.6 Lung Particle Deposition

Each container of three sets of rat lungs were imaged at TEs of 8.2, 40, 100 and 200 msec, with an imaging time of approximately 3.5 hours. Imaging time was determined by several factors including 1) the repetition time (TR = 2 sec), so that longitudinal effects on the MR signal could be minimized, 2) the number of echo times (four in this sequence), 3) the number of phase encoding steps (i.e. 256 steps), 4) the number of slices (~32), and 5) the fact that data was collected in duplicate, to reduce the signal to noise ratio. Mean and standard deviation of R_2^* values were computed from each slice by drawing ROIs around the left lung. ROIs were defined for each rat individually and the main bronchioles were used as an anatomical reference. The left lung was selected to be analyzed because it comprises of only one lobe, whereas the right lung consists of four lobes. Sub ROIs delimiting the central and peripheral regions were defined as follows: for the transaxial slices located in the mid-portion of the lung (i.e. for the slices encompassing the region surrounding the main bronchus), both a central and peripheral region was defined on each slice as shown in Figure 4.4, while the transaxial slices located at the apex and the base of the lung only included peripheral tissue. The central region was then summed together to form a 3D central region. Similarly, all peripheral regions were added together to form a 3D peripheral region. In this manner the central region made up about 25% of the lung with the remaining 75% consisted of the peripheral region. With this definition, both the central and peripheral regions contained small airways and parenchyma, whereas the central region also included large and medium sized airways. Relative dispersion ($RD = \frac{SD}{mean}$) was computed for each ROI. The higher the RD, the more heterogeneous the R_2^* measurement within the ROI.

On average, the left lung spanned 23 ± 3 slices of the 32 images within the MR data set. The distribution of R_2^* along the apex to base of the left lung was assessed by grouping slices in ten bins uniformly distributed along the apex-base axis. Each bin contained R_2^* values for two or three images (ie: covering approximately 3 mm in the superior inferior direction).

Particle concentration (C_{part}) was computed by

$$C_{part} = \frac{R_2^* - R_{2_{control}}^*}{m} \tag{4.2}$$

where $R_{2_{control}}^*$ is the mean R_2^* for all of the control lungs and m is the slope calculated from the particle concentration calibration experiment (Figure 4.3). The implicit assumption made by using the same slope (m) to calculate the concentration of deposited particles in the lung is that the presence of particles affect R_2^* independently of the medium in which the particles were embedded in (lung tissue in fixative or agarose-fixative solution). A similar assumption was made in a previous particle concentration MR study by Martin et al. [13] who used a linear relationship between particle concentration and T_1 measurements to quantify particle deposition in mice.

Particle concentration was calculated for each voxel within each ROI for all control and exposed lungs. For each rat, normalized regional C_{part} was obtained

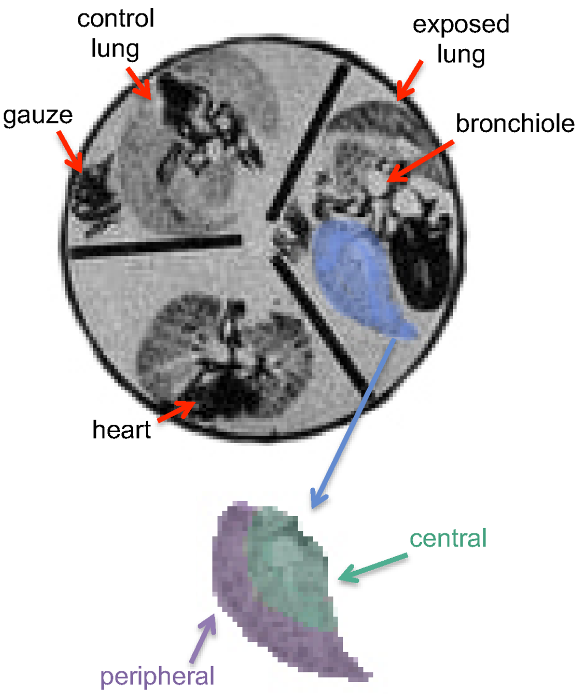

Figure 4.4: Top Panel: An example MR image of the polyacrylate container housing three sets of rat lungs. A control lung is shown in the top left position and two exposed lungs in the bottom and right positions of the container. The lung outlined in blue is an example of an ROI drawn for the left lung. Bottom Panel: The two regions analyzed; the outer (purple) ROI represents the periphery of the lung and the inner (green) ROI represents the central region, which contains large and small airways as well as peripheral tissue.

by dividing each voxel in the central and peripheral regions by the mean C_{part} for the entire left lung. Mean and SD of central and peripheral particle concentration ($\frac{\mu g}{mL}$) was computed from all the voxels spanning each 3D region for each exposed rat. the mean particle concentration of the central (c) and peripheral (p) regions was used to calculate the central to peripheral ratio, $\frac{c}{p}$.

Finally, to check for gravitational dependence on particle deposition resulting from any gravitationally-induced differences in ventilation, two additional ROIs were drawn. The ROIs were defined such that approximately half of the lung was outlined as the dependent (dorsal) and half the lung was the non-dependent (ventral) regions of the exposed lung. The ratio of dependent to non-dependent region of the lung was then calculated.

4.2.7 Statistical Analysis

Data for R_2^*, RD and C_{part} were grouped on the basis of three categorical variables: (i) percent axial distance from the apex of the lung (10 levels), (ii) ROI (2 levels: central and peripheral), and (iii) exposure condition (2 levels: control and exposed lungs). A two-way ANOVA for correlated samples was used to test for differences in R_2^* across the lung depth for the control and exposed lungs (Figure 5.11), and to test for differences in R_2^*, RD, and C_{part} for each ROI for the control and exposed lungs (Table 4.1). Post-ANOVA, pair-wise comparisons using Bonferroni adjustments were performed for tests showing significant F ratios. To compare each region within each category (i.e.: control and exposed separately) a one-way ANOVA test was used with the Tukey Multiple Comparison post-hoc test (Table 4.1). The paired t-test was used to compare overall central to peripheral concentrations. Significant differences were accepted at the $p < 0.05$ level. Outliers were determined using the Grubbs test and removed from the data analyses. All statistical analyses were performed with Prism (GraphPad, San Diego, CA). One set of lungs from the exposed group was removed from the data shown in Figure 5.11 as it was determined to be a statistical outlier and its R_2^* values were similar to the control lungs, suggesting that this rat did not receive any particles.

4.3 Results

4.3.1 Field Homogeneity

Figure 4.5 shows the axial-averaged R_2^* and the respective SD within slices for the field homogeneity tests. When the polyacrylate container was imaged on its own, R_2^* varied considerably both between slices and within an image slice, as demonstrated by the large SD bars. The signal decay rate was greatest at both ends of the container and least in the center slices. In contrast, when the container was submerged in a larger cylinder filled with water, R_2^* did not vary either in the axial direction or within each slice. These results suggest that the field inhomogeneities in the container arise predominately from the air/container interface and these field inhomogeneities were removed when the polyacrylate container was submerged in the large cylinder of water. Therefore, for all subsequent imaging sessions the container was submerged and secured in the center of the water-filled cylinder.

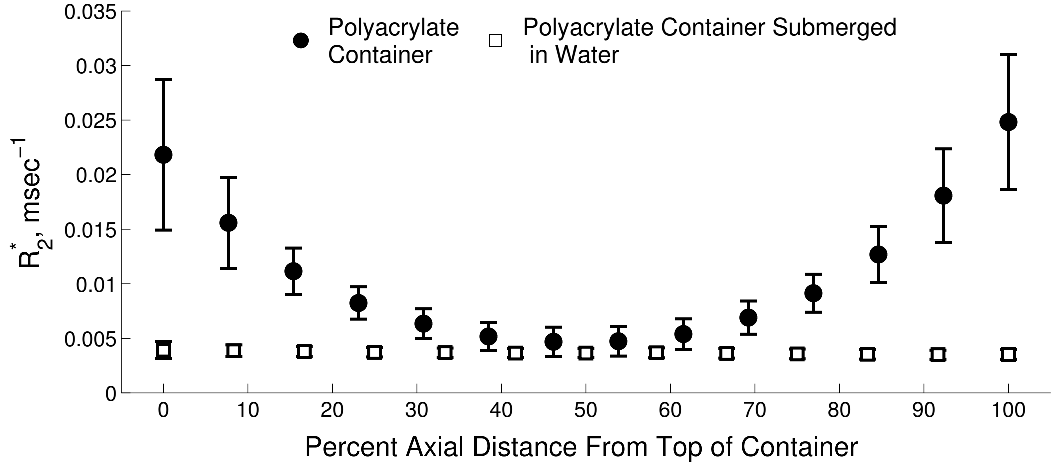

Figure 4.5: R_2^* measurements from field homogeneity experiments. The circles represent the measurements when the polyacrylate container was imaged on its own and the squares represent data from the polyacrylate container submerged in a larger container filled with water, with error bars representing the inter-voxel variation (SD) within an image (SD for the data with the submerged container is smaller than the symbols). The submerged container showed no R_2^* variation along the axis as well as a small standard deviation within the image.

4.3.2 Particle Concentration Calibration

The left panel of Figure 4.3 shows the R_2^* map of the particle concentration phantom. Particle concentration was highest for the brightest circle and decreases counterclockwise around the image. The right panel of Figure 4.3 shows the measured R_2^* for the two experiments performed with the phantom made of a solution of agarose in fixative and the linear relationship between the measured R_2^* and the known particle concentration. The slope of the calibration curve was 0.00107 $\frac{\mu g}{mL*sec}$ with a R^2 of 0.98. The slope was re-calculated using only the data for the three lowest particle concentrations (0, 1.56, 3.13 $\frac{\mu g}{mL}$) and was 0.00105 $\frac{\mu g}{mL-sec}$. This small change (1.7 %) suggests that the particle slope was not highly influenced by the higher concentrations. The slope of the calibration curve from the phantom made with PBS was 0.00126 $\frac{\mu g}{mL-msec}$ and was not statistically different from that obtained with the fixative-agarose phantom ($p = 0.876$).

4.3.3 R_2^* in the Control and Exposed Lungs

An example of the increased signal decay rate in a voxel containing particles and lung tissue, compared to a particle-free voxel with only lung tissue, is shown in Figure 4.2. One set of lungs from the exposed group was removed from the data shown in Figure 5.11, as it was determined to be a statistical outlier, and the R_2^* values were similar to the control lungs, suggesting that there likely was an error in the particle exposure for this rat. The R_2^* values are plotted in Figure 5.11 based on their apex to base location in the lung for both the control (open squares) and exposed lungs (black circles). Data are shown as means ± SD, averaged over all animals in each group. Overall, R_2^* in the exposed lungs was significantly higher than in the control lungs ($p < 0.001$) for the entire left lung. In each group, R_2^* was not affected by the slice's superior-inferior position, except at the base and apex of the lung of the exposed animals, where R_2^* was significantly higher than in the other slices (see Figure 5.11). As there was little variance in R_2^* in the superior-inferior direction of the lung, the bin averaged R_2^* did not depend on the number of image slices within a bin. R_2^* and its relative dispersion are listed in Table 4.1 for the entire left lung and for the central and peripheral regions, respectively. Statistical comparison between the control and exposed groups is also shown along with the statistical analysis within each group. The relative regional volume of the central and peripheral regions were 26.6 ± 1.6 % and 73.3 ± 2.3 % for the control lungs and 25.8 ± 3.9 % and 74.1 ± 4.4 % for the exposed lungs, respectively. For all regions, R_2^* was significantly higher in the exposed lungs than in the control lung. As expected, there was no significant difference in R_2^* between regions for the control lungs. In the exposed lungs, R_2^* was significantly lower in the central region when compared to the entire lung and was significantly higher in the peripheral region compared to the central region. However, R_2^* in the peripheral region did not significantly differ from R_2^* in the entire lung.

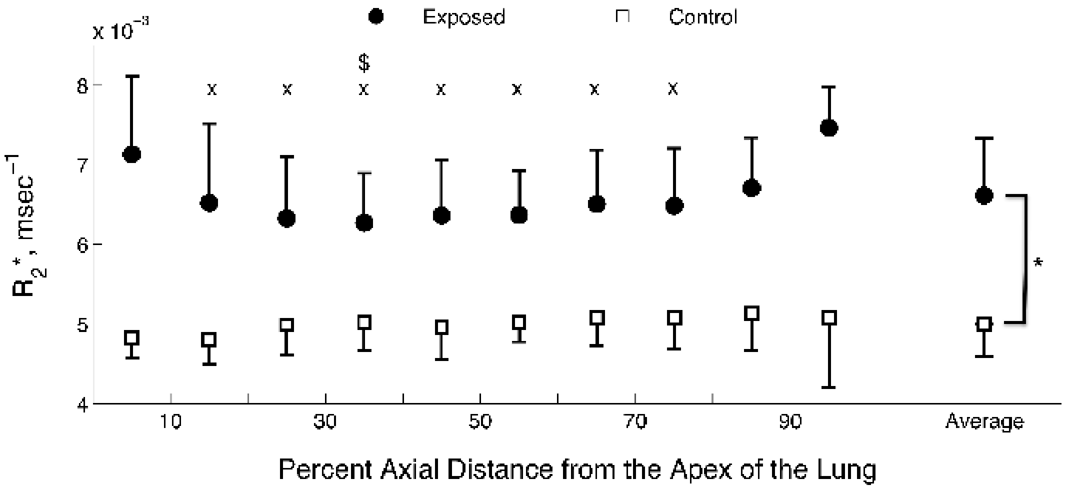

Figure 4.6: Average R_2^* measurements from the apex to the base of the left lung for the control and exposed rats. Error bars represents the inter-rat variability (SD). The R_2^* measurements did not change significantly in the axial direction for the control regions. The base R_2^* was significantly different ($p<0.05$) from slices marked with × and the apex R_2^* was significantly ($p<0.05$) different from slices marked with \$. * $p < 0.001$

Compared to controls, RD was significantly higher for all regions of the exposed lungs (Table 4.1). Within each group, there was a significantly higher RD in the central region when compared to the entire lung with a relative increase of 27.8 ± 20.0 % and 17.9 ± 13.2 % for the control and exposed lungs, respectively.

4.3.4 Particle Concentration

The particle concentration in the exposed lung was 1.42 ± 0.60 $\frac{\mu g}{mL}$ (mean ± SD) with a 95 % confidence interval ranging from 1.34 to 1.49 $\frac{\mu g}{mL}$. Using the slope derived from the PBS phantom, the particle concentration was 1.19 $\frac{\mu g}{mL}$, i.e: 16 % lower than the particle concentration calculated from the calibration curve

Table 4.1: R_2^*, Relative Dispersion (RD) and Particle Concentration for the Entire, Central and Peripheral regions of the left lung with statistical comparison between group (E vs. C) and within each group (C, E). ↑ (↓) indicate an increase (decrease) for $p < 0.05$, $p < 0.01$, $p < 0.001$, with 1, 2 or 3 arrows, respectively.

R_2^* $msec^{-1}$

	Control (C)	Exposed (E)	E vs. C		C	E
Entire Lung	0.0050 ± 0.0003	0.0065 ± 0.0006	↑↑↑	Central vs. Entire	N.S.	↓
Central	0.0051 ± 0.0003	0.0061 ± 0.0004	↑↑	Peripheral vs. Entire	N.S.	N.S.
Peripheral	0.0050 ± 0.0003	0.0067 ± 0.0004	↑↑↑	Peripheral vs. Central	N.S.	↑↑

RD of R_2^*

	Control	Exposed	E vs. C		C	E
Entire Lung	0.192 ± 0.032	0.258 ± 0.026	↑	Central vs. Entire	↑	↑
Central	0.240 ± 0.049	0.309 ± 0.043	↑	Peripheral vs. Entire	N.S.	N.S.
Peripheral	0.169 ± 0.030	0.234 ± 0.025	↑	Peripheral vs. Central	↓↓↓	↓↓

Particle Concentration $\frac{\mu g}{mL}$

	Control	Exposed	E vs. C		C	E
Entire Lung	0.00 ± 0.30	1.42 ± 0.60	N.A.	Central vs. Entire	N.A.	↓
Central	0.03 ± 0.31	1.00 ± 0.39	N.A.	Peripheral vs. Entire	N.A.	N.S.
Peripheral	-0.02 ± 0.30	1.54 ± 0.70	N.A.	Peripheral vs. Central	N.A.	↑↑

obtained from the phantom made with fixative. The central to peripheral ratio, $\frac{c}{p}$, was 0.65 ± 0.12. The $\frac{c}{p}$ ratio was independent of the slope used, as the relationship between R_2^* and particle concentration was linear. To eliminate any differences in exposure concentrations, the regional particle concentration was normalized by the total particle concentration for each rat. The peripheral normalized concentration (1.10 ± 0.04) was significantly higher ($p < 0.003$) than the central normalized concentration (0.68 ± 0.11). This normalized particle concentration was similar between rats, with a RD of 0.15 and 0.03 for the central and peripheral regions, respectively, However, there was a high variability in particle concentration within each rat, for both the central (RD = 2.45 ± 1.53) and peripheral regions (RD = 1.18 ± 0.51).

In the gravitational analysis, the ratio of the concentration of deposited particles in the non-dependent to the dependent region of the lung was 1.45 ± 0.77. This gravitational ratio was not statistically different than 1, suggesting that there was no relationship between particle deposition and gravity.

4.4 Discussion

The principal objective of this study was to use magnetic resonance imaging to determine the regional distribution of aerosol deposition in the lungs of small animals. Few studies have used aerosolized MR contrast agents to evaluate pulmonary drug delivery [13, 19] and the majority of these previous studies have used MR contrast agents to study regional lung ventilation [4, 9, 14, 21]. Sood et al. [19] ventilated piglets with aerosolized Gd-DTPA and imaged them in a 4T MR scanner using a T_1 weighted spin-echo sequence. Pulmonary aerosol deposition was then assessed by increases in signal intensity on the MR images of exposed animals compared to baseline conditions in the same animals. Martin et al. [13] exposed mice to iron oxide particles and used an inversion-recovery fast spin echo pulse sequence to quantify longitudinal relaxation time (T_1) of the lungs. Regional concentration of deposited particles was then assessed by differences in T_1 values between a group of exposed mice and a group of controls. In this study, we focused on the decay rate, R_2^*, to quantify aerosol deposition in the lungs of ventilated Wistar rats. We showed that lungs exposed to SPIO particles had a significantly higher R_2^* than particle-free lungs. Additionally, we found that for these particles, the deposition in the peripheral region was significantly higher than in the central region, with a $\frac{c}{p}$ of 0.65 ± 0.12.

4.4.1 R_2^* in the Control and Exposed Lungs

R_2^* was significantly higher in the exposed lungs (Figure 5.11) because of the increase in magnetic field inhomogeneities resulting from the presence of SPIO particles in the lung tissues. While R_2^* was also relatively constant over most of the lung slices of the exposed animals, R_2^* was higher at the base and apex of the lungs when compared to the other slices (Figure 5.11). While the central slices contained both lung parenchyma (peripheral region) and conducting airways (central region), the base and the apex of the lung mainly included lung parenchyma for which R_2^* was significantly higher than in the central region (Table 4.1). Therefore, the higher R_2^* at the apex and base of the lung likely resulted because these regions only contained peripheral tissue where concentration of the deposited particles was higher than in the central region. Other factors such as variability in the lung thickness or in the MR measurements are unlikely to explain the higher R_2^* measured at the apex and the base of the lung. Indeed, variability in lung thickness from apex to base of the lung had little effect on R_2^*, as there was no change in R_2^* along the depth of the control lungs. Measurement variability also appeared to be minimal based on data obtained from two different imaging sessions of the same exposed lung, where averaged R_2^* varied by about 0.08 %.

The impact of lung structure on the relative dispersion (RD) of R_2^* was characterized by RD values measured in the control lungs. The increase in RD between the control and exposed lungs reflected the dispersion which resulted from the presence of particles that were deposited in the lungs of exposed animals. RD was highest in the central region in both the control and exposed lungs (Table 4.1). This is likely the result of more heterogeneity in lung density in this region as some of the large airways had diameters comparable or even larger than the in-plane voxel size of 0.5 mm. As a result, some of the voxels of the central region only contained fixative (low R_2^*) while other contained a combination of airway wall, lung parenchyma, deposited particles and fixative (high R_2^*). Comparing the central region to the entire lung, there was a higher percent change in RD for the exposed lungs compared to the control lungs, indicating that some particles deposited on the large airways. There was no difference in the percent change in RD from peripheral to entire lung region between the control and exposed lungs. However, R_2^* was higher in the peripheral region of the exposed lungs than in the control lungs. This suggests that deposition in the lung periphery was uniform between voxels, however it is unknown if this uniformity still exists at the sub-voxel level. It should also be noted that the increase in RD between control and exposed lungs most likely reflects the presence of deposited particles and is not the result of signal noise. When up to five times the standard deviation of the noise was added to the signal intensity of one exposed lung, RD increased by 3.4 % above that calculated from the original dataset (no added noise). Such an increase is much smaller than the increase in RD seen between the exposed and control rats.

4.4.2 Particle Concentration

Using the linear relationship found between R_2^* and particle concentration in the phantom experiment (Figure 4.3), the concentration of particles was determined in both the control and exposed lungs (see Table 4.1). As expected, particle concentration (C_{part}) averaged zero in the control lungs. The standard deviation of C_{part} in the control rats (Table 4.1) represents the variability in the measurements due to the presence of residual blood and tissue density unevenness, both of which affect R_2^*. However, this variability was small compared to the concentration of particles found in the exposed rats (Table 4.1). The uncertainty in the slope derived from the phantom calibration had a minimal impact on the particle concentration in the exposed lungs as the 95 % confidence interval of C_{part} was less than the standard deviation of C_{part} between rats. The variability in C_{part} between rats was most likely due to differences in exposure concentrations, as the variability in morphometry between rats of the same strain, weight, sex and health is minimal [15].

The concentration of particles in the periphery was 54 % higher than in the central region of the left lung. These results agree with a previous study by Raabe et al. [16], where Fisher rats were exposed to radiolabeled particles ranging between 0.3 and 10 μm through nose-only breathing. Deposition in the bronchial and pulmonary regions was quantified based on estimation of total inhaled activity and on activity measured from the deposited particles in the two regions of the lung. For 1 μm-diameter particles the study found that more particles deposited in the lung periphery than in the bronchioles. However, a $\frac{c}{p}$ ratio could not be calculated from this data as the bronchial and peripheral regions were defined differently. More recently, Kuehl et al. [11] investigated aerosol deposition patterns of radiolabeled polydisperse particles with MMAD of 0.5, 1, 3 and 5 μm using SPECT/CT techniques both in rats and mice. Regional deposition was quantified using an onion model [11]. Similar to this study, Kuehl et al [11] found that, for 1 μm particles, deposition was higher in the lung periphery than in the central airways, however a central to peripheral ratio was not provided.

While the actual number of particles was not measured during each animal exposure, deposition efficiency was estimated based on average concentration of aerosol generated by the nebulizer (5000 $\frac{particles}{mlofair}$, see Methods section) and on the calculated concentration of deposited particles in the lung. For a breathing frequency of 80 $\frac{breaths}{min}$, a tidal volume of 2 ml, an exposure time of 40 min and assuming the aerosol delivery was distributed in proportion to regional volume (left lung is 36 % of total lung volume [15]), a total of $11.5 * 10^6$ particles was delivered to the left lung. Based on the concentration of deposited particles calculated in this study, $2.67 * 10^6$ particles (i.e. 23 %) of particles delivered to the left lung deposited. Assuming that aerosol deposition is proportional to the lung volume, 23 % of particles delivered to the rat deposited in the whole lung. Raabe et al. [16] reported particle deposition as a percentage of total deposition in the pulmonary (11 %), bronchial (8.2 %), larynx (1.3 %), trachea (0.14 %), skull (1.1 %) and GI tract (7.6 %) for 1.03 μm diameter particles. Using this data, the estimated deposition percentage for particles only delivered to the lung (as is the case for mechanical ventilation) would be $\frac{19.3}{90} = 21\%$, a value close to that found in the present study.

In a modeling study, Darquenne et al. [6] showed that the delivery of inhaled aerosols into the lung segments was dominated by convective processes for specific particle sizes and breathing flow rates characterized by the Stokes' number. The Stokes' number is a non-dimensional parameter that denotes the importance of inertial forces acting on the particle and is defined as:

$$Stk = \frac{\rho_p d_p^2 u}{18 \mu d} \tag{4.3}$$

where ρ_p is the density of the particle, d_p is the diameter of the particle, u is the velocity of the fluid, μ is the viscosity of air and d is the diameter of the airway. The study of Darquenne et al. [6] suggested that when the Stokes' number within the trachea was less than 0.01, particles and gas flow were proportionally distributed to the lung segments with minimal deposition in the central airways. For a tracheal diameter of 0.23 cm [15] and the experimental conditions used in this study, the Stokes number in the trachea was 0.0068, supporting the findings of enhanced particle deposition in the lung periphery compared to the central region.

Finally, no differences was found in particle deposition in the gravitational dependent and non-dependent regions of the lung. The lack of gravitational dependence is most likely because the gravitational height of the lung was small. Verbanck et al. [25] also showed there was no gravitational influence on ventilation in the rat lung.

4.4.3 Comparison with other MR Techniques: Advantages and Limitations

Most of the previous MR studies of aerosol inhalation in small animals were based on the longitudinal relaxation time T1 [13, 19, 20]. Using ventilated newborn pigs, Sood et al. [19] acquired serial T_1-weighted images of the lungs, kidneys, liver, skeletal muscle and heart before and during a 90-minute exposure to aerosolized Gd-DTPA. All images were taken at the same anatomical location and showed a significant increase in signal intensity in the lungs and kidneys during aerosolization. The significant increase in signal intensity in the kidneys but not in the other organs suggested extensive alveolar absorption in the interstitial compartment, i.e the extravascular and extracellular water spaces of the lungs. They also observed higher increase in signal intensity in the kidneys compared to the lungs, which may have been due to a combination of rapid clearance from the lungs, prompt elimination and concentration by the kidneys and better MR visualization of a solid organ free of air/tissues interfaces. While images were acquired in-vivo, no quantification of aerosol deposition or assessment of regional distribution of deposited particles was performed. In a follow-up study, the same group [20] acquired 3D images of piglets ventilated with aerosolized Gd-DPTA, however aerosol delivery to the lungs was indirectly measured through increase in signal intensity in the kidneys and again no quantification of aerosol deposition was reported.

Aerosolized iron oxide particles have also been previously used as a contrast agent to measure aerosol delivery to the lungs. Martin et al. [13] determined the concentration of deposited particles delivered to mice in nose-only inhalation chambers. Imaging was performed post-mortem. They used a calibration of the changes of T_1 values to the concentration c of iron particles ($\frac{1}{T_1} = \frac{1}{T_{10}} + \alpha c$), where T_{10} is the baseline relaxation time constant of the tissue (i.e baseline T_1 prior to particle inhalation) and α is a constant determined based on experiments in agar phantoms over the same concentration range as in the present study (i.e. 0 to 20 $\frac{\mu g}{mL}$). While performed in-situ, the lung vasculature had a large effect on T_1 values. This effect was minimized by eliminating all voxels in the lung ROI that had a signal intensity greater than a threshold value. Such post-processing resulted in the removal of a significant number of voxels mainly in the central region of the lungs. Further, the average T_1 relaxation times in control animals decreased with time after death, most likely because of redistribution of water between the airway surface liquid, interstitial, and vascular spaces of the lung. This required a correction to be applied to the data so that any decrease in T_1 was directly correlated to the presence of deposited particles. Even though it had some limitations, this study was the first attempt at quantifying the number of deposited particles in lung tissues using MRI.

The present study focuses on R_2^* decay rates rather than T_1 relaxation times to quantify distribution of deposited particles within the lungs. It also has the advantage of avoiding any effect of the vasculature on the measured signals. Indeed, blood (that also contains iron) was removed from the lung vasculature before the lung was perfusion-fixed at a controlled lung volume. Lungs were fixed though the vasculature rather then by instillation in order to minimize any potential dislocation of deposited particles during the fixation process. Once fixed, the lungs were submerged in fixative under gentle vacuum to remove air from the lungs. Doing so minimized potential air/tissue artifacts that could alter the measurements. Unlike in the Martin et al. study [13], all voxels in the selected ROI could be used, as there was no interference between the signal from the vasculature and from the presence of iron particles. As such, regional distribution of deposited particles could be performed for various ROIs. However, the technique did not allow for absolute quantification of lung deposition as no in-line monitoring of inhaled concentration was available in the exposure system. Finally, it should be noted that both the technique presented here and that used by Martin et al. [13] allow for detecting similar levels of particle concentration ($\sim 1 \frac{\mu g}{mL}$).

While the resolution (0.5 x 0.5 x 1 mm) of the MR data presented here was sufficient to determine regional deposition, individual airways were not clearly distinguishable on the images except for the large airways. An increased resolution may allow for detecting particles deposited on medium-sized airways. Such higher resolution may be obtained in MR scanner with stronger magnetic field (i.e.: 7T or 11.7T) than that used in this study (3T) without sacrificing signal intensity. However, the larger magnetic field may cause an increase in air-tissue interface signal decay and therefore making the imaging more susceptible to trapped air bubbles, blood and other causes of susceptibility artifacts.

While all these studies performed in animals with Gd-DTPA or iron particles showed the feasibility of using MRI to measure aerosol delivery, only one preliminary study [10] has been performed in humans to date. To apply these MR techniques to human studies, one has to consider the sensitivity of the techniques, i.e. their ability to detect changes in relaxation times induced by the presence of particles. Based on studies in animals, Thompson and Finlay [23] estimated that using Gd-DTPA, a relatively large amount of contrast agent ($\sim$ 0.5 mg) per voxel would be needed while much smaller amount of iron oxide would be required. Finally, it should be noted that while techniques used by Sood et al [20] and Martin et al [13] have the potential to be applied to humans, because of its invasiveness, the technique described in this paper is not intended for use in humans but rather in animals where detailed maps of deposited particles can be obtained both in health and disease models.

4.4.4 Comparison with Radionuclide Imaging Techniques: Advantages and Limitations

Other imaging methods, such as gamma scintigraphy [3, 5, 24, 29], PET [7] and SPECT [8, 11], are also used to study aerosol deposition and clearance. Gamma scintigraphy and SPECT both image ^{99m}Tc radiolabeled particles, whereas PET uses positron-emitting radionuclides that may be attached directly to the drug molecule. Gamma scintigraphy is likely the most widely used technique, however, data can only be viewed in two dimensions, which limits regional deposition analysis. Also, the 2D nature of the images complicates the analysis of the left lung because of overlapping activity from the stomach. These limitations disappear with SPECT, as it provides 3D images of aerosol deposition but analysis of deposition data is more complex than that for data obtained by gamma scintigraphy. PET provides greater image resolution than gamma scintigraphy or SPECT, however PET scanners are currently not widely available. Furthermore, attaching the radionuclides to the drug molecule is expensive and half-lives of the radiotracers are rather short. In order to relate the deposition maps to anatomy, all three imaging modalities require additional CT imaging.

Several studies have used radionuclide imaging to study aerosol deposition in healthy [2, 11] and diseased rodents [22, 26]. Using scintillation counting on small lung sections, Asgharian et al. [2] measured total deposition in rats following nose-only exposure to $^{56}FeCl_3$ particles with aerodynamic diameters ranging from 0.9 to 4.2 μm. They found that total lung deposition was less than 10 % for most particles sizes except for the 3.5 μm diameter particles, where deposition was about 15 %. Sweeney et al. [22] exposed healthy and elastase-induced emphysematous hamsters to ^{99m}Tc-sulfer colloid aerosol with a MMAD of 0.45 μm and found that total particle deposition was lower and heterogeneity of particle deposition higher in elastase-treated animals than in controls. Additionally, Sweeney et al. [22] found that deposition was higher in the large airways and lower in the lung parenchymal in the elastase-treated hamsters, compared to the healthy hamsters. Wu et al. [26] used SPECT/CT imaging to determine clearance rates in a guinea pig model of COPD. They exposed [^{99m}Tc]DTPA particles (particle size not given) to control and cigarette-exposed guinea pigs and found that the clearance rate was higher in cigarette-exposed animals than in controls. Also using SPECT/CT imaging, Kuehl et al. [11] determined regional deposition in healthy rats and mice exposed to four sets of polydispersed particles with MMAD of 0.5, 1.0 3.0 and 5.0 μm. Particle deposition in the lung increased with decreasing particle sizes, whereas the deposition in the oral/nasal area increased with increasing particle sizes. Using an in-house onion model, Kuehl et al. [11] also showed that deposition increased as the distance from the center of mass of the lung increased.

The SPECT/CT study performed by Kuehl et al. [11] is probably the most comparable to this MRI dataset. As similar image resolution was used in Kuehl et al's study (0.4 x 0.4 x 0.4 mm compared to 0.5 x 0.5 x 1.0 mm in this current study), no resolution advantage is shown with either SPECT or MRI in animal imaging. However, compared to the current study, advantages in SPECT lay 1) in the ability to image the lungs in-vivo therefore requiring less sample preparation and 2) in the ability to quantify particle burden in other organs such as stomach and liver. As with the MRI method presented here, the deposition quantified by Kuehl et al. [11] needs to be validated.

4.4.5 Conclusion

This study demonstrated the feasibility of using MRI to detect and quantify regional aerosol particle deposition in the lung. While previous MR studies [13, 19] have utilized the reduction in T_1 relaxation times to quantify regional delivery of inhaled aerosol, this study evaluated the potential use of R_2^* measurements to assess aerosol deposition, as R_2^* is sensitive to the local field inhomogeneities caused by the SPIO particles. We showed that, compared to control animals, R_2^* was higher in rats exposed to 0.95 μm particles and that R_2^* was proportional to the concentration of deposited particles. In agreement with previous studies [11, 16], we also showed that particle deposition was higher in the lung periphery than in the central region as evidenced by a $\frac{c}{p}$ ratio of 0.65. These data strongly support the use of MRI techniques to assess aerosol deposition in small animals by measuring signal decay rate R_2^*. The methods described in this paper can readily be applied to various exposures with different aerosol sizes and/or in animal with various disease models.

4.5 Acknowledgements

Chapter 4, in full, is a reprint of the materials as it appears in Annals of Biomedical Engineering as Jessica M. Oakes, Miriam Scadeng, Ellen C. Breen, G.

Kim Prisk, Chantal Darquenne. ”Regional Distribution of Aerosol Deposition in Rat Lungs Using Magnetic Resonance Imaging”, *Annals of Biomedical Engineering.* 41(5): 967-978. 2013. The dissertation author was the primary investigator and author of this paper.

4.6 Bibliography

4.6.1 References

[1] Aspinall, V., M. O'Reilly. Respiratory deposition and inhalability of monodisperse aerosols in Long-Evans rats. Butterworth Heinemann, 2004.

[2] Asgharian, B,. J. Kelly. E. W.Tewksbury. Introduction to veterinary anatomy and physiology. Toxicological Sciences, 71:104-111,2003.

[3] Bennett, W. D., M. Herbst, N. E. Alexis, K. L. Zeman, J. Wu, M. L. Hernandez, and D. B. Peden. Effect of inhaled dust mite allergen on regional particle deposition and mucociliary clearance in allergic asthmatics. Clinical and Experimental Allergy, 41:1719–1728, 2011.

[4] Berthezene, Y., V. Vexler, O. Clement, A. Mulher, M. E. Moseley, and R. C. Brasch. Contrast enhanced MR imaging of the lung: assessment of ventilation and perfusion. Radiology, 183:667–672, 1992.

[5] Brown, J. S., Zeman, K. L., Bennett, W. D. Ultrafine particle deposition and clearance in the healthy and obstructed lung. American Journal of Respiratory and Critical Care Medicine, 166:1240–1247, 2002.

[6] Darquenne, C., C. van Ertbruggen, and G. K. Prisk. Convective flow dominates aerosol delivery to the lung segments. Journal of Applied Physiology, 111:48–54, 2011.

[7] Fleming, J. S. and J. H. Conway. Three dimensional imaging of aerosol deposition. Journal of Aerosol Medicine, 14:147–153, 2001.

[8] Fleming, J. S., M. Quint, L. Bolt, T. B. Martonen, and J. H. Conway. Comparison of SPECT aerosol deposition data with twenty-four-hour clearance measurements. Journal of Aerosol Medicine, 19:261–267, 2006.

[9] Haage, P., G. Adam, S. Karaagac, J. Pfeffer, A. Glowinski, S. Dolmen, and R. W. Gunther. Mechanical delivery of aerosolized gadolinium-DTPA for pulmonary ventilation assessment in MR imaging. Investigative Radiology, 36:240–243, 2001.

[10] Haage, P., S. Karaagac, E. Spuntrup, H. T.Truong, T. Schmidt, R. W. Gunther. Feasibility of pulmonary ventilation visualization with aerosolized magnetic resonance contract media. Investigative Radiology, 40:85–88, 2005.

[11] Kuehl, P. J., T. L. Anderson, G. Candelaria, B. Gershman, K. Harlin, J. Y. Hesterman, T. Holmes, J. Hoppin, C. Lackas, J. P. Norenberg, H. Yu, and J. D. McDonald. Regional particle size dependent deposition of inhaled aerosols in rats and mice. Inhalation Toxicology, 24:27–35, 2012.

[12] Laube, B. L. The expanding role of aerosols in systemic drug delivery, gene therapy, and vaccination. Respiratory Care, 50:1161–1176, 2005.

[13] Martin, A. R., R. B. Thompson, and W. H. Finlay. MRI measurement of regional lung deposition in mice exposed nose-only to nebulized superparamagnetic iron oxide nanoparticles. Journal of Aerosol Medicine and Pulmonary Drug Delivery, 21:335–342, 2008.

[14] Misselwitz, B., A. Muhler, I. Heinzelmann, J. Bock, and H. Weinmann. Magnetic resonance imaging of pulmonary ventilation. Initial experiences with gadolinium-DTPA-based aerosol. Investigative Radiology, 32:797–801, 1997.

[15] Oakes, J. M., M. Scadeng, E. C. Breen, A. L. Marsden, and C. Darquenne. Rat airway morhometry measured from in-situ mri-based geometric models. Journal of Applied Physiology, 112:1921–1931, 2012.

[16] Raabe, O. G., M. A. Al-Bayati, S. V. Teague, and A. Rasolt. Regional deposition of inhaled monodisperse coarse and fine aerosol particles in small laboratory animals. Annals Occupational Hygiene, 32:53–63, 1988.

[17] Raabe, O. G., H. C. Yeh, G. J. Newton, R. F. Phalen, and D. J. Velasquez. Deposition of inhaled monodisperse aerosols in small rodents. Inhaled Particles, 4:3 – 21, 1975.

[18] Sanjar, S. and J. Matthews. Treating systemic diseases via the lung. Journal of Aerosol Medicine, 14:51–58, 2001.

[19] Sood, B. G., Y. Shen, Z. Latif, X. Chen, J. Sharp, J. Neelavalli, A. Joshi, T. L. Slovis, and E. M. Haacke. Aerosol delivery in ventilated newborn pigs: an MRI evaluation. Pediatric Research, 64:159–164, 2008.

[20] Sood, B. G., Y. Shen, Z. Latif, B. Galli, E. J. Dawe, and E. M. Haacke. Effective aerosol delivery during high frequency ventilation in neonatal pigs. Asian Pacific Society of Respirology, 15:551–555, 2010.

[21] Suga, K., N. Ogasawara, T. Tsukuda, and N. Matsunaga. Assessment of regional lung ventilation in dog lungs with Gd-DTPA aerosol ventilation MR imaging. Acta Radiologica, 43:282–291, 2002.

[22] Sweeney, T. D., J. D. Brain, S. a. Leavitt, and J. J. Godleski. Emphysema alters the deposition pattern of inhaled particles in hamsters. The American Journal of Pathology, 128:19–28, 1987.

[23] Thompson, R. B. and W. H. Finlay. Using MRI to measure aerosol deposition. Journal of Aerosol Medicine and Pulmonary Drug Delivery, 25:55–62, 2012.

[24] Usmani, O. S., M. F. Biddiscombe, and P. J. Barnes. Regional lung deposition and bronchodilator response as a function of beta2-agonist particle size. American Journal of Respiratory and Critical Care Medicine, 172:1497–1504, 2005.

[25] Verbanck, S., N. Gonzalez-Mangado, G. Peces-Barba, and M. Paiva. Multiple-breath washout experiments in rat lungs. Journal of Applied Physiology, 71:847–854, 1991.

[26] Wu, Y., C. J.Kotzer, S. Makrogiannis, G. A.Logan, H. Haley, M. S.Barnette, S. K.Sarkar. A noninvasive [99mTc]DTPA SPECT/CT imaging methodology as a measure of lung permeability in a guinea pig model of COPD.. Molecular Imaging and Biology, 13:923-929,2011.

[27] Zarogoulidis, P., E. Chatzaki, K. Porpodis, K. Domvri, W. Hohenforst-Schmidt, E. Goldberg, N. Karamanos, and K. Zarogoulidis. Inhaled chemotherapy in lung cancer: future concept of nanomedicine. International Journal of Nanomedicine, 7:1551–1572, 2012.

[28] Zarogoulidis, P., N. Papanas, G. Kouliatsis, D. Spyratos, K. Zarogoulidis, and E. Maltezos. Inhaled insulin too soon to be forgotten. Journal of Aerosol Medicine and Pulmonary Drug Delivery, 24:213–223, 2011.

[29] Zeman, K. L., J. Wu, and W. D. Bennett. Targeting aerosolized drugs to the conducting airways using very large particles and extremely slow inhalations. Journal of Aerosol Medicine, 23:363–369, 2010.

[30] Zhang, J., L. Wu, H.-K. Chan, and W. Watanabe. Formation, characterization, and fate of inhaled drug nanoparticles. Advanced Drug Delivery Reviews, 63:441–455, 2011.

Chapter 5

MRI Assessment of Particle Deposition in Emphysematous Rats

5.1 Introduction

Emphysema is a chronic obstructive pulmonary disease (COPD) and is primarily characterized by alveolar wall destruction [25], alveolar space enlargement, decrease in small airway diameter [16], and increase in tissue compliance. In the United States, 3.7 million people [1] have been diagnosed with emphysema. However, it is not well understood how emphysema influences the deposition of inhaled aerosols in the lung. For example, Brand et al. [4] found no difference in particle deposition between healthy, emphysematous and cystic fibrosis patients for 4 ± 1.6 μm diameter particles. In a different study, Sweeney et al. [24] found total less deposition and higher non-uniformity of deposition of 0.45 μm diameter particles in elastase-treated hamsters compared to healthy hamsters. The disease has been shown to cause an increase in exhaled aerosol bolus dispersion in emphysema subjects compared to healthy patients [4, 13] or dogs [22], suggesting that particle distribution in the lung is more heterogeneous in emphysematous when compared to healthy patients.

It has been well documented that rodents treated with elastase develop panacinar type emphysema [3, 15]. Panacinar emphysema is associated with alpha1-antitrypsin deficiency and typically is found in elderly patients. Unlike centriacinar emphysema, which is commonly caused by cigarette smoking and primarily destroys the respiratory bronchioles, panacinar emphysema causes enlargement of the respiratory bronchioles, alveolar ducts and alveolar sacs [15]. Elastase-treated rodents have larger linear mean intercepts [12], tidal and total lung volume [6], and tissue compliance [8, 11] compared to healthy rodents. In mice, it has been shown that elastase-treated mice have an increase in the heterogeneous distribution of tissue compliance, compared to healthy mice [11]. Recently, MRI studies have shown decreased fractional ventilation and increased apparent diffusion coefficients in elastase-treated rats, compared to healthy rats [6, 7].

The goal of this current study was to determine the differences in total deposition and in the distribution of deposited particles in both healthy and elastase-treated rats. To do this, healthy and emphysematous rats were mechanically ventilated to either particle-laden air (MMAD of 1.218 μm) or particle-free air. Following the procedure outlined by Oakes et al. [19], the lungs were fixed in-situ, excised and imaged in a 3T magnetic resonance (MR) scanner. The signal decay rate, R_2^* was quantified in both the non-exposed and exposed healthy and emphysematous rats. Concentration of deposited particles was estimated based on calibration curves between particle concentration and R_2^* [19]. Differences in deposition between the healthy and emphysematous rat lungs was assessed for the five rat lobes, central and peripheral regions of each lobe and at several axial intervals from the apex to base of the lung. This study is the first to determine changes in deposition in mechanically ventilated healthy and emphysematous rat lungs.

5.2 Methods

5.2.1 Animal Preparation

This study protocol was approved by the University of California San Diego Institutional Animal Care and Use Committee (IACUC). Healthy six week old male Wistar rats (n = 13) were orotracheally instilled with with porcine pancreatic elastase (Sigma Aldrich) (125 units per kg of body weight) diluted in 0.5 mL of saline. After instillation, the rats were gently rocked to ensure homogenous enyzme exposure. After instillation the rats were returned to their cages and provided food and water ad libitum and were on a 12 hour lights on and 12 hour lights off cycle. Rats were studied six weeks later.

Eleven healthy (H) weight-matched rats (body weight = 402 ± 23 grams) were added to the group of elastase treated (E) rats (body weight = 420 ± 39 grams). All rats were connected to a mechanical ventilator and exposed to either particle-free air (H: n = 5: E n = 6) or particle - laden air (H: n = 6, E: n = 7) for 40 minutes. Details of the particle exposure system is given in Oakes et al. [19]. The breathing frequency and tidal volume were controlled by the pump; breathing frequency = 80 $\frac{breaths}{min}$ and tidal volume = 2.2 mL. The pump controlled the inhalation part of the breath and the rat passively exhaled into a 1 cm P_{peep} reservoir during the exhalation part of the breath. Pressure was measured with a catheter at the trachea. The aerosol was made of monodisperse magnetic polystyrene particles with a geometric diameter of 0.95 μm and a density of 1.35 $\frac{g}{cm^3}$ suspended in water at a 1:4 ratio [19]. The MMAD of the particles was 1.218 μm.

After the exposure rats were given a lethal dose of pentobarbital sodium intraperitonally. Details of the lung preparation are given in Oakes et al. [19] and in Chapter 4. Briefly, the lungs were vascular perfused to remove all of the blood and then fixed at an airway pressure of 20 cm H_2O with 3 % glutaraldehyde mixed in 0.01 M phosphate buffer solution. After preparation the lungs were stored in MR compatible containers (three lungs per container) for three months and then degassed under a light vacuum for approximately 2 weeks. Before imaging the MR compatible container was placed in a large cylindrical vessel [19] and filled with water to avoid air/container interfaces.

5.2.2 MR Imaging and Image Processing

The imaging protocol is described in detail in Chapter 4 and in Oakes et al. [19]. Briefly, the MR compatible container was imaged with a 3T General Electric Signa HDX MR scanner. A gradient echo sequence was employed with a flip angle of 20°, a TR of 2 seconds, a field of view of 13 cm and echo times of 8.2, 40, 100 and 200 msecs. A GE 18 cm diameter transmit and receive knee coil was used. The resulting images had a in-plane resolution of 500 μm and thickness of 1 mm.

The signal decay rate, R_2^* was calculated at a per-voxel basis [19] for each axial slice. Regions of interest (ROI) were hand drawn around each lobe of the lung. The five rat lobes (left lung: left lobe, right lung: apical, intermediate, diaphragmatic and cardiac lobes [18]) were identified from the images. Additionally, ROIs were drawn around the central and peripheral regions of each lobe, as described previously [19].

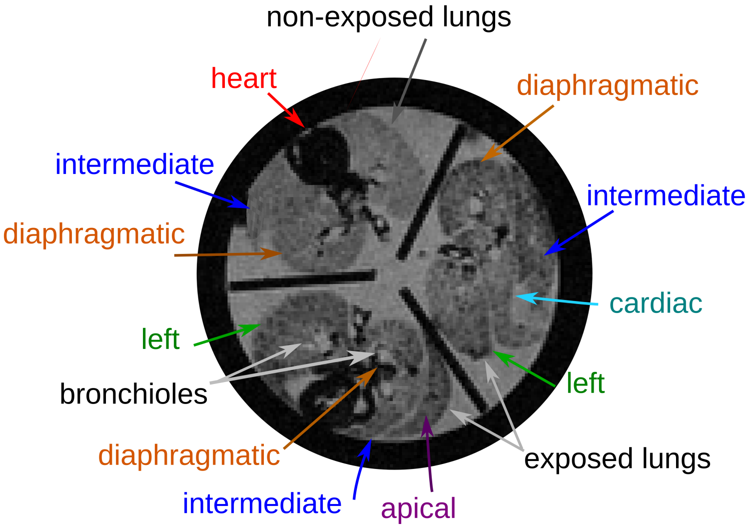

Figure 5.1: Representative MR image of control and exposed lungs with lobes identified.

5.2.3 Particle Concentration

As described previously [19], the particle concentration was calculated on a per voxel basis by employing a linear relationship determined from a calibration phantom

$$C_{part} = \frac{R_2^* - R_{2,control}^*}{m} \tag{5.1}$$

where R_2^* is the voxel's signal decay rate, $R_{2,control}^*$ is the mean R_2^* for the control non-exposed lungs and m is the slope derived from the particle concentration calibration experiment, $m = 0.00107\frac{\mu g}{mL-sec}$. The mean $R_{2,control}^*$ varied based on lobe as well as region of the lung, i.e. central and peripheral regions had different $R_{2,control}^*$ (see Results section). Therefore, the $R_{2,control}^*$ of each region of the healthy or emphysema control lungs, was used for each corresponding region of the exposed lungs. In addition, any particle concentration values that were negative were set to a zero particle concentration.

The distribution of particle concentration along the apex to base of each lobe was assessed by grouping slices in bins uniformly distributed along the apex to base axis. The left and diaphragmatic lobes had 10 bins each, the intermediate and apical lobes had 5 bins each and the cardiac lobe had 4 bins. Each bin contained two to three images.

5.2.4 Alveolar Morphometry

After MR imaging, 7 healthy and 7 emphysema lungs were randomly chosen for the alveolar morphometry analysis. Before being prepared each lobe's volume was measured. Once the volumes were measured, each lobe was placed in phosphate buffer solution (PBS) for 30 minutes on a mixing table to remove some of the fixative. Then approximately 3 mm slices were taken from the middle of each lobe and the rest of the lobe was stored away. Each 3 mm slice was mixed with increasing amounts of ethanol until the lungs were in 100 % ethanol. Then the lungs were placed in melted paraffin mixed with citrosolve. After 4 hours, the lungs were placed in 100 % melted paraffin and stored in a hot water bath for 12 hours.

Next, the 3 mm slices were placed in a wax holder until the paraffin solidified. Once ready, the 3 mm slices were sliced into 7 μm thick slices with a manual slicer and put on a glass slide. Afterwards each slide was mixed with increasing amount of water until the slides were in 100 % water. The slides were stained for 3 mins in Haris Modified Hematoylin (Fisher Scientific) and then brought back to 100 % ethanol by immersing the slides in water-ethanol solution with increasing amounts of ethanol. Once prepared, the slides were imaged on Hamamatsu NanoZoomer 2.0 HT Slide Scanning System at a 20 times magnification.

Linear mean intercepts were calculated from the NanoZoomer images. Traditionally, linear mean intercepts are calculated by drawing a line on the image and then calculating the number of times the alveolar septa crosses the line. Here, a MATLAB code was developed to determine the linear mean intercept. First, the images were turned into a binary images such that black is 0 and white is 1. With this definition, the black areas are tissue and the white areas are the airspaces. Then, for every 10 vertical lines, the number of times that white turned to black was counted. The length of time images was divided by the number of times the alveolar septa crossed. The code was validated against traditional linear mean intercept methods for accuracy.

5.2.5 Statistical Analysis

All data are presented as the mean ± the standard deviation. Two way ANOVA was used to compared emphysema versus healthy rats. If the two way ANOVA passed, standard t-tests were employed to test the difference between individual lobes or areas of the lung. Bonferonni correction was then implemented to determine if the p-value passed the significance level. A repeated measures ANOVA was applied to test differences within each subset of animals. To test if values were different than expected values a standard t-test was used with values compared to the expected value of 1. All p-values are presented. Statistical significance was applied at the $p < 0.05$ level.

5.3 Results

5.3.1 Alveolar Space Morphometry

Figure 5.2 shows a representative image of the left lung of a healthy (panel A) and emphysematous (panel B) rats. The emphysematous image not only has larger airspaces but also collapsed airway spaces between the larger airspaces, compared to the healthy image. The linear mean intercepts (L_M) for the healthy and emphysema rats are shown in Figure 5.3. As expected, the L_M was on average larger in the emphysematous rats compared to the healthy rats, however the increase was not statistically significant. The greatest change was found for the left, diaphragmatic and cardiac lobes.

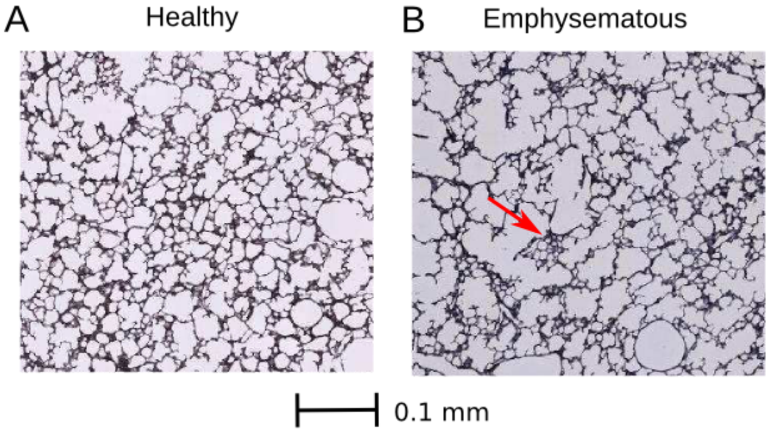

Figure 5.2: Representative images that were used for the linear mean intercept analysis. Examples are from the diaphragmatic lobe for a healthy (left panel) and emphysematous (right panel) rat. The red arrow is pointing to an area where collapsed airways were present.

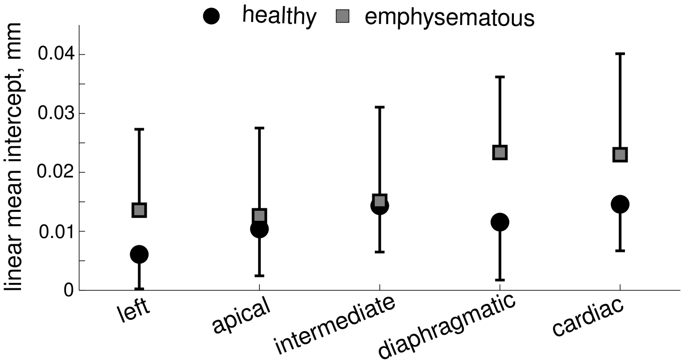

Figure 5.3: Linear mean intercepts found from healthy and emphysematous rat lungs. No statistical significance was found when comparing the emphysema values to the healthy values. The smallest p-value was for the diaphragmatic lobe, p = 0.068.

5.3.2 Signal Decay Rate in Healthy and Emphysematous Lungs

Non-Exposed Rats

As shown in Figure 5.4A, R_2^* was significantly higher in the emphysema non-exposed rats (p = 0.048) compared to the healthy non-exposed rats. The left and cardiac lobes of the emphysema rat had a significantly higher (without Bonferonni correction) R_2^* compared to the corresponding healthy lobes. While not statistically significant, the diaphragmatic lobe of the emphysema rat also had higher R_2^* compared to the healthy rat. The relative percent increase of the emphysema compared to the healthy non-exposed rats and the corresponding p-values are given in Table 5.1.

In the healthy non-exposed rats there was no different in R_2^* among lobes (see Figure 5.4 and Table 5.2). However, there was a significant difference between lobes (p = 0.023) for the emphysematous non-exposed rats.

There was no change in R_2^* between the central and peripheral regions for the healthy non-exposed lungs. In contrast the emphysematous lungs, the peripheral region had a lower R_2^* than the central region, as shown in Table 5.3. R_2^* was significantly less in the central regions for the left and intermediate lobes compared to the healthy central regions.

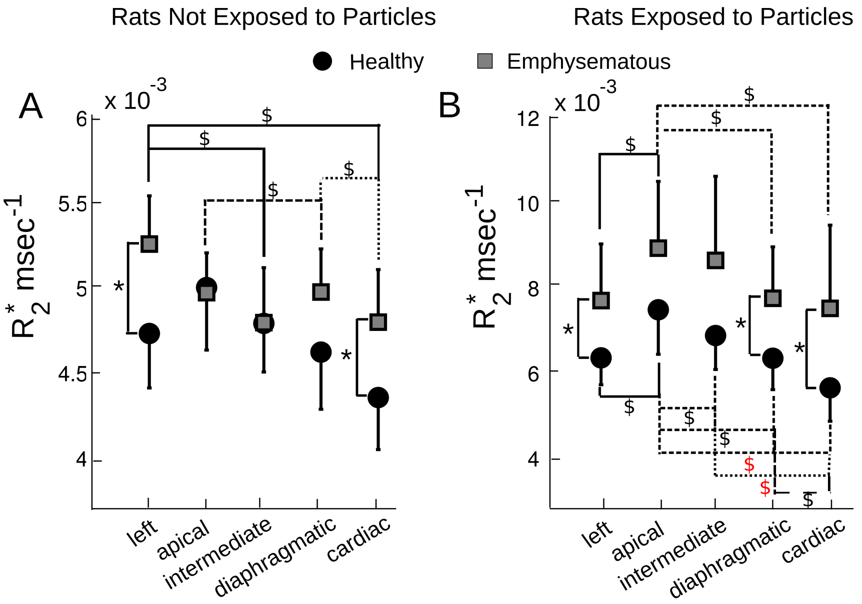

Figure 5.4: Comparison of R_2^* in healthy and emphysematous rat lungs for rats not exposed to particles (left panel) and for rats exposed to particles (right panel). There was a statistically significant higher R_2^* in emphysema compared to healthy for the control rats (p = 0.042) and for the exposed rats (p = 0.036). Black starts indicate the statistics pass a significance level of $p < 0.05$ and red starts pass the Bonferonni correction of $p < 0.01$. Statistics comparing intra-disease and between diseases for each lobe are shown in Tables 5.1 and 5.2

Relative dispersion (RD) is a measure of the heterogeneity of the distribution of R_2^* in the ROI. In the lungs not exposed to particles, RD is essentially a representation of the heterogeneous distribution of tissue or airways. As shown in Figure 5.5, there was no difference in RD between lobes for the healthy rat. However, not only was RD higher in the left, diaphragmatic and cardiac lobes of the emphysematous rat, compared to the healthy rat, but there was a difference in RD between lobes. The relative change in RD for each lobe and it's corresponding p-value is given in Table 5.4.

Table 5.1: Comparison of R_2^* Between Healthy and Emphysematous Rats. P values for comparing R_2^* between healthy and emphysema lobes for control and exposed lungs. Bonferonni correction would indicate significance for $p < 0.01$. Red values would pass statistical level of $p < 0.05$. No values passed Bonferonni criteria for multiple comparisons.

	Non-Exposed Rats		Exposed Rats	
	Relative Change %	p-value	Relative Change %	p-value
Left	11.1	0.021	21.1	0.042
Apical	-0.60	0.322	19.3	0.075
Intermediate	0.095	0.735	25.6	0.062
Diaphragmatic	7.62	0.092	22.2	0.027
Cardiac	10.16	0.042	33.0	0.049

Exposed Rats

As the iron oxide particles create local field inhomogeneities in the magnetic field, it is expected that the presence of the particles would cause a increase in the signal decay rate, R_2^* [19]. Additionally, as we have shown that the signal decay rate is linearly proportional to the concentration of the iron particles [19], it is expected that a larger R_2^* would result in a larger particle concentration. As Figure 5.4B shows, there was a statistically significant higher R_2^* in the emphysematous exposed rats compared to the healthy rats ($p = 0.036$). The left, diaphragmatic and cardiac lobes all had a significantly higher R_2^* compared to their corresponding healthy exposed lobes (see Table 5.1).

While there was no significant change in R_2^* between lobes of the healthy non-exposed rats, there was a difference between lobes in the healthy exposed rats (see Table 5.2). Differences in inter-lobe deposition was also found for the emphysematous cases. In both the healthy and emphysematous case the apical lobe had the highest R_2^* values (see Figure 5.4). With Bonferonni correction, the Apical lobe had a statistically significant higher R_2^* compared to the cardiac and intermediate lobes (Table 5.2). On the other hand, none of the lobes had Bonferonni statistically higher R_2^* in the emphysema cases, which may mainly be due to the high inter-rat variability.

Table 5.2: P-Values Found for Comparison of R_2^* Between Lobes. P values for comparing R_2^* between lobes for healthy and emphysema control and exposed cases. Lobe comparisons should be compared to the Bonferonni correction of $p < 0.005$. Blue values passed Anova test for $p < 0.05$, blue values passed statistical test for $p < 0.05$ and bold values based Bonferonni correction for multiple comparisons, $p < 0.005$.

			Non-Exposed Rats		Exposed Rats	
			Healthy	Emphysematous	Healthy	Emphysematous
	Anova		0.112	0.023	0.001	0.021
Left	vs.	Apical	0.219	0.117	0.022	0.008
Left	vs.	Intermediate	0.797	0.036	0.178	0.121
Left	vs.	Diaphragmatic	0.642	0.097	0.973	0.892
Left	vs.	Cardiac	0.109	0.022	0.058	0.757
Apical	vs.	Intermediate	0.149	0.215	0.011	0.329
Apical	vs.	Diaphragmatic	0.128	0.899	0.026	0.013
Apical	vs.	Cardiac	0.070	0.049	**0.001**	0.013
Intermediate	vs.	Diaphragmatic	0.487	0.198	0.128	0.096
Intermediate	vs.	Cardiac	0.121	0.984	**0.002**	0.096
Diaphragmatic	vs.	Cardiac	0.347	0.032	0.027	0.634

As shown in Table 5.3, for all lobes except the Diaphragmatic, there was a higher percent change in comparing peripheral to central region R_2^* in the emphysematous rats compared to the healthy rats. Additionally, both the apical and the cardiac lobes in the emphysematous rats had a statistical significantly higher, with Bonferonni correction, peripheral deposition than central deposition. The same was found for the cardiac lobe of the healthy exposed rats.

In the control lungs, relative dispersion (RD) was a measure of the heterogeneity of the tissue in the lobe. In the exposed lungs in addition to the heterogeneity of the tissue, RD is a gauge of the disperse distribution of particles in the lobe. For the exposed rats, RD was higher in the emphysematous rats, for all lobes, as shown in Figure 5.5. However, there was no difference between lobes, for both the healthy and emphysematous exposed rats. The percent change in RD in emphysema compared to healthy rats is shown in Table 5.4.

Table 5.3: Comparison of R_2^* Between Peripheral and Central Region for All Rats. Red values indicate statistical significance at the $p < 0.05$ level and bold values indicate the values pass the Bonferonni comparison for $p < 0.005$. Lobe comparisons should be compared to the Bonferonni correction of $p < 0.005$. Blue values passed Anova test for $p < 0.05$, blue values passed statistical test for $p < 0.05$ and bold values based Bonferonni correction for multiple comparisons, $p < 0.005$.

	Non-Exposed Rats				Exposed Rats			
Lobe	Healthy		Emphysematous		Healthy		Emphysematous	
	Relative Change %	p-value	Relative Change %	p-value	Relative Change %	p-value	Relative Change %	p-value
Left	-1.55	0.078	-5.76	0.030	9.08	0.065	21.89	0.010
Apical	-1.37	0.644	-4.44	0.075	13.75	0.028	23.51	**0.004**
Inter.	-1.82	0.314	-3.00	0.049	5.70	0.220	10.75	0.033
Dia.	-3.23	0.336	-3.90	0.101	8.73	0.121	5.87	0.315
Card.	-1.42	0.531	-0.91	0.787	11.58	**0.003**	15.84	**0.004**

Table 5.4: Comparison of RD Between Healthy and Emphysematous Rats. Average ± standard deviation between rats of relative dispersion of particle deposition within a lobe. P-values are for t-test. Values should be compared to the Berforonni correction of significance for $p = 0.01$.

	Non-Exposed Rats		Exposed Rats	
Lobe	Relative % Change	p-value	Relative % Change	p-value
Left	27.9	0.050	18.5	0.031
Apical	2.64	0.754	20.6	0.171
Intermediate	-3.1	0.735	27.4	0.042
Diaphragmatic	11.9	0.349	26.2	0.045
Cardiac	23.0	0.088	35.9	0.030

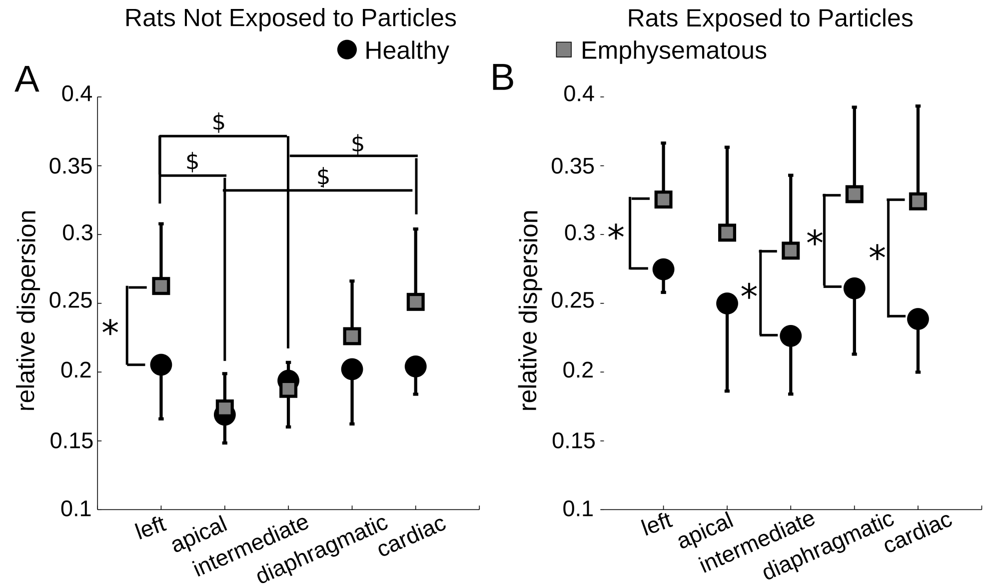

Figure 5.5: Relative dispersion in each lobe for rats not exposed to particles (left panel) and rats exposed to particles (right panel). RD in the emphysematous rats was significantly higher than in healthy rats for both the non-exposed rats (p =0.048) and the exposed rats (p = 0.032).

5.3.3 Particle Concentration

Figure 5.6 shows representative maps of particle concentration (Eq. 5.1) for each voxel in a healthy and a emphysematous left lobe. As can be seen from Figure 5.6, there were areas of zero particle concentration. These areas were mainly the large airways, as can be clearly seen from Figure 5.6B. These areas would mainly include fixative, and therefore it is expected that these areas would have no particle in them. In addition, it can be clearly seen from Figure 5.6 that there was more areas of high particle concentration ($> 7 \frac{\mu g}{mL}$) in the emphysematous lobe than in the healthy lobe. The particle concentration was also quite heterogeneously distributed.

While not statistically significant (p = 0.069), particle concentration tended to be higher in the emphysematous rats compared to the healthy rats. The emphysematous rats had a 80.87 % higher in deposition in the intermediate lobes and 98 % higher deposition in the cardiac lobes, compared to the healthy rats (see Table 5.5). In the healthy exposed rats, the apical lobe had a higher concentration than

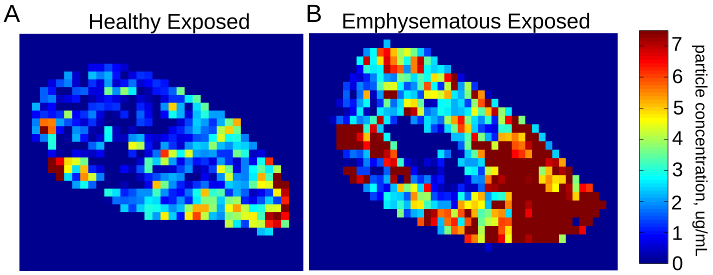

Figure 5.6: Representative particle concentration maps for healthy (panel A) and emphysematous (panel B) exposed rats.

the other lobes and was significantly higher for the cardiac lobe. The same trend was shown for the emphysematous lungs, where particle concentration was higher in both the apical and intermediate lobes, compared to the other three lobes.

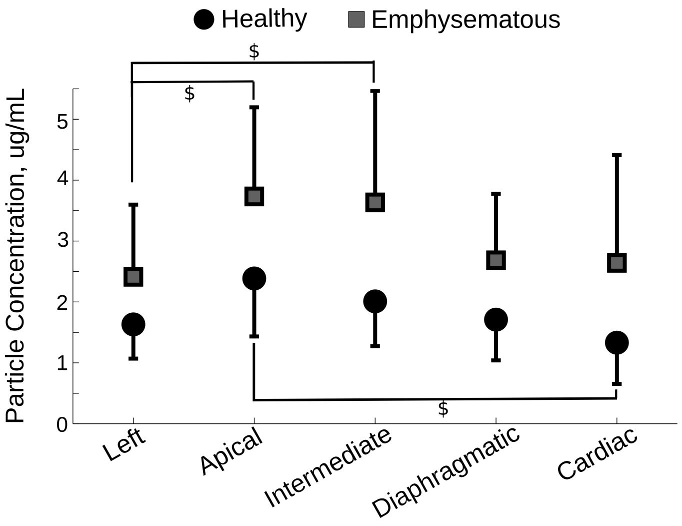

Figure 5.7: Average particle concentration in each lobe of the healthy and emphysematous exposed rat lungs. Error bars represent the standard deviation between rats and * denotes statistically significant difference between lobes. The particle concentration tended to be higher in the emphysema rats compared to the healthy rats (p = 0.069)

Figure 5.8 shows the central and peripheral particle concentration for each lobe in the healthy and exposed rats. Particle concentration always tended to be higher in the peripheral region, compared to the central region (Figure 5.8 and

Table 5.5: Comparison of Emphysematous to Healthy Particle Concentration. Relative percent difference in total particle concentration of emphysema rats compared to healthy rats. P values are for uncorrected t-test, i.e. Bonferonni correction would indicate significance at 0.005 level.

Lobe	Entire Lobe Relative % Change	Central Region Relative % Change	Peripheral Region Relative % Change
Left	47.9	7.7	59.3
Apical	56.54	36.2	61.6
Intermediate	80.97	71.2	83.4
Diaphragmatic	57.2	71.3	49.7
Cardiac	98.7	126	93.1

Table 5.5). However, there was no statistical difference in particle concentration between regions for the healthy rat, except for the cardiac lobe. In contrast, particle concentration was significantly higher in the peripheral region than in the central region for the left, apical, intermediate and cardiac lobes of the emphysematous rats (Figure 5.8). The relative change of peripheral deposition compared to central deposition and their corresponding p-values are given in Table 5.8.

The $\frac{c}{p}$ ratio for each lobe is given in Figure 5.9. While there wasn't a statistically different $\frac{c}{p}$ between the emphysematous and healthy rats, there was some difference between lobes for the emphysematous rats. As shown in Figure 5.9 the diaphragmatic emphysematous lobe had a $\frac{c}{p}$ of 0.86, while the left emphysematous lobe $\frac{c}{p}$ of 0.53.

The particle concentration in each lobe was normalized by the total particle concentration in the two lungs and is shown in Figure 5.10A. There was no difference between the healthy and emphysematous rats. This normalized deposition fraction was normalized by the lobe volume and is shown in Figure 5.10B. While there was relatively no difference between healthy and emphysematous rats in the particle concentration normalized by volume (Figure 5.10B), there was difference in comparing these values to 1. A value of 1 would indicate that number of particles depositing in a lobe is directly proportional to the lobe's volume. However, for the emphysematous rats, the deposition in the left lobe was lower than 1 and

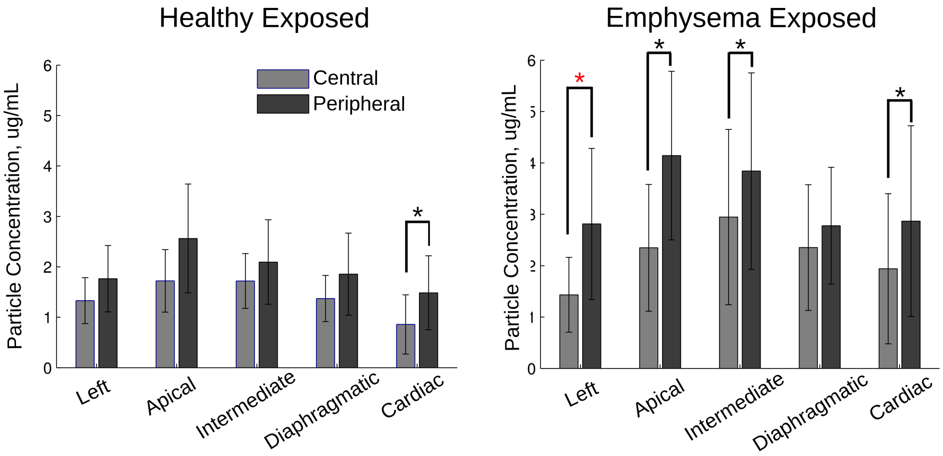

Figure 5.8: Particle concentration in the central and peripheral regions of each of the lobes. Left panel is for the healthy exposed rats and the right panel is the emphysema exposed rats. * denotes statistical significance without correction and * denotes statistical significance with Bonferonni correction of ($p < 0.005$).

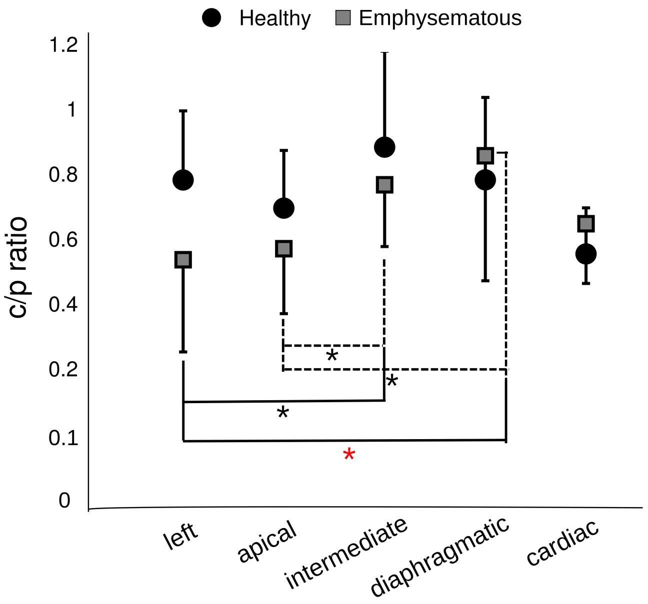

Figure 5.9: The $\frac{c}{p}$ ratio for healthy and emphysematous exposed rats. No significant difference was found between healthy and emphysematous rats.

the apical and intermediate lobes was greater than 1.

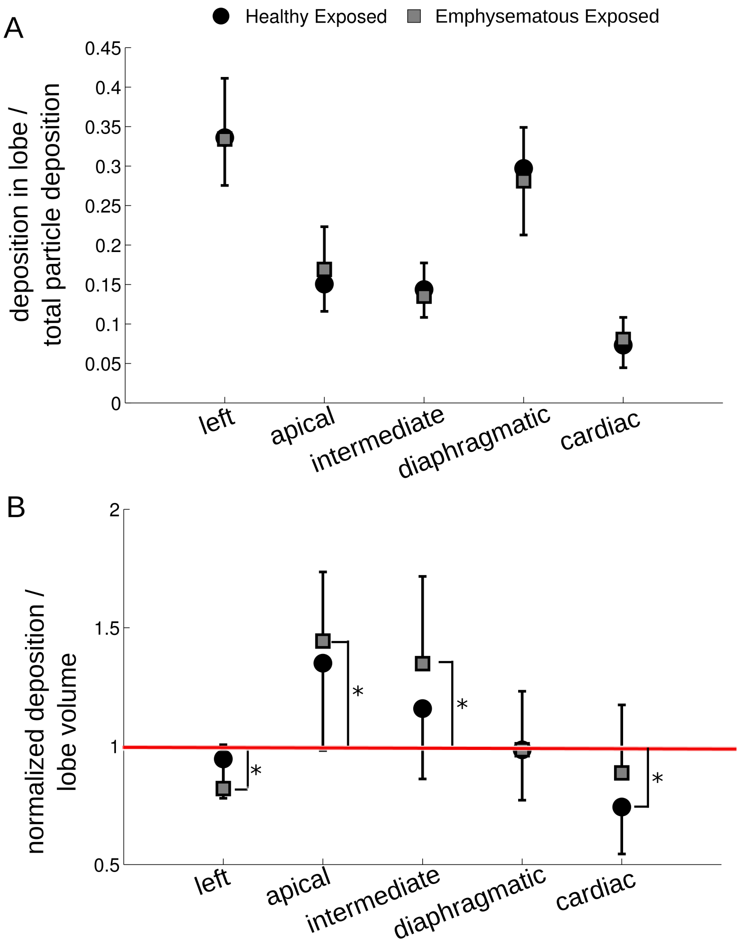

Figure 5.10: Particle deposition in lobe normalized by the total deposition in the lung (panel A) and normalized deposition divided by the lobe volume (panel B). There was no difference between healthy and emphysema rats.

The particle concentration along the trans-axial axis is shown in Figure 5.11. For most cases, the emphysematous lungs varied most from the healthy lungs at either the very base or apex of the lung.

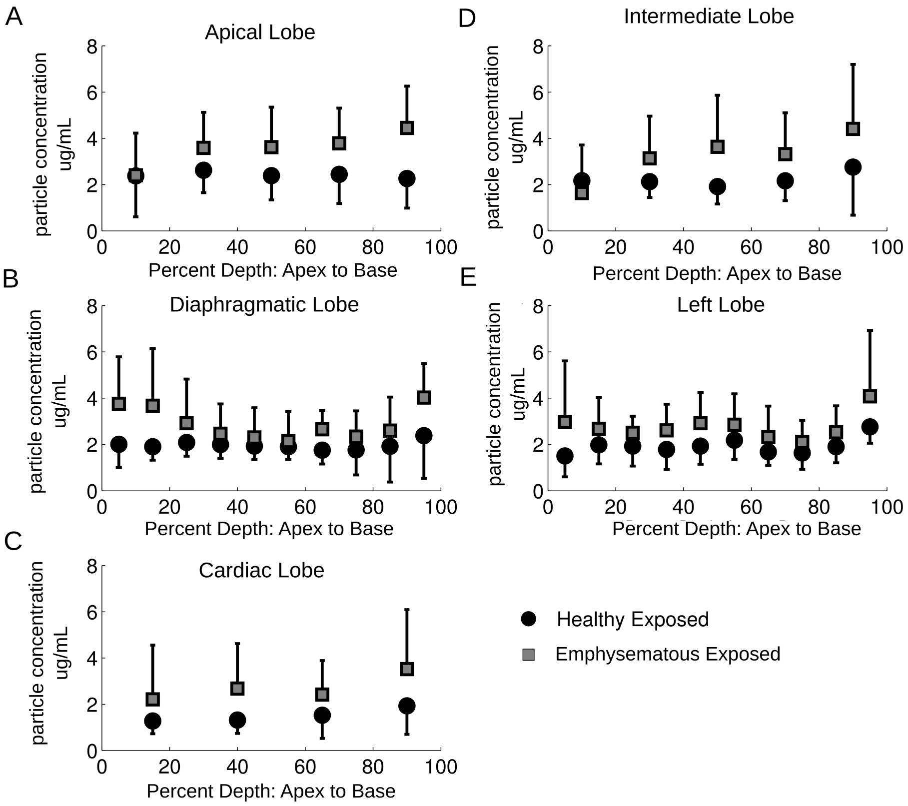

Figure 5.11: Particle deposition at 4 depth levels for healthy and emphysema exposed rats. No statistical significance was found between the healthy and emphysema rats for each lobe. However, at 50 % depth there was a statistical significance between emphysema and healthy rats (p = 0.004) and at 75 % (p = 0.039).

5.4 Discussion

5.4.1 Disease Presence

In this study two independent measures were taken to quantify the presence of emphysema in the elastase treated rats. The linear mean intercept is a measure of the alveolar space and is expected to be larger in the presence of emphysema [20, 26]. Therefore, typically L_M is employed to quantify the degree of emphysema. However, as discussed by Parameswaran et al. [20], L_M is not a reliable measure of heterogeneous emphysema. In the initial stages of emphysema, the disease is heterogeneously distributed in the lung. It has been shown by Borzone et al. [3] that elastase-treated rats only develop a mild case of emphysema. Therefore, as mild cases of emphysema are heterogeneously distributed in the lung, it is assumed that in this case the rat's disease is heterogeneously distributed. Nonetheless, the L_M was measured in 7 healthy and 7 emphysematous rats and compared. While not significant, the L_M was higher in the emphysematous rats compared to the healthy rats, as shown in Figure 5.3. In particular, the L_M was higher in the left, diaphragmatic and cardiac lobes.

In addition to the L_m, the R_2^* was measured in the healthy and emphysema non-exposed rats. As R_2^* is a measure of the heterogeneity of the local MR field inhomogeneities, it is reasonable to assume that an increase in R_2^* is a result in heterogeneity of the tissue within a voxel. On the other hand, RD is a measure of the heterogeneity of R_2^* for the entire lobe. Therefore, as both RD (see Figure 5.5A) and R_2^* (see Figure 5.4A) suggests, the left, diaphragmatic and cardiac lobes all had increased heterogeneity in the magnetic field on both a voxel basis (R_2^*) and on a whole lobe basis (RD). This increase in R_2^* is consistent with a previous study performed by Quintana et al. [21]. The group found that the signal intensity was less in elastase-treated spontaneously breathing rats imaged with a gradient echo sequence compared to healthy rats imaged at the same echo time.

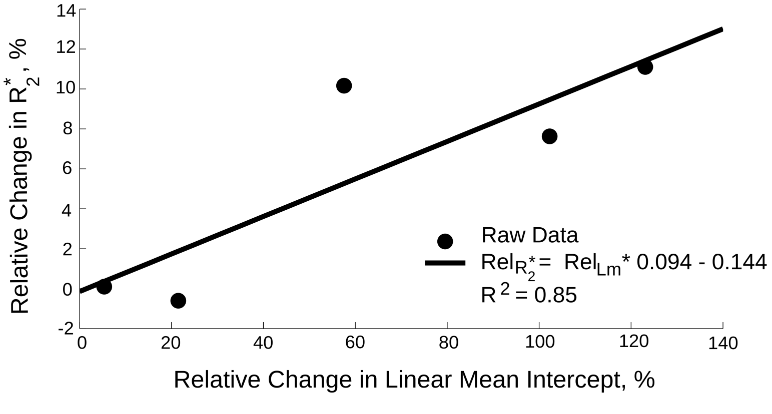

Figure 5.12: Relationship between percent increase in R_2^* and percent increase in linear mean intercept of emphysema rats compared to healthy rats.

The higher values of L_m and R_2^* in the left, diaphragmatic and cardiac lobes suggest that the disease mainly developed in the lobes rather than the intermediate and apical lobes with lower values of L_m and R_2^*. The relationship between the change in R_2^* f and L_m for the emphysematous rats with respect to the healthy rats is shown in Figure 5.12. As the coefficient of determination, R^* indicates, there is a linear relationship between R_2^* and L_m. Therefore, as this data suggests, R_2^* may be employed to determine the level of emphysema presence in the lung.

It is very possible that our method of intertracheal induction of elastase caused the elastase to only go in the left, diaphragmatic and cardiac lobes. The apical and intermediate lobes branch at a larger bifurcation angle than the other three lobes [18], and therefore the elastase may not have spread as readily in these lobes. Additionally, the intermediate lobe is a triple bifurcation and flow is more likely to go to the cardiac and diaphragmatic lobes (see Chapter 5). The relative change in R_2^* in the emphysematous rats compared to the healthy rats along the trans-axial axis is shown in Figure 5.13. As can be seen from Figure 5.13 the emphysema seems to be contained to the base of the three diseased lobes.

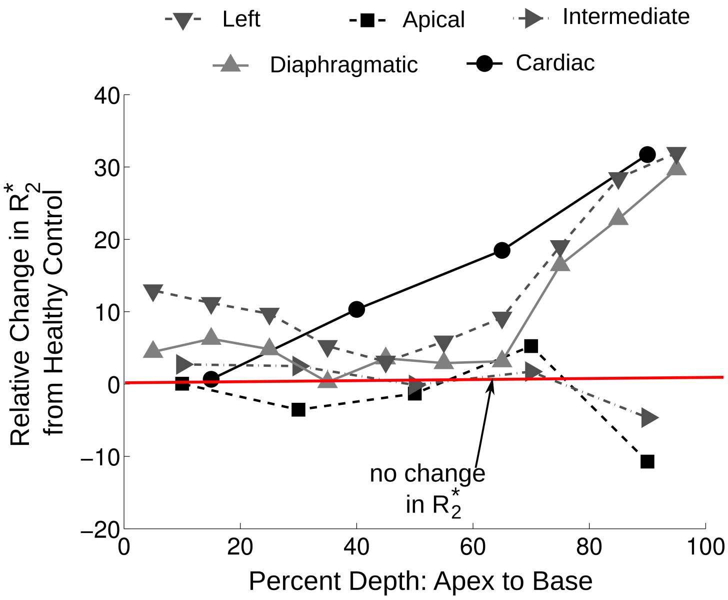

Figure 5.13: Relative change in emphysematous non-exposed rats to healthy non-exposed rats. Cardiac, intermediate and left lobes are the diseased lobes.

5.4.2 Effect of Particles on the MR Signal Decay Rate

Iron oxide particles create local disturbances in the magnetic field and therefore cause an increase in the signal decay rate, R_2^*. As shown in Figure 5.2, there was a statistically significantly higher R_2^* in the emphysematous rat lobes compared to the healthy rat lobes. The emphysematous rats had a $\sim 24\%$ higher R_2^* compared to the healthy rats. It is unlikely that differences in R_2^* were due to the disease alone (i.e. not particles), as the relative change in non-exposed rats was R_2^* was $\sim 5.7\%$ higher in the emphysematous rats compared to the healthy rats, which is much less than the change found in the exposed rats. The relationship of R_2^* between lobes was quite similar between the healthy and diseased rats, as shown Figure 5.2. Both the healthy and emphysematous rats had the highest R_2^* in the apical and intermediate lobes, and the lowest R_2^* in the cardiac lobes.

R_2^* was almost always higher in the peripheral region of the lung compared to the central region (see Table 5.3 and Figure 5.14). Figure 5.14 shows the relationship between the percent change in R_2^* for the exposed rats compared to the non-exposed rats. As can be seen, the emphysematous rats had about 1.61 times greater relative change in R_2^* than the healthy rats.

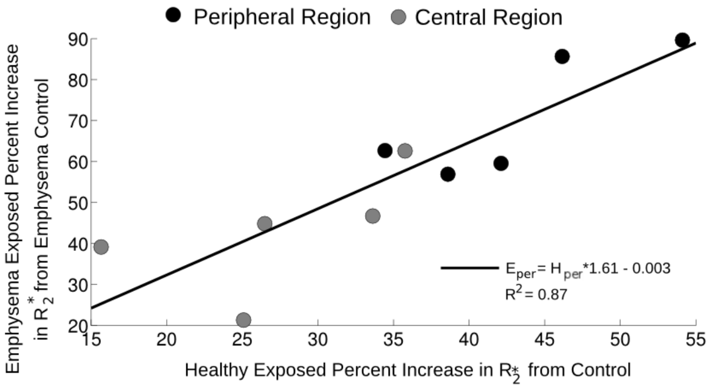

Figure 5.14: Relative change in R_2^* in exposed rats compared to non-exposed rats. The relative change in the emphysema rats was 1.6 times greater than the relative change in healthy rats

It is expected that the elastase-treated rats have areas of low ventilation and gas trapping [7]. As R_2^* is greatly influenced by air bubbles, i.e. air causes a rapid decay in MR signal, it is possible that the higher R_2^* in the emphysematous rats is caused by micro-bubbles. However, this is highly unlikely as the lungs were stored in fixative for at least three months and were degassed under a light vacuum for two weeks prior to imaging [19]. Additionally, bubbles are clearly distinguishable on the MR image, as bubbles create a rapid decay in the signal as and bubbles influence the surrounding voxels. The ROIs were drawn to avoid any bubbles present. As discussed previously, [19] the coefficient of determination, R^2, was determined for each voxel's R_2^* fit and any voxel with a $R^2 < 0.75$ was removed from the analysis. Areas with bubbles did not pass this R^2 criteria.

The relative dispersion, a measure of heterogeneity, was significantly higher (p = 0.032) in the emphysematous rats, compared to the healthy rats (Figure 5.5). Additionally, the RD was highest in the three lobes that contain most of the disease; left, diaphragmatic and cardiac lobes. Not only does emphysema cause a heterogeneous distribution of alveolar space, but it also causes a heterogeneous distribution of tissue compliance [11]. Therefore the higher RD in the emphysematous rats is likely due to both morphophonemic and tissue compliance differences in the lung. Differences in tissue compliance between all areas of the lung may result in the lung expanding and contracting in a non-uniform fashion. Due to this heterogeneity, it is likely that areas of the lung are emptying at different times (see Chapter 6) and this may cause an increase in RD in particle deposition.

5.4.3 Particle Concentration

As particle concentration is directly proportional to R_2^* [19], particle concentration was higher in the emphysematous rats compared to the healthy rats, as shown in Figure 5.7. However this increase in deposition was not statistically significant (p = 0.069). This is likely because of how the particle concentration was calculated. The average R_2^* for each lobe and region for the non-exposed healthy or emphysematous rats was used in equation 5.1. However, as shown in Figure 5.13, the R_2^* varied along axial depth in the emphysematous rats (i.e. most emphysematous tissues seemed to be located at the base of each lobe). Therefore, future analysis should include these changes when calculating the particle concentration.

For three lobes (left, apical and intermediate) the $\frac{c}{p}$ ratio was higher in healthy rats than in the emphysematous rats (see Figure 5.9). This essentially means that there was more central deposition, compared to peripheral deposition in these regions of the healthy lungs compared to the emphysematous lungs. However, $\frac{c}{p}$ remained relatively constant across the 5 healthy lobes. In contrast, the $\frac{c}{p}$ ratio was not constant in the emphysematous lungs (Figure 5.9).

Surprisingly, there was no difference in normalized particle deposition between the healthy and emphysematous rats (see Figure 5.10A). Therefore, even though there was higher particle concentration in the emphysematous lungs, there was no difference in the distribution of particles, at least at the lobar level. Differences in the distribution of particles may be found if normalized deposition was investigated within regions inside a lobe. Certainly, as the RD suggests (see Figure 5.5), there is an increased heterogeneous distribution of particles in the emphysematous lung. Figure 5.10B shows the normalized lobar deposition divided by the lobe volume. While there was no significant difference in the volume normalized deposition, there were differences in comparing these values to 1. A value of 1 would indicate that the particle deposition in a given lobe is directly proportional to its lobe volume. For all healthy lobes, except the cardiac lobe, this was statistically the case. However, in the emphysematous rats volume normalized deposition was less than 1 in the left lung and greater than 1 in the apical and intermediate lobes. Therefore, these data suggest in emphysema the number of particles depositing in a given lobe is not directly proportional to the lobe's volume.

5.4.4 Comparison with Previous Studies

There have been relatively few studies of particle deposition in emphysematous lungs. However, the studies that have been done have generally found particle deposition to be less in emphysematous rodents compared to healthy rodents [5, 24]. In hamsters, Sweeney et al. [24] found less deposition for 0.45 μm diameter particles in spontaneously breathing emphysematous hamsters than in healthy control hamsters. However, it is likely that the hamsters had severe emphysema while the rats in this current study had only mild emphysema. As discussed by Borzone et al. [3], rats that received more elastase than hamsters (rats received 3 doses, 7 days apart, of 55 U / 100 g of body weight and the hamsters had one dose of 55 U / 100 grams of body weight) [3], had a less severe emphysema compared to the hamsters. Emphysema was characterized based on alveolar space enlargement and the pressure/volume curve relationship. These differences, as well as exposure difference between Sweeney et al. [24] may contribute to the different deposition findings. In a different study, Damon et al. [5] found less deposition in emphysematous rats compared to healthy rats. However, these rats were exposed nose only (free breathing) to $2 \pm 1.84\mu m$ MMAD particles. As the rats were able to breathe on their own, there may be differences in deposition due to breathing rates as well as differences due to particle size. As the emphysematous rats tend to breathe at higher tidal volumes and breathing frequencies [6], it is more likely for particles to deposit due to impaction in the nose of the emphysematous rats compared to the healthy rats.

Several studies [10, 14] have looked at the influence of harmful particles in both healthy and emphysematous mice. For example, Inoue et al. [10] concluded that there was no difference in morphological changes between the mice treated with just elastase with the group treated with a combination of elastase and a single dose of diesel exhaust. In a different study Lopes et al. [14] found that elastase treated mice exposed to disease particles for two months had statistically significant higher linear mean intercepts, collagen fibers in the alveolar septa and expression of 8-isoprostane than elastase treated mice exposed to particle-free air. Interestingly, the group [14] also found that there was no differences between healthy mice exposed to disease exhaust or to particle free air. This data suggests that emphysema increases the susceptibility to inhaled harmful particulates when exposed over a long period of time.

In addition to animal and human experiments, in-vitro models [2, 17], empirical models [23] and numerical CFD models [9] have been developed to study particle deposition in healthy and emphysematous lungs. In a replica in-vitro alveolar sac model, Oakes et al. [17] and Berg et al. [2] hypothesized that particle deposition would be less in emphysematous alveolar sacs compared to healthy alveolar sacs. However, even though it is true that particles would have further distance to travel to reach the alveolar wall, it is possible that particles become trapped in the emphysematous regions of the lung and therefore would eventually deposit after several breathing cycles. None of these model were able to simulate the heterogeneous distribution of emphysema in the whole lung and its influence on particle deposition.

5.4.5 Study Limitations and Future Work

This work examined the relative change in particle concentration between the healthy and emphysematous rats. Therefore, the percentage of inhaled particles depositing in the lung was not assessed. Future studies should determine the particle concentration in respect to the amount of particles inhaled. Despite this, particle concentrations between healthy and emphysematous rats was able to be determined as well as differences in lobar, region (central versus peripheral) and along the axial depth.

As shown in Figure 5.13, the emphysematous rats had differences in R_2^* along the apex to base axis. Therefore, when particle concentration is calculated, these differences should be taken into account, especially for the left, diaphragmatic and cardiac lobes. Doing this may change the particle concentration results and show statistical significance between the emphysematous and healthy particle concentrations, as currently the p-value is only marginally significant ($p = 0.069$).

5.4.6 Conclusion

This work is the first to study the differences in particle deposition between healthy and emphysematous rats that were mechanically ventilated to monodisperse particles with MMAD of 1.22 μm. As the rats were mechanically ventilated, deposition changes between emphysematous and healthy rats was only due to morphological or tissue compliance changes, not breathing parameters. As evident by R_2^* and L_M in the control rats, the left diaphragmatic and cardiac lobes contained most of the disease with the disease being localized at the bottom of the lung. In both the healthy and emphysematous rats, the apical and intermediate lobes had higher particles concentrations compared to the other three lobes. There was on average $\sim 68\%$ higher deposition in the emphysematous rats compared to the healthy rats ($p = 0.069$). The $\frac{c}{p}$ ratio in the healthy rats was on average 0.74 ± 0.12 in the healthy lobes and was 0.67 ± 0.14 in the emphysematous rats. However, unlike the healthy rats, there was statistical differences in the $\frac{c}{p}$ ratio between lobes in the emphysematous rats.

5.5 Bibliography

[1] American Lung Association, 2009.

[2] Berg, E. J., and Robinson, R. J. Stereoscopic particle image velocimetry analysis of healthy and emphysemic alveolar sac models. *Journal of biomechanical engineering 133*, 6 (June 2011), 061004.

[3] Borzone, G., Liberona, L., Olmos, P., Sáez, C., Meneses, M., Reyes, T., Moreno, R., and Lisboa, C. Rat and hamster species differences in susceptibility to elastase-induced pulmonary emphysema relate to differences in elastase inhibitory capacity. *American journal of physiology. Regulatory, integrative and comparative physiology 293*, 3 (Sept. 2007), R1342–9.

[4] Brand, P., Schulte, M., Wencker, M., Herpich, C. H., Klein, G., Hanna, K., and Meyer, T. Lung deposition of inhaled alpha1-proteinase inhibitor in cystic fibrosis and alpha1-antitrypsin deficiency. *The European Respiratory Journal 34*, 2 (Aug. 2009), 354–60.

[5] Damon, E. G., Mokler, B. V., and Jones, R. K. Influence of elastase-induced emphysema and the inhalation of an irritant aerosol on deposition and retention of an inhaled insoluble aerosol in Fischer-344 rats. *Toxicology and applied pharmacology 67*, 3 (Mar. 1983), 322–30.

[6] Emami, K., Cadman, R. V., Woodburn, J. M., Fischer, M. C., Kadlecek, S. J., Zhu, J., Pickup, S., Guyer, R. a., Law, M., Vahdat, V., Friscia, M. E., Ishii, M., Yu, J., Gefter, W. B., Shrager, J. B., and Rizi, R. R. Early changes of lung function and structure in an elastase model of emphysema–a hyperpolarized 3He MRI study. *Journal of applied physiology (Bethesda, Md. : 1985) 104*, 3 (Mar. 2008), 773–786.

[7] Emami, K., Chia, E., Kadlecek, S., Macduffie-Woodburn, J. P., Zhu, J., Pickup, S., Blum, A., Ishii, M., and Rizi, R. R. Regional correlation of emphysematous changes in lung function and structure: a comparison between pulmonary function testing and hyperpolarized MRI metrics. *Journal of Applied Physiology 110*, 1 (Jan. 2011), 225–35.

[8] Hantos, Z., Adamicza, A., Jánosi, T. Z., Szabari, M. V., Tolnai, J., and Suki, B. Lung volumes and respiratory mechanics in elastase-induced emphysema in mice. *Journal of Applied Physiology 105*, 6 (Dec. 2008), 1864–72.

[9] Harding, E. M. *Particle Deposition in Replica Healthy and Emphysematous Using Computational Fluid Dynamics*. PhD thesis, 2010.

[10] Inoue, K.-i., Koike, E., and Takano, H. Comprehensive analysis of elastase-induced pulmonary emphysema in mice: effects of ambient existing particulate matters. *International immunopharmacology 10*, 11 (Nov. 2010), 1380–9.

[11] Ito, S., Ingenito, E. P., Arold, S. P., Parameswaran, H., Tgavalekos, N. T., Lutchen, K. R., and Suki, B. Tissue heterogeneity in the mouse lung: effects of elastase treatment. *Journal of applied physiology (Bethesda, Md. : 1985) 97*, 1 (July 2004), 204–12.

[12] Johanson, W. G., and Pierce, a. K. Lung structure and function with age in normal rats and rats with papain emphysema. *The Journal of Clinical Investigation 52*, 11 (Nov. 1973), 2921–7.

[13] Kohlaufl, M., Brand, P., Scheuch, G., Meyer, T., Schulz, H., Haussinger, K., and Heyder, J. Aerosol Morphometry and Aerosol Bolus Dispersion in Emphysema and Lung Fibrosis. *Journal of Aerosol Medicine 13*, 2 (2000), 117–124.

[14] Lopes, F. D. T. Q. S., Pinto, T. S., Arantes-Costa, F. M., Moriya, H. T., Biselli, P. J. C., Ferraz, L. F. S., Lichtenfels, A. J., Saldiva, P. H., Mauad, T., and Martins, M. a. Exposure to ambient levels of particles emitted by traffic worsens emphysema in mice. *Environmental research 109*, 5 (July 2009), 544–51.

[15] March, T. H., Green, F. H. Y., Hahn, F. F., and Nikula, K. J. Animal models of emphysema and their relevance to studies of particle induced disease. *Inhalation toxicology 12*, February (2000), 155–187.

[16] McDonough, J. E., Yuan, R., Suzuki, M., Seyednejad, N., Elliot, W. M.,Sanchez, P. G.,Wright, A. C., Gefter, W., Litzky, L., Coxson, H. O., Par, P. D., Sin, D. D., Pierce, R. A., Woods,

J. C., Mcwilliams, A. M., Mayo, J. R. Lam, S. C., Cooper, J. D., Hogg, J C. Small airway obstruction and emphysema in chronic obstructive pulmonary disease. *The New England Journal of Medicine 365*, 2011 1567–1575.

[17] Oakes, J. M., Day, S., Weinstein, S. J., and Robinson, R. J. Flow field analysis in expanding healthy and emphysematous alveolar models using particle image velocimetry. *Journal of Biomechanical Engineering 132*, 2 (Feb. 2010), 021008.

[18] Oakes, J. M., Scadeng, M., Breen, E. C., Marsden, A. L., and Darquenne, C. Rat airway morhometry measured from in-situ mri-based geometric models. *Journal of Applied Physiology 112*, 12 (Mar. 2012), 1921–1931.

[19] Oakes, J. M., Scadeng, M., Breen, E. C., Prisk, G. K., and Darquenne, C. Regional Distribution of Aerosol Deposition in Rat Lungs Using Magnetic Resonance Imaging. *Annals of Biomedical Engineering 41* (Jan. 2013), 967–978.

[20] Parameswaran, H., Majumdar, A., Ito, S., Alencar, A. M., and Suki, B. Quantitative characterization of airspace enlargement in emphysema. *Journal of applied physiology 100*, 1 (Jan. 2006), 186–93.

[21] Quintana, H. K., Cannet, C., Zurbruegg, S., Blé, F.-X., Fozard, J. R., Page, C. P., and Beckmann, N. Proton MRI as a noninvasive tool to assess elastase-induced lung damage in spontaneously breathing rats. *Magnetic resonance in medicine : official journal of the Society of Magnetic Resonance in Medicine / Society of Magnetic Resonance in Medicine 56*, 6 (Dec. 2006), 1242–50.

[22] Rosenthal, F. S. Aerosol deposition and dispersion characterize lung injury in a canine model of emphysema. *Journal of applied physiology 78* (1995), 1585–1595.

[23] Sturm, R., and Hofmann, W. Stochastic simulation of alveolar particle deposition in lungs affected by different types of emphysema. *Journal of Aerosol Medicine 17*, 4 (Jan. 2004), 357–72.

[24] Sweeney, T. D., Brain, J. D., Leavitt, S. a., and Godleski, J. J. Emphysema alters the deposition pattern of inhaled particles in hamsters. *The American Journal of Pathology 128*, 1 (July 1987), 19–28.

[25] Thurlbeck, W. M., and Muller, N. L. Emphysema: Definition, Imaging, and Quantification. *American Journal of Roentgenology 163* (1994), 1017–1025.

[26] Tolnai, J., Szabari, M. V., Albu, G., Maár, B. a., Parameswaran, H., Bartolák-Suki, E., Suki, B., and Hantos, Z. Functional and morphological assessment of early impairment of airway function in a rat model of emphysema. *Journal of Applied Physiology 112*, 11 (June 2012), 1932–9.

[27] Zarogoulidis, P., Chatzaki, E., Porpodis, K., Domvri, K., Hohenforst-Schmidt, W., Goldberg, E., Karamanos, N., and Zarogoulidis, K. Inhaled chemotherapy in lung cancer: future concept of nanomedicine. *International Journal of Nanomedicine 7* (2012), 1551–1572.

[28] Zarogoulidis, P., Papanas, N., Kouliatsis, G., Spyratos, D., Zarogoulidis, K., and Maltezos, E. Inhaled insulin too soon to be forgotten. *Journal of Aerosol Medicine and Pulmonary Drug Delivery 24*, 5 (2011), 213–223.

Chapter 6

In-Silico Modeling of Airflow and Particle Deposition

6.1 Introduction

Simulations of airflow in the lung are useful for augmenting experimental knowledge and understanding physiology only if they can accurately model in vivo respiratory conditions. Computational fluid dynamics (CFD) can complement experimental efforts by providing information that cannot be easily measured experimentally, or motivating new targeted experiments. To be physiologically meaningful, these in-silico simulations must accurately model respiratory anatomy and physiology. Due to the vast range of length scales in the lung, complex geometry and pulmonary tissue mechanics, it is currently impossible to model the lung in full because of the extensive computational costs and lack of data. Therefore, multi-scale methods must be employed that incorporate realistic 3D CFD geometry of the upper structures coupled to lower-dimensional models that represent the rest of the respiratory system.

Currently there are no CFD models that study how emphysema alters particle deposition in the conducting airways of the lung. Deposition in emphysematous lungs has been previously studied in human patients [7], animal models [58], in vitro models [44], and empirical models [57], however several questions remain unanswered. For example, Sweeney et al. [58] found a decrease in particle deposition in a emphysematous hamster model compared to healthy hamsters, while Brand et al. [7] found no changes in deposition in emphysematous human patients compared to healthy patients. Empirical [54, 57] and experimental in-vitro models [44] have supported the findings of decreased deposition in emphysema. In human studies, it has been found that deposition increased 50 percent in COPD patients compared to healthy subjects [5], however the authors hypothesized that this was due to increased airway resistance in bronchitis, rather than the changes that occur in emphysema.

While there have been many numerical studies that have investigated airflow (e.g. [3, 29, 41]) and particle deposition (e.g. [11, 36, 43, 65, 68]) and distribution [17] in the lung, relatively few studies have incorporated patient or animal specific geometry and breathing parameters. Fortunately, recent advances in medical imaging have made it possible to create 3D airway geometries of the upper airways [19] and tracheobronchial regions of the lung [23, 46]. As shown by several groups, the airflow [18, 20, 40, 64, 67] and particle deposition [12, 28, 43] in the lung is highly dependent on the geometry. Boundary conditions that describe the upstream and downstream mechanics outside of the 3D domain must be defined on the inlets and outlets for all CFD simulations. Traditionally, constant pressure [18] or flow rate [10, 29] boundary conditions have been applied at the mouth or trachea. Additionally, constant pressure [14, 18, 29, 56] or flow rate [10, 40] boundary conditions are typically implemented at the distal airway outlets. However, as the flow structures in the lung change in time, CFD simulations should model the unsteady nature of breathing, to determine airflow [37] and particle [12] deposition patterns in the lung. Consequently, appropriate boundary conditions must be devised.

In recent years, multi-scale modeling techniques have been developed to study the cardiovascular system (e.g. [27, 33, 35, 39, 60, 62, 63]). However, not until recently have these multi-scale methods been applied to the respiratory system [3, 30, 34, 37]. Typically, a multi-scale numerical model includes a 3D CFD description of the large airways and a 1D [37] or 0D [3, 34] lower-dimensional model that represents the smaller airways and peripheral tissue. With such multi-scale models, it is possible to perform unsteady simulations, where both the airflow and pressure may accurately be solved for [30]. However, if proper care is not taken to accurately model lung physiology, the flow and pressure will not be accurately captured. For example, imposing constant flow or pressure boundary conditions may result in the flow and pressure being in phase and / or unrealistically low mean pressure values. Employing impedance distal boundary conditions on a human 3D lung CFD model, Comerford et al. [13] demonstrated that the downstream impedance significantly influences the overall pressure field, but has little effect on the flow velocity. Additionally, while several groups [3, 30, 34, 37] have made significant advances in multi-scale respiratory modeling, none of these works directly parameterized their lower dimensional models from animal or patient in-vivo specific data.

Despite being used extensively for toxicology [31, 66] and therapeutic studies [1] there have been relatively few airflow [14, 40, 53] and particle deposition [32] numerical simulations in the rat lung. In recent work, Minard et al. [40] showed good agreement between airflow in the conducting airways from both CFD and MRI flow measurements under steady state conditions. Unsteady CFD simulations were performed by Schroeter et al. [53] and Jiang et al. [32] including only the rat's nose. Some groups have developed empirical models to predict particle deposition in the rat [2, 51], however there currently are no 3D simulations of particle transport and deposition in rat airways.

The goal of the current work was to develop a multi-scale respiratory model to simulate airflow and particle deposition to replicate animal aerosol exposure experiments [47] in both healthy and emphysematous rats. In the first section of this paper, the global respiratory resistance and compliance were inferred by solving a well-known two-component lumped parameter model (0D global model) [4] from aerodynamics measurements taken during the exposure experiments. The multi-scale airflow simulations were performed by coupling MRI-derived 3D rat conducting airways [46] to the lower dimensional 0D global model in the second section of the manuscript. Finally, once the airflow was solved for, particles were tracked in the 3D domain during inspiration and their deposition sites within the 3D model and delivery distribution of particles into the five rat lobes were determined. Simulations were performed for a healthy rat lung, a lung with homogeneously distributed emphysema, and five different cases of heterogeneous emphysema. Furthermore, the influence of particle size and rat position were investigated. This study is the first to (1) solve a multi-scale airflow model parameterized directly from in-vivo experimental data, (2) solve for airflow and particle deposition in the rat airways under unsteady breathing conditions, and (3) to predict the influence of emphysema on deposition and distribution of particles in the upper airways of the lung.

6.2 Materials and Methods

The computational models developed herein were based on breathing parameters from aerosol exposure experiments previously performed on rats [45, 47]. The global respiratory values, i.e. resistance and compliance, were estimated from airway pressure and the breathing parameters measured during the experiments. Based on this 0D global respiratory model, a multi-scale 3D-0D airflow CFD scheme was then devised to simulate the experiments and study other configurations. Particle deposition was then simulated throughout inspiration, matching as closely as possible the experimental conditions.

The rat aerosol exposure protocol is described in detail elsewhere. [45, 47] Five healthy and five elastase induced emphysematous [45] anesthetized rats (body weight of 409 ± 25.6 grams and 432 ± 46.1 grams, respectively) were mechanically ventilated to particle-laden air. The experimental setup is shown in Figure 6.1A. During inhalation, the piston pump pushed 2.2 mL of particle-laden air (particle concentration of approximately $\frac{5000}{mL_{air}}$ [47]) into the lung at a breathing frequency (BF) of 80 $\frac{breaths}{min}$. The particles had a geometric diameter of 0.95 μm, with a coefficient of variance of < 0.5 %, and a density of 1.35 $\frac{g}{cm^3}$ [47]. At the end of inhalation, the pump switched from the rat to the aerosol bag and drew fresh particle-laden air into the pump. At this time, the rat passively exhaled through a tube into a jar filled with water. This tube was immersed into water at a depth of 1 cm, subjecting the rat to a constant end expiratory pressure (P_{Peep}) of 1 cmH_2O. The time varying pressure was measured with a catheter throughout the breathing cycle near the rat's trachea (see Figure 6.1A).

6.2.1 Estimation of Global Respiratory Parameters from Experimental Data

Each rat's global respiratory parameters were estimated based on the available experimental data. The pressure at the trachea (P(t)), total inhaled volume, breathing frequency (BF) and the inhalation time were either measured or imposed by the pump. The time varying flow rate and volume were not measured during the experiments. Therefore, a two component lumped parameter model (linear compartment model) was chosen [4] to model the overall resistance (R) and compliance (C) of the respiratory system:

$$R\frac{dV_{total}(t)}{dt} + \frac{V_{total}(t)}{C} = P(t) - P_0, \tag{6.1}$$

where $V_{total}(t)$ is the total volume of air in the lungs, $\frac{dV_{total}(t)}{dt}$ is the flow rate, P(t) is the pressure at the trachea, and P_0 is the pleural pressure. As the rats were ventilated at a breathing frequency and tidal volume representative of normal breathing, it was appropriate to assume linear resistance and compliance [22]. At the end of expiration, the flow rate was zero and the volume and pressure satisfied $V_{min} = (P_{peep} - P_0)C$, and therefore by defining the tidal volume (inhaled volume) as $V = V_{total}(t) - V_{min}$, the global respiratory model can also be written as:

$$R\frac{dV}{dt} + \frac{V(t)}{C} = P(t) - P_{peep} \tag{6.2}$$

where P_{peep} is the constant end expiratory pressure, 1 cm H_2O. The equation was solved with an implicit Euler time stepping scheme. Pressure was imposed after filtering out the high frequency experimental noise. The pressure curves for representative healthy and emphysematous rats are shown in Figure 6.2A. As the R and C parameters were unknown, equation 6.2 was solved using a large range of R and C values. A unique R and C pair was found for each rat satisfying the following constraints from the experimental data: a) the maximum volume was the one imposed by the pump (i.e. 2.2 mL) and b) inspiration ended as set by the pump (i.e. time of maximum volume was $\frac{1}{2BF}$). It has previously been shown that respiratory resistance increases during exhalation [50], therefore the resistance during exhalation was set to 1.5 times the resistance during inhalation.

Once the R and C parameters were found for each rat, the volume and flow rate throughout the full breathing cycle were numerically calculated by solving equation 6.2. The average and standard deviation between rats in each category were calculated for the maximum pressure, resistance, compliance, maximum flow rate during inhalation and maximum flow rate during exhalation. An unpaired two-tailed t-test was used to determine if the global respiratory parameters were significantly different between the healthy and emphysema rats.

6.2.2 Coupled Multi-scale Simulation and Analysis

The 3D geometric model was previously created from MR images [46] with the open source software, Simvascular (simtk.org) [52] and is shown in Figure 6.1B. The airway geometry did not include the upper respiratory passages as they were bypassed during the exposure experiments (animals were tracheotomized). Therefore, the geometry started at the trachea and ended at the five distal airways, each corresponding to one of the five rat lobes. As the conducting airways were not influenced by emphysema, as confirmed by measuring the airway diameter from the MR images, the same geometric model was used for the healthy and emphysema simulations.

A custom stabilized finite element Navier-Stokes solver was employed to simulate airflow in the 3D model, assuming rigid walls and Newtonian flow with a density of $1.2 * 10^{-6} \frac{g}{mm^3}$ and viscosity of $1.81 * 10^{-5} \frac{g}{mm-s}$. A custom linear solver with resistance based preconditioning and a combination of GMRES and conjugate gradient methods was used for the linear system of equations in the flow solver [25]. Anisotropic mesh adaptation based on the Hessian of the velocity field was performed for the airway model, to ensure mesh convergence of the solution

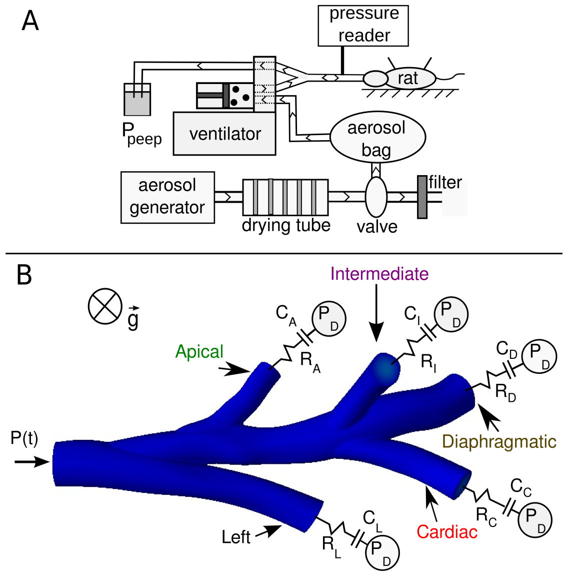

Figure 6.1: Panel A: Schematic of the aerosol exposure system used for the rat experiments. [47] The mechanically driven piston pump delivered particle-laden air to the rats during inspiration. Rats passively exhaled to a positive end expiratory pressure (P_{Peep}) container during expiration. Panel B: Illustration of the 3D rat CFD airway geometry [46] connected to Neumann boundary conditions. Time varying pressure was imposed at the trachea and RC models were connected to the distal airways.

[42]. Mesh independence of the solution was determined by computing the root mean squared error of the flow rate at the trachea face. For each 3D simulation a time step of 10^{-4} seconds was employed, with 8 nonlinear iterations per time step. Simulations were run for 3 respiratory cycles to insure convergence to a periodic solution.

The 3D Navier-Stokes domain was coupled to the pressure (at the trachea face) and the 0D model (at the distal faces) through an implicit two-way coupling algorithm with Neumann boundary conditions [27] (i.e. at each 3D nonlinear iteration flow rate was passed to the 0D model and pressure was passed back to the 3D model). A time step of 10^{-3} seconds was used to solve the 0D model at each 3D nonlinear iteration. The pressure applied at the trachea face was the same experimental pressure from which the global parameters were estimated (see Figure

6.2A). To prevent numerical divergence, backflow stabilization [26] was employed at the trachea and distal faces. The 0D models represented the respiratory networks not included in the 3D model (i.e. downstream airways and tissue). With this type of multi-scale coupling, the dynamics of the entire respiratory system can be modeled in a coupled fashion. The distal 0D models were the two-component lumped parameter models described by Eq. 6.2. While there have been a few recent studies that measure ventilation in rat lungs [16, 24], none of these have measured the ventilation distribution to each lobe. However, Raabe et al. [49] measured the lobar distribution of 0.52 μm particles in spontaneously breathing rat lungs and found the distribution of deposited particles to be mainly proportional to lung volume. Particles of this size have minimal intrinsic properties and consequently they closely trace the convective flow in the lung. Therefore, for each lobe, the parameters $R_{distal,i}$ and $C_{distal,i}$ were computed assuming that the flow distribution to each lobe was proportional to its volume:

$$C_{distal,i} = \alpha_i C \tag{6.3}$$

$$R_{distal,i} = \frac{R}{\alpha_i} \tag{6.4}$$

where α_i is the volume of each lobe, divided by the total lobe volume [46].

One healthy and one emphysema rat were chosen for the simulation. Their global R and C values are given in Table 6.1 and their pressure curves are shown in Figure 6.2. Six cases of emphysema were simulated, homogeneously distributed emphysema and five cases representing heterogeneous emphysema, assuming that the emphysema was contained in only one lobe. In these heterogeneous emphysema cases the emphysema pressure (see Figure 6.2) was applied to the trachea and the healthy resistance values $R_{distal,i}$ were applied to each distal face. The healthy resistance values were used because there was no difference in emphysema and healthy resistances (see Results). The healthy compliance values $C_{distal,i}$ were applied to four of the distal faces. The compliance at the remaining face $C_{distal,i}$ was defined such that the sum of all other $C_{distal,i}$ was equal to the total emphysema compliance. With this definition, 4 lobes would be considered healthy and 1 lobe would be considered diseased. Each of the five heterogeneous emphysema simulations represented a different diseased lobe. For all simulations, the $R_{distal,i}$ during exhalation was 1.5 times greater than the $R_{distal,i}$ during inhalation.

Airflow postprocessing of the results and particle tracking were based on the last respiratory cycle. Airway resistance of the 3D model was calculated by dividing the pressure drop at maximum flow rate ($P_{trachea,\text{ max. inspiration}}$ - $P_{distal,\text{ max. inspiration}}$, $P_{distal,\text{ max. expiration}}$ - $P_{trachea,\text{ max. expiration}}$, P_{distal} being the most extreme pressure among the distal airways compared to the trachea pressure) in the 3D model by the flow rate at the trachea ($Q_{\text{max. inspiration}}$, $Q_{\text{max. expiration}}$). Lobar distribution of flow was determined by normalizing the total volume of air delivered to each lobe by the total inhaled volume.

6.2.3 Lagrangian Particle Tracking

Once the airflow simulations were completed, rigid spherical particles were tracked in the 3D model by solving the Maxey-Riley equation [38]. For small particles the Faxen correction and Basset/Boussinesq memory terms may be neglected [38]. Therefore, the Maxey-Riley equation reduces to

$$\left(\rho_p + \frac{1}{2}\rho_f\right)\frac{d\vec{v}(\vec{x}(t))}{dt} = (\rho_p - \rho_f)\vec{g} + \frac{3}{2}\rho_f\frac{D\vec{u}(\vec{x},t)}{Dt} - \frac{9}{2}\frac{\mu}{a^2}(\vec{v}(\vec{x}(t)) - \vec{u}(\vec{x},t)) \ , \quad (6.5)$$

where $\vec{v}$ is the particle velocity, a is the particle radius, μ is the viscosity of air, ρ_p is the particle density, ρ_f is the fluid density, $\vec{u}$ is the flow velocity, and $\vec{x}$ is the position of the particle. The derivative $d/dt = \partial/\partial t + v \cdot \nabla$ is evaluated along the particle path whereas the derivative $D/Dt = \partial/\partial t + u \cdot \nabla$ is evaluated following a fluid element. The aerosol particles were assumed to be inert and monodisperse with a diameter of 0.95 μm and density of 1.35 g cm^{-3}, to match the exposure experiment [47]. Equation (6.5) was solved analytically for $\vec{v}(x_j(t_i))$, the velocity of the particle j at arbitrary time t_i as a function of the other variables (namely $\vec{u}(t_i)$ as obtained from interpolation and $\frac{D\vec{u}}{Dt}(t_i)$ as obtained by linear interpolation of the velocity field data and second order accurate central difference formula for the spatial and temporal derivatives). Once the velocity of the particle at time t_i was obtained, the position at time t_{i+1} was updated. This last time step was performed by employing an explicit Euler discretization scheme with a time step ($dt = t_{i+1} - t_i$) of 10^{-5} sec [9, 55]. Flow velocity, $\vec{u}$, was found for each particle position using linear space-time interpolation from the velocity field mesh. The gravitational vector, $\vec{g}$, was positioned to represent a rat in the supine position, similar to that of the experiments [47].

Particle seed locations were uniformly defined over the trachea face. As the particle deposition in the model is highly dependent on their starting location [36], the number of particles released was proportional to the local flow velocity. With this definition, more particles were released at the center of the model and at times of high flow velocity. The particles were seeded at the inlet throughout inhalation. Once the particles came in contact with the 3D wall boundary they were assumed to be deposited. Particle distribution to each lobe was determined by counting the number of particles exiting from each distal face. To ensure there was no other dependence on the particle starting location, the spatial density of the particles was increased until there was no change in deposition or distribution of particles. The number of particles deposited, suspended in the 3D domain, and delivered to each lobe was summed at the end of inhalation.

In addition, massless particles were tracked in the 3D velocity field by solving $\frac{d\vec{x}}{dt} = \vec{u}(\vec{x}, t)$. A forth order Runge-Kutta time stepping scheme was employed to track the particle's position over time. Pathlines were created by tracking the massless particles in the 3D domain.

6.3 Results

6.3.1 Global 0D Parameters

The maximum pressure measured at the trachea was lower ($p = 0.012$) in the emphysematous rats compared to the healthy rats (Table 6.1 and Figure 6.2A). While only marginally significant ($p = 0.085$), the compliances in the emphysema rats tended to be higher than in the healthy rats. The respiratory resistances were not significantly different ($p = 0.53$). As expected, the inhalation flow rates and volumes were the same between all rats, as this was controlled by the ventilator

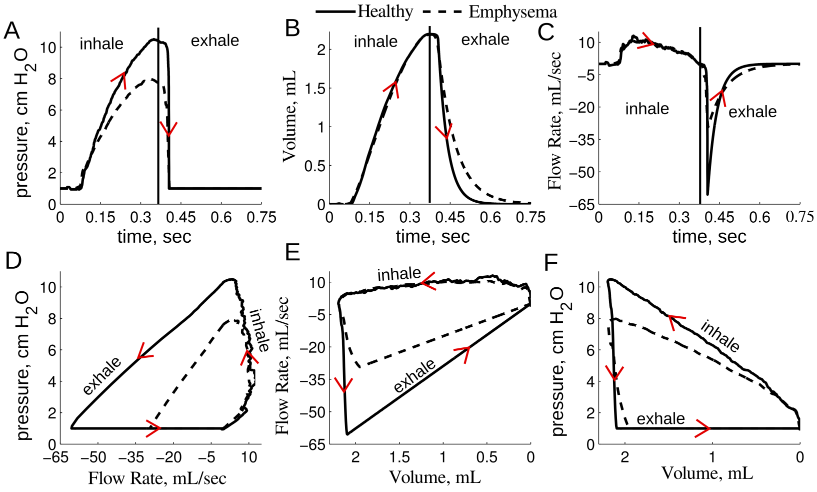

Figure 6.2: Global 0D model solution for one healthy and emphysematous representative rat. Panel A: Experimental pressure tracing used to solve Eq. 6.2 and applied to the trachea face for the multi-scale CFD simulations. Panels B and C: The 0D volume and flow rate solution. Panels D, E and F: The pressure and flow rate loop, flow rate and volume loop and pressure volume loops. Arrows show the direction of the breathing cycle, beginning with inspiration.

pump and the same settings were used for all experiments. The maximum exhalation flow rate tended to be larger in the healthy rats, than in the emphysematous rats (see Table 6.1), however there was no statistical significance ($p = 0.4$) between the groups. As shown in Figure 6.2, the decay rate of the expiration volume was less for the emphysema rats. The pressure versus flow curve and the flow versus volume curve were more restrictive for the emphysema rat, compared to the healthy rat (Figure 6.2D and E). The pressure peaked slightly before the volume in both groups, as shown in Figure 6.2A, B and F.

6.3.2 Multi-Scale CFD Simulations

The finite element mesh of the 0D-3D CFD simulation was adapted until there was less than 2 % difference in the inlet flow rate between successive adaptation steps. The final mesh resulted in $\sim 3.5 * 10^4$ elements. Figure 6.3 shows the flow rate and pressure for the healthy rat (Figure 6.3A and C) and the homoge-

Table 6.1: Global 0D model parameters. Simulation model parameters were used for the determination of the 0D distal parameters according to equations 6.3 and 6.4. Average values were between all healthy and emphysema rats. Values are labeled based on whether they were measured during the experiment (black), estimated from solving Eq. 6.2 (bold), or predicted from model (gray)

		Maximum Pressure cm H_2O	Inhale Resistance, R_{in} $\frac{cmH_2O-s}{cm^3}$	Exhale Resistance R_{ex} $\frac{cmH_2O-s}{cm^3}$	Compliance $\frac{cm^3}{cmH_2O}$	Maximum Inhale Flow $\frac{mL}{sec}$	Maximum Exhale Flow $\frac{ml}{sec}$
healthy	Average For All Rats	10.60 ± 1.19	**0.22 ± 0.12**	0.33 ± 0.18	**0.25 ± 0.04**	**11.3 ± 1.39**	-31.5 ± 19.23
	Representative Case	10.50	**0.098**	0.147	**0.236**	**12.63**	-55.61
Emphysematic	Average For All Rats	7.90 ± 1.43	**0.18 ± 0.05**	0.27 ± 0.08	**0.37 ± 0.14**	**11.2 ± 1.41**	-22.8± 8.41
	Representative Case	8.00	**0.135**	0.167	**0.330**	**10.47**	-29.85

nous emphysema rat (Figure 6.3B and D). In both cases the flow rate measured at the trachea was similar to the flow rate found with the global 0D model, except at peak expiration. At this time, the flow rate at the trachea was slightly less than the global 0D prediction. This decrease was caused by the pressure drop between the trachea and the distal airways (Figure 6.3C and D) and the resulting resistance in the 3D airways. Indeed, the predicted pressure drop to each lobe, as shown in Table 6.2, was over 30 times greater during maximum exhalation than during maximum inhalation for the healthy rat. The same trend was found for the homogeneous emphysema case, as the pressure drop was very small for both.

Figures 6.3E and F show the resulting flow rates for the apical heterogeneous emphysema case. The increased compliance in the apical lobe, due to the disease localization, caused the lobe to fill and empty more slowly than in the healthy lobes. Additionally, as shown in Figure 6.3F, the time for the flow to change from inspiration to expiration was the same for all the healthy lobes. However the apical flow changed direction 0.014 seconds after the healthy lobes. Therefore during this short time, air was both exiting and entering from the lobes into the 3D model. Similar behavior was observed for the other four heterogeneous emphysema cases.

As expected, the airflow delivery to each lobe for the healthy and homoge-

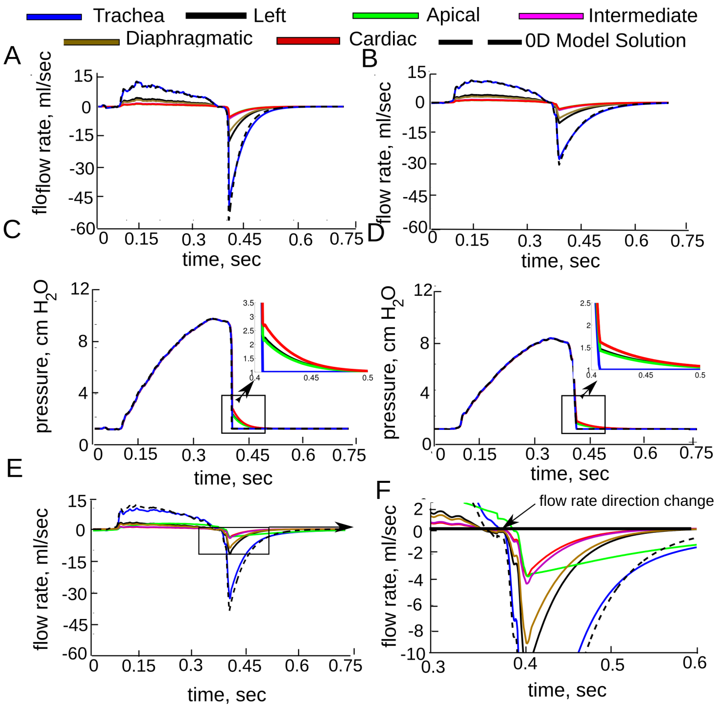

Figure 6.3: Computed flow rate and average pressure at each face for healthy (panels A and C), homogeneous emphysema (panels B and D) and heterogeneous emphysema (apical lobe) (panels E and F). The simulated flow rate at the trachea was similar to the 0D model solution, except during maximum exhalation where the 3D pressure drop was the greatest (shown in panels C and D). Panel F shows the delay in the flow direction change and slower emptying in the diseased lobe.

neous emphysema cases was the same as the applied flow distribution (Table 6.2). In each of the heterogeneous emphysema cases flow increased in the lobe that contained the disease and decreased in the healthy lobes. This resulted in a higher pressure drop for the diseased lobe and a lower pressure drop for the healthy lobes.

Flow Profiles in the 3D Model

Velocity profiles were plotted i) at the trachea, ii) at the first main bifurcation and iii) at the triple bifurcation (Figure 6.4) at six time points in the respiratory cycle. Figure 6.5 shows the flow profiles for multiple locations in the 3D model at

Table 6.2: Airflow Delivery to Each Lobe Normalized by the Inhaled Volume, %. Multi-scale CFD results for each of the seven simulations preformed.

	Left	Apical	Intermediate	Diaphragmatic	Cardiac
Alpha [46]	0.359	0.110	0.135	0.280	0.116
Healthy	0.358	0.110	0.135	0.279	0.116
Homo. Emphysema	0.359	0.110	0.135	0.280	0.116
Left Diseased	**0.529**	0.0801	0.0983	0.204	0.0844
Apical Diseased	0.279	**0.306**	0.105	0.218	0.090
Inter. Diseased	0.274	0.0840	**0.339**	0.214	0.0884
Dia. Diseased	0.263	0.0806	0.0988	**0.469**	0.0848
Card. Diseased	0.278	0.0852	0.104	0.217	**0.315**

Pressure Drop From Trachea Face During Maximum Inhalation, cmH_2O

	Left	Apical	Intermediate	Diaphragmatic	Cardiac
Healthy	0.037	0.048	0.052	0.016	0.034
Homo. Emphysema	0.036	0.043	0.044	0.022	0.034
Left Diseased	**0.057**	0.037	0.032	0.016	0.023
Apical Diseased	0.027	**0.063**	0.028	0.009	0.022
Inter. Diseased	0.029	0.038	**0.069**	0.019	0.036
Dia. Diseased	0.028	0.041	0.058	**0.038**	0.045
Card. Diseased	0.030	0.038	0.048	0.027	**0.048**

Pressure Drop From Trachea Face During Maximum Exhalation, cmH_2O

	Left	Apical	Intermediate	Diaphragmatic	Cardiac
Healthy	1.38	1.25	1.87	1.82	1.86
Homo. Emphysema	0.464	0.431	0.626	0.616	0.627
Left Diseased	**0.718**	0.632	0.909	0.894	0.907
Apical Diseased	0.676	**0.636**	0.926	0.912	0.926
Inter. Diseased	0.682	0.654	**0.944**	0.927	0.939
Dia. Diseased	0.711	0.683	0.991	**0.989**	0.998
Card. Diseased	0.664	0.616	0.911	0.897	**0.914**

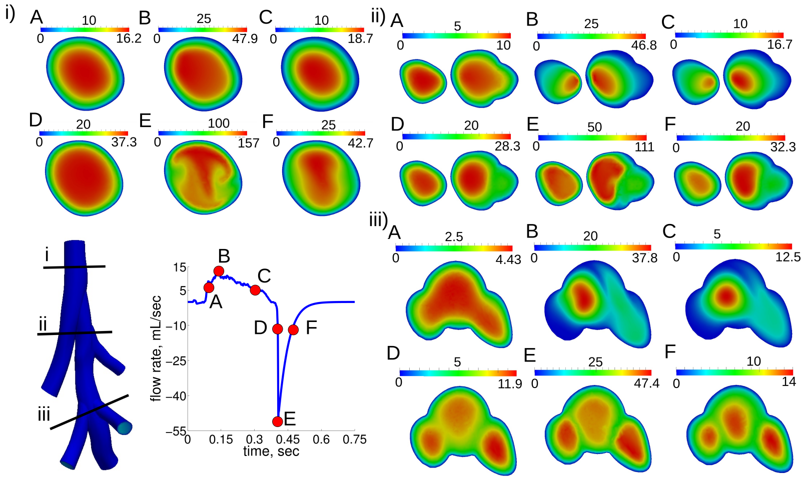

Figure 6.4: Velocity magnitude for three locations (1-3) at six time points (A-F) for the healthy case. Time points at A and C are at the same flow rate with A being before maximum inspiration (B) and C being after maximum inspiration. D and F are at the same flow rate, with D being before the maximum expiration (E) and F being after the maximum expiration.

the same time points. Even though the flow rate magnitude was the same at time points A and C (Figure 6.4), before and after maximum inhalation, respectively, the flow structures were quite different. At maximum inhalation the flow changed from being nearly parabolic in every airway (Figure 6.4 iiA and Figure 6.5A) to being skewed towards the inside of the bifurcations (Figure 6.4 iiB and Figure 6.5B). These flow structures remained during the deceleration phase of inspiration (Figure 6.4 iiC and Figure 6.5C). At position iii Figure 6.4), the flow began to recirculate from the diaphragmatic lobe to the intermediate lobe at maximum inspiration (Figure 6.4 iiiB and Figure 6.5B). During expiration, even though the flow magnitude varied much more than during inspiration, the flow structures remained quite similar throughout the expiration phase at both position ii and iii (Figure 6.4 and Figure 6.5). Velocity profiles in the lobe airways were shaped by the airways' curvature, merging upwards in the trachea. There, flow was initially almost flat but developed complex structures at maximum expiration (Figure 6.4 iE).

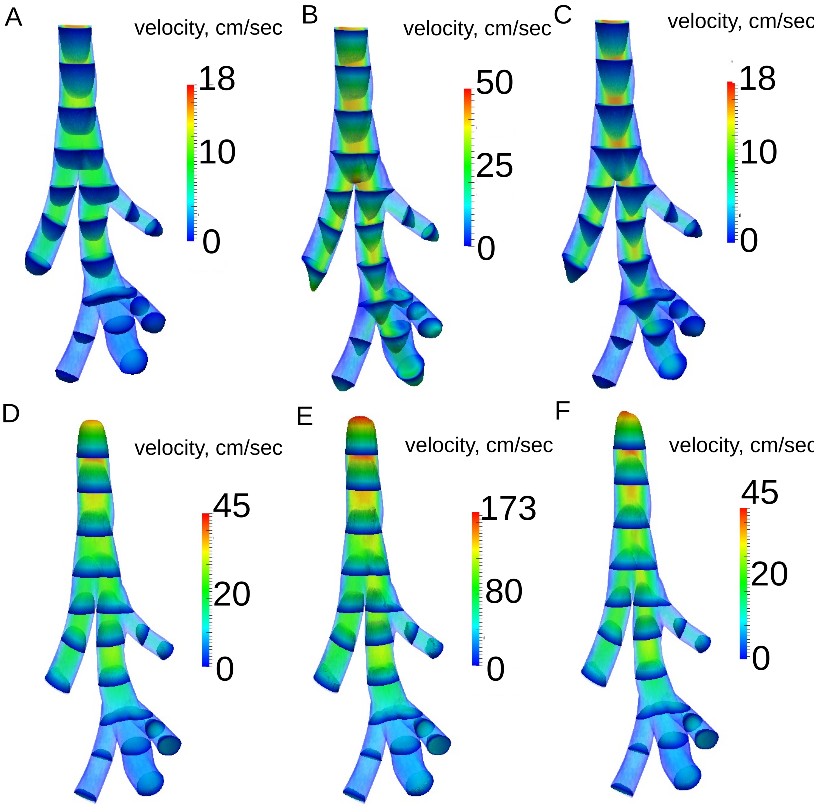

Figure 6.5: 3D rendering of the velocity magnitude for the healthy simulation at six time points (A-F). Flow profiles' shapes were normalized by the maximum velocity in the 3D domain at each time point.

The fluid velocity and massless fluid particle pathlines for homogeneous emphysema and apical heterogeneous emphysema are shown in Figure 6.6 for the same three time points during inspiration. The velocity magnitude was not only different in the diseased lobe airways, but also in other parts of the domain. For example, the transient flow was higher in the trachea at time point A for the apical diseased case. In the homogeneous emphysema case (Figure 6.6 1A-1C) there was more recirculation between the diaphragmatic and intermediate lobes than in the apical diseased case (Figure 6.6 2A-2C). Figure 6.6 2A-2C also shows that the increased airflow delivery to the diseased lobe (apical lobe) occurred only after maximum inspiration (panel C).

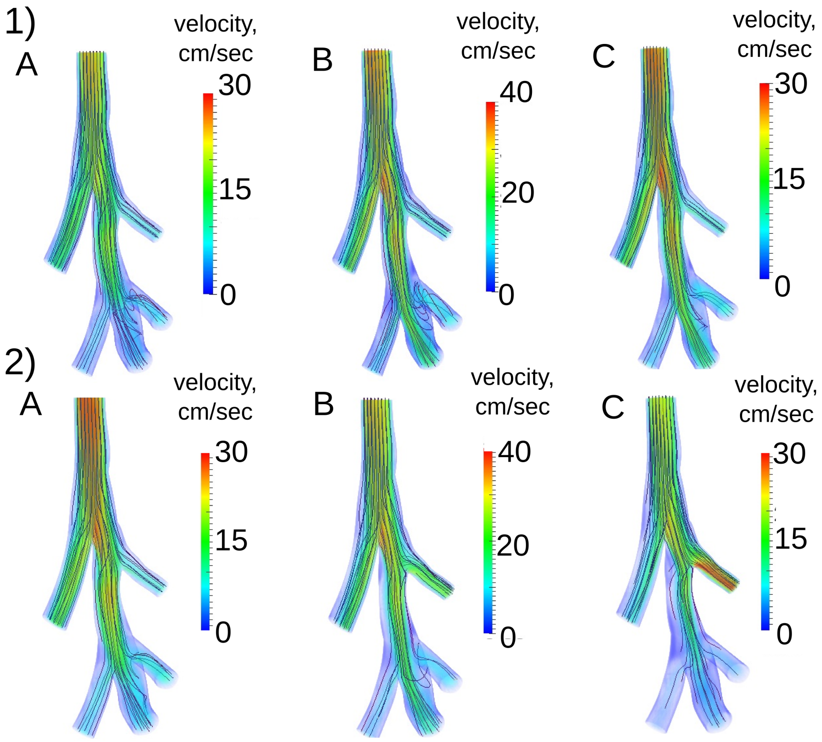

Figure 6.6: 3D rendering of the velocity magnitude and massless fluid particle pathlines for homogeneous emphysema (panels 1A - 1C) and for heterogeneous emphysema (apical lobe diseased) (panels 2A - 2C). Time points are the same as shown in Figure 6.4. The color scale is the same for each time point.

6.3.3 Particle Deposition and Distribution

Convergence in the number of deposited particles was reached when there was less than 1 % difference in particle deposition with increasing particle seeding densities. Convergence was achieved with a 2000 particle seed density was used, which resulted in $\sim 1.7\ 10^7$ total particles released during inspiration. Figure 6.7A shows the number of particles delivered to each lobe normalized by the total number of particles simulated, while Figure 6.7B shows the total number of particles exiting the 3D domain to each lobe normalized by the number of particles exiting, divided by the flow fraction values given in Table 6.2. There was no difference in the normalized distribution of particles between the healthy and homogeneous emphysema cases. However, there was an increase in delivery of particles to the diseased lobe and consequently a decrease in delivery of particles to the healthy lobes, for the heterogeneous emphysema cases. The increase in delivery of particles to the diseased lobe was mainly due to the increased flow to this lobe, as shown in Figure 6.7B. Additionally, it should be noted, that while the delivery of particles delivered to the apical and diaphragmatic lobes was proportional to the flow fraction, this was not the case for the left, intermediate and cardiac lobes. Using the healthy case as an example, the particle delivery to the left lobe was 4% higher than the flow delivered and 7 and 8 % less than the flow delivered for the intermediate and cardiac lobes, respectively.

Only 0.64 and 0.61% particles were deposited in the 3D geometric model for the healthy and homogeneous emphysema cases, respectively. There was no difference in the particle deposition locations between the healthy and homogeneous emphysema cases. As shown in Figure 6.8, there were common areas of deposition for all emphysema cases simulated. In particular, particles deposited mainly at the first and second bifurcations. Additionally, particles deposited at the back wall of the airway after the second bifurcation, as flow velocity decreased in this area, as shown in Figure 6.6. In the cases of apical, cardiac and intermediate heterogeneous emphysema, there was an increase in particle deposition on the wall of the airway leading to the diseased lobe.

6.4 Discussion

6.4.1 Global Respiratory Parameter Estimation

The global respiratory parameters were estimated from the breathing maneuvers taken during the aerosol exposure experiments. These global resistances and compliances agreed well with previously published data, [24, 50, 59] despite the limited by available experimental data, as neither flow rate nor volume curves were collected during the experiments. For example, Rubini et al. [50] reported the total respiratory resistance to be 0.25 ± 0.05 $\frac{cmH_2O-s}{cm^3}$ during inspiration and 0.33 ± 0.15 $\frac{cmH_2O-s}{cm^3}$ during expiration for 300 gram healthy Wistar rats ventilated with a tidal volume of 1 ml and a constant flow rate of 4 $\frac{ml}{s}$. These values are similar to those reported here for healthy rats; 0.22 ± 0.12 $\frac{cmH_2O-s}{cm^3}$ and 0.33 ± 0.18 $\frac{cmH_2O-s}{cm^3}$ for inspiration and expiration, respectively. In a different study, Tolnai et al. [59] reported respiratory compliance in healthy (C = 0.459 $\frac{cm^3}{cmH_2O}$) and elastase-treated (C = 0.744 $\frac{cm^3}{cmH_2O}$) Sprague-Dawley rats with body weight of 470 grams. Similar compliances were found in a study by Emami et al. [24] for healthy (C = 0.61 ± 0.12 $\frac{cm^3}{cmH_2O}$) and elastase-treated (C = 0.92 ± 0.16 $\frac{cm^3}{cmH_2O}$) Sprague-Dawley rats with mean body weight of 531 grams. While both of these studies reported higher compliance values than those reported here (healthy: C = 0.25 ± 0.04 $\frac{cm^3}{cmH_2O}$, emphysema: C = 0.37 ± 0.14 $\frac{cm^3}{cmH_2O}$), the relative increase in compliance between emphysema and healthy rats was similar; Tolnai et al: 1.6 times larger, Emami et al: 1.5 times larger, and this study: 1.4 times larger in emphysema compared to healthy. Variances between these studies may be attributed to differences in strain, body weight, and pulmonary function test measurement techniques. Indeed, Tolnai et al [59] estimated parameters by fitting a constant-phase model to impedance data. In contrast, both of these studies [24, 59] measured airway resistance and found no difference between the healthy and emphysematous rats. It should be noted that it is most likely that a mild to moderate case of emphysema was induced [6] and it is likely that respiratory resistance would increase with the severity of emphysema. In addition, if the resistance in emphysema is markedly different from the normal case during expiration only, then additional experimental measurements would be necessary to infer this information from the data. This would however not change the particle simulation results, as they were performed during inspiration.

To test the robustness of the parameter estimation method, the same procedure was repeated on two additional pressure curves collected for the same rat. The average resistance between the three curves was 0.338 ± 0.044 $\frac{cmH_2O-s}{cm^3}$ and the average compliance was 0.233 ± 0.006 $\frac{cmH_2O-s}{cm^3}$, resulting in a relative dispersion (RD = standard deviation normalized by the mean) of 0.13 and 0.03 for resistance and compliance, respectively. This intra-animal RD was less than the inter-animal RD for the healthy rats: 0.54 and 0.16 for resistance and compliance, respectively. In an additional test, a linear least squares fitting method was employed to estimate the global parameters to compare to the integration method used to solve Eq. 6.2. To do this, inhaled volume was estimated by recording and measuring the linear displacement of the ventilator pump. This method resulted in similar resistance, 0.296 versus 0.240 $\frac{cmH_2O-s}{cm^3}$, and compliance, 0.304 versus 0.302 $\frac{cm^3}{cmH_2O}$,as the original method for a single rat, respectively. While the least squares method may be more robust, as it uses the entire volume curve to estimate the parameters, there was potential for experimental error in estimating the pump volume displacement. Additionally, there was sensitivity in matching the start time of the volume and pressure curves, resulting in the inability to estimate parameters for several rats. Therefore, to employ such a method in future work, the pressure and volume curves should be measured simultaneously using a more reliable method to obtain the volume or flow rate.

The global volume and flow rate curves are highly dependent on the global respiratory resistance and compliance. To demonstrate this, Eq. 6.2 was solved by applying varying compliances (C = 2, 3.3, 4 and 5 $\frac{cm^3}{cmH_2O}$) and using the emphysema pressure curve (Figure 6.2A) and resistance ($R_{in} = 0.135\frac{cmH_2O-s}{cm^3}$ and $R_{ex} = 0.203\frac{cmH_2O-s}{cm^3}$). As shown in Figure 6.9A-B, for the same pressure curve, the maximum volume and flow rate during inspiration increased with increasing compliance. Additionally, the volume and flow rate decay time during exhalation increased as the compliance increased. As the compliance decreased, the flow rate versus volume curve (Figure 6.9C) became more restrictive. Therefore, as the tissue compliance increases, the lung becomes floppy and unable to recoil, as in the case of emphysema. Additionally, higher compliances result in larger functional residual capacity (FRC), or volume of the lung at its relaxed state. As the tissue compliance decreases the lung becomes stiff and unable to expand, as in the case of lung fibrosis.

6.4.2 Multi-scale CFD Simulations

Multi-scale numerical simulations were performed by coupling the 3D Navier-Stokes equations to a 0D global lumped parameter model. This enabled coupling between the downstream respiratory dynamics and the conducting trachea-bronchial region. Without this model, or with simpler boundary conditions, the pressure and flow would be in phase. To demonstrate this, an additional simulation was performed. Here, the healthy flow rate curve (see Figure 6.2) was applied at the trachea and a zero pressure boundary condition was applied at the distal faces. With this definition, the pressure drop from the trachea to each distal airway was the same. As a result the inhaled air would travel on the path of least resistance. For this case, the volume of air exiting the model, normalized by the total volume, was 0.289, 0.129, 0.007, 0.493, and 0.082 for the left, apical, intermediate, diaphragmatic and cardiac lobe, respectively. This led to as much as 95% difference in the flow distribution using the RC model (Table 6.2) compared to the multi-scale simulations. This significant difference highlights the importance of performing respiratory CFD with realistic boundary conditions if unsteady simulations are performed. Boundary condition choices would have less influence in steady flow simulations, as the primary difference was in the compliances between the healthy and emphysematous cases.

t would be necessary to tune the downstream 0D resistances [61] so that the total resistance (the resistance in 3D domain - computed as explained in Section "Coupled Multi-scale Simulation and Analysis" - plus the downstream 0D resistances) match the 0D global resistance if the airway resistance of the 3D model was the same order of magnitude as the total airway resistance. However, since the resistance in 3D airways was very small, i.e during inspiration the airway resistance on average was $3.51 * 10^{-5} \frac{cmH_2O-s}{cm^3}$ in the healthy rat (compared to the 0D global resistance of 0.098 $\frac{cmH_2O-s}{cm^3}$), it was unnecessary to tune the distal resistances. The resistance in the 3D domain during maximum exhalation flow rate was $3.54 * 10^{-4} \frac{cmH_2O-s}{cm^3}$, which was 10 times greater than during inhalation. This indicates that resistance is non-constant, at least during these short periods of high flow rates. Using the airway geometric dimensions given in Oakes et al. [46], the airway resistance was estimated by the relationship for Poiseuille flow, $R = \frac{8\mu L}{2\pi r^4}$, where L is the length of the airway and r is the airway radius. This resulted in an airway resistance of 9.93 $10^{-4} \frac{cmH_2O-s}{cm^3}$, which was in-between the resistance found during inhalation and exhalation. Therefore Poiseuille resistance approximation is appropriate if the resistance in the first couple of airway generations of the rat was needed.

Comparison to Previous Airflow Studies

The velocity field in the 3D domain was qualitatively compared to results given in Minard et al. [40]. In this study, Minard et al. [40] performed steady CFD simulations and compared flow profiles to those measured directly from a rat with MRI. The velocity field from our simulations was selected at the time points during inhalation with similar flow rates (2 $\frac{cm^3}{sec}$) than in the Minard et al. study. For the time point *before* maximum inspiration, the velocity field qualitatively compared well with Minard et al. [40]. However at the time point following maximum inspiration the velocity fields were different due to the unsteady effects of deceleration (see Figure 6.5C). This comparison underlines the importance of performing unsteady simulations, as the flow dynamically changes throughout inspiration. The 3D geometry of Minard et al. [40] was more extensive than this current study, however there was little qualitative difference in flow profiles at 2 $\frac{cm^3}{sec}$. In addition to the flow profiles, the flow distribution to each lobe was compared to data measured with MRI. The normalized flow distribution in the present study was 0.359, 0.116, 0.135, 0.28, 0.11, which compares well to Minard et al.'s values of 0.351, 0.119, 0.101, 0.333, 0.095 for the left, apical, intermediate, diaphragmatic, and cardiac lobes, respectively. Differences between the two studies may be attributed to differences in strain (Sprague-Dawley [40] versus Wistar), animal weight (267 grams [40] versus 531 grams) and breathing patterns (unsteady [40] versus steady).

6.4.3 Particle Deposition and Distribution

In this study, the deposition and distribution of particles in the lung were shown to be dependent not only on the flow distribution between lobes, but also on the airways 3D geometry. The decrease in delivery of particles relative to the lobar flow in both the cardiac and intermediate lobes (Figure 6.7, compared to the other three lobes, was most likely due to the triple bifurcation and its influence on the flow field in these regions (see Figure 6.6). In regions dominated by convective transport the likelihood of a particle to follow the flow depends on the Stoke's number [17, 21], defined as:

$$Stk = \frac{\rho_p d_p^2 u}{18 \mu d} \tag{6.6}$$

where ρ_p is the particle density, d_p is the particle diameter, u is the mean flow velocity and d is the airway diameter. In a previous modeling study performed on idealized human geometry, Darquenne et al. [17] concluded that convective flow was the main determinant of particle distribution in the lung at least down to the level of the lung segment when Stk in the trachea was less than 0.01. At the trachea, Stk was 0.0028 for the current study. The particles did deviate from the flow, as shown in Figure 6.7B, however by no more than 8% (similar to the variation discussed in Darquenne et al. [17]) The distribution of particles may be explained by the flow patterns. Indeed, the velocity profile at peak inspiration (see Figure 6.5B and C) was slightly pointing towards the left lobe. Not only will particles at these peak flow areas have greater inertia, there will be more particles released at this location, as the particle release density was proportional to the local velocity at its starting location. Both of these factors may bias the particles towards the left lobe. The recirculation area (see Figure 6.5B and C and Figure 6.6) also influenced the distribution of particles to the diaphragmatic, intermediate and cardiac lobes.

Less than 1 % of the 0.95 μm particles deposited in the 3D model for all healthy and diseased cases considered (see Figure 6.8). Particles mainly deposited at the first and second bifurcations for all diseased cases considered. However, in the case of heterogeneous emphysema, more particles deposited on the walls of the branches leading to the diseased lobe. Deposition in the 3D airways was also predicted by solving empirical models for gravitational sedimentation [8] and inertial impaction [48] using an average flow rate of 9 $\frac{cm^3}{s}$. For 0.95 μm diameter particles, it was estimated that 0.89 % of particles deposited due to inertia and 0.23 % of particles deposited due to gravitational sedimentation. Considering that these calculations did not take unsteadiness into account, the deposition prediction was close to that found with the numerical simulations.

Table 6.3: Percentage of particles deposited in the 3D geometry for rats in the supine and standing position for particle diameters of 1, 3 and 5 μm.

Position:	supine			standing	
Particle Diameter:	1 μm	3 μm	5 μm	1 μm	3 μm
Healthy	0.64	2.68	9.81	0.95	2.97
Homogenous Emphysema	0.61	2.54	8.56	1.31	3.11
Apical Diseased	0.76	2.35	9.24	1.48	2.25

The influence of rat position and particle size was investigated by tracking 0.95, 3 and 5 μm diameter particles with the rat in both the supine and standing positions (see Table 6.3 and Figure 6.10). As expected, the number of deposited particles in the 3D model increased with increasing particle size (Table 6.3). Additionally, for most cases, the deposition increased when the rat was in the standing position and there were more particles depositing on the front face of the diaphragmatic airway (see Figure 6.10B and D). This is mainly because flow and gravity are in the same direction and therefore particles are more likely to impact the curved airway faces (due to bifurcations or longitudinal curvature). As shown in Figure 6.10 the deposition patterns for 3 μm diameter particles were remarkably different between the homogeneous emphysema and the apical diseased cases. This was mainly because when the apical lobe was diseased, the flow slowed down in the other airways (see Figure 6.6), leading to increased particle deposition. Finally, the number of 3 μm particles deposited in a rat in the supine position was estimated by solving the empirical formulas given by Cai et al. [8] and Pich et al. [48]. Unlike for the 0.95 μm diameter particles, the empirical formulas overestimated deposition; 8.86 % of particles deposited due to impaction and 2.31 % of particles deposited due to sedimentation. The total deposition of 11.17 % was significantly higher than the 2.68 % found during the current unsteady numerical simulations. This is an example where numerical simulations may be used to study the hypotheses on which empirical formulas are based.

Comparison with Aerosol Experimental Data

In healthy black and white hooded rats of body weight of approximately 300 grams in free breathing exposure, Raabe et al. [49] found that particles deposition, normalized by lung volume, was 1.01, 1.12, 0.95, 0.96, 1.00 for the left, apical, intermediate, diaphragmatic and cardiac lobes, respectively. Assuming that the number of particles deposited in each lobe is proportional to the number delivered to the lobe, we would predict that normalized deposition of 1.04, 0.982, 0.928, 1.03, 0.923 for the left, apical, intermediate, diaphragmatic and cardiac lobes, respectively, a difference of less than 10%. One exception was in the apical lobe, in which Raabe et al. [49] found a 12 % higher normalized deposition than the current study would suggest.

Exposing free breathing hamsters to 0.45 μm aerosol, Sweeney et al. [58] found significantly less deposition of 0.45 μm in emphysematous hamsters than in age-matched healthy hamsters. Additionally, the authors found that the particle deposition was more heterogeneously distributed in the emphysema hamsters than in the healthy animals. While the deposition downstream of the 3D model in the current study was not determined, the increased delivery of particles to the diseased lobe suggests that more particles would be available to deposit in emphysematous regions of the lung, in disagreement with Sweeney et al's findings [58]. It should be noted that while the diseased lobe in our model of heterogeneous emphysema had a larger compliance than the healthy lobes, resistance in the diseased lobe was kept similar to that of the healthy ones, as the resistance between the healthy and emphysematous rats was found to be the same. However, the loss of elastic recoil in the emphysematous lobe may increase the resistance of the small airways [15]. Such increase in resistance would be expected to limit ventilation in the subtended parenchymal region, hence limiting the delivery of aerosols in the diseased lobe and subsequent deposition. Finally, while reasonable in a homogeneous lung, our assumption of deposition being proportional to aerosol delivery may not be as suitable in a lung with heterogeneous compliance. These differences between our model predictions and experimental observations will help refining our approach in future studies.

6.4.4 Study Limitations and Future Work

Global resistance and compliance were estimated by solving a two-component lumped parameter RC model with pressure tracings collected during the experiments. As the flow and volume curves were not measured during the aerosol exposure experiments, it was impossible to determine a time varying resistance and compliance. However, as the rats were ventilated at tidal breathing, it is appropriate to assume a constant resistance and compliance [22]. Despite this limitation, the global resistance and compliance agreed favorably with previous studies [**?**, 24]. Moreover, if other data enable to describe how resistance and compliances change dynamically (e.g. with the flow rate), this information can be readily integrated in the current framework.

Our multi-scale approach enabled realistic unsteady simulations, and more accurately predicted flow distribution in each lobe compared to the constant pressure boundary conditions. However, the distal resistance and compliance were partitioned based on the sub-tending lobar volume. Pulmonary ventilation may not be directly proportional to the lobe volume; only a few experimental studies [24, 40] have investigated ventilation in the rat lung. Despite this, the flow distribution to each lobe matched well with flow measured with MRI [40]. Additionally, in this work, emphysema was modeled as homogeneous or only contained in one lobe. However, it is likely that the disease affects the whole lung in a heterogeneous fashion rather than being restricted to one specific lobe. Nonetheless, our simulations, can be used to offer insights into the relation between the disease, airflow and particle delivery.

While particle transport was simulated throughout unsteady inspiration, particles were not tracked once they left the 3D domain or during exhalation. Determining particle deposition downstream of the 3D model would require either a more extensive 3D model, a mean multiple path deposition model [2], or a 1D description of airflow and particle deposition. In spite of this, the model was able to match both experimental [49] and empirical models [8, 48] reasonably well.

6.5 Conclusion

This study was the first to (1) model airflow in the rat airways by solving a 0D global model and then a multi-scale 3D-0D model that were parameterized from experimental data, (2) determine particle deposition in the large airways and particle distribution in the rat lobes under unsteady breathing conditions, and (3) understand the influence of emphysema on the deposition and distribution of 0.95 μm diameter particles. As the 3D-0D multi-scale respiratory model showed, there was an increase in delivery of air and particles to the diseased lobe, because of the lobe's increased compliance. This finding suggests that, while emphysema reduces area for gas exchange to occur, airflow may be increased to the diseased regions, resulting in reduction of airflow to the healthy regions. Even though more particles are delivered to the diseased regions, it is unknown how they deposit once they leave the 3D domain. However, if the air becomes trapped, there may be an increase in deposition in emphysema due to gravitational sedimentation. In addition to the increase in particle delivery to the diseased lobe, there was a greater number of particles depositing in the 3D domain in the localized diseased cases compared to the healthy or homogeneously distributed emphysema case. This was mainly because there was more particle-laden air traveling through these airways. While this increase in deposition was small (0.76 % in apical diseased versus 0.61 % in homogeneous emphysema), the influence of disease on deposition may become more significant in a model that includes more airway generations. Both the particle size and the position of the rat changed the percent deposition in the 3D model; deposition was higher for increasing particle diameter, and deposition was higher for the rat in the standing position, compared to the supine position. Finally, the particle deposition empirical models studied here [8, 48] predicted a higher deposition compared to the 3D numerical simulations. This is probably because the 3D numerical simulations were unsteady, whereas the empirical models do not account for the influence of unsteady flow.

6.6 Acknowledgements

Chapter 6, in full, is a reprint of the materials as it may appear in Annals of Biomedical Engineering as Jessica M. Oakes, Alison Marsden, Celine Grandmont, Shawn Shadden, Chantal Darquenne, Irene Vignon-Clementel ”Towards Animal Specific Airflow Simulation and Particle Deposition in Health and Emphysema: From In-Vivo to In-Silco Experiments”, *Submitted.*. The dissertation author was the primary investigator and author of this paper.

6.7 Bibliography

[1] Agu, R. U., and Ugwoke, M. I. In vitro and in vivo testing methods for respiratory drug delivery. *Expert Opinion Drug Delivery2 1* (2011), 57–69

[2] Angivel, S., and Asgharian, B. A Multiple-Path Model of Particle Deposition in the Rat Lung. *Toxicological Sciences 28*, 1 (Nov. 1995), 41–50

[3] Baffico, L., Grandmont, C., and Maury, B. Multiscale Modeling of the Respiratory Tract. *Mathematical Models and Methods in Applied Sciences 20*, 01 (2010), 59.

[4] Bates, J. H. T. and B. Suki. Assessment of peripheral lung mechanics. *Respiratory Physiology & Neurobiology*, 163 (2008), 54–63.

[5] Bennett, W. D., K. L. Zeman, C. Kim, J. Mascarella, D. William, L. Kirby, and J. Enhanced. Enhanced Deposition of Fine Particles in Copd Patients Spontaneously Breathing At Rest. Inhalation Toxicology, 9(1):1–14, 1997.

[6] Borzone, G., L. Liberona, P. Olmos, C. Sáez, M. Meneses, T. Reyes, R. Moreno, and C. Lisboa. Rat and hamster species differences in susceptibility to elastase-induced pulmonary emphysema relate to differences in elastase inhibitory capacity. *American journal of physiology. Regulatory, integrative and comparative physiology*, 293 (2007) :R1342–9.

[7] Brand, P., Schulte, M., Wencker, M., Herpich, C. H., Klein, G., Hanna, K., and Meyer, T. Lung deposition of inhaled alpha1-proteinase inhibitor in cystic fibrosis and alpha1-antitrypsin deficiency. *The European Respiratory Journal 34*, 2 (Aug. 2009), 354–60.

[8] Cai, F. and C. Yu. Inertial and interceptional deposition of spherical particles and fibers in a bifurcating airway. *Journal of Aerosol Science*, 19 (1988), 679–688.

[9] Carr, I. A., N. Nemoto, R. S. Schwarz, and S. C. Shadden. Size dependent predilections of cardiogenic embolic transport. *Am J. Physiol Heart Circ Physiol.*

[10] Choi, J., Tawhai, M. H., Hoffman, E. a., and Lin, C.-L. On intra- and intersubject variabilities of airflow in the human lungs. *Physics of fluids 21*, 10 (Oct. 2009), 101901.

[11] Comer, J. K., C. Kleinstreuer, S. Hyun, and C. S. Kim. Aerosol transport and deposition in sequentially bifurcating airways. *Journal of Biomechanical Engineering*, 122 (2000), 152–8.

[12] Comerford, A., G. Bauer, and W. A. Wall. Nanoparticle transport in a realistic model of the tracheobronchial region. *nternational Journal for Numerical Methods in Biomedical Engineering*, 26 (2010), 904–914.

[13] Comerford, A., Förster, C., and Wall, W. a. Structured tree impedance outflow boundary conditions for 3D lung simulation. *Journal of Biomechanical Engineering 132*, 8 (Aug. 2010), 081002:1–10.

[14] Corley, R. A., Kabilan, S., Kuprat, A. P., Carson, J. P., Minard, K. R., Jacob, R. E., Timchalk, C., Glenny, R., Pipavath, S., Cox, T., Wallis, C. D., Larson, R. F., Fanucchi, M. V., Postlethwait, E. M., and Einstein, D. R. Comparative Computational Modeling of Airflows and Vapor Dosimetry in the Respiratory Tracts of Rat , Monkey , and Human. *Toxicological Sciences 128*, 2 (2012), 500–516

[15] Cotes, J. E., D. J. Chinn, M. R. Miller Lung function: physiology, measurement and application to medicine Sixth Edition, Blackwell Publishing, 2006

[16] Couch, M. J., A. Ouriadov, and G. E. Santyr. Regional ventilation mapping of the rat lung using hyperpolarized ???Xe magnetic resonance imaging. *Magnetic Resonance in Medicine*, 68 (2012), 1623–31.

[17] Darquenne, C., Van Ertbruggen, C., and Prisk, G. K. Convective flow dominates aerosol delivery to the lung segments. *Journal of Applied Physiology 111*, 1 (July 2011), 48–54

[18] De Backer, J. W., Vos, W. G., Burnell, P., Verhulst, S. L., Salmon, P., De Clerck, N., and De Backer, W. Study of the variability in upper and lower airway morphology in Sprague-Dawley rats using modern micro-CT scan-based segmentation techniques. *The Anatomical Record 292*, 5 (May 2009), 720–7.

[19] De Backer, J. W., Vos, W. G., Burnell, P., Verhulst, S. L., Salmon, P., De Clerck, N., and De Backer, W. Study of the variability

in upper and lower airway morphology in Sprague-Dawley rats using modern micro-CT scan-based segmentation techniques. *The Anatomical Record 292*, 5 (May 2009), 720–7..

[20] de Rochefort, L., L. Vial, R. Fodil, X. Maître, B. Louis, D. Isabey, G. Caillibotte, M. Thiriet, J. Bittoun, E. Durand, and G. Sbirlea-Apiou. In vitro validation of computational fluid dynamic simulation in human proximal airways with hyperpolarized 3He magnetic resonance phase-contrast velocimetry. *Journal of Applied Physiology*, 102 (2007), 2012–23.

[21] de Vasconcelos, T. F., B. Sapoval, J. S. Andrade, J. B. Grotberg, Y. Hu, and M. Filoche. Particle capture into the lung made simple? *Journal of applied physiology* , 110 (2011), 1664–73.

[22] Diamond, L. and M. O'Donnell. Pulmonary mechanics in normal rats. *Journal of Applied Physiology*, 43 (1997), 942–8.

[23] EINSTEIN, D. R., NERADILAK, B., POLLISAR, N., MINARD, K. R., WALLIS, C., FANUCCHI, M., CARSON, J. P., KUPRAT, A. P., KABILAN, S., JACOB, R. E., AND CORLEY, R. A. An automated self-similarity analysis of the pulmonary tree of the Sprague-Dawley rat. *Anatomical Record 291*, 12 (Dec. 2008), 1628–48.

[24] EMAMI, K., CHIA, E., KADLECEK, S., MACDUFFIE-WOODBURN, J. P., ZHU, J., PICKUP, S., BLUM, A., ISHII, M., AND RIZI, R. R. Regional correlation of emphysematous changes in lung function and structure: a comparison between pulmonary function testing and hyperpolarized MRI metrics. *Journal of Applied Physiology 110*, 1 (Jan. 2011), 225–35

[25] Esmaily Moghadam, M., Y. Bazilevs, and A. L. Marsden. A new preconditioning technique for implicitly coupled multidomain simulations with applications to hemodynamics. *Computational Mechanics.*

[26] Esmaily Moghadam, M., Y. Bazilevs, T.-Y. Hsia, I. E. Vignon-Clementel, and A. L. Marsden. A comparison of outlet boundary treatments for prevention of backflow divergence with relevance to blood flow simulations. *Computational Mechanics*, 48 (2011), 277–291.

[27] Esmaily Moghadam, M., I. E. Vignon-Clementel, R. Figliola, and A. L. Marsden. A modular numerical method for implicit 0D/3D coupling in cardiovascular finite element simulations. *Journal of Computational Physics.*

[28] Fetita, C., S. Mancini, D. Perchet, F. Prêteux, M. Thiriet, and L. Vial. An image-based computational model of oscillatory flow in the proximal part of tracheobronchial trees. *Computer Methods in Biomechanics and Biomedical Engineering*, 8 (2005), 279–293.

[29] Gemci, T., Ponyavin, V., Chen, Y., Chen, H., and Collins, R. Computational model of airflow in upper 17 generations of human respiratory tract. *Journal of Biomechanics 41*, 9 (Jan. 2008), 2047–54..

[30] Gravemeier, V., Comerford, A., Yoshihara, L., and Ismail, M. A novel formulation for Neumann inflow boundary conditions in biomechanics. *International Journal for Numerical Methods in Biomedical Engineering 28* (2012), 560–573.

[31] Griffiths, N. M., Van der Meeren, A., Fritsch, P., Abram, M.-C., Bernaudin, J.-F., and Poncy, J. L. Late-occurring pulmonary pathologies following inhalation of mixed oxide (uranium + plutonium oxide) aerosol in the rat. *Health Physics 99*, 3 (Sept. 2010), 347–56.

[32] Jiang, J., and Zhao, K. Airflow and nanoparticle deposition in rat nose under various breathing and sniffing conditions. *Journal of Aerosol Science 41*, 11 (2011), 1030–1043.

[33] Kung, E., Baretta, A., Baker, C., Arbia, G., Biglino, G., Corsini, C., Schievano, S., Vignon-Clementel, I. E., Dubini, G., Pennati, G., Taylor, A., Dorfman, A., Hlavacek, A. M., Marsden, A. L., Hsia, T.-Y., and Migliavacca, F. Predictive modeling of the virtual Hemi-Fontan operation for second stage single ventricle palliation: two patient-specific cases. *Journal of Biomechanics 46*, 2 (Jan. 2013), 423–9.

[34] Kuprat, A., Kabilan, S., Carson, J., Corley, R., and Einstein, D. A bidirectional coupling procedure applied to multiscale respiratory modeling. *Journal of Computational Physics In-Press*.

[35] Laganà, K., G. Dubini, F. Migliavacca, R. Pietrabissa, G. Pennati, A. Veneziani, and A. Quarteroni. Multiscale modelling as a tool to prescribe realistic boundary conditions for the study of surgical procedures. *Biorheology*, 39 (2002), 359–64.

[36] Longest, P. W. and S. Vinchurkar. Effects of mesh style and grid convergence on particle deposition in bifurcating airway models with comparisons to experimental data. *Medical Engineering and Physics*, 29 (2007), 350–66.

[37] Malve, M., Chandra, S., Lopez-Villalobos, J.L., Finol, E.A., Ginel, A., Doblare, M. CFD analysis of the human airways under impedance- based boundary conditions: application to healthy, diseased and stented trachea. *Computer Methods in Biomechanics and Biomedical Engineering*, March (2013), 37–41.

[38] Maxey, M. R. and J. J. Riley. Equation of motion for a small rigid sphere in nonuniform flow.pdf. *Physics of Fluids*, 26 (1983), 883–889.

[39] Migliavacca, F., R. Balossino, G. Pennati, G. Dubini, T.-Y. Hsia, M. R. de Leval, and E. L. Bove. Multiscale modelling in biofluidynamics: application to reconstructive paediatric cardiac surgery. *Journal of Biomechanics*, 39 (2006):1010–20.

[40] Minard, K. R., Kuprat, A. P., Kabilan, S., Jacob, R. E., Einstein, D. R., Carson, J. P., and Corley, R. a. Phase-contrast MRI and CFD modeling of apparent (3)He gas flow in rat pulmonary airways. *Journal of magnetic resonance 221* (May 2012), 129–138

[41] Monjezi, M., R. Dastanpour, M. Saidi, and a.R. Pishevar. Prediction of particle deposition in the respiratory track using 3D1D modeling. Scientia Iranica, 19(6):1479–1486, 2012.

[42] Müller, J., O. Sahni, X. Li, K. E. Jansen, M. S. Shephard, and C. a. Taylor. Anisotropic adaptive finite element method for modelling blood flow. *Computer Methods in Biomechanics and Biomedical Engineering*, 8(2005). 295–305.

[43] Nowak, N., P. P. Kakade, and A. V. Annapragada. Computational Fluid Dynamics Simulation of Airflow and Aerosol Deposition in Human Lungs. *Annals of Biomedical Engineering*, 31 (2003), 374–390.

[44] Oakes, J. M., Day, S., Weinstein, S. J., and Robinson, R. J. Flow field analysis in expanding healthy and emphysematous alveolar models using particle image velocimetry. *Journal of Biomechanical Engineering 132*, 2 (Feb. 2010), 021008

[45] Oakes, J. M., M. Scadeng, E. Breen, and C. Darquenne. Aerosol Deposition In Healthy And Emphysematous Rat Lungs Measured With MRI. *American Journal Respiatory Critical Care Medicine*, 183 (2011), A2463.

[46] Oakes, J. M., Scadeng, M., Breen, E. C., Marsden, A. L., and Darquenne, C. Rat airway morhometry measured from in-situ mri-based geometric models. *Journal of Applied Physiology 112*, 12 (Mar. 2012), 1921–1931.

[47] Oakes, J. M., M. Scadeng, E. C. Breen, G. K. Prisk, and C. Darquenne. Regional Distribution of Aerosol Deposition in Rat Lungs Using Magnetic Resonance Imaging. *Annals of Biomedical Engineering*, 41 (2013) :967–978.

[48] Pich, J. Theory of gravitational deposition of particles from laminar flows in channels. *Journal of Aerosol Science*, 3 (1972), 351–361.

[49] Raabe, O. G., H. C. Yeh, G. J. Newton, R. F. Phalen, and D. J. Velasquez. Deposition of inhaled monodisperse aerosols in small rodents. *Inhaled Particles*, 4 (1975), 3 – 21.

[50] Rubini, A., E. L. Carniel, A. Parmagnani, and A. N. Natali. Flow and volume dependence of rat airway resistance during constant flow inflation and deflation. *Lung*, 189 (2011), 511–8.

[51] Schmid, O., Bolle, I., Harder, V., Karg, E., Takenaka, S., Schulz, H., and Ferron, G. a. Model for the deposition of aerosol particles in the respiratory tract of the rat. I. Nonhygroscopic particle deposition. *Journal of Aerosol Medicine and Pulmonary Drug Delivery 21*, 3 (Sept. 2008), 291–307.

[52] Schmidt, J. P., S. L. Delp, M. A. Sherman, C. A. Taylor, V. S. Pande, and R. B. Altman. NIH Public Access. Proceedings of the IEEE, special issue on Computational System Biology, 96(8):1266–1280, 2008.

[53] Schroeter, J. D., Kimbell, J. S., Gross, E. a., Willson, G. a., Dorman, D. C., Tan, Y.-M., and Clewell, H. J. Application of physiological computational fluid dynamics models to predict interspecies nasal dosimetry of inhaled acrolein. *Inhalation Toxicology 20*, 3 (Feb. 2008), 227–43.

[54] Segal, R. A., Hill, C., Carolina, N., and Shearer, M. Computer simulations of particle deposition in the lungs of chronic obstructuve pulmonary disease patients. *Inhalation Toxicology 14* (2002), 705–720.

[55] Shadden, S. C. FlowVC (Version 1) [Computer Software]. https://github.com/FlowPhysics/flowVC.

[56] Soni, B., and Thompson, D. Effects of temporally varying inlet conditions on flow and particle deposition in the small bronchial tubes. *International Journal for Numerical Methods in Biomedical Engineering 28* (2012), 915–936.

[57] Sturm, R., and Hofmann, W. Stochastic simulation of alveolar particle deposition in lungs affected by different types of emphysema. *Journal of Aerosol Medicine 17*, 4 (Jan. 2004), 357–72.

[58] Sweeney, T. D., Brain, J. D., Leavitt, S. a., and Godleski, J. J. Emphysema alters the deposition pattern of inhaled particles in hamsters. *The American journal of pathology 128*, 1 (July 1987), 19–28.

[59] Tanoli, T. S. K., Woods, J. C., Conradi, M. S., Bae, K. T., Gierada, D. S., Hogg, J. C., Cooper, J. D., and Yablonskiy, D. a. In vivo lung morphometry with hyperpolarized 3He diffusion MRI in canines with induced emphysema: disease progression and comparison with computed tomography. *Journal of Applied Physiology 102*, 1 (Jan. 2007), 477–84.

[60] Torii, R., M. Oshima, T. Kobayashi, K. Takagi, and T. E. Tezduyar. Computer modeling of cardiovascular fluidstructure interactions with the deforming-spatial-domain/stabilized spacetime formulation. *Computer Methods in Applied Mechanics and Engineering* 195(2006),1885–1895.

[61] Troianowski, G, C. A. Taylor, J. A. Feinstein, and I. E. Vignon-Clementel. Three-dimensional simulations in Glenn patients: clinically based boundary conditions, hemodynamic results and sensitivity to input data *Journal of Biomechanical Engineering*, 133 (2011):111006.

[62] Urquiza, S. A., P. J. Blanco, M. J. Venere, and R. A. Feijo. Multidimensional Modelling for the Carotid Artery Blood Flow. *Computer Methods in Applied Mechanics and Engineering*, 195 (2006), 4002–4017.

[63] VIGNON-CLEMENTEL, I., ALBERTOFIGUEROA, C., JANSEN, K., AND TAYLOR, C. Outflow boundary conditions for three-dimensional finite element modeling of blood flow and pressure in arteries. *Computer Methods in Applied Mechanics and Engineering 195*, 29-32 (June 2006), 3776–3796.

[64] WALL, W. A., WIECHERT, L., COMERFORD, A., AND RAUSCH, S. Towards a comprehensive computational model for the respiratory system. *International Journal for Numerical Methods in Biomedical Engineering 26* (2010), 807–827.

[65] Walters, D. K. and W. H. Luke. Computational fluid dynamics simulations of particle deposition in large-scale, multigenerational lung models. *Journal of Biomechanical Engineering*, 133 (2011):011003.

[66] WICHERS, L. B., ROWAN, W. H., NOLAN, J. P., LEDBETTER, A. D., MCGEE, J. K., COSTA, D. L., AND WATKINSON, W. P. Particle deposition in spontaneously hypertensive rats exposed via whole-body inhalation: measured and estimated dose. *Toxicological Sciences 93*, 2 (Oct. 2006), 400–10.

[67] YIN, Y., CHOI, J., HOFFMAN, E. A., TAWHAI, M. H., AND LIN, C.-L. Simulation of pulmonary air flow with a subject-specific boundary condition. *Journal of Biomechanics 43*, 11 (Aug. 2010), 2159–63.

[68] ZHANG, H., AND PAPADAKIS, G. Computational analysis of flow structure and particle deposition in a single asthmatic human airway bifurcation. *Journal of Biomechanics 43*, 13 (Sept. 2010), 2453–9.

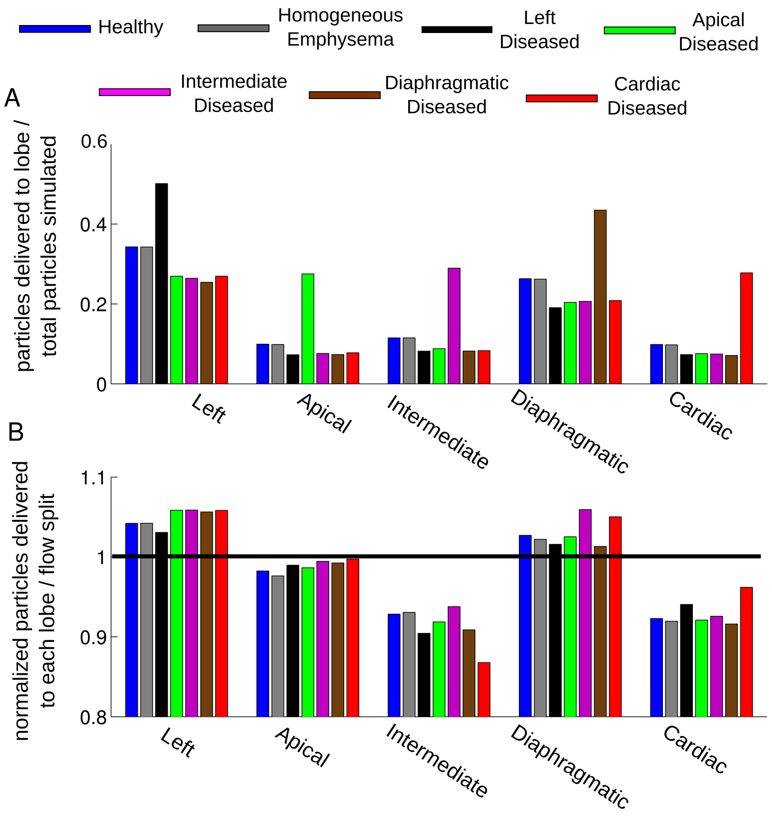

Figure 6.7: Panel A: Normalized number of particles exiting to each lobe. Panel B: Normalized number of particles delivered to each lobe (number of particles exiting to lobe divided by total number of particles exiting) divided by the flow split values given in Table 6.2.

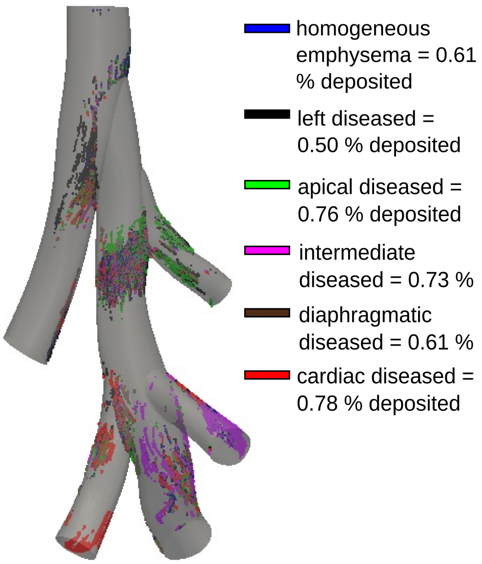

Figure 6.8: Particle deposition in the 3D model for 0.95 μm diameter particles with the different colors representing the 6 different cases of emphysema simulated. The percentage of total deposition in the 3D domain is also given for each emphysema case.

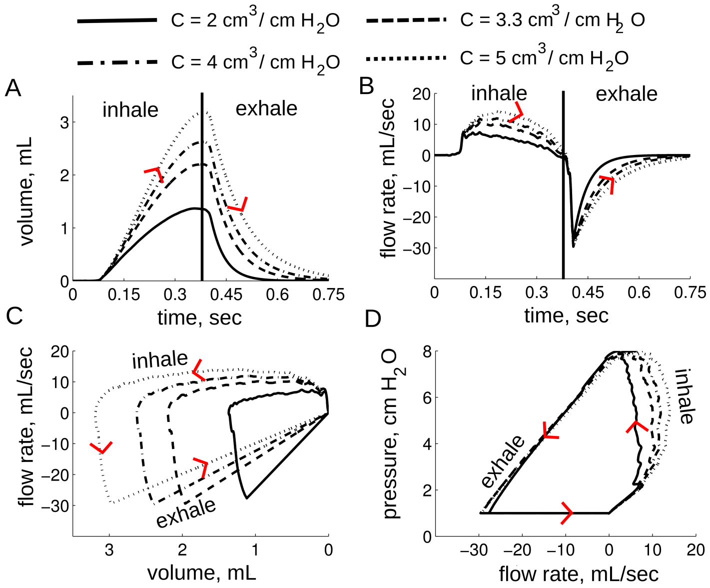

Figure 6.9: Predictive inhaled volume and flow rates using the emphysema pressure tracing (Figure 6.2A) and resistance ($R_{in} = 0.135\frac{cmH_2O-s}{cm^3}$ and $R_{ex} = 0.202\frac{cmH_2O-s}{cm^3}$) with varying compliances. C = 3.3 was the compliance found for the representative emphysema rat.

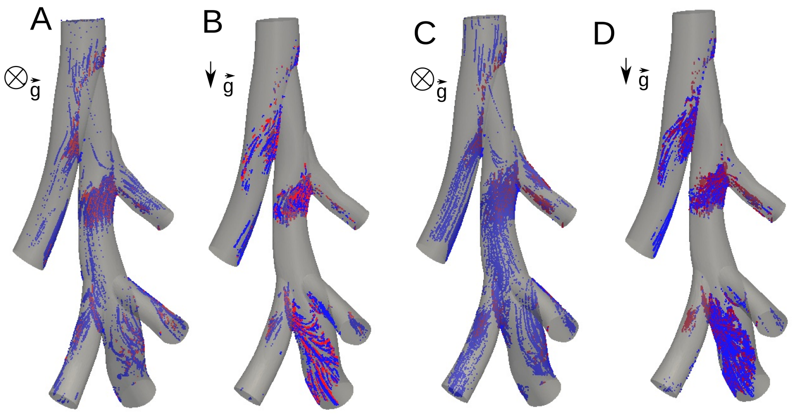

Figure 6.10: Particle deposition in homogeneous emphysema for rat in supine and standing position (panels A and B, respectively) and for heterogeneous emphysema (apical diseased) for rat in supine and standing position (panels C and D, respectively). Red particles are 1 micron in diameter and blue particles are 3 microns in diameter.

Chapter 7

Extended Airway Model and Comparison of Experimental and Simulated Deposition Data

7.1 Introduction

The main challenge in modeling airflow and particle deposition in the lung lies in the ability to directly validate models with either human or animal in-vivo experimental data. Only a few computational fluid dynamics (CFD) studies have validated their respiratory models with either replica experimental models [3, 5, 6] or in-vivo animal models [7]. Currently, no CFD prediction of particle deposition have been compared to in-vivo human deposition data. Recently, Minard et al. [7] compared CFD and magnetic resonance imaging (MRI) velocity fields in the airways of rats. However, no work has been done to directly validate numerical particle deposition predictions with experimental data. To move towards performing in-vivo particle deposition validation, respiratory CFD models must accurately mimic the experiments that they are being compared to. Due to the vast length scales of the lung, complex geometry and pulmonary tissue mechanics, it is currently impossible to model the lung in full because of the extensive computational costs and lack of data. Therefore, multi-scale methods must be employed that incorporate realistic 3D CFD geometry coupled to lower-dimensional downstream models.

In this study, multi-scale CFD simulations were performed on rat airway geometry derived from MR-images [8]. Particles with diameters of 0.95 μm were tracked in the flow field during inspiration. Airflow and particle deposition sites were compared for healthy, homogeneous and localized emphysema cases. The disease locations were defined based on the emphysematous rat experiments (see Chapter 5). Therefore, emphysematous regions of the lung were located at the base of the left, diaphragmatic and cardiac lobes. The normalized delivery of particles to each lobe were compared to the normalized MRI deposition data for both the the healthy and emphysematous rat lungs.

7.2 Methods

This work extends on the multi-scale airflow simulations presented in Chapter 6. Previously, the global respiratory resistance (R) and compliance (C) were determined by numerically solving

$$R\frac{dV}{dt} + \frac{V(t)}{C} = P(t) - P_{peep} \tag{7.1}$$

where $V(t)$ was the inhaled volume $P(t)$ was the pressure measured at the trachea and P_{peep} was 1 cm H_2O. The global resistance and compliance values found for a representative healthy ($R_{H,global} = 0.098\frac{cmH_2O-s}{cm^3}$, $C_{H,global} = 0.236\frac{cm^3}{cmH_2O}$) and emphysematous ($R_{E,global} = 0.135\frac{cmH_2O-s}{cm^3}$, $C_{E,global} = 0.330\frac{cm^3}{cmH_2O}$) rat (see Chapter 6) were employed in these simulations.

7.2.1 Numerical Simulations

The 3D Navier-Stokes equations were solved in a rat airway geometry derived from MR images (see Chapter 3 [8]). The airway geometry consisted of up to 14 airway generations and 79 terminal branches (see Figure 7.1). Throughout the rest of the text the 14 generation model is called the "extended airway model" and the model presented previously in Chapter 6 is called the "5 airway model".

Neumann boundary conditions were employed at the trachea face and at each of the distal airway faces using methods described elsewhere (see Chapter 2, Chapter 6). The distal resistance ($R_{i,j}$) and compliance ($C_{i,j}$) used to solve each lumped parameter model Eq. 7.1 at each distal face for the healthy and homogeneous emphysema cases were determined assuming that (1) the airflow delivered each lobe is proportional to the lobe's volume and (2) that the mean flow rate exiting the 3D domain is directly proportional to the airways cross-sectional area. Therefore, defining α_j volume fraction for each lobe, the resistance and compliance for each lobe is defined as

$$C_j = \alpha_j C_{global} \tag{7.2}$$

$$R_j = \frac{\alpha_j}{R_{global}} \tag{7.3}$$

where j is the subscript denoting each lobe. The resistance and compliance for each airway were found by solving

$$C_{i,j} = \frac{A_{i,j} C_j}{\sum_{i=1}^{N} A_{i,j}} \tag{7.4}$$

$$R_{i,j} = \frac{R_j \sum_{i=1}^{N} A_{i,j}}{A_{i,j}} \tag{7.5}$$

where the subscript i denotes the airway number, N is the total number of airways in a lobe and $A_{i,j}$ is the cross-sectional of each airway face. With these definitions, the summation of the distal resistances and compliances equal the global resistance and compliance. However, the 3D airways do not have negligible resistance and compliance as they did for the 5 airway model (see Chapter 6), as there are many more airways included in this extended model. Therefore, the distal resistance values must be tuned such that the volume of air exiting out each airway is as expected ($V_{i,j} = \frac{A_{i,j}}{\sum_{i=1}^{N} A_{i,j}} V_T$, where V_T is the total volume inhaled, and that the total simulated resistance equals the expected global resistance. To save on computational cost, the resistance values were first tuned with steady simulations and then tuned further for the unsteady case.

Two steady simulations were performed by prescribing a constant flow rate equal to the mean flow rate during inhalation at the average flow rate ($Q_{avg} = 7.4\frac{cm^3}{sec}$) or at the maximum flow rate ($Q_{max} = 13.022\frac{cm^3}{sec}$) at the trachea and resistance values found from Eq. 7.5 at each of the outlets. Tuning was performed by updating the the distal resistances by solving

$$R_{i,j}^{k+1} = \frac{Q_{i,j}R_{i,j}^{3D,k}}{Q_{avg,i,j}} \tag{7.6}$$

where $k+1$ denotes the updated resistance value and $Q_{i,j}^{3D,k}$ is the flow rate exiting each airway. Tuning for the steady simulations were performed until there was less than 5 % difference between the expected flow and the simulated flow. Once the correct resistance values for the steady case were determined, the unsteady simulations were performed. The resistance was then tuned by solving

$$R_{i,j}^{k+1} = \frac{\bar{P}_{i,j}^{3D,k} - \bar{P}_{i,j}^{d,k}}{\bar{Q}_{i,j}^{T,k}} \tag{7.7}$$

where $\bar{Q}_{i,j}^{T,k}$ is the average expected flow rate, $\bar{P}_{i,j}^{3D,k}$ is the mean pressure at each distal value found from the simulation and $\bar{P}_{i,j}^{d,k}$ is defined as

$$\bar{P}_{i,j}^{d,k} = \bar{Q}_{i,j}^{3D,k}R_{i,j}^{k} + \bar{P}_{i,j}^{3D,k} \tag{7.8}$$

where $\bar{Q}_{i,j}^{3D,k}$ is mean flow rate found from the simulation. This tuning was performed until there was less than 5 % from the expected and simulated average flow rate. In addition to the mean steady case a steady simulation was performed at maximum flow rate ($Q_{avg} = 13.0\frac{cm^3}{sec}$).

One simulation representing localized emphysema was performed. The location of the diseased regions were determined based off of information found from the experimental data (see Chapter 5). The experimental data suggested that the elastase created emphysema-like damage to the base of the cardiac, diaphragmatic and left lobes (see Figure 7.1). As the resistance remained unchanged between the healthy and emphysematous rats (see Chapter 5), the resistances for all airways of the localized emphysema cases were the same as those used for the homogeneous emphysema simulations. The localized emphysema case's healthy lobes (apical and intermediate) $C_{i,j}$ were defined as the same as the healthy simulations. The diseased lobes total compliance (diaphragmatic, cardiac and left lobes) were defined such that the total compliances of all the lobes equaled $C_{E,global}$. The lobes individual compliance was then divided based off of the lobe's volume. The diseased airways were defined with Eq. 7.4.

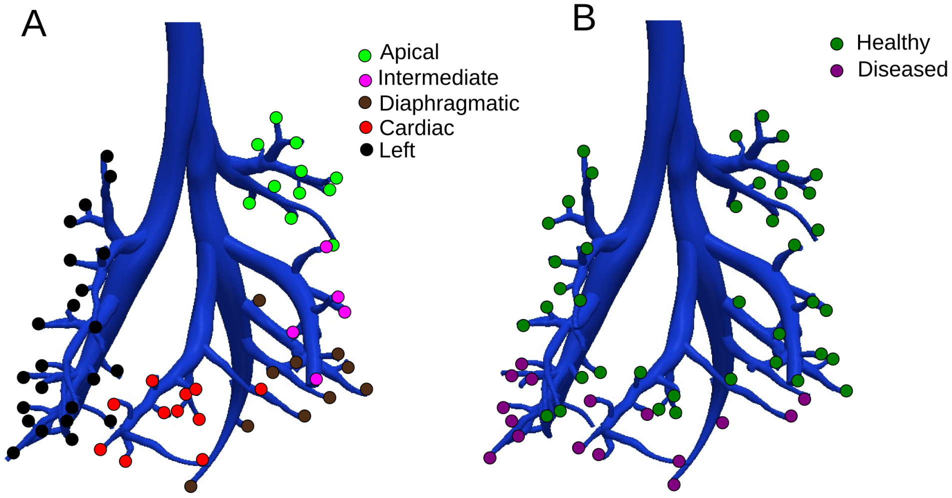

Figure 7.1: Airways leading to the left, apical, intermediate, diaphragmatic and cardiac lobes are outlined (panel A) and the healthy and diseased regions are outlined for the localized emphysema case (panel B).

Once the airflow in the 3D domain was found, inert, mono-disperse particles with a diameter of 0.95 μm and a density of 1.35 $\frac{g}{cm^3}$ were tracked throughout inspiration as described in Chapter 6. Total deposition, number of particles exiting each lobe and number of particles depositing on the walls airways within a lobe were determined from the simulation results.

7.2.2 Comparison of Simulated and Experimental Data

The number of particles exiting to each lobe, including the particles depositing on the airways within a lobe, were counted and normalized by the total number of particles simulated and was denoted the "delivery fraction." Doing this assumes that the number of particles depositing downstream of the 3D domain is

Table 7.1: Airflow Delivery to Each Lobe normalized by the Inhaled Volume, %. Percentage of flow exiting to each lobe for two steady cases at mean and maximum flow rate and unsteady case averaged over the entire cycle. For the mean and maximum flow steady cases the same resistances values were used for the distal airway boundary conditions.

	Expected	Steady Mean	Steady Max	Unsteady
Left	35.9	36.0	35.46	35.7
Apical	11.0	10.89	10.74	10.9
Intermediate	13.5	13.42	13.51	13.4
Diaphragmatic	28.0	28.0	28.55	27.8
Cardiac	11.6	11.67	14.60	11.5

proportional to the number of particles delivered to the lobe. This delivery fraction was compared to the deposition fraction found experimentally. The "deposition fraction" is defined as the number of particles depositing in each lobe, normalized by the total number of particles deposition in the rat lung.

The delivery and deposition fraction were normalized by the lobe volume percentage to determine the volume normalized delivery/deposition fraction. The delivery and deposition fraction comparison as well as the volume normalized delivery/deposition fractions were performed for both the healthy and emphysematous rat lungs.

7.3 Results

7.3.1 Healthy Airflow

The airflow delivery to each lobe for the mean steady flow case was less than 1% different from the expected flow division (see Table 7.1. For the maximum steady flow case, where the same resistances values as the steady flow case was employed, there was a 25% difference in the simulated flow versus the expected flow for the cardiac lobe. There was less than 1 % between the simulated and expected flow for the unsteady case.

The velocity and corresponding streamlines for the unsteady and steady simulation are shown in Figure 7.2 for maximum flow rate and Figure 7.3 for mean flow rate. As Figure 7.2 shows, flow structures developed in the unsteady case that did not occur in the steady case. These flow structures developed during the acceleration phase of the cycle and continue to be present throughout the rest of inspiration (see Figure 7.3. The flow in the steady cases (see Figure 7.3C and Figure 7.2B) slowed in the areas of the model where the cross-sectional area increased, as outlined by the red arrows on the Figures.

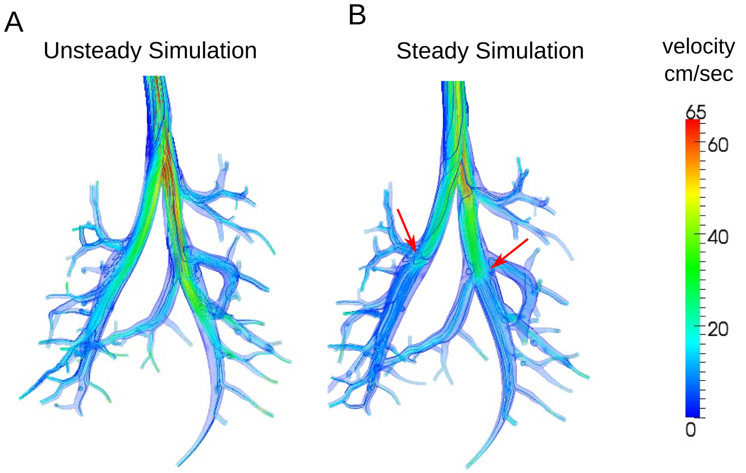

Figure 7.2: Comparison between unsteady (panel A) and steady (panel B) simulations at maximum flow rate, $1.3 * 10^4$.

The average velocity and streamlines for the extended airway model is compared to the 5 airway model in Figure 7.4. The flow structures in the extended airway model are more complex than the 5 airway model, as shown by the red arrows.

The airway resistance at maximum inspiration is shown in Figure 7.5. The airway resistance was calculated by dividing the pressure drop at the time of maximum inhalation flow rate in the 3D model by the maximum inhalation flow rate. Airway resistance tended to be higher for the small airways, as the pressure drop was highest for these airways.

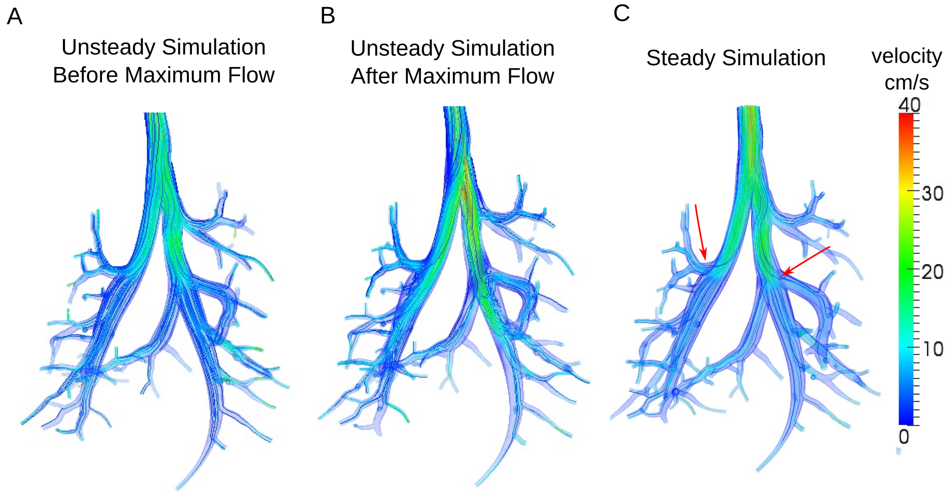

Figure 7.3: Comparison between unsteady (panels A and B) and steady (panel C) at the mean flow rate of 7.4 * 10^3. The unsteady simulation velocity plots are at the same flow rate as the steady simulation, but panel is is before maximum inspiration and panel B is after maximum inspiration.

7.3.2 Healthy Deposition

Simulated Deposition

Deposition locations for the unsteady and mean and maximum steady cases are shown in Figure 7.6. The percentage of particles that deposited in the 3D domain was 6.06%, 3.79%, and 6.28% for the unsteady, steady simulation at mean flow rate and steady simulation at maximum flow rate, respectively. Particles deposited at the bifurcation areas, areas where the flow slowed down (see Figure 7.3 for the unsteady case. In contrast, the deposition sites were much smaller and more compiled in the steady simulations (see Figure 7.6B and C).

Deposition hot spots for the extended model and the 5 airway model are shown in Figure 7.7. Both the extended and 5 airway model predicted deposition at the bifurcation areas (green arrows). However, the 5 airway model predicted deposition at the triple bifurcation area (red arrow), which was not a predicted spot for the extended model.

The number of particles depositing on the wall of the airways in each lobe is

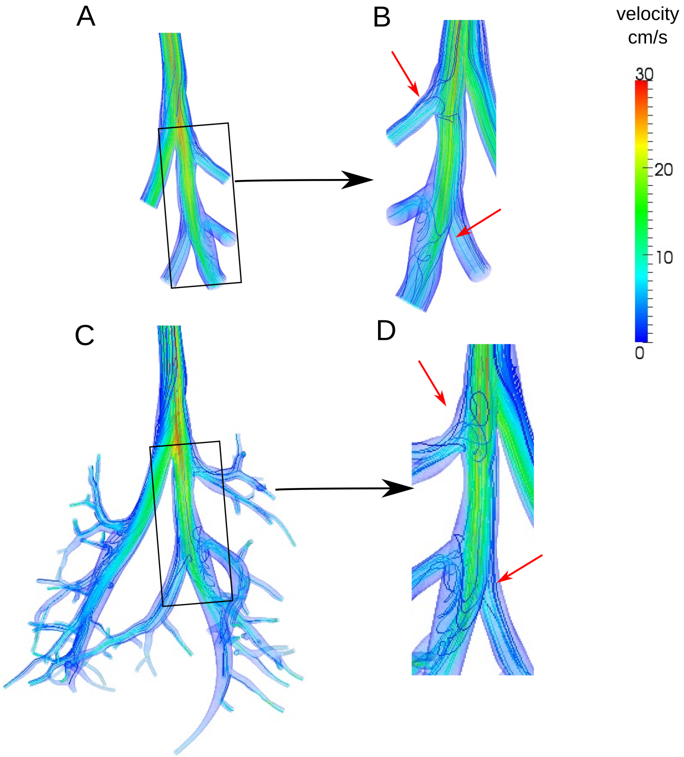

Figure 7.4: Comparison of the 5 airway model (panels A and B) to the extended airway model (panels C and D). Panels B and D are zoomed into backside of the regions outlined for the 5 airway model and extended airway model, respectively.

shown in Figure 7.8. The left lobe had the highest number of deposited particles, as this lobe contained more airways than any of the other lobes, i.e. 31 terminal airways.

Comparison of Simulated and Experimental Results

Figure 7.9 shows the normalized delivery of particles to each lobe and compared to the normalized experimental deposition data. Assuming that deposition of particles downstream of the 3D domain is directly proportional to the delivery of particles, there was good agreement between the simulated and experimental data. For all the lobes, the extended airway model was closer to the average experimental values than the 5 airway.

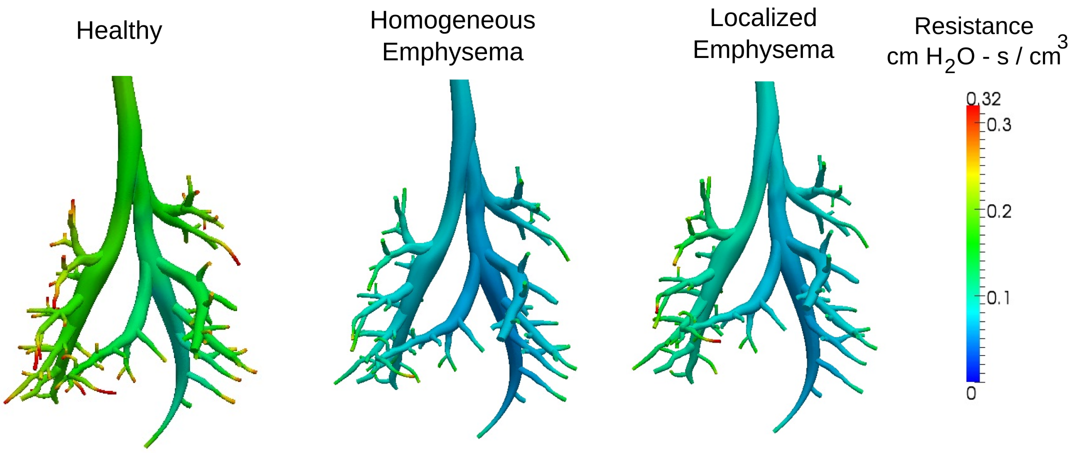

Figure 7.5: Airway resistance at maximum inspiration for healthy, homogeneous emphysema and localized emphysema simulations.

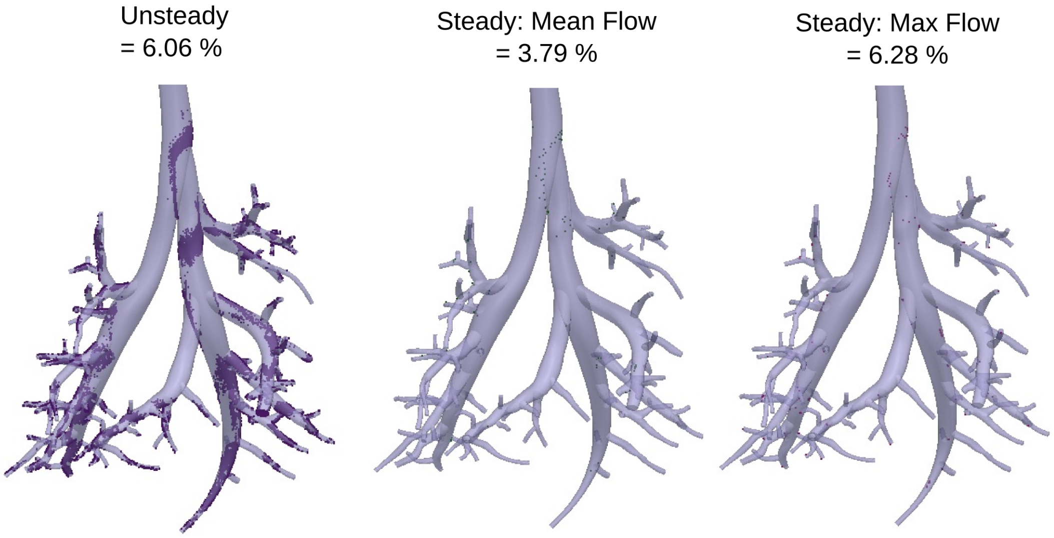

Figure 7.6: Comparison between unsteady simulation and steady simulations at mean and maximum flow rate.

Figure 7.10 shows the delivery/deposition fraction values shown in Figure 7.9 normalized by the lobe volume percentage. A value of 1 would indicate that

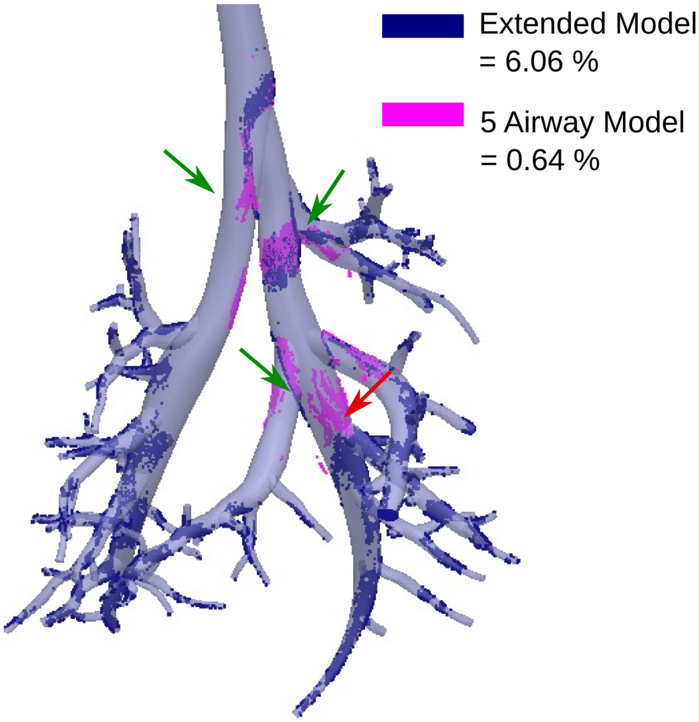

Figure 7.7: Comparison of deposition hot spots and total deposition with the 5 airway model and the full model.

particle delivery/deposition was directly proportional to the lobe volume percentage. For all cases the extended lobe matched slightly better to the experimental data than the 5 airway model. Both the simulated normalized particle delivery and experimental normalized deposition data was almost 1, therefore indicating that particle delivery to each lobe was proportional the the lobe volume.

7.3.3 Emphysema Airflow

Table 7.2 gives the flow division to each lobe for the homogeneous and localized emphysema cases with the extended and 5 airway model. The localized models both had a decrease in airflow delivery to the apical and intermediate lobes, compared to the homogeneous emphysema cases. However, the extended localized emphysema case also had a slight decrease in airflow delivery to the cardiac and diaphragmatic lobes and and a 30 % increase in delivery to the left lobe versus

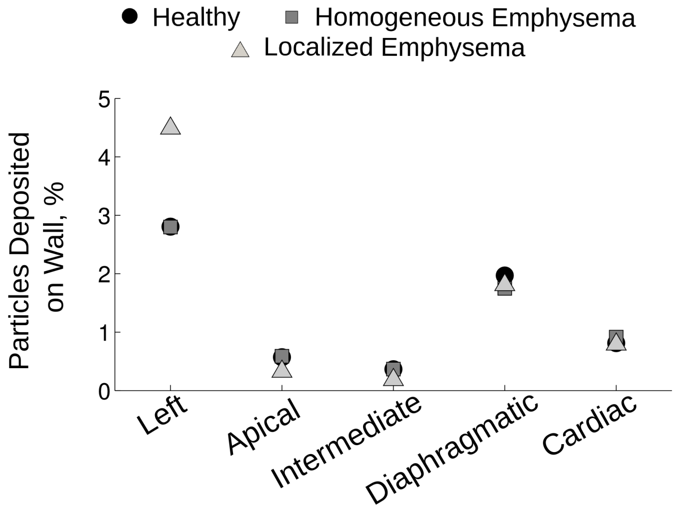

Figure 7.8: Percent of particles depositing on walls of the airways leading to the five rat lobes.

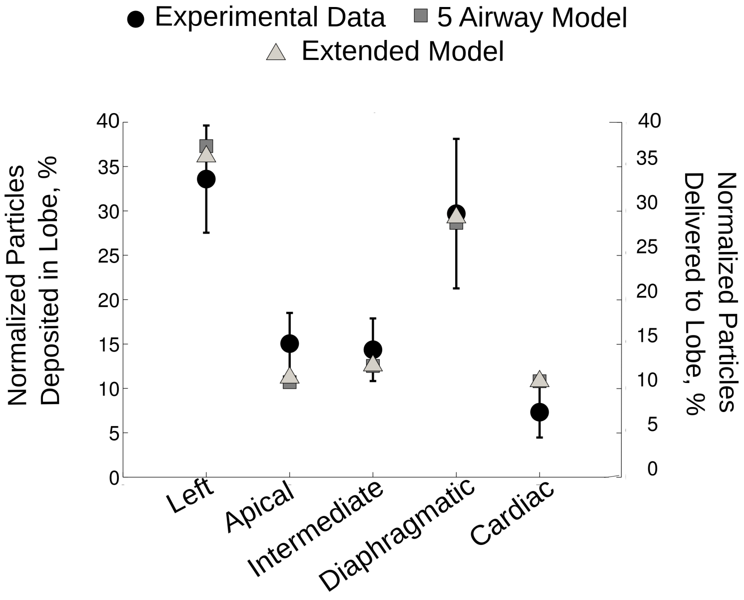

Figure 7.9: Deposited particles in each lobe found from MRI experiments normalized by the total deposition and the number of particles delivered to each lobe normalized by the total number of particles exiting 3D model.

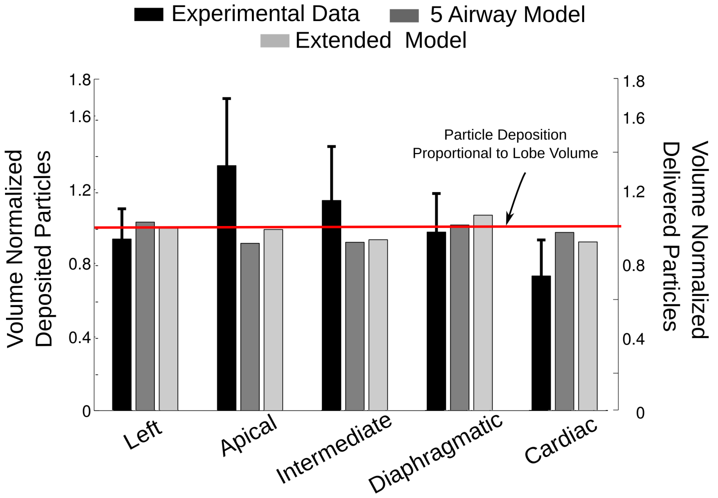

Figure 7.10: Particles deposited (experimental) or delivered (numerical) to each lobe, normalized by the lobe volume. A value of 1 would indicate that the deposition/delivery was proportional to the lobe volume.

only 8.9 % increase found in the 5 airway model. There was no changes in airflow delivery to the diaphragmatic and cardiac lobes.

Figure 7.11 shows the time averaged airflow in the localized emphysema cases for the 5 airway model and for the extended model. The velocity was greater in the trachea in the extended airway model compared to the 5 airway model. Panels B and D show the backside of the zoomed in regions outlined in Figure 7.11. The flow structures were more complex in the extended airway model (shown

Table 7.2: Airflow Delivery to Each Lobe Normalized by the Inhaled Volume, % for Emphysema Cases. Percent of flow leaving each lobe for the healthy, homogeneous and localized emphysema cases.

	Full Lung Model		5 Airway Model	
	Homogeneous	Localized	Homogeneous	Localized
Left	36.9	46.8	35.8	39.0
Apical	11.4	7.3	11.0	8.0
Intermediate	13.1	8.7	13.5	9.8
Diaphragmatic	26.3	25.2	27.9	30.5
Cardiac	12.0	11.6	11.6	12.7

with the purple arrow) than in the 5 airway model. However, flow structures were more complex in the 5 airway model at the triple bifurcation (shown with the red arrow).

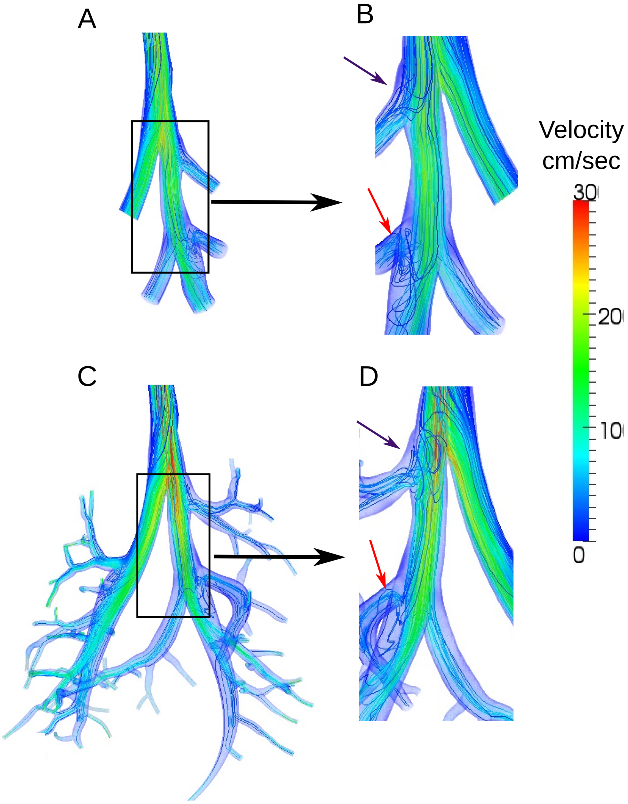

Figure 7.11: Time -averaged velocity for the 5 airway model (panels A and B) and full lung model (panels C and D) for localized emphysema cases. Panels B and D are zoomed into the backside of the outlined regions for the 5 airway and extended airway models, respectively.

The flow rate at the trachea throughout the breathing cycle is shown in Figure 7.12 for the homogeneous and localized emphysema cases. The flow rate during inspiration matched well to the 0D model solution for the homogeneous case. However, the flow rate was slightly faster for the localized emphysema case, especially at the deceleration areas. Figure 7.13 shows the mean flow rate (averaged for all the distal faces) of the healthy and diseased airways of the left lung. The diseased airways flow rate is not only larger than the healthy regions, but the shape and maximum flow rate time is different.

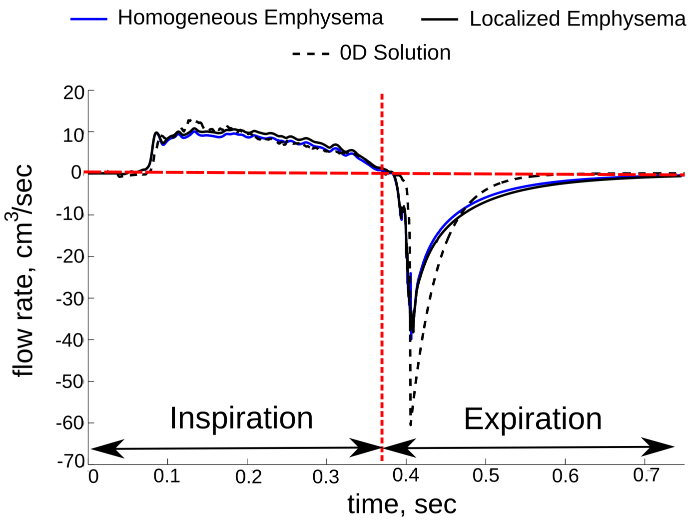

Figure 7.12: Velocity comparison between 5 airway model (panel A) and full lung model (panel B) for localized emphysema case

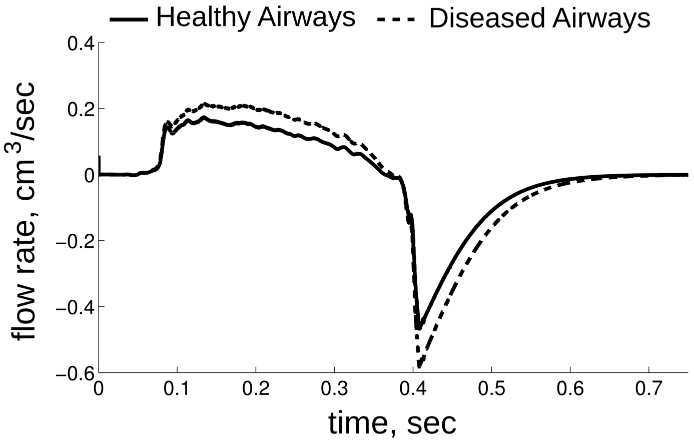

Figure 7.13: Mean flow rate in healthy and diseased regions of the left lobe for the localized emphysema case.

Figure 7.14 compares the time averaged velocity in the homogeneous (panel A) and localized emphysema (panel B) cases. The flow speed was higher in the left airways in the localized emphysema case (shown by red arrows) compared to the homogeneous emphysema case. However, the flow was slower in the apical and intermediate lobes. These findings agree with the flow split percentages given in Table 7.2.

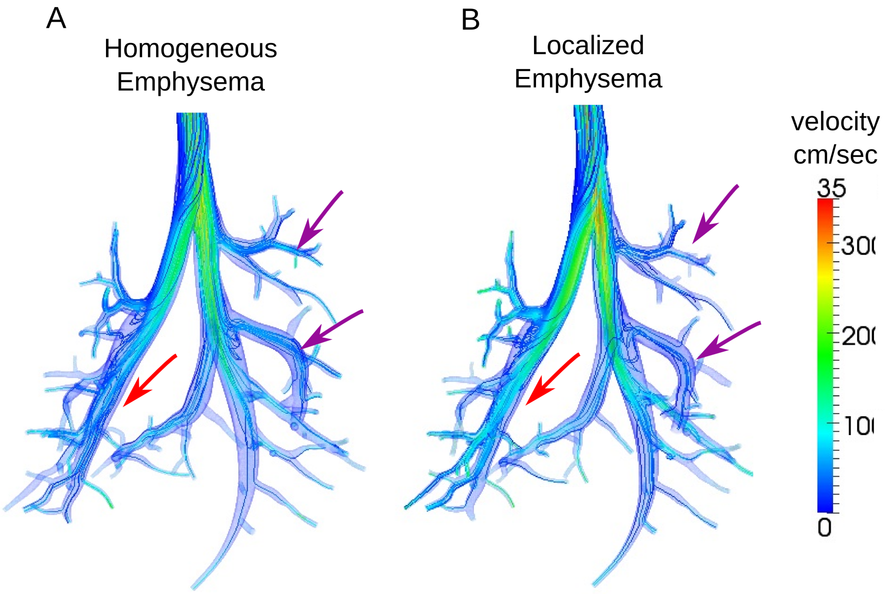

Figure 7.14: Average velocity with streamlines in 3D domain of homogeneous emphysema (panel A) and localized emphysema (panel B).

The pressure drop from the trachea to each of the airways at the time of maximum inspiration is shown in Figure 7.15. In general, the pressure drop was higher in the localized emphysema case compared to the homogeneous emphysema case. Additionally, the pressure drop was highest for the small airways in the left lobe and in the cardiac lobe. The resistance at the time of maximum inspiration in the homogeneous and localized emphysema cases are shown in Figure 7.5. Like the pressure drop, the airway resistance was higher in the localized emphysema case and was highest for the small airways.

The vorticity at maximum inspiration for the homogeneous and localized emphysema cases is shown in Figure 7.16. Areas of large vorticity were found for the small airways and at the bifurcation areas. The localized emphysematous lung had larger regions of high vorticity, as shown by the white arrows.

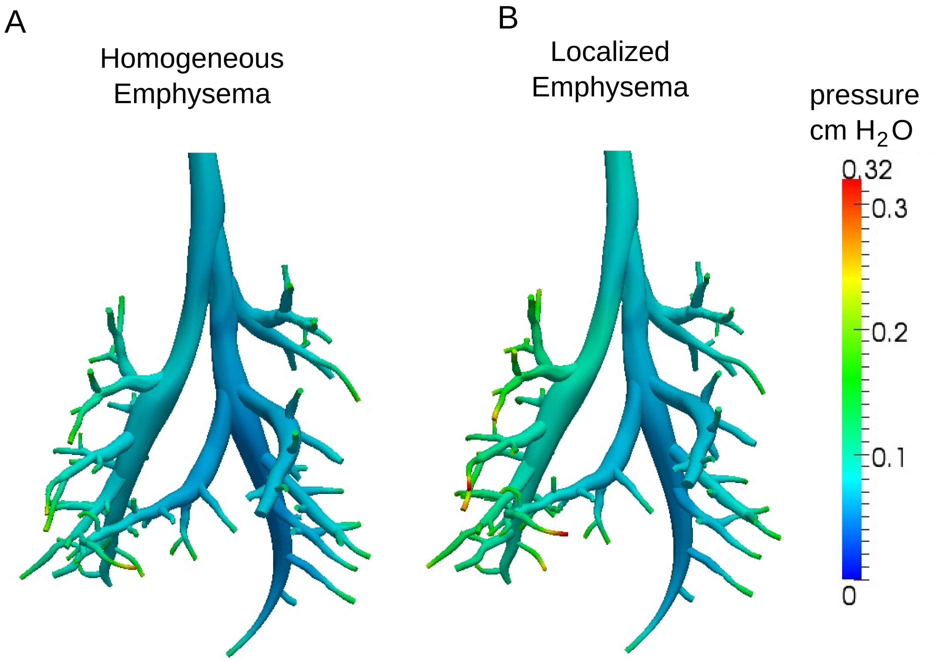

Figure 7.15: Average pressure drop in homogeneous (panel A) and localized (panel B) emphysema.

7.3.4 Emphysema Deposition

Simulated Deposition

Table 7.3 shows the percent change in deposition on the airway walls from the healthy to the emphysema cases. There was a $\sim$ 60 % greater number of particles depositing on the left airway face for the localized emphysema case compared to the homogeneous emphysema case. There was $\sim$ 43 and $\sim$ 50 % less particles to deposit on the faces of the the healthy lobes.

Deposition locations for homogeneous and localized emphysema cases are shown in Figure 7.17. Particle deposition was highest for the localized emphysema case, where 6.80 % of the particles deposited compared to 5.79 % for the homogeneous emphysema case. The localized emphysema had more particles deposit at the triple bifurcation area as well as in the left lobe, as shown by the black arrows.

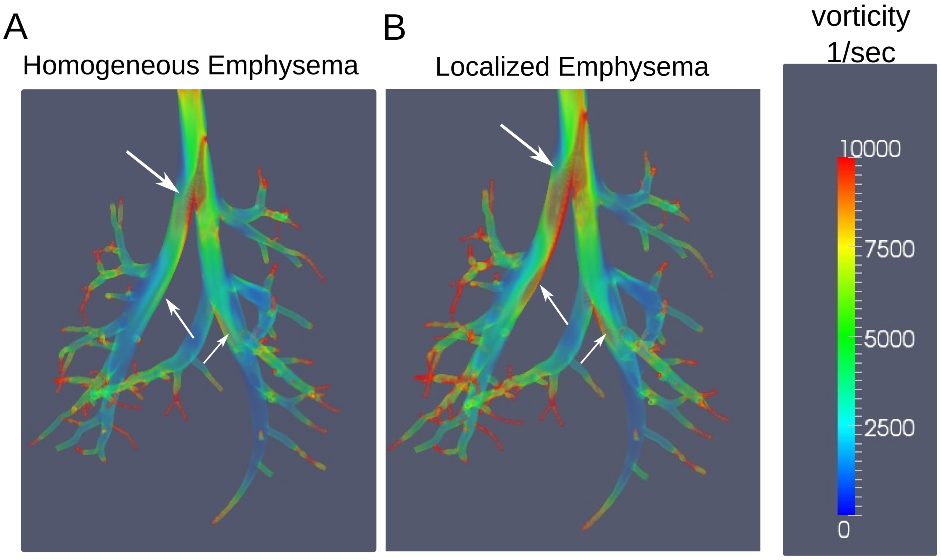

Figure 7.16: Vorticity at maximum inspiration for homogeneous emphysema (panel A) and localized emphysema (panel B).

Comparison of Simulated and Experimental Results

Figure 7.18 shows experimental deposition delivery fraction for the emphysematous rats and the normalized particle delivery fraction for the homogeneous and localized emphysema cases. The homogeneous emphysema simulation agreed well with the experimental data. However, the localized emphysema did not. The localized emphysema over predicted deposition in the left lobe and under predicted deposition healthy lobes (apical and intermediate).

Table 7.3: Percent change from healthy simulation for the number of particles to deposit on airway walls in each lobe

	Homogeneous	Localized
Left	-0.20	59.95
Apical	2.97	-42.9
Intermediate	0.46	-49.54
Diaphragmatic	-11.22	-8.14
Cardiac	12.57	-2.59

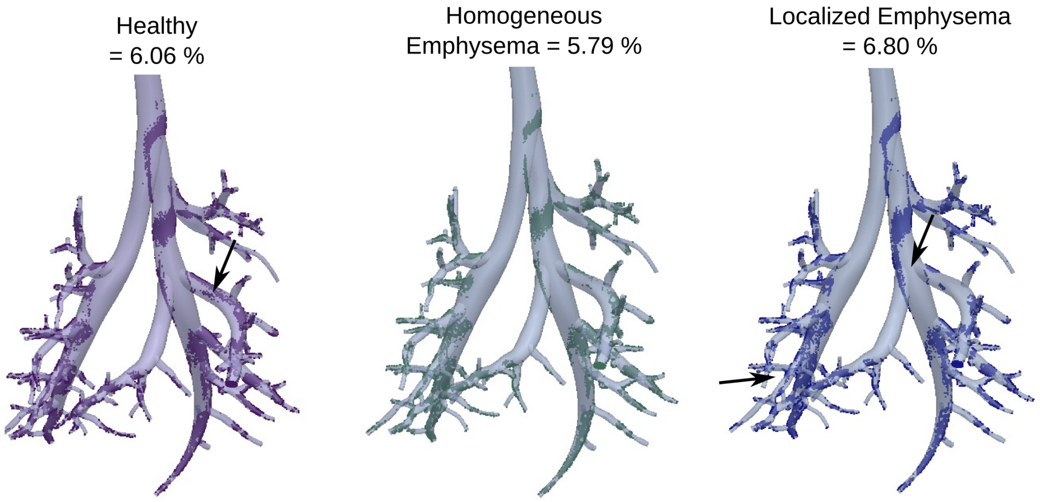

Figure 7.17: Deposition of particles in healthy, homogeneous and localized emphysema simulated models.

The volume normalized deposition and particle delivery data is shown in Figure 7.18. Even though the normalized deposition in the left lobe for the localized emphysema case over predicted the deposition, the volume normalized deposition matched well the experimental data.

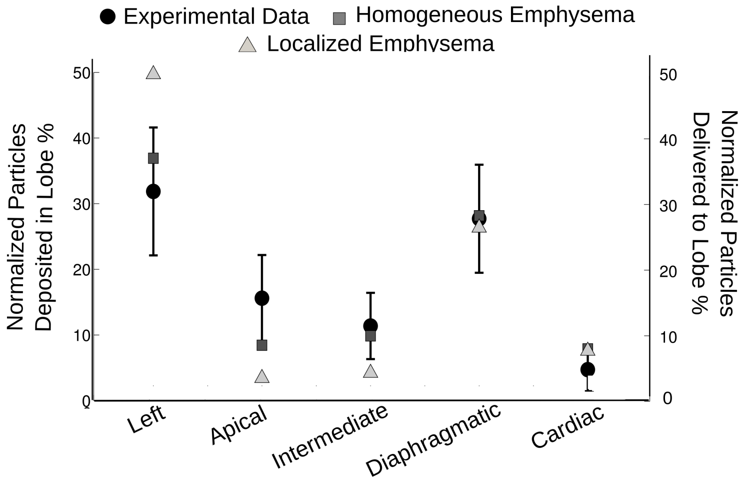

Figure 7.18: Deposited particles in each lobe found from MRI experiments normalized by the total deposition and the number of particles delivered to each lobe normalized by the total number of particles exiting 3D model.

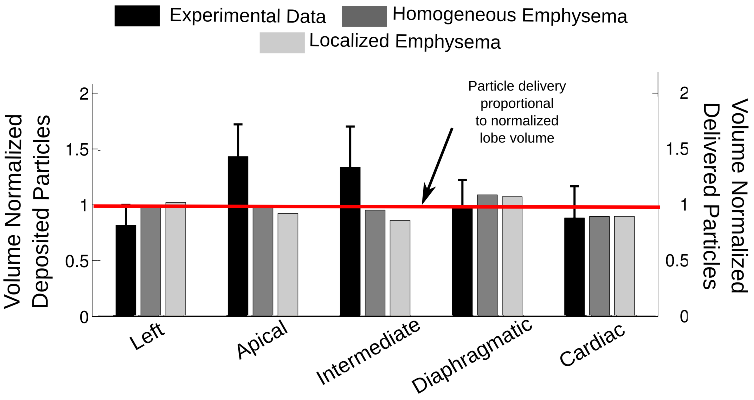

Figure 7.19: Particles deposited (experimental) or delivered (numerical) to each lobe, normalized by the lobe volume. A value of 1 would indicate that teh deposition/delivery was proportional to the lobe volume.

7.4 Discussion

Before this work, no studies have focused on comparing CFD simulated deposition prediction to animal experimental deposition data. Furthermore, little work has been done in understanding the influence of emphysema on particle deposition in the conducting airways as well as the distribution in the lung. This study expanded on the multi-scale framework developed in Chapter 6. The 5 airway model that was employed in Chapter 6 was extended to include up to 14 airway generations (see Chapter 2).

Unsteady and steady airflow simulations were performed for the healthy rat case. Several groups present steady particle deposition simulations [2, 4, 11]. However, it is unknown how these deposition predictions relate to unsteady breathing. Figures 7.2 and 7.3 show the difference in airflow between steady and unsteady simulations. Not only does the flow develop over time, as demonstrated by the evolving streamlines in Figure 7.3A and B, but there are also more complex flow structures in the unsteady simulations compared to the steady simulations. These different flow structures highly influence the particle deposition sites. For example, as Figure 7.6 shows, the deposition hot spots are quite different between the unsteady and steady simulations. In the unsteady simulations, particles deposit at the back of the wall of the airways, as this is the direction gravity is pointing, and at the bifurcation areas. However, in the steady cases the particles pile on top of each other and do not spread out. Simulations were performed with the same spatial density of particles at the inlet as well as for the same amount of time. Therefore, differences lie only in the different flow fields between the unsteady and steady simulations. Sensitivity on the particle seeding was performed for the unsteady case, however was not performed for the steady cases. Therefore, future studies should perform a seeding sensitivity analysis to ensure that this is not causing the differences between the steady and unsteady cases.

The flow and particle deposition sites were different between the 5 airway model and the extended airway model. If the geometry was exactly the same and the boundary conditions, and backflow stabilization were implemented correctly, then there should not be a difference between the 5 airway and extended airway models. However, the geometry was different near the outlets of the 5 airway model (see Figure 7.4). In constructing the 5 airway model, the airways were cut before the next bifurcation. For example, the extended airway model's apical lobe bifurcates where the 5 airway model does not. The differences in the flow field (Figure 7.4) and in the particle deposition sites (Figure 7.7) highlights the importance of including all of the airways that are available. If a true comparison on the effect of the boundary condition was desired, than the geometries between the 5 airway and extended airway models should be exactly the same.

The cardiac, diaphragmatic and left lobes were defined to contain the disease in the localized emphysema simulation. This was done by increasing the compliance in these lobes compared to the homogeneous and healthy simulations. Even though this was the case, the volume of air going to the cardiac and diaphragmatic lobes did not increase compared to the homogeneous simulation. Only the volume to the left lobe increased. The volume of air going to a lobe is defined based on the boundary conditions as well at the resistance in the 3D domain. Therefore, it is possible that the resistance going to the cardiac and diaphragmatic airways was greater than the left airway.

Good agreement was shown between the experimental and simulated deposition data. As the particles were not tracked once they left the 3D domain, it is unknown the fate of these particles downstream of the model. In reality, some of these particles will deposit and some of them will be exhaled. In Chapter 4, we predicted that 20 % of the inhaled particles deposited during the aerosol exposure experiments. Therefore, as only ∼6% of the particles deposited in the 3D model about 14 % must deposit downstream. Nonetheless, at this point it is reasonable to assume that some proportional of the delivered particles deposited. Therefore, Figures 5.10 and 7.18 both were created assuming that the number of particles to deposit was directly proportional the amount of particles delivered to that region of the lung. Therefore, differences in the experimental and simulated data may be contributed to not knowing the fate of the particles downstream. Determining the fate of the particles once they leave the 3D domain is a focus of future work.

The total percentage of deposition in the 3D model decreased in the homogeneous emphysema case and increased in the localized emphysema case compared to the healthy simulations. Homogeneous emphysema may be present in severe emphysema, as the disease has influenced most of the lung. In hamsters, Sweeney et al. [10] found decreased deposition in the emphysematous hamsters compared to the healthy hamsters. The 4.60% decrease in the homogeneous simulation compared to the healthy simulation matched the findings found by Sweeney et al. [10]. As hamsters are more susceptible to elastase [1] than rats, it may be assumed that these hamsters has a severe degree of emphysema, which may be similar to the homogeneous cases simulated in this chapter. The localized emphysema case, which may be representative of mild to moderate emphysema, had a ∼ 12 % increase in deposition compared to the healthy simulations and 16.7 % increase in deposition compared to the homogeneous case. This increase in deposition is in general agreement to the deposition data presented in Chapter 5 for the homogeneous and emphysematous rats. In Chapter 5, we found a 65 % increase in deposition in the emphysematous rats compared to the healthy rats. Therefore, as these numerical simulations suggest, 16.7 % of this increase in deposition was in the conducting airways included in the 3D model and 48.3 % were downstream of the 3D model.

In addition to not knowing the downstream deposition, the percent flow rate exiting each airway was unknown. Even though it is a reasonable to make the assumption that airflow is proportional to the cross-sectional area of the airway, this has never been measured. Alternatively, the downstream morphometry may be used to estimate the volume of the airways downstream from each of the terminal branches of the extended airway model. Detailed morphometric data is available [9] and may be used in future studies to determine the volume of air downstream of each terminal branch.

The disease location in the localized emphysema case was determined from the experimental data presented in Chapter 6. However, as shown in Figure 7.18, the homogeneous emphysema case more accurately predicted deposition than the localized emphysema case. This may be because (1) the diseased regions have higher small airway resistance that was not accounted for, (2) the disease may be not uniformly spread across the diseased regions, (3) the disease may be located in additional areas that was not account for in the localized emphysema model. Future work may alter the disease locations, such that future information about the disease location may be determined from the simulations.

7.4.1 Conclusion

This work extended on the 0D-3D multi-scale framework developed in Chapter 6. Here, an extended airway model was employed for the multi-scale simulations. As the airway resistance in this extended airway model was the same order of magnitude as the total respiratory resistance, the distal resistance values were tuned to achieve the desired flow split. The airflow structures were more complex and the particle deposition hot spots larger in the unsteady simulations compared to the steady simulations. There was less deposition in the homogeneous case and more deposition in localized emphysematous case compared to the healthy simulations. These findings are in agreement with studies that studied severe emphysema [10] and with this study that studied mild to moderate emphysema (see Chapter 5). Overall, particle delivery fractions were similar to the deposition fractions found experimentally for both the healthy and emphysematous rats. Considering the experimental error in working with rats, this good agreement was very encouraging. In the future, simulations should take into consideration the airways downstream of the 3D domain such that particle transport may be simulated through both inspiration and expiration.

7.5 Bibliography

[1] Borzone, G., Liberona, L., Olmos, P., Sáez, C., Meneses, M., Reyes, T., Moreno, R., and Lisboa, C. Rat and hamster species differences in susceptibility to elastase-induced pulmonary emphysema relate to differences in elastase inhibitory capacity. *American journal of physiology. Regulatory, integrative and comparative physiology 293*, 3 (Sept. 2007), R1342–9.

[2] Darquenne, C., Van Ertbruggen, C., and Prisk, G. K. Convective flow dominates aerosol delivery to the lung segments. *Journal of Applied Physiology 111*, 1 (July 2011), 48–54.

[3] de Rochefort, L., Vial, L., Fodil, R., Maître, X., Louis, B., Isabey, D., Caillibotte, G., Thiriet, M., Bittoun, J., Durand, E., and Sbirlea-Apiou, G. In vitro validation of computational fluid dynamic simulation in human proximal airways with hyperpolarized 3He magnetic resonance phase-contrast velocimetry. *Journal of Applied Physiology 102*, 5 (May 2007), 2012–23.

[4] Longest, P. W., Tian, G., and Hindle, M. Improving the lung delivery of nasally administered aerosols during noninvasive ventilation-an application of enhanced condensational growth (ECG). *Journal of aerosol medicine and pulmonary drug delivery 24*, 2 (Apr. 2011), 103–18.

[5] Longest, P. W., Tian, G., Walenga, R. L., and Hindle, M. Comparing MDI and DPI aerosol deposition using in vitro experiments and a new stochastic individual path (SIP) model of the conducting airways. *Pharmaceutical Research 29*, 6 (June 2012), 1670–88.

[6] Ma, B., and Lutchen, K. R. CFD simulation of aerosol deposition in an anatomically based human large-medium airway model. *Annals of Biomedical Engineering 37*, 2 (Feb. 2009), 271–85.

[7] Minard, K. R., Kuprat, A. P., Kabilan, S., Jacob, R. E., Einstein, D. R., Carson, J. P., and Corley, R. a. Phase-contrast MRI and CFD modeling of apparent (3)He gas flow in rat pulmonary airways. *Journal of magnetic resonance 221* (May 2012), 129–138.

[8] Oakes, J. M., Scadeng, M., Breen, E. C., Marsden, A. L., and Darquenne, C. Rat airway morhometry measured from in-situ mri-based geometric models. *Journal of Applied Physiology 112*, 12 (Mar. 2012), 1921–1931.

[9] Raabe, O. G., Yeh, H. C., Schum, G. M., and Phalen, R. F. Tracheobronchial geometry; human, dog, rat, hamster. Tech. rep., Lovelace foundation for medical education and research, Alburquerque, New Mexico, 1976.

[10] Sweeney, T. D., Brain, J. D., Leavitt, S. a., and Godleski, J. J. Emphysema alters the deposition pattern of inhaled particles in hamsters. *The American journal of pathology 128*, 1 (July 1987), 19–28.

[11] Walters, D. K., and Luke, W. H. Computational fluid dynamics simulations of particle deposition in large-scale, multigenerational lung models. *Journal of Biomechanical Engineering 133*, 1 (Jan. 2011), 011003.

Chapter 8

Conclusion and Future Work

8.1 Conclusion

8.1.1 Summary

This dissertation focused on determining particle deposition sites in healthy and emphysematous rats lungs. To do this, numerical and experimental tools were employed and the results from these separate methods were compared to each other. First, healthy rat airway geometries were extracted from MR images and validated against previous morphometric studies. Next, a novel MRI method was developed to quantify particle deposition sites in healthy rat lungs exposed to iron oxide particles. This MRI framework was then employed to study the differences in total and spatial distribution of particle deposition in healthy and emphysematous rat lungs. A multi-scale 0D-3D airflow simulation framework was developed to mimic the healthy and emphysematous rat experiments and to study particle deposition sites in the MRI-derived rat airway geometry. This numerical framework was then expanded to simulate airflow and particle transport in an expanded airway model. Healthy, homogeneous and localized emphysema cases were simulated. The spatial distribution of particles in the rat lung found experimentally and numerically were compared.

This study was the first to gather in-situ morphometric measurements and to generate and measure airway geometry of healthy Wistar rat lungs for airways with diameters greater than 0.4 mm. The airway diameter, length, bifurcation and gravitational angles were compared between four rats for the first four airway generations and little inter-animal variability was found. This low variation strongly suggested that a generic model may adequately describe the airway morphometry of rats of similar size and health. The morphometric measurements taken in this study were compared to previous studies [3, 6, 8] and showed good agreement for the airway length, gravitational, minor bifurcation, and rotational angles. However, the major bifurcation angles were larger than the previous studies and the airway diameters were smaller than found in the previous studies. The rat lungs proved to have both dichotomous and monopodial branching characteristics, depending on the lobe and location in the lung. Organizing the measurements using the diameter- defined Strahler ordering scheme resulted in low intra-order variability for airway lengths and diameters and was shown to be a useful tool to calculate physiological parameters such as lung resistance.

This study was the first to demonstrate the feasibility of using MRI to detect and quantify regional aerosol particle deposition sites in the lung using a gradient echo pulse sequence. While previous MR studies [7, 10] utilized the reduction in T_1 relaxation times to quantify regional delivery of inhaled aerosol, this study evaluated the potential use of R_2^* to assess aerosol deposition. The MRI signal decay rate, R_2^*, is a direct measurement of the field inhomogeneities caused by the super-paramagnetic iron oxide (SPIO) particles. This study showed that, compared to control animals, R_2^* was higher in rats exposed to particles with mass mean aerodynamic diameter (MMAD) of 1.22 μm. A linear relationship between R_2^* and particle concentration was quantified from an agarose phantom filled with a range of known particle concentrations. Employing this linear relationship, the particle concentration in the rat lungs was $1.42 \pm 0.60 \ \frac{\mu g}{mL}$. The particle concentration in the lung periphery (p) was 54 % higher than in the central (c) airways, resulting $\frac{c}{p}$ ratio of 0.65. This finding was in agreement to previous rat exposure studies that utilized similar particle size [5, 9].

The MRI tools developed in this dissertation were then employed to study total deposition and spatial distribution of particles in healthy and emphysematous rat lungs. Particle deposition sites have never before been quantified in mechanically ventilated emphysematous rat lungs. The signal decay rate, R_2^* and linear mean intercepts, L_M, were determined for the five lobes of the healthy and emphysematous rat lungs. As determined from R_2^* and L_M in the non-exposed emphysematous rats, the left, diaphragmatic, and cardiac lobes contained the majority of the damaged tissue. Additionally, the R_2^* values in the control lungs suggested that the disease was localized at the base of the left, diaphragmatic and cardiac lobes. In both the healthy and emphysematous rats, the apical and intermediate lobes had higher particles concentrations compared to the other three lobes. There was on average $\sim 68\%$ higher deposition in the emphysematous rats compared to the healthy rats ($p = 0.069$). The $\frac{c}{p}$ ratio was on average 0.74 ± 0.12 and 0.67 ± 0.14 in the healthy and emphysematous rats, respectively. However, unlike the healthy rats, there were statistical differences in the $\frac{c}{p}$ ratio between the lobes of the emphysematous rats. The data suggests that the morphometric and tissue compliance changes that occurred in the emphysematous rats resulted in increased particle deposition in the emphysematous rats compared to the healthy rats.

The multi-scale 0D-3D numerical simulations developed in this dissertation were the first to (1) model airflow in the rat airways by solving a multi-scale 0D-3D model that was parameterized directly from experimental data, (2) determine particle deposition and distribution in the rat lungs under unsteady breathing conditions and (3) understand the influence of emphysema on the deposition and distribution of particles in the lung. The global respiratory resistance did not change between the healthy and emphysematous rat lungs, however the compliance was higher ($p = 0.085$) in the emphysematous rats ($C = 0.37 \pm 0.14 \frac{cm^3}{cmH_2O}$) compared to the healthy rats ($C = 0.25 \pm 0.04 \frac{cm^3}{cmH_2O}$). The 0D-3D multi-scale simulations were performed by coupling 3D MR-derived rat airways to a resistance/compliance (RC) lumped parameter model. Particles were tracked in the flow field by solving the Maxey-Riley particle transport equations. The results showed showed that there was an increase in delivery of airflow and particles to the diseased lobe, which was most likely due to the lobe's increased tissue compliance. This finding suggests that, while emphysema reduces area for gas exchange to occur, airflow may be increased to the diseased regions, resulting in reduction of airflow to the healthy regions. Even though more particles are delivered to the diseased regions, it is unknown how they deposit once they leave the 3D domain. However, if the air becomes trapped, there may be an increase in deposition in emphysematous rats compared to healthy rats because of gravitational sedimentation. There was also a greater number of particles depositing in the 3D domain in the localized diseased cases compared to the healthy or homogeneously distributed emphysema case. This was mainly because there was more particle-laden air traveling through these airways.

Spatial distribution of particle deposition determined from CFD models have never before been compared to deposition sites in either animal or human lungs. The 3D model of the 0D-3D numerical framework was extended to include up to 14 airway generations. With this extended model, airflow and particle deposition were simulated in healthy, homogeneous and localized emphysema cases. The location of diseased tissue was determined based from the findings from the experimental data, i.e. the disease was localized at the base of the left, diaphragmatic and cardiac lobes. The delivery of particles to each lobe, normalized by the total number of particles delivered to the rat estimated in the simulations were compared to the deposition in each lobe normalized by the total deposition measured experimentally. Good agreement was found between the experimental and numerical deposition data for the healthy and homogeneous emphysematous rats. However, the localized emphysema simulated cases over predicted deposition in the left lobe and under predicted deposition in the diaphragmatic lobe. This difference may be justified to the fact that it is currently unknown how many particles deposit once they leave the 3D domain. In addition to the spatial distribution of particles in the lung, the simulations predicted that 5.92%, 6.80% and 7.64 % of the inhaled particles deposited in the numerical simulations for the healthy, homogeneous and localized emphysema cases, respectively. This resulted in a 29.1 % increase in the localized emphysematous case compared to the healthy case. This finding was in general agreement to the experimental finding that particle deposition was 62.5 ± 44.4 % higher in the central airways of the emphysematous rats compared to the healthy rats. The central region of the experimental data also contained airways downstream of the 3D CFD model therefore justifying the difference between the simulated and experimental findings.

8.1.2 Broader Impact

The study of particle deposition in the lung is applicable to both toxicology studies of inhaled pollutants and medical studies focused on the development of aerosolized therapeutics. Deposition mechanisms in the lung is mainly a function of the airflow and the particle diameter, shape and density. Therefore, findings from studies that use physiologically relevant particle sizes may be extrapolated to understand drug or pathogenic particles of the same size. In this study, deposition sites of particle with MMAD of 1.22 μm were determined both experimentally and numerically. Particles of similar size are found in diesel exhaust, cigarette smoke and therapeutics [4]. Therefore, findings from this dissertation may be of interest to both clinical aerosol scientists and toxicologists.

The deposition sites of particles in rat lungs were determined in this study. Rats are widely used in both toxicology studies and therapeutic studies to either test the effectiveness and safety of new drugs or to determine the health effects of pollutants. However, before this study, the fate of these particles after entering the lung was unknown, as typically only their overall impact on the rat is known. Quantifying the spatial deposition of these inhaled particles will allow for better understanding of the relationship between deposition sites and physiological reactions.

It remains unknown how data from animal aerosol exposure studies extrapolate to humans. Many animal experiments are invasive and therefore cannot be performed on humans. The advantage of respiratory in-silico models lie in their ability to predict particle deposition sites without performing invasive procedures. However, before this study, none of the current CFD models had been validated with either animal or human experimental deposition data. The multi-scale models developed in this study showed good agreement with measured experimental data. Therefore, the framework developed here may be eventually extrapolated to human geometry and breathing conditions to study particle deposition in patients.

Currently 3.7 million Americans have been diagnosed with emphysema [1], yet it is still unknown the fate of inhaled particles in this susceptible population. Some studies have found decreased deposition in emphysema [11], while other studies have found increased deposition in emphysema [2]. Emphysema is a chronic disease that is either caused by pollutant inhalation or alpha-1 deficiency. There is no cure for this disease and it gradually worsens over time. This dissertation showed that there was higher deposition in emphysematous rats compared to healthy rats. This new information may be used to develop evidence based standards for patients suffering from emphysema or to develop aerosol therapeutics that are designed for emphysema patients.

8.2 Future Work

8.2.1 Particle Deposition During Inhalation and Exhalation

Currently, no CFD models have been able to simulate particles through both inspiration and expiration. This is mainly because it is not currently computationally feasible to model all length scales of the lung. Therefore, simulations typically only track particles during inhalation, as was done in this dissertation. An alternative to this would be to develop a multi-scale model that couples the 3D Navier-Stokes equations solved in the conducting airways to the 1D Navier Stokes equations solved in the downstream small airways. Then, the terminal bronchioles may either be connected to empirical equations of the acinus or to a 3D deformable alveolar model [12]. With this approach, the 3D particle transport equations may be connected to the 1D particle transport equations allowing particles to be simulated throughout inspiration and expiration.

8.2.2 Optimization of Particle Deposition

Previous computational studied have studied the influence of particle size and breathing characteristics on particle deposition in the lung. However, none of these studies have performed a formal optimization of these parameters. An optimization study would allow for a wide range of parameters and their interaction to be studied. For example, the particle size, shape and density may be used as design parameters. In addition, the optimal release time of particles in the breathing cycle as well as the spatial density of the particles may be determined. The breathing parameters, such as flow rate, inhaled volume and breathing frequency may be also studied to determine their influence of particle deposition in the lung.

8.2.3 Multi-scale Modeling

The computational work presented in this dissertation is multi-scale in the sense that 3D models are connected to 0D reduced order models. However, the idea of multi-scale may be extended to include biological reactions or influence of particle deposition on whole body reactions. Therefore, future multi-scale models may also include mucociliary clearance of particles or macrophage uptake of particles into the body. The impact of particles entering the body may be determined from a multiple organ study.

8.2.4 Experimental Deposition Data

The experimental data presented in this dissertation was determined by employing highly invasive techniques. Currently 3D PET, SPECT and MRI measures are being developed to study particle deposition in humans with limited invasiveness. However, these studies currently do not provide the level of detail of deposition sites as those provided by CFD studies. As equipment and contrast agents are developed, it is highly likely that these studies will improve and therefore computational models may be validated at a finer scale than that presented within this dissertation.

8.3 Bibliography

[1] American Lung Association, 2009.

[2] W. D. Bennett, K. L. Zeman, C. Kim, J. Mascarella, D. William, L. Kirby, J. Enhanced Enhanced Deposition of Fine Particles in Copd Patients Spontaneously Breathing At Rest. *Inhalation Toxicology*, 9:1-14, 1997.

[3] Daniel R Einstein, Blazej Neradilak, Nayak Pollisar, Kevin R Minard, Chris Wallis, Michelle Fanucchi, James P Carson, Andrew P Kuprat, Senthil Kabilan, Richard E Jacob, Richard A Corley, An automated self-similarity analysis of the pulmonary tree of the Sprague-Dawley rat.. *The Anatomical Record*, 291:1628-1648, January 2008.

[4] John S Fleming, Matthew Quint, Livia Bolt, Ted B Martonen, and Joy H Conway. Comparison of SPECT aerosol deposition data with twenty-four-hour clearance measurements. *Journal of Aerosol Medicine*, 19(3):261–267, January 2006.

[5] Philip J Kuehl, Tamara L Anderson, Gabriel Candelaria, Benjamin Gershman, Ky Harlin, Jacob Y Hesterman, Thomas Holmes, John Hoppin, Christian Lackas, Jeffrey P Norenberg, Hongang Yu, Jacob D McDonald, Regional particle size dependent deposition of inhaled aerosols in rats and mice. *Inhalation Toxicology*, 24:27-35, 2012.

[6] Dongyoub Lee, Michelle V Fanucchi, Charles G Plopper, Jennifer Fung, and Anthony S Wexler. Pulmonary architecture in the conducting regions of six rats. *Anatomical Record*, 291(8):916–26, August 2008.

[7] Andrew R Martin, Richard B Thompson, and Warren H Finlay. MRI measurement of regional lung deposition in mice exposed nose-only to nebulized superparamagnetic iron oxide nanoparticles. *Journal of Aerosol Medicine and Pulmonary Drug Delivery*, 21(4):335–342, December 2008.

[8] O G Raabe, H C Yeh, G M Schum, and R F Phalen. Tracheobronchial geometry; human, dog, rat, hamster. Technical report, Lovelace foundation for medical education and research, Alburquerque, New Mexico, 1976.

[9] Otto G. Raabe, Mohamed A. Al-Bayati, Stephen V. Teague, and Amiram Rasolt. Regional deposition of inhaled monodisperse Coarse and fine aerosol particles in small laboratory animals. *Annals Occupational Hygiene*, 32(6):53–63, 1988.

[10] Beena G Sood, Yimin Shen, Zahid Latif, Xinguang Chen, Jody Sharp, Jaladhar Neelavalli, Aparna Joshi, Thomas L Slovis, and E M Haacke. Aerosol delivery in ventilated newborn pigs: an MRI evaluation. *Pediatric Research*, 64(2):159–164, August 2008.

[11] T D Sweeney, J D Brain, S a Leavitt, and J J Godleski. Emphysema alters the deposition pattern of inhaled particles in hamsters. *The American journal of pathology*, 128(1):19–28, July 1987.

[12] Josué Sznitman, Thomas Heimsch, Johannes H Wildhaber, Akira Tsuda, and Thomas Rösgen. Respiratory flow phenomena and gravitational deposition in a three-dimensional space-filling model of the pulmonary acinar tree. *Journal of biomechanical engineering*, 131(3):031010, March 2009.